Organic and Polymer Nonlinear Optical Micro-Resonators – A Single-Particle Micro-Spectroscopy Investigation

A Thesis Submitted for the Degree of

Doctor of Philosophy

by

VATTIKUNTA RADHIKA



School of Chemistry
University of Hyderabad
Hyderabad-500046
India
December-2019

Dedicated to

my

beloved parents

and sister

CONTENTS

Declaration		ı
Certificate		II
Acknowledge	ements	III-IV
List of Acrony	yms	V-XI
Chapter-1	Introduction	1-40
	1.1. Optical micro-resonators	1
	1.1.1. Fabry-Pérot (F-P) micro-resonators	2
	1.1.2. Whispering-gallery-mode micro-resonators (WGMRs)	5
	1.1.2.1. Mode structure	7
	1.1.2.2. Free spectral range (FSR)	9
	1.1.2.3. Quality (Q)-factor	10
	1.1.2.4. Photon life time (au_P)	13
	1.1.2.5. Polymer WGMRs	14
	1.1.2.6. WGMRs from dye doped polymer	15
	1.1.2.7. WGMRs from a blend of metallo- conjugated polymer and polystyrene (PS)	16
	1.1.2.8. WGMRs from charge transfer (CT) organic molecules and polymers	17
	1.1.2.8.1. WGMRs from intra molecular charge transfer (ICT) organic molecules	18
	1.1.2.8.2. WGMRs from inter molecular charge transfer polymers	19
	1.1.2.9. WGMRs from chiral molecules	21
	1.2. Nonlinear optical (NLO) properties	22

	1.2.1. Two photon absorption (TPA) and emission	24
	1.2.2. Molecules for two photon luminescence (TPL)	27
	1.3. Self-assembly	29
	1.4. Aggregation behavior in conjugated polymer	31
	1.5. Carbon dots (CDs)	34
	1.5.1. Optical properties of CDs	35
	1.6. Overview of thesis	37
Chapter-2	Flexible Micro-Ribbons and Rigid Micro-Rods from Self-	41-58
	Assembly of "Chalcone" Type Push-Pull Dye Molecules for	
	Vis/NIR Range F-P Micro-resonators	
	2.1. Abstract	42
	2.2. Introduction	42
	2.3. Results and Discussion	43
	2.3.1. Syntheses	43
	2.3.2. FTIR and Raman spectroscopic studies	47
	2.3.3. Optical properties of , (2E,4E)-1-(2-hydroxyphenyl)-5-	47
	(pyren-1-yl)penta-2,4dien-1-one (HPPD) and 2,2- difluoro-4-((1E,3E)-4-(pyren-1-yl)buta-1,3-dienyl)-2H-	
	benzo[d][1,3,2]dioxaborinin-3-ium-2-uide (HPPD-BF)	
	2.3.3.1. FL lifetime studies	49
	2.3.4. Self-assembly of HPPD and HPPD-BF	50
	2.3.5. Disassembly study of micro-ribbons	51
	2.3.6. Crystal structure of HPPD	52
	2.3.7. Single-particle micro-spectroscopy studies of HPPD	54
	2.3.9. Single-particle microscopic studies of HPPD-BF	57
	2.4. Summary	57

Chapter-3	2D Arrangement of Polymer Micro-Spheres	
	Photonic Cavities Doped with Novel N-Rich Carbon	59-72
	dots (CDs) Display Enhanced One- and TPL Driven	00 12
	by Optical Resonances	
	3.1. Abstract	60
	3.2. Introduction	60
	3.3. Results and Discussion	61
	3.3.1. Synthesis of CDs	61
	3.3.2. Optical properties of CDs	62
	3.3.3. Structural analysis of CDs	63
	3.3.4. Preparation of PS-CDs micro-spheres	66
	3.3.5. Microscopic studies of PS-CDs micro-spheres	67
	3.3.6. Single-particle microscopic studies of PS-CDs micro-spheres	68
	3.3.7. FL life time studies of PS-CDs micro-spheres	70
	3.3.8. NLO Studies of PS-CDs micro-spheres	71
	3.4. Summary	72
Chapter-4	Micro-Resonators from CT in Polymer Particles - toward Enhanced and Tunable Two-Photon Emission	I 73-94
	4.1. Abstract	74
	4.2. Introduction	74
	4.3. Results and Discussion	75
	4.3.1. Synthesis of 1-(4-vinylphenyl)-pyrene (1) monomer,	75
	Copolymer poly(styrene-co-4-(1-pyrene)styrene-co-	
	divinylbenzene) (PN) and preparation of PN-TCNB and	1
	PN-TCNQ CT complexes	
	4.3.2. NMR spectroscopy analysis of PN, PN-TCNB and	78
	PN-TCNQ CT complexes	

4.3.3. FTIR spectroscopy analysis of PN, PN-TCNB and F TCNQ	PN- 80
4.3.4. Thermal properties of PN, PN-TCNB and PN-TCNQ	81
4.3.5. Optical properties of PN, PN-TCNB and PN-TCNQ in DMF solvent	81
4.3.6. Optical properties of PN, PN-TCNB and PN-TCNQ in solid state	1 83
4.3.7. Self-assembly of PN, PN-TCNB and PN-TCNQ in to micro-spheres	85
4.3.8. Microscopic studies of PN, PN-TCNB and PN-TCNQ micro-spheres	85
4.3.9. Raman spectra of PN-TCNB and PN-TCNQ	86
4.3.10. Lifetime imaging of PN, PN-TCNB and PN-TCNQ micro-spheres	87
4.3.11. Single-particle microscopic studies of PN, PN-TCN and PN-TCNQ micro-spheres	B 88
4.3.12. Nonlinear absorption co-efficient (eta) measurement	s 90
4.3.13: TPL Studies of PN, PN-TCNB and PN-TCNQ	91
4.4. Summary	93
Chapter-5 Laser-Driven shifting of H-type Electronic Coupling to J- type in NLO Chiral Polymer Micro-Resonators - A Single- Particle Investigation	95-120
5.1. Abstract	96
5.2. Introduction	96
5.3. Results and Discussion	99
5.3.1. Syntheses of monomers and polymers	99
5.3.2. NMR spectroscopy analysis of R- and S-2,2'-diethoxy- 1,1'-binaphthyl-co-1,4-diethynyl-2,5-dioctyloxy Benzene (R- and S-BP)	103

	5.3.3. Number average molecular weight M_n of R- and S- BP polymers	105
	5.3.4. FTIR spectroscopy analysis of R- and S-BP polymers	105
	5.3.5. Differential scanning calorimetry of R- and S-BP polymers	105
	5.3.6. Optical properties of R- and S-BP polymers	106
	5.3.7. Self-assembly of R- and S-BP polymers	108
	5.3.8. Microscopic studies of R- and S-BP micro-spheres	108
	5.3.9. Aggregation behavior of R- and S-BP polymers	109
	5.3.10. Single-particle microscopic studies of R- and S-BP micro-spheres	111
	5.3.11. NLO microscopy studies of R- and S-BP micro- spheres	113
	5.3.11.1. Polymer chain packing dependent electronic coupling of R- and S-BP micro-sphere	114
	5.3.11.2. CD-TPL studies of R- and S-BP micro-	118
	resonators	
5.4.	Summary and Conclusion	119
Chapter-6	Conclusions	121-12
	Appendix A (Materials)	125
	Appendix B (Instrumentation)	126
	Appendix C (Crystal data)	131
	Research Publications	133
	Presentations in Conferences and Symposiums	134
	References	135
	CV	151

DECLARATION

I hereby declare that the matter embodied in this thesis entitled "Organic and

Polymer Nonlinear Optical Micro-Resonators – A Single-Particle Micro-Spectroscopy

Investigation" is the result of investigations carried out by me at School of Chemistry, in

the University of Hyderabad, Hyderabad, India under the supervision of Prof. Rajadurai

Chandrasekar.

In keeping with the general practice in reporting scientific observations, due

acknowledgements have been made wherever the work described is based on the finding

of other investigators. Any omission that might have occurred due to oversight or error in

judgement is regretted.

Vattikunta Radhika

Reg. No: 13CHPH14

ı



CERTIFICATE

This is to certify that the thesis entitled "Organic and Polymer Nonlinear Optical Micro-Resonators – A Single Particle Micro-Spectroscopy Investigation" submitted by Vattikunta Radhika bearing registration number 13CHPH14 in partial fulfillment of the requirements for award of Doctor of Philosophy in the School of Chemistry is a bonafide work carried out by her under my supervision and guidance. This thesis is free from plagiarism and has not been submitted previously in part or in full to this or any other University or Institution for award of any degree or diploma. Further the student has 3 publications before submission of the thesis for adjudication and has produced evidences for the same in the form of reprints.

Parts of this thesis have been published in the following four publications:

- 1. V. Radhika et. al. Chem. Phys. Chem. 2016, 17, 3435. (Chapter-2)
- 2. D. Venkatakrishnarao et. al. *Adv. Opt. Mater.* **2017**, *5*, 1700695. (Chapter-3)
- 3. V. Radhika et. al. ACS Appl.Mater.Interfaces.2018, 10, 16723. (Chapter-4)
- 4. V. Radhika et. al. Manuscript is to be communicated. (Chapter-5)

She has also presented oral/poster presentations in the following conferences:

- 1. Poster presentation in EAS-8-2017, CSIR-NIIST, Thiruvanthapuram, Kerala, India.
- 2. Poster presentation in CHEMFEST-2017, SoC, UoH, Hyderabad, India.
- 3. Oral presentation, CHEMFEST-2018, SoC, UoH, Hyderabad, India.

Further the student has passed the following courses towards fulfillment of coursework requirement for Ph. D.:

	Course	Title	Credits	Pass/Fail
1.	CY-801	Research Proposal	3	Pass
2.	CY-805	Instrumental Methods A	3	Pass
3.	CY-806	Instrumental Methods B	3	Pass
4.	CY-850	Chemistry of Materials	3	Pass

Prof. Rajadurai Chandrasekar (Thesis Supervisor)

Dean School of Chemistry

ACKNOWLEDGEMENTS

First of all, I would like to express my sincere thanks to my supervisor, Prof. Rajadurai Chandrasekar, without his innovative thoughts, feel for interesting ideas; it would not have been possible to accomplish my dissertation. I am indebted to him for suggesting the topic of *Optical Micro-Resonators*, which he gave me when I first joined in his group. I take this opportunity to express my gratitude towards my mentor for the immensely useful discussions during group meetings. Instead of being in the limelight, my supervisor guided, encouraged and provided support from the back of the stage. His way of approaching a scientific problem, interpreting the data, developing concepts and reaching a conclusion instigated me to improve substantially in the scientific research. It has been a wonderful experience working with him. I hope I can keep this scientific experience as a source for inspiration and creativity for my future endeavors.

Also I would like to acknowledge my doctoral committee members Prof. Pradeepta K. Panda and Prof. K. Muralidharan for their valuable suggestions. I thank the present and former Deans Prof. T. P. Radhakrishnan and Prof. M. Durgaprasad for the excellent facilities in the department. My special gratitude to Prof. Sri Ram Gopal Narahariseety, Prof. D. Narayana Rao, Chakradhar Sahoo, School of Physics, University of Hyderabad for NLO studies and fruitful collaboration.

I am very much thankful to Prof. Dr. Klaus Müllen (Max-Planck-Institut für Polymerforschung), for his support throughout my research work.

The five years in RC lab were intellectually very stimulating and I am grateful for the numerous discussions with past and present students and postdocs: Dr. Dasari Venkatakrishna rao, Dr. U. Venkataramudu, Dr. M. Annadhasan, J. Ravi, M. Jyothi, V. Vinay. A. Vinod, Rohullah, Anand, Sai Prasanna Kumar, Hemanth, and Raviteja.

I extend my gratitude to financial sponsor, UGC, New Delhi for providing research fellowship, as well as CIL for various instrument facilities. I am thankful to HCU for the excellent atmosphere and world class research facilities. It's my pleasure to acknowledge all non-teaching staff, Dr. M. Durgaprasad for TEM, AFM analysis, Mr. Sunil for FESEM analysis, Mr. Durgesh for NMR measurements, Parveige for ESI-Mass studies, Bhaskar for LCM analysis.

I am grateful to my family for their unconditional love, support and inspiration. I am forever indebted to my dad, who encouraged me to take Ph.D. at UOH. Specially my mom, who always inspires me to move forward in life. My sister stands by me always when I am in need. I would like to acknowledge this thesis to them I am really fortunate to have the best friends: Sree Laksmi, Vanaja, Ashwini, Srujana, Narasimhulu, sateesh, Ashok, Sneha for their support and encouragement.

V. Radhika

List of Acronyms

ACN	Acetonitrile
AFM	Atomic force microscope
AIBN	Azobisisobutyronitrile
ASE	Amplified spontaneous emission
BTH	Benzothiadiazole
BODIPY	4,4-difluoro-4-bora-3a,4a-diaza-s-indacene
BDT	4,7-bis(2-ethynyl-5-thienyl)-2,1,3-benzothiadiazole
BPP	2,6-bis(pyrazolyl)pyridine
С	Concentration of the sample
CCDC	Cambridge crystallographic data centre
CD	Circular dichroism
CDs	Carbon dots
CIE	Commission Internationale de l'Eclairage
CNDPASDB	(1,4-Bis(α-cyano-4-diphenylaminostyryl)-2,5-diphenylbenzene
¹³ C-NMR	Carbon nuclear magnetic resonance
COM	Confocal optical microscope
CPL	Circularly polarized luminescence
СТ	Charge transfer
CW	Continuous wave
DDQ	dichlorodicyanoquinone
DLS	Dynamic light scattering
DMF	N, N-dimethylformamide
DPPDO	1,5-diphenyl-1,4-pentadien-3-one
DSC	Differential scanning calorimetry
DVB	Divinylbenzene
E _A	Electron affinity
Ea	Atomic field strength

E B	Binding energy					
Eb	Exciton binding energy					
Ee	Energy of the excited state					
E_g	Energy of the ground state					
ΔΕ	Energy difference between ground and excited state					
E(t)	Time-dependent electric field strength					
Eı	Electric field intensity					
EDXS	Energy dispersive x-ray spectroscopy					
EM	Electro magnetic					
E-P	Exciton polariton					
ET	Electron transfer					
EtOH	Ethanol					
eV	Electron volt					
FESEM	Field emission scanning electron microscopy					
FL	Fluorescence					
FLIM	Fluorescence life time imaging microscopy					
F-P	Fabry-Pérot					
FRET	Fluorescence resonance energy transfer					
fs	Femtosecond					
FSR	Free spectral range					
FWHM	Full width at half maximum					
GM	Göppert-Mayer					
GPC	Gel permeation chromatography					
h	Planck's constant					
HDMAC	3-[4-(dimethylamino) phenyl]-1-(2-hy-droxyphenyl) prop-2-en-1-one					
¹ H-NMR	Proton nuclear magnetic resonance					
НОМО	Highest occupied molecular orbital					
HPPD	(2E,4E)-1-(2-hydroxyphenyl)-5-(pyren-1-yl)penta-2,4dien-1-one					

HR-TEM H Hz H I I I O	benzo[d][1,3,2]dioxaborinin-3-ium-2-uide High resolution TEM Hertz Intensity of the laser beam propagating along the z-axis Optical intensity Ionisation energy Intensity of incident light				
Hz Hz III	Hertz Intensity of the laser beam propagating along the z-axis Optical intensity Ionisation energy				
I II	Intensity of the laser beam propagating along the z-axis Optical intensity Ionisation energy				
I _a (Optical intensity Ionisation energy				
	Ionisation energy				
I _D					
	Intensity of incident light				
lo li					
$I(x,\lambda)$	Intensity of TPA light				
ICT I	Intra-molecular charge transfer				
IR I	Infrared				
J J	Joules				
I A	Angular mode number				
L	Micro-cavity length				
LCRM L	Laser Confocal Raman Microscope				
LCP L	Left circularly polarised light				
LUMO L	Lowest unoccupied molecular orbital				
$\overline{M_n}$	Number average molecular weight				
MHz N	Megahertz				
m.p.	Melting point				
$M(\vartheta)$	Photon density				
mJ N	Millijoules				
mW N	Milli Watt				
N N	No. of atoms per unit volume (number density)				
N ₂ F	Probability of TPA				
N _{gs}	Number of molecules per unit volume in the ground state				
N _{TPA} N	Number of molecules per unit volume in the excited state due to TPA				
n _{eff} E	Effective refractive index				
NA N	Numerical Aperture				

NIR	Near infrared					
<i>n</i> J	Nano Joule					
NLO	Nonlinear optics					
nm	Nanometer					
NMR	Nuclear magnetic resonance					
ns	Nano second					
P(t)	Time-dependent electric polarization					
$P^{(3)}(t)$	Time-dependent third-order nonlinear electric polarization					
PBI	Perylene bisimide					
PDA	Pyridine Diamine					
PDT	Photo dynamic therapy					
PDMS	Polydimethylsiloxane					
PL	Photoluminescence					
PMMA	Poly (methyl methacrylate)					
PN	Poly(styrene-co-4-(1-pyrene)styrene-co-divinylbenzene)					
PS	Polystyrene					
PS-CDs	Carbon dots doped polystyrene					
PVK	Polyvinylcarbazole					
PXRD	Powder x-ray diffraction					
QED	Quantum electrodynamics (QED)					
Q-factor	Quality factor					
q	Radial mode number					
R ₁	Reflectivity of front mirror					
R ₂	Reflectivity of rear mirror					
RCP	Right circularly polarised light					
RT	Room temperature					
SAED	Selected area electron diffraction					
SEC	Size-exclusion chromatography					
SEM	Scanning electron microscopy					

SERS	Surface-enhanced Raman scattering					
SNCs	Slab-nanocrystals					
SQDs	Inorganic semiconductor quantum dots					
SWCNTs	Single-wall carbon nanotubes					
t	Time					
τ _{avg}	Average FL life time					
T _{FL}	Photon decay time					
T(I _o)	Non linear transmission					
τρ	Photon life time					
TBAA	Tetrabutylammonium acetate					
THF	Tetrahydrofuran					
TCSPC	Time-correlated single photon counting					
TCBD	Tetracyanobutadiene					
TDSB	1, 4-dimethoxy-2,5-di[4'-(methylthio) styryl]benzene					
TCNB	Tetracyanobenzene					
TCNQ	Tetracyanoquinone					
TCNE	Tetracyanoethylene					
TE	Transverse electric					
TEM	Transmission electron microscope					
THF	Tetrahydrofuran					
T_{g}	Glass transition temperature					
TGA	Thermogravimetric analysis					
TIR	Total internal reflection					
TM	Transverse magnetic					
TPA	Two photon absorption					
TPL	Two photon luminescence					
TPL-CD	Two photon luminescence-circular dichroism					
UCPL	Up-converted PL					
UV	Ultra violet					

V _m	Mode volume					
Vis	Visible					
W	Width					
WGM	Whispering-gallery-mode					
XPS	X-ray photoelectron spectroscopy					
XRD	X-ray diffraction					
μ	Electric dipole moment of an atom					
μm	Micrometer					
χ ⁽¹⁾	Linear electric susceptibility					
χ ⁽²⁾	Second -order NLO electric susceptibility					
χ ⁽³⁾	Third-order NLO electric susceptibility					
εο	Free space permittivity					
ΔG°	Gibbs free energy difference					
Im (χ ⁽³⁾)	Imaginary part of the third-order nonlinear susceptibility					
Φ _{FL}	Quantum yield					
r _{res}	Radius of the resonator					
2πθ/ω	Angular frequency					
θ	Frequency of resonance mode					
Δθ	Line width of frequency of resonance mode					
α	One-photon absorption co-efficient					
β	TPA co-efficient					
Δ	Heat					
δ	NMR chemical shift reported in ppm					
λ	Resonating wavelength					
Δλ	Spacing between two adjacent modes					
λ _m	Reference peak wavelength					
λ_{max}	Wavelength maximum or absorption maximum					
λ _{ex}	Excitation wave length					
μJ	Micro joules					

π-π	Pi-Pi interactions
σ ₂	TPA cross section
Θ	Torsional angle
0D	Zero-dimensional
1D	One-dimensional
2D	Two-dimensional
3D	Three-dimensional
$ar{artheta}$	Wave number
°C	Celsius
KDa	Kilo Dalton
Rf	Retention factor
μL	Micro litre
mg	Milli gram
mL	Milli litre
μm	Micro meter
mm	Milli meter
ppm	Parts per million
min	Minute
mJ/cm ²	Intensity of pulse laser

1.1. Optical micro-resonators:

Optical resonators or cavities whose diameter is in the range of 1-20 μ m trap light to tiny volumes by resonant circulation. Thus, light-matter interactions take place several times in the optical resonators and consequently, emit the enhanced light at distinct resonant frequencies. [1,2] Devices constructed using optical micro-resonator are necessary for an extensive variety of uses such as enhancement, suppression, and even reverse the spontaneous emission of atoms/molecules in the micro-resonators, strong matter-field coupling resonator, quantum electrodynamics and dynamic filters in optical communication. [3,4] Further, optical micro-resonators are essential in the fabrication of microscale lasers, optical filters, nonlinear frequency synthesizers, [5,6] optical combs [7] and clocks [8] in quantum optics. Optical micro-resonators and gain media are fundamental components for generating the micro-lasers. [9] The gain medium enables the amplification of incoming light through stimulated emission, and the micro-resonator offers feedback for the light present in the gain medium. [10,11] Many π -conjugated organic molecules and polymers have four-level fluorescence (FL) processes yielding very high quantum yields (Φ_{FL}), thereby making them perfect contenders as gain media in micro-lasers. [12]

Inorganic micro-resonators the mirror-like facets are oriented in suitable orientation, providing high light reflectivity. Further, the surface quality (smoothness and defects) of the organic micro-resonator needs to be higher than that of an optical waveguide. Thus, optical scattering or leakage through defects will be minimized, which increases the light-trapping efficiency of micro-resonator. The captured light can reflect back and forth, or circulate leading to optical interference in the micro-resonator. Organic micro-structures with even shapes and high refractive indices (*n*>1.6) than the surroundings (mica, silica, etc.) can serve as high-quality micro-resonators. ^[13] Especially, the design and manufacturing of novel micro-resonators have been turned out to be the utmost main division in the area of organic micro-lasers. For instance, through crystal growth and self-assembly, resonators based on one-dimensional (1D) micro-wires and two-dimensional (2D) micro-plates have been fabricated. ^[14]

Generally, micro-resonators can be classified based on the direction of light confinement as,

- Fabry-Pérot (F-P) micro-resonators^[15]
- Whispering-gallery-mode (WGM) micro-resonators^[16]

Typically, 1D micro-structure usually functions as F-P resonators, whereas 2D or 0D structures act as WGM micro-resonators (Fig. 1.1). In this thesis work describes, F-P and WGM

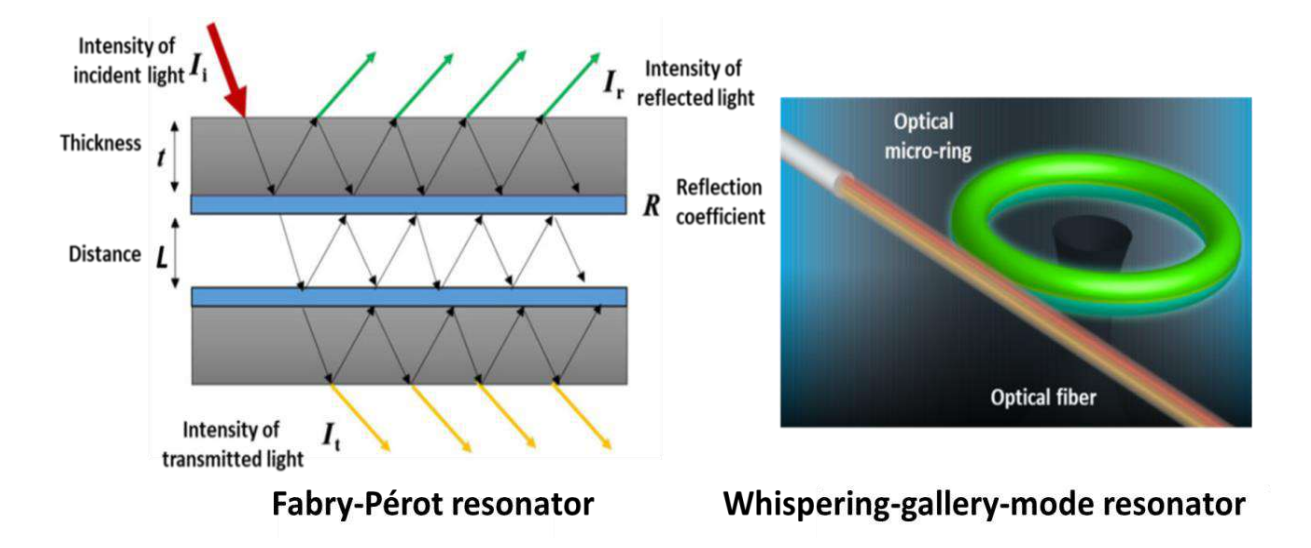


Figure 1.1: Micro-resonator configurations according to different light confinement methods. [Figure adopted from the references 17 and 18]

resonators made from organic and polymers through a bottom-up approach. Therefore, a short introduction to resonators is given in the following sections.

1.1.1. F-P micro-resonators:

F-P interferometer^[19] was first designed by Charles Fabry and Alfred Pérot for resolving the spectrum of light. F-P resonator consists of a pair of highly reflective plane mirrors with

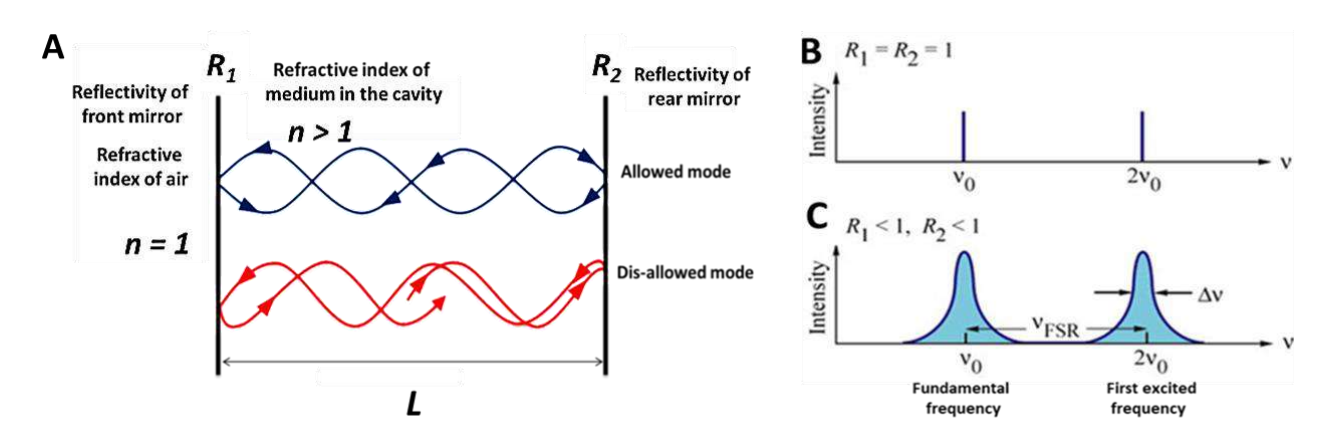


Figure 1.2: A) Schematic illustration of allowed and disallowed optical modes in an F-P resonator consisting of two coplanar reflectors. Optical mode density for a resonator with B) no mirror losses ($R_1 = R_2 = 100\%$) and C) mirror losses.^[20]

partial transmittance aligned opposite to each other (perpendicular to the optical axis), which are separated by some distance. When the incident light strikes one of these mirrors of a resonator with an angle greater than critical angle, [total internal reflection (TIR); n of the surrounding medium i.e., air n = 1 and that of the resonator n > 1] it enters through that mirror and reflected back and forth multiple times in between these mirrors. These multiple reflections lead to the superposition of all the reflected light waves which results in the electromagnetic (EM) field build up between these mirrors. Due to destructive interference, some reflected waves cancel each other out. However, those waves which interfere constructively lead to the optical modes or peaks in the FL spectrum (Fig. 1.2). EM field profile that defines the path and frequency of the resonating light is termed as the mode. In between the resonant modes, the nodes can be seen because of destructive interference of the light.

The above graphical representation of F-P resonator elucidates that the two reflectors of reflectivity R_1 and R_2 , which are separated by a distance L with a medium having n > 1. The optical path length of one round trip of the resonator is 2L, which is an integral multiple of resonant wavelength (λ) .

$$2nL = P \lambda \qquad ----- \blacktriangleright (1.1)$$

Where P is the longitudinal mode number. For a given optical resonator, numerous modes are allowed. Figures 1.2 B and C show the transmittance of light through a resonator with R = 1 and R < 1, respectively. In the frequency domain, the transmittance peak separation is referred to as the *free spectral range* (FSR), as shown in Fig. 1.2 C. The modes produced in the F-P resonator are normally longitudinal modes. [21] Longitudinal modes generation in the optical resonator is familiarized with the discourse of the F-P resonator. Longitudinal optical modes govern the radiative frequencies which fulfil the wavelength requirements of the optical microresonator. F-P resonators are utilized in controlling the linewidth of the laser as well as in the development of laser resonators. Further, F-P resonators isolate a single wavelength of light; they are instrumental in making wavelength filters, or calibration tool instruments.

Yao and his co-workers have described the mechanism of light propagation in the F-P resonator using exciton-polariton (EP)^[22-24] theory by taking organic micro-fibre active waveguide.^[25] One of the ends of the micro-fibre was excited using laser, which leads to the generation of excitons (electron-hole pair). The produced excitons further combine with photons resulting in the formation of EPs. At the opposite terminal of the micro-fibre, most of the EPs are transformed into low energy photons via charge recombination. Essentially these

photons are FL coming out from the distal terminal owing to the radiative recombination of the electron-hole pairs. Along with FL, a portion of the EPs can be redirected to the fibre by reflection at the distal terminal of the wire. Such a boundary can act as partially reflecting mirror of an F-P resonator. The FSR is related to micro-resonator length (*L*) through the following equation.

FSR (or)
$$\Delta \lambda = \frac{\lambda_m^2}{2 n_{eff} L}$$
 ----- (1.2)

Where λ_m is the reference peak wavelength, $\Delta\lambda$ is the difference in the frequency between two sequential resonant modes, and n_{eff} is the frequency-dependent effective refractive index. From eq. 1.2 one can see that: (i) FSR decreases with the increase of the micro-resonator length and (ii) in a given resonator the FSR values drop rapidly at higher light frequencies as $n_{eff}(\omega)$.

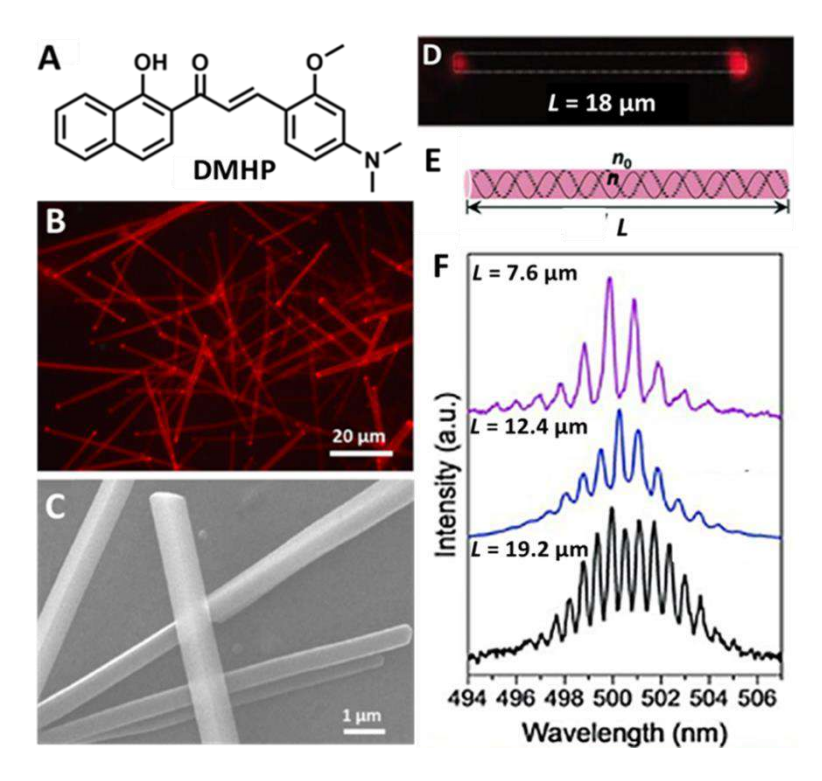


Figure 1.3: A) Molecular structure of (*E*)-3-(4-(dimethylamino)-2-methoxyphenyl)-1-(1-hydroxynaphthalen-2-yl) prop-2-en-1-one (DMHP). B) The FL microscopy image of the organic micro-rods excited with ultraviolet (UV) light (380 nm). C) FESEM image of the DMHP micro-rods. D) Confocal microscope image of the organic micro-wire with bright red spots at ends under 488 nm Ar⁺ laser point illumination. E). Schematic illustration showing a DMHP organic micro-rod as an optical waveguide, and with two ends defining an F-P resonator. F) Size-dependent F-P modes of micro-rods.^[26]

Liao et al. have reported a micro-rod composed of (E)-3-(4-(dimethylamino)-2methoxyphenyl)-1-(1-hydroxynaphthalen-2-yl)prop-2-en-1-one (DMHP). Owing to electron-donating behaviour of dimethylamino and methoxy groups and electron-withdrawing nature of carbonyl group, DMHP emits FL in the red region of the electromagnetic spectrum (Fig. 1.3 A) through intramolecular charge transfer (ICT) process. Single-crystalline micro-rods were prepared by selfassembling the DHMP in DCM/EtOH (1:1) solvent mixture (Fig. 1.3 B). Here, the natural shape of the crystal was determined by the equilibrium thermodynamics and kinetic conditions. The field emission electron microscopy (FESEM) confirmed that as-prepared micro-rods have rectangular cross-sections (Fig. 1.3 C). Upon optical excitation with 488 nm continuous wave (CW) laser, the micro-rod exhibited optical waveguiding tendency with bright red colour FL spots at the two ends (Fig. 1.3 D). Figure 1.3 E portrays that these micro-rods operate as F-P type optical feedback system. Here, the crystalline end facets of the micro-rod reflect red FL light thereby the light propagates back to the opposite end facet along the long axis of the micro-rod leading to bright tips. To study the size-dependency of optical resonance (as per eq. 1.2), several individual micro-rods with varying lengths were investigated in single-particle micro-FL spectroscopy measurements. Upon increasing the length (L) from 7.6 µm to 19.2 µm (Fig. 1.3) F), the FSR values decreased, confirming the optical resonance.

1.1.2. WGM micro-resonators (WGMRs):

Optically transparent circular micro-resonator can confine the light by TIR when the n of the resonators is greater than that of the surrounding medium (Fig. 1.4 A). The circularly confined light undergoes multiple reflections along the periphery of the resonator and returns to the same point in phase, forming resonating *standing waves*. [27] As a result, optical modes appear at different resonant frequencies, known as WGMs. The name originates from acoustic whispering observed at the dome (diameter = 40 m) of St. Paul's Cathedral in London by Lord Rayleigh. [28,29] Acoustic whispering gallery modes also occur in the central dome (D = 37.8 m) of the Gol Gumbaz, which is the second-largest dome in the world (Fig. 1.4 B). The resonance condition for the occurrence of WGMs is that the round trip length ($2\pi r$) of the resonator in which light propagates should be an integral multiple of the resonating wavelength (λ). The resonance condition can be expressed as

$$m\lambda = 2\pi r n_{eff}$$
 ----- (1.3)

Where m is an integer number associated with the angular momentum of the propagating photon inside the resonator, and r is the resonator radius. Under resonance conditions, the

circulating light intensity is allowed to enhance when the rate at which light is coupled to the micro-resonator is balanced by the rate at which it is lost.

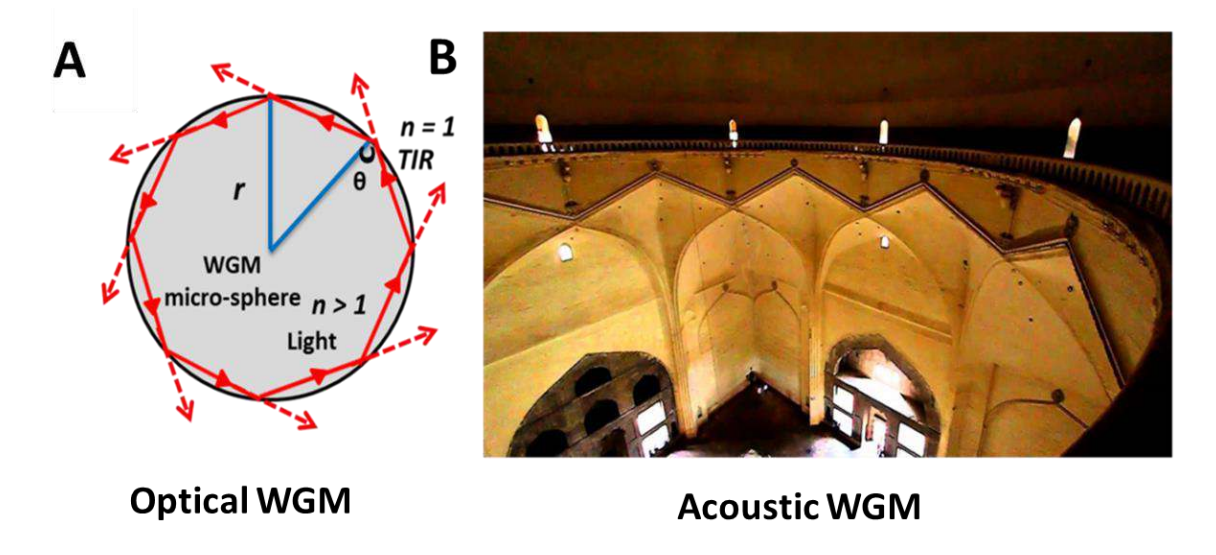


Figure 1.4: A) Schematic illustration of light confinement inside a WGM optical micro-resonator by TIR when incident angle (θ) greater than the critical angle. B) Picture of the interior of the dome of Gol Gumbaz.^[29]

Micro-resonators that are made from dielectric compounds such as silica, glasses, polymers and aerosol droplets though provide high *Q*-factor [described in detail in section 1.1.2.3], miniaturization of them are quite complicated. Further, incorporation of active optical gain material into these glassy resonators is difficult. These complications can be overcome by inorganic semiconductor materials having high optical gain. Currently, in WGM resonators FL organic dyes are used as gain materials to attain resonance modes at various wavelengths of interest. Optical resonators fabrication can also be achieved by top-down (wet-etching, various lithography techniques) and bottom-up (self-assembly, crystallization) techniques. [32-34]

To achieve high *Q*-factor, dyes are mixed with organic, or polystyrene (PS),^[35,36] poly(methyl methacrylate) (PMMA),^[37,38] and polydimethylsiloxane (PDMS).^[39,40] The properties of optical resonators supporting WGMs mainly depend on its shape and composition. WGMs not only supported by resonators having 0D micro-spherical geometry but also can exist in several geometrical structures like micro-hemisphere,^[40] micro-discs, ^[41,42] micro-rings,^[42,43] micro-toroids,^[44,45] cylindrical optical fibres and interesting structures like micro-bottles, micro-bubbles.^[38] Normally, FL molecules exhibit FL spectrum when excited in their electronic absorption region. Nevertheless, the same molecule when it is embedded into micro-

resonators displays several sharp distinct peaks (modes) in the FL spectrum due to the *Purcell* effect.^[46]

WGM resonances in these structures depend on the geometry (morphology) and n (dielectric property). Therefore, WGMs are also known as morphology-dependent resonances (MDRs). Furthermore, the evanescent wave present at the periphery of the resonator may be greatly affected by to external perturbations, which will alter the effective path taken by light inside the micro-resonators and thereby causing a shift in resonance peak (mode). [47] Excellent properties like small mode volume (V_m) [the ratio between energy stored inside the resonator in the mode and the maximum energy density of that mode], high photon density, [48] extremely small spectral linewidth, high-quality Q-factor of WGM resonators make them interesting for several applications. The above-said properties are applicable in nonlinear optical (NLO) process, low threshold micro-lasers, [49-51] high resolution spectroscopy, Raman sources, communications, sensitive micro-sensors like strong and label-free biosensors, [37,47] optical switching, in telecommunications as add-drop filters, notch filters, displacement measurements and to achieve amplified spontaneous emission.

1.1.2.1. Mode structure:

WGMs in resonators are described by three mode numbers, namely radial (q), azimuthal (m), and polar/angular (I) mode numbers, that are characteristically $m\gg 1$, $I\gg 1$, and $q\ge 1$, respectively. $^{[53]}$ m specifies the number of maxima of EM field within the equatorial direction. m takes the values of -I to +I. The numbers of peaks in the radial plane of the EM field inside the resonator is given by q. I provides the number of wavelengths in a round trip inside the resonator i.e., field oscillations in the polar direction. Modes having a single intensity maximum in the radial plane, which is restricted to the resonator/ambient boundary are said to be *first-order modes* (q=1). When the mode satisfies the following condition I=m, then the WGM is known as *fundamental mode* and the EM field is spread close to the equatorial plane. Comprehensive details about these mode numbers can be acquired from the finite-difference time-domain (FDTD) numerical simulation of the emission spectrum with WGMs. The electric field distribution for various mode numbers inside a WGMR is given in **Figure 1.5**. [54]

Each mode in WGMRs is defined by its polarization as transverse electric (TE) and transverse magnetic (TM).^[59] In TE mode the electric field is transverse to the direction of wave propagation and magnetic field is not purely transverse ($E_I = 0$, $H_I \neq 0$), whereas in TM mode,

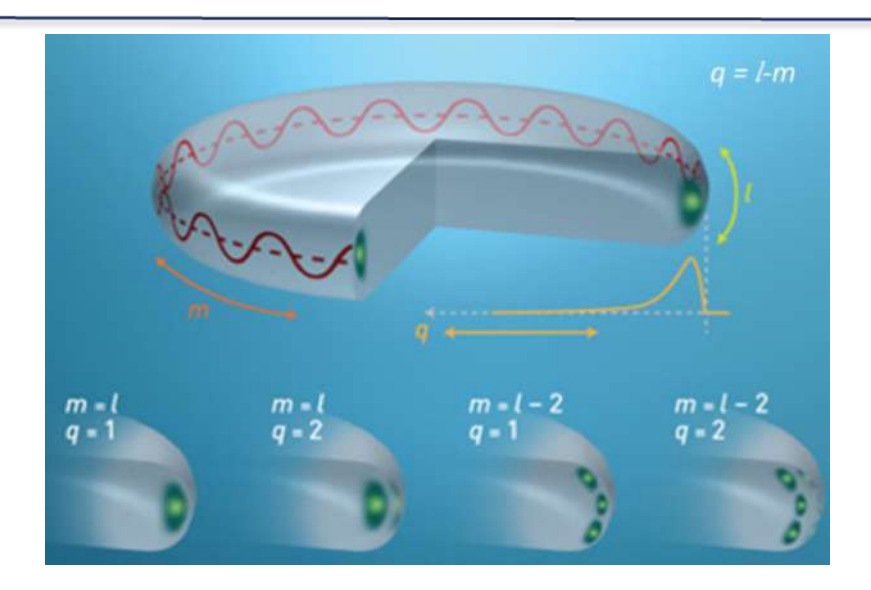


Figure 1.5: Spatial structure of WGMs with mode numbers (q, l and m). The electric field distributions are shown for various radial mode numbers q, and azimuthal mode numbers m. [Figure adopted from reference 54]

simply magnetic field is perpendicular to the direction of the propagating wave and electric field is not completely transverse ($H_I = 0$, $E_I \neq 0$). In general TM mode appear at lower wavelength followed by TE mode as per the following equations:^[55]

$$\lambda_{TE} \approx \frac{2\pi R n_1}{p + 1.856 p^{\frac{1}{3}} + \left(\frac{1}{2} - \frac{n_1}{\sqrt{n_1^2 - 1}}\right)}$$
 (1.4)

$$\lambda_{TM} \approx \frac{2\pi R n_1}{p + 1.856 p^{\frac{1}{3}} + \left(\frac{1}{2} - \frac{1}{n_1 \sqrt{n_1^2 - 1}}\right)}$$
 (1.5)

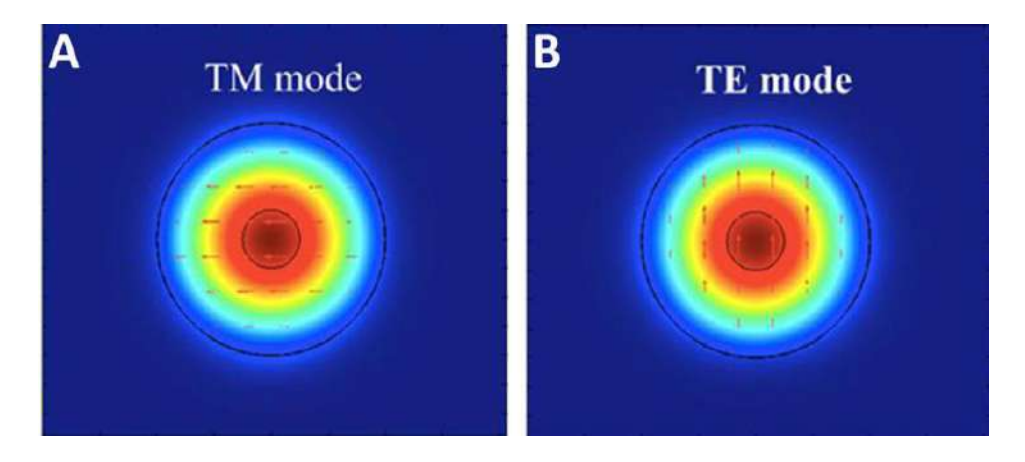


Figure 1.6: The electric field distribution for TE mode A) and B) TM mode. [56]

From the above expressions, it can be said that $\frac{n_1}{\sqrt{n_1^2-1}} > \frac{1}{n_1\sqrt{n_1^2-1}}$. [57] The TM and TE modes are

orthogonal to each other, shown in the simulation figures (**Fig. 1.6 A and B**). WGMRs are characterized by the resonator properties namely, FSR, Q-factor, V_m , photon lifetime (τ_P).

1.1.2.2. FSR:

FSR is an important parameter in WGMRs. The change in the frequency in the adjacent optical modes such as mode of order m and its next highest order mode m+1 (i.e., the spacing between two neighbouring TM or TE modes).

$$FSR = \Delta \lambda = \lambda_m - \lambda_{m+1} \qquad ----- \blacktriangleright (1.6)$$

FSR is connected to the resonator size (r) and wavelength maximum (λ_m) of the optical mode by the following equation:^[58]

FSR (or)
$$\Delta \lambda = \frac{\lambda_m^2}{2\pi r \, n_{\text{eff}}}$$
 ------ (1.7)

Where r is the radius of the resonator, $n_{\rm eff}$ is the frequency-dependent effective refractive index. From the equation (1.7), it can be clearly seen that FSR varies inversely with resonator length (effective radius) of the resonator. Therefore, micro-resonators with smaller radius (r) have larger FSR. Furthermore, $V_{\rm m}^{[30,59]}$ influences the FSR of the modes, smaller the $V_{\rm m}$ of the resonator, higher the value of the FSR.

The relationship between FSR and r can be understood by taking a WGM resonator composed of poly (9,9-dioctylfluorene-*alt*-benzothiadiazole) (F8BT).^[60] F8BT possesses electron-accepting benzathiadiazole and electron releasing alkylated fluorine in the polymer backbone providing high Φ_{FL} , which is required for high optical gain (Fig. 1.7 A). Here, to make the F8BT-based micro-spheres emulsion-solvent-evaporation method was followed. Cetyl trimethyl ammonium bromide (CTAB) water solution was injected with a solution of F8BT in chloroform to yield micelles. The F8BT molecules were embedded into water-repelling CTAB micelles upon constant stirring. The F8BT polymer whose back-bone bears a considerable amount of steric hindrance adds to the interfacial tension results in spherical structures upon vaporization of solvent molecules. The FESEM images indicated the spherical nature of the micro-spheres in addition to their smooth surface. Here, the surface smoothness provided WGMs with high Q-factors (Fig. 1.7 B). The FL image revealed the yellow color emission of micro-spheres (Fig.1.7 C). Further,

the FSR values decreased with increasing the micro-sphere size from 3.2 to 8.6 μm, confirming the size-dependency of the resonating modes as per eq. 1.7. (**Fig.1.7 D**).

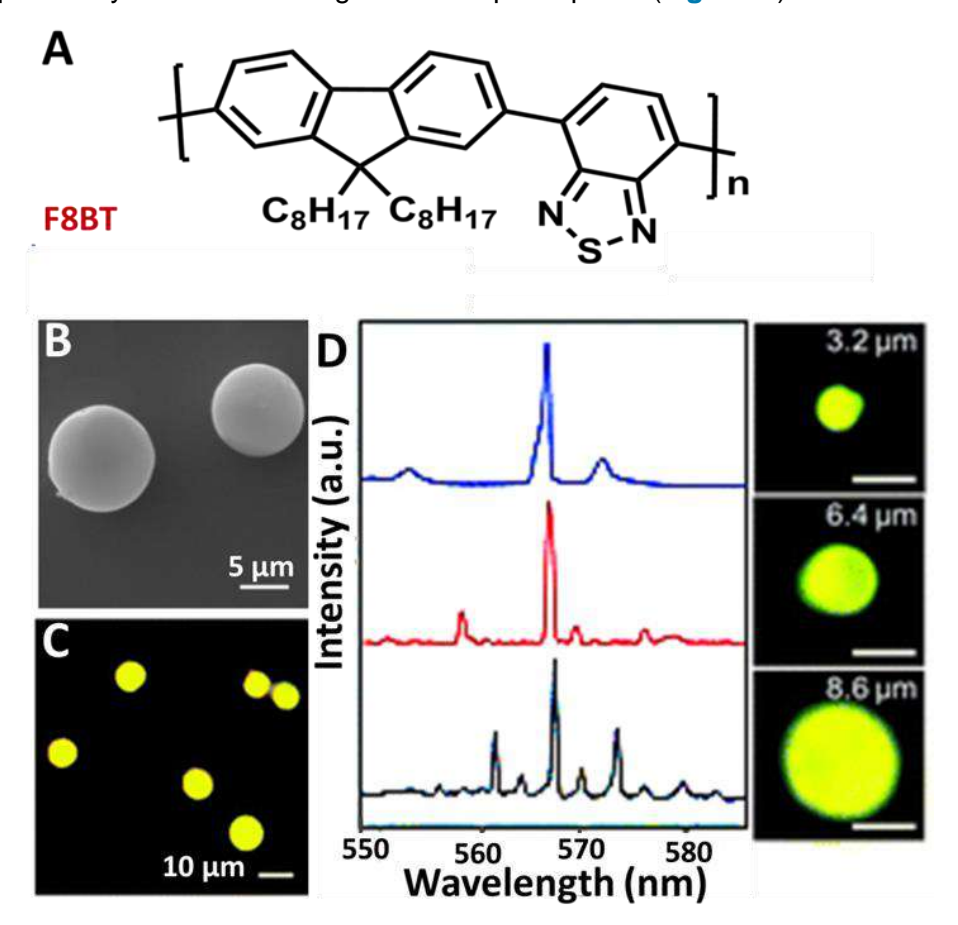


Figure 1.7: A) Structure of poly (9,9-dioctylfluorene-*alt*-benzothiadiazole) (F8BT). B) FESEM image of smooth-surfaced micro-spheres. C) Confocal microscope image of yellow emitting micro-spheres upon excitation with 488nm Ar⁺ CW laser. D) Single-particle FL spectra of F8BT micro-spheres with three different diameters displaying size-dependent WGM resonance. The right end shows the corresponding micro-sphere images.^[61]

1.1.2.3. *Q*-factor:

It is a parameter used for the determination of the operational bandwidth of a microresonator. From eq. 1.8, it is clear that when the linewidth of a mode decreases the Q-factor increases. Therefore, Q-factor can be quantified as the ratio of maximum peak wavelength λ_{max} to the full-width-at-half-maximum (FWHM) of the resonance peak $\Delta \lambda_{fwhm}$. [59]

$$Q = \frac{\lambda_{max}}{\Delta \lambda_{fwhm}}$$
 (1.8)

It can also be stated as the frequency of resonance mode having a high intensity to that of line width, which can be explained by the following expression

$$Q = \frac{\vartheta}{\varDelta\vartheta} \qquad \qquad ----- \blacktriangleright (1.9)$$

It is also termed as the ratio of the power stored to the energy loss per cycle.

$$Q = \frac{power\ stored}{power\ loss} \qquad ----- \blacktriangleright (1.10)$$

WGM resonators will have a high Q-value if there is a low loss of the optical resonator. There are several loss mechanisms that can contribute to the overall loss of the resonator. In a realistic condition, the Q-factor is determined by the absorption loss (Q_{abs}) , inherent seepage of light connected to flawed reflection ensuing from the defective curvature of micro-resonator (Q_{curv}) , loss due to light scattering from the unevenness of the micro-resonator surface (Q_{scat}) and the loss induced by waveguide coupling (Q_{coup}) . All of them are intrinsic losses except Q_{coup} , which is an extrinsic loss. Finally, Q-factor can be obtained by the following equation such as

$$\frac{1}{Q_{total}} = \frac{1}{Q_{abs}} + \frac{1}{Q_{curv}} + \frac{1}{Q_{scat}} + \frac{1}{Q_{coup}} - ------ (1.11)$$

The loss resulting from the material absorption is an important limitation to the WGMRs. For that, it is necessary to select a material with a little absorption loss. The scattering loss is due to surface irregularities and contaminants on the resonator surface. It is possible to minimize the loss by refining the fabrication method to lower the roughness of the resonator surface. Mostly, for organic/polymer WGMRs *Q*-factors range from 10³ to 10⁶ said to be high and those exceeding 10⁷ to be ultrahigh. [62,63] Micro-resonators having large *Q*-factors are extensively used in micro-lasers.

In this context, Chandrasekar and his coworkers have demonstrated a perovskite doped polymer micro-spherical resonators with a *Q*-factor of 2000. In order to prepare the micro-spheres, to a solution of PS (25 mg/4 mL of DMF), 20 µL of 0.05 M benzyl ammonium lead iodide (BALI) in DMF was added, followed by ultra-sonication for 30 s. Later, 1 mL of millipore water was mixed to the prepared solution and left undisturbed for 10 min at r.t. Later, 100 µL of the obtained solution was drop-casted on a coverslip and left undisturbed to allow slow solvent evaporation to obtain micro-particles (**Fig. 1.8 A**). Single-particle micro-spectroscopy experiments were carried out on confocal optical microscopy (backscattering mode) to examine

the photonic properties of micro-structures. Upon electronic excitation of an edge of a single micro-sphere with CW laser (Ar⁺ 488 nm; power: 10 mW; objective: 150x) exhibited FL in the

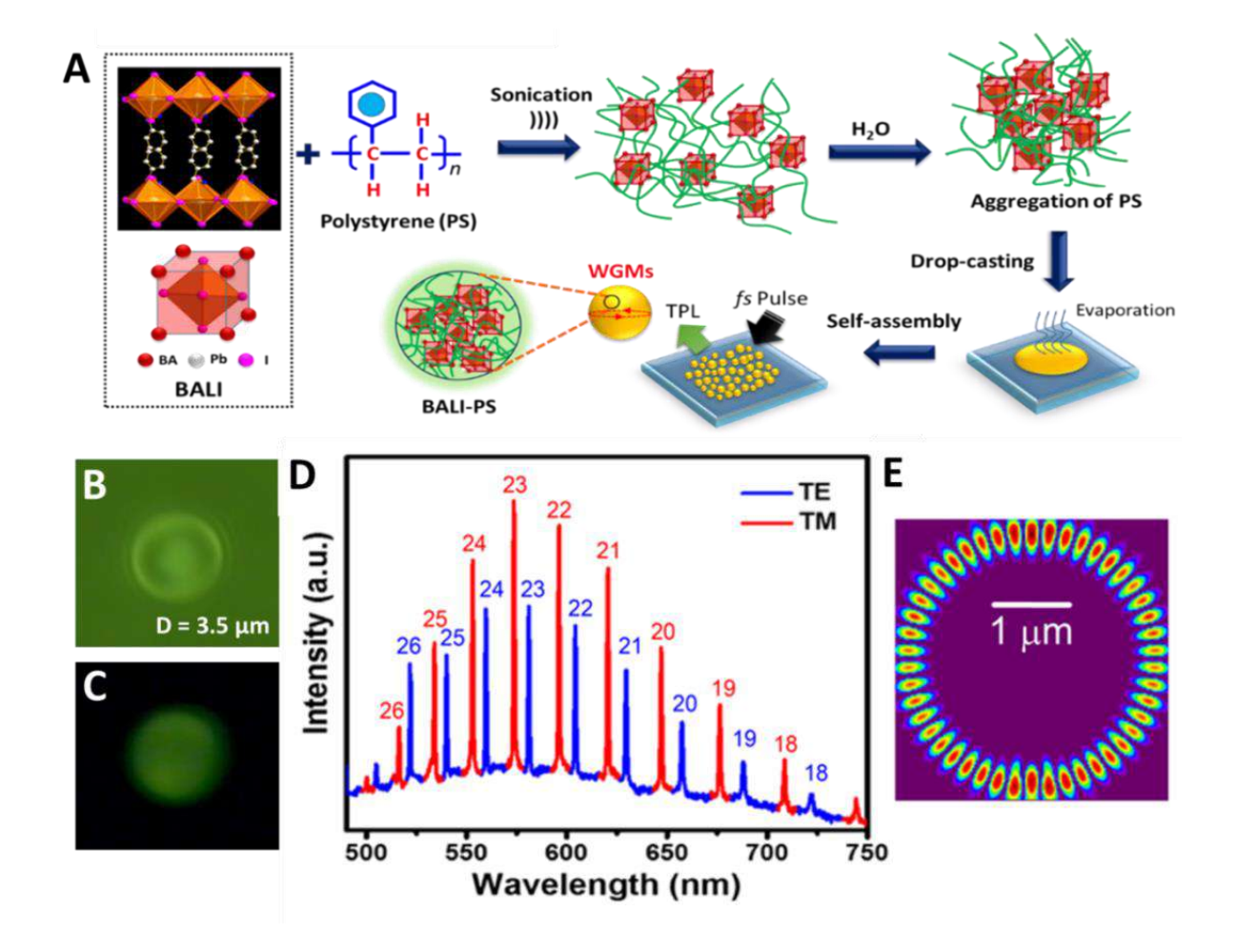


Figure 1.8: A) Fabrication of BALI-PS composite micro-spherical WGMRs via self-assembly method. B) and C) shows the bright field and FL images of a BALI-PS composite micro-resonator excited with CW laser (488 nm). D) Single-particle FL spectrum of micro-spherical WGM resonator. E) FDTD numerical simulation of a micro-spherical resonator displaying the electric field distribution for TE_{23} and the corresponding mode volume 1.83 μ m³. [64]

green region of the EM spectrum with several pairs of wavelength-dependent peaks identified as WGMs (**Fig. 1.8 B and C**). Another important characteristic of the WGM spectrum is without FL background, which directs toward high Q-resonators. A 2D FDTD method was used to calculate the WGM spectrum (for q = 1; m = l) and the spreading of the electric field within the micro-resonator. The pair of peaks were assigned as TM and TE with different azimuthal mode numbers from TM_{18} - TM_{27} and TE_{18} - TE_{27} , respectively (**Fig. 1.8 D**). The calculations also displayed that the electric field is highly concentrated along the periphery of the micro-

resonator (for TE₂₃) (Fig. 1.8 E). The approximate TE₂₃ mode volume of micro-spheres is calculated to be $1.83 \, \mu m^3$.

1.1.2.4. Photon Life Time (τ_P):

Normally Q-factor quantifies the time taken by a photon for residing inside the microresonator (τ_P). τ_P is different from photon decay lifetime (τ_{FL}) which counts the time required for a photon to decay from the excited state during spontaneous emission. Q-factor is connected to the τ_P of the resonator by the following equation: [30,59]

$$\tau_P = \frac{Q}{2\pi\theta} \qquad \qquad ----- \blacktriangleright (1.12)$$

Where $2\pi\vartheta$ is linear frequency. From the above relation, it can be said that the Q-factor has a linear relationship with the τ_P . That means, if a micro-resonator has a higher Q-value, the line width of the resonance peaks will be narrowed, leads to the high photon energy, subsequently, τ_P will be longer inside the resonator. When Q_{scat} and Q_{abs} are minimal in the resonator, photon stays more time in the resonator and it results in longer propagation time of photon. Therefore, the higher the τ_P value better is the light-matter interaction.

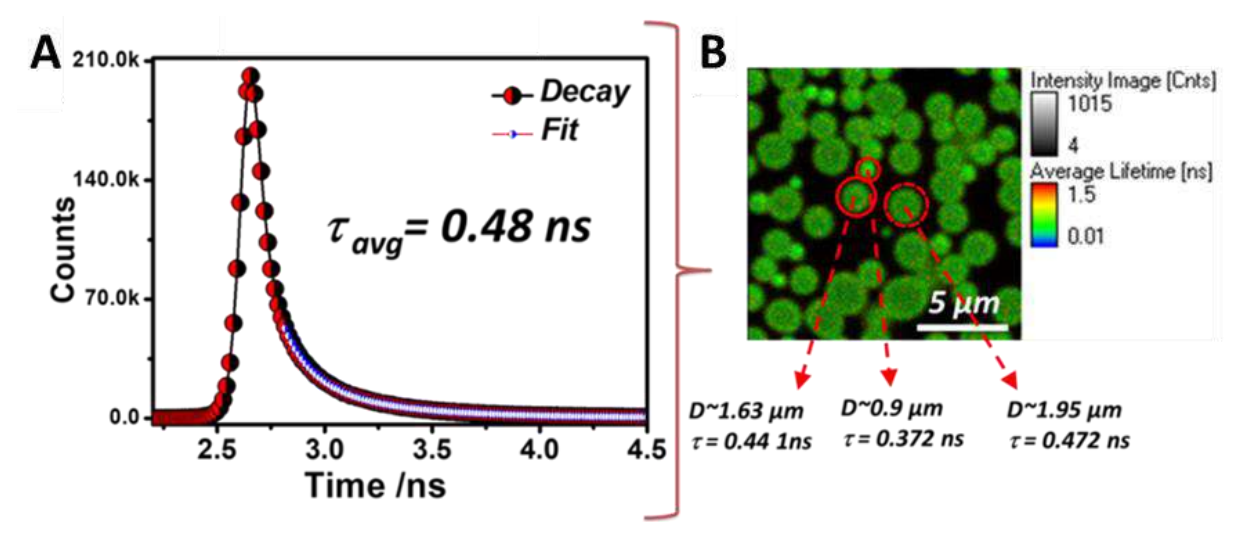


Figure 1.9: A) FL average decay lifetime profile of curcumin dye and B) The equivalent FLIM image in the right section. In dotted circles in the FLIM images display size-dependent lifetime values.

In case of curcumin dye, the fluorescence lifetime imaging microscopy (FLIM) images of micro-particles of 15×15 μ m² area displayed an average FL decay lifetime values (τ_{avg}) of 0.485 ns (**Fig. 1.9 A**). This value was higher compared to the value observed for corresponding homogeneous thin films ($\tau_{avg} = 0.291$ ns).^[68] Remarkably, micro-particles also displayed a

variable τ_p for the particle of different sizes (Fig. 1.9 B). The larger micro-particles trap more light than smaller ones producing larger Q-factors, which subsequently increase the τ_P values.

1.1.2.5. Polymer WGMRs:

In recent times, due to its high exciton binding energy (E_b) (Frenkel exciton $E_b = 0.1$ to 1.0 eV) and ease of production, WGMRs made of organic^[33,34] and polymer (π -conjugated, ^[60,69-71] charge transfer (CT), ^[72] or dye-doped^[35,40,73-75]) have emerged to compete with the inorganic WGMRs. Organic resonators pave the path for better bandgap tunability and solution processability. These outstanding properties make them appropriate for the fabrication of self-assembled optical micro-resonators with resonance emission extending from UV to near-infrared (NIR).

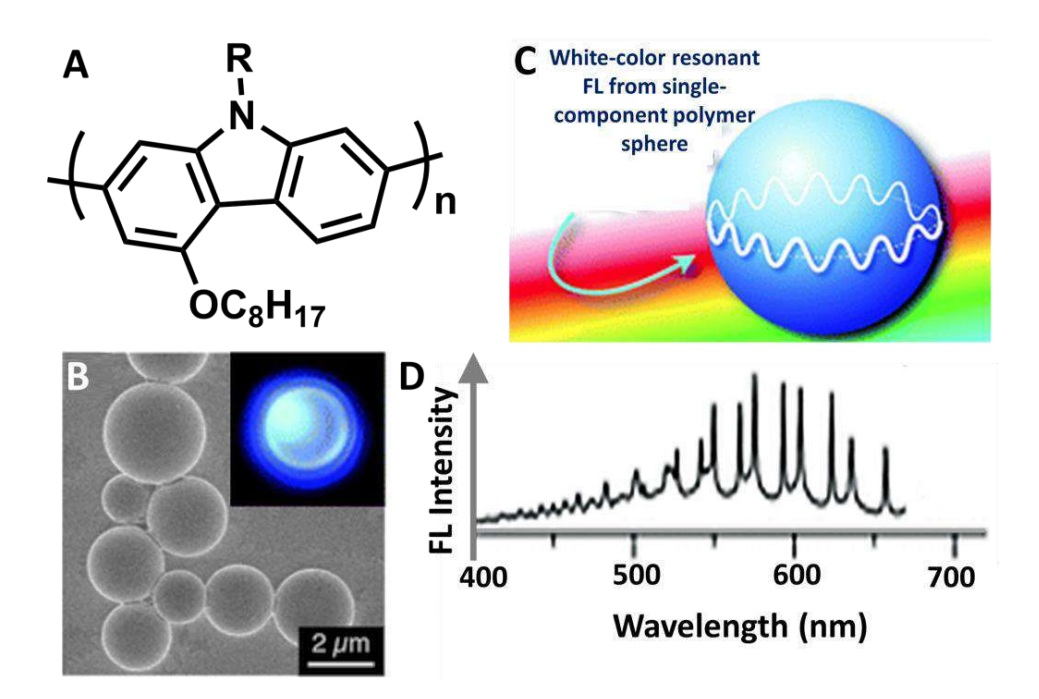


Figure 1.10: A) Structures of poly(2,7-carbazole) with an alkyl side chain (**PCzs**). B) SEM images of self-assembled micro-spheres. The inset shows the white light-emitting micro-sphere under excitation with 488 nm CW laser. C) Graphical representation of white light-emitting micro-sphere exhibiting WGMs. D) FL spectra with WGMs covering the entire visible region.^[76]

Generally, inorganic molecules and polymers, the line-width of FL appear in the of ~50–100 nm. To achieve white light emission covering the whole of the vis region, thus, binary or ternary fluorophores are employed.^[77] Yamamoto et al. have prepared Poly-(2,7-carbazole) derivatives with an alkyl side chain (**PCzs**) to prepare white light-emitting WGMRs (**Fig. 1.10 A**). **PCzs** self-

assembled into smooth-surfaced micro-spheres in CHCl₃/MeOH solvent mixture by vapour diffusion method. The FESEM analysis confirmed the spherical geometry of the micro-structures (Fig. 1.10 B). PCz micro-spheres exhibit white FL when excited with 488 nm CW laser and the spectrum consisted of WGMs covering the whole visible spectral range (inset of Fig. 1.10 B and D). The extremely wide photoluminescence window with white FL occurs from the incomplete oxidation of PCz upon excitation with CW laser. These white light resonators in the micron scale can be utilized as full-color light sources in the photonic applications. [79]

1.1.2.6. WGMRs from dye-doped polymer:

In order to achieve low threshold lasing, the optical resonators should possess perfect boundary and very smooth surface. So that they can act as an efficient optical gain medium. For that, a highly stable, optically transparent, and flexible PS matrix is usually selected as an ideal candidate for attaining high-quality micro-resonators. Moreover, incorporation of organic dye molecules to the polymer solution can display good compatibility as a guest molecule with the polymer host for attaining low threshold organic dye-doped polymer lasers (Fig. 1.11).

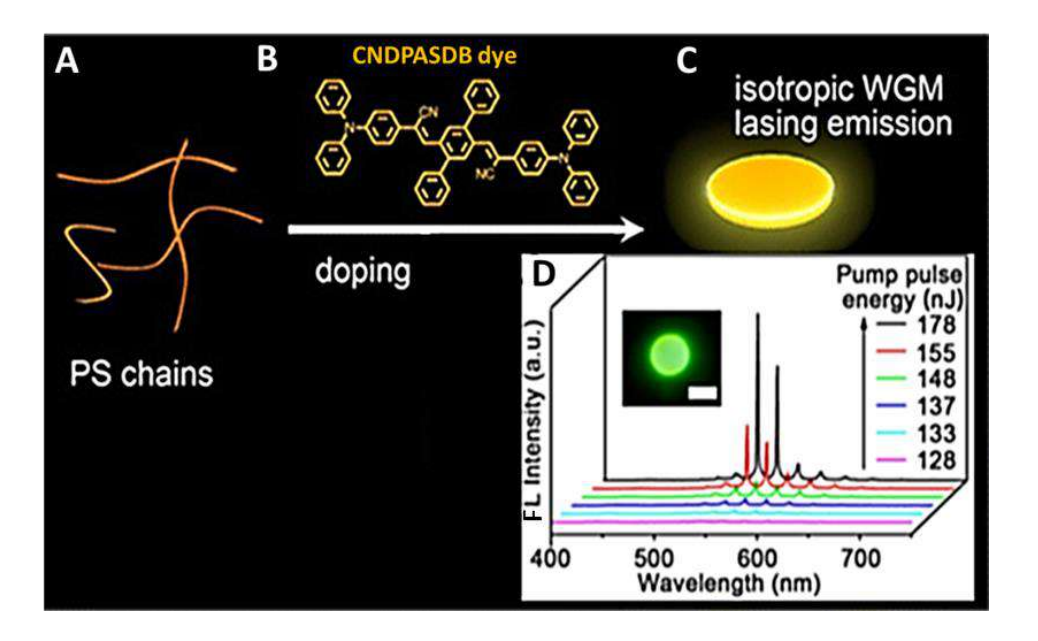


Figure 1.11: A) Schematic representation of PS chains. B) Chemical structure of **CNDPASDB**. C) Dye doped PS micro-disk. D) WGM lasing from micro-disk upon excitation with femtosecond (fs) pulse laser. [80]

In 2015, Zhao et al. have mixed PS ($\overline{M_n}$ = 2,500 kDa) (**Fig. 1.11 A**) with an efficient organic laser dye, namely 4-Bis(α -cyano-4-diphenylaminostyryl)-2,5-diphenylbenzene

(CNDPASDB) in DMF solution (Fig. 1.11 B). Later, they have added a small amount of H_2O , followed by ultrasonication to produce an emulsion. Then, two glass substrates with a tiny gap were used as a template for drying and flattening of the dye-doped polymer micelle. Finally, it facilitates the formation of flexible, small V_m , high-quality micro-disk WGM laser (Fig. 1.11 C). [80] The circular shape and smooth surface make the micro-disks suitable for generating WGM. Besides, the aromatic groups of polymer would have effective π - π interactions with chromophore leading to good compatibility with dye molecules. This prompted them to fabricate potential WGM lasers by the incorporation of organic dyes into polymers. Bright ringshaped FL at the periphery of the micro-disk was observed upon excitation with ultra-fast pulse lasers (Fig. 1.11 D Inset). As the power of pulse laser increased, FL intensity of the peaks increased and the FWHM of the peaks decreased confirming lasing from the micro-disks.

1.1.2.7. WGMRs from a blend of metallo-conjugated polymer and PS:

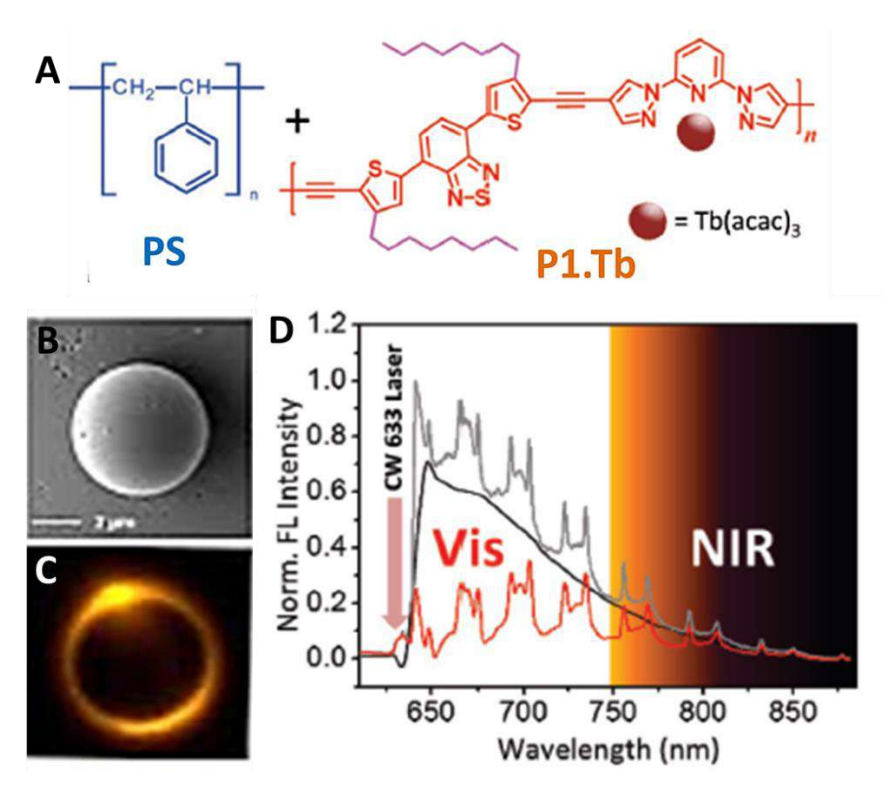


Figure 1.12: A) Chemical structure of a blend of polystyrene and **P1.Tb** used for self-assembly. B) FESEM image of a single polymer blend micro-sphere. C) FL image of a micro-sphere excited with a 633 nm laser. D) Single-particle FL spectra of the corresponding micro-sphere emitting WGMs in the Vis–NIR range. Spectra with (tangential excitation) and without (excitation at the centre) WGM resonance are shown in black and grey lines, respectively. The background-subtracted spectrum is shown in the red line.^[71]

Till 2015, there have been no reports on optical resonators fabricated from polymer and metallo-conjugated polymer blends. The micro-spheres formed from the self-assembly of pure metallo-conjugated polymer did not serve as WGMRs due to the presence of defects in the micro-structures. To overcome this, Chandrasekar group have blended the metallo-conjugated polymer poly[4,7-bis(3-octylthiophene-2-yl)benzothiadiazole-co-2,6-bis(pyrazolyl)pyridine] $(\overline{M_n})$ ~10.7 kDa) coordinated to Tb(acac)₃ (P1-Tb) in the PS matrix. The metallo-conjugated polymer (P1-Tb) was obtained by copolymerizing 4,7-bis(2-ethynyl-5-thienyl)-2,1,3-benzothiadiazole with 2.6-bis(pyrazolyl)pyridine regioselectively (4,4") followed by successive coordination with metal Tb(acac)₃ (Fig. 1.12 A). They have self-assembled the polymer blend in THF/H₂O mixture and produced defect-free micro-spheres (Fig. 1.12 B). The resulting micro-spheres emitted orange-yellow color FL covering the Vis-NIR region (Fig. 1.12 C). During the singleparticle micro-FL spectroscopy studies, tangential excitation of a micro-sphere with 633 nm laser exhibited WGMs in the FL spectrum with a Q-factor of 700 (Fig. 1.12 D). Further, the micro-spheres exhibited 7 times enhancement in FL intensity in comparison to metalloconjugated polymer micro-spheres owing to amplified light-matter interaction within the high-0 micro-resonator.[81,82]

1.1.2.8. WGMRs from CT organic molecules and polymers:

CT or donor (D)-acceptor (A) complexes can be formed due to transfer of electronic charge partly from D to A. As a result of CT, the D and A moieties acquire partial positive and negative charge, forming cation and anion, respectively producing coupled ions. Small ionization energy (I_D) of the D molecule and huge electron affinity (E_A) of the A molecule are essential for the formation of a CT complex.^[83] For spatial association, proper overlapping between the corresponding D and A molecular orbitals and similar symmetry are essential. If there is a little increase in energy when the D and A interaction, a minimal amount of charge usually transferred, which leads to a weaker CT complex. The interactions among D and A moieties surge with the decrease in the difference between I_D - E_A, forming a strong CT complex. Further, choosing strong D and strong A also allows the complete transfer of an electron from D to A is probable in the ground state. CT complex can be formed by the assembly of two or more molecules (*intermolecular CT*) or of various functional groups of a molecule (*intramolecular CT*).^[84]

1.1.2.8.1. WGMRs from intramolecular charge transfer (ICT) organic molecules:

Generally, a π -conjugated complex containing D and A moieties connected via a π -conjugated bridge favours the ICT (intramolecular CT) process. Photophysical properties like photon decay time (τ_{FL}), Φ_{FL} , particularly the bandgap of the above-mentioned organic moieties, are firmly based on ICT. The properties mentioned above can be easily altered by appropriate adjustment of the chemical structures of D, A and the π -conjugated linkers. Therefore, the conjugative effect, push-pull electronic effect and the distorted configuration in organic dyes would significantly influence the ICT band. Usually, ICT molecules can exhibit visible emissions due to optical transitions. The CT band is the ultimate characteristic criterion for the formation of a CT complex, resulting in typically intense colour for those molecules.

The ICT is affected by the nature of both the substituents and the solvent polarity. [87] The red shift[88,89] of FL spectra than that of the UV spectra in various solvents indicates more ICT attributes and large dipole moment (μ) of excited state than that of the ground state. Therefore, all physical properties can be modified through solvent polarity and varying electron-donating abilities of D molecules. The efficiency of D-A conjugation in the ground state is determined not only by the CT band but also ground state data, for example, 13 C-NMR chemical shifts, the quinoid character of aromatic rings and change in bond length in X-ray crystal structures, theoretical calculations or redox potentials. $^{[90,91]}$ The capability to regulate the magnitude of CT in D- π -A system is a vital aspect for establishing practical applications like designing of NLO materials. Importance of D- π -A systems is still increasing, for understanding their excellent optoelectronic properties, namely, second- and third-order $^{[92-94]}$ NLO effects and their capability for use as innovative functional materials in molecular devices.

For instance, π -conjugated molecule **HDMAC** containing electron-donating dimethylamino group and electron attracting carbonyl group exhibits FL in the red region by ICT process (Fig. 1.13 A). **HDMAC** self-assembled into micro-structure in DCM, and further, FESEM analysis confirmed the 2D square-shape of the as-prepared micro-structures (Fig. 1.13 C). Furthermore, the micro FL images showed brighter FL along the boundary of the micro-disk than at the centre (Fig. 1.13 B). This implies that the micro-disk can serve as the high quality 2D WGM micro-resonator, where photons are circulated along the four facets via TIR. More significantly, the multimode WGM lasing spectrum was collected from the micro-disk (Fig. 1.13 D). These organic micro-structures could be used as laser sources and may be used in integrated microchip.

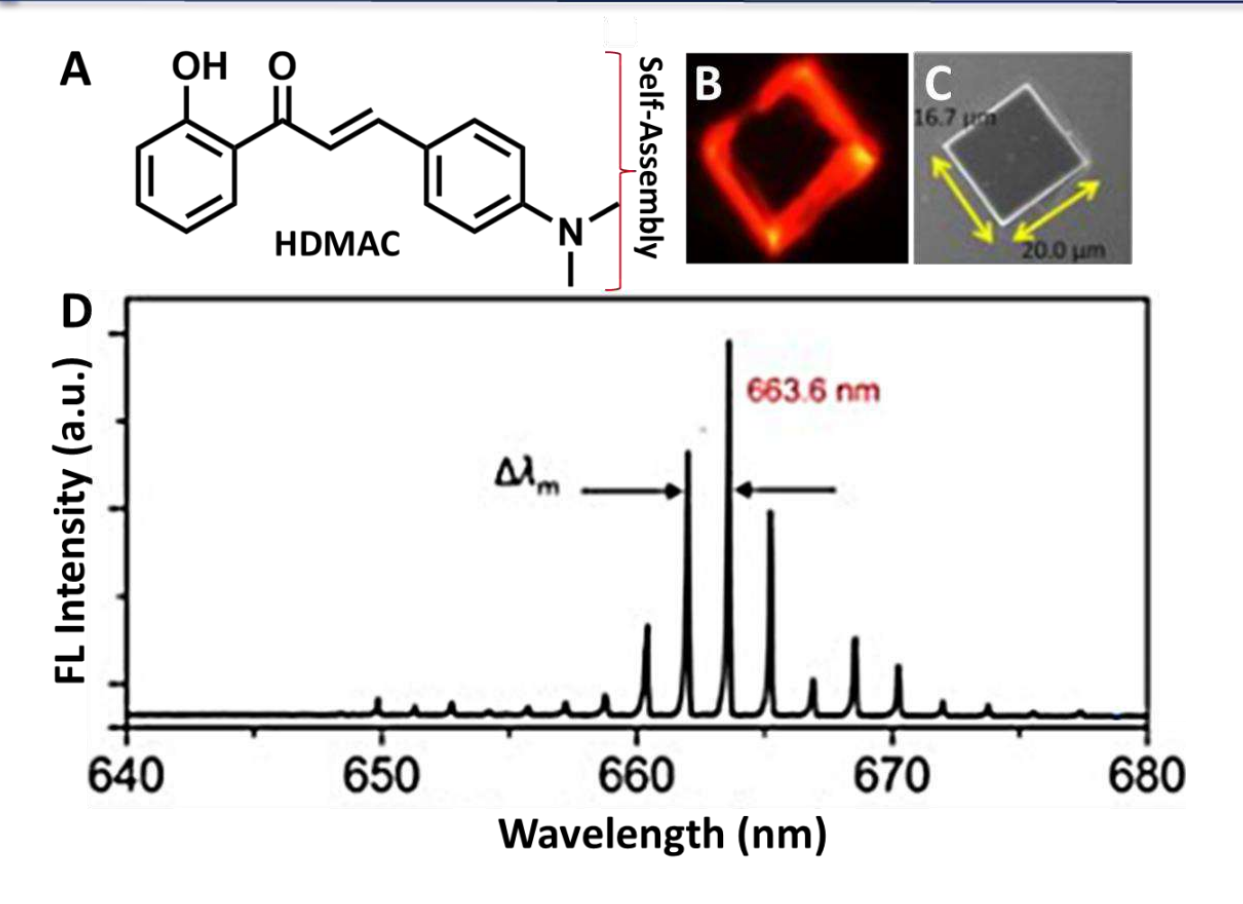


Figure 1.13: A) Molecular structure of 3-[4-(dimethylamino)phenyl]-1-(2-hydroxyphenyl)prop-2-en-1-one (**HDMAC**). B) Confocal microscope image of the 2D micro-disk. C) FESEM image of the micro-disk. D) WGM lasing spectra for the micro-disk upon 800 nm fs pulse laser excitation. [95]

1.1.2.8.2. WGMRs from intermolecular CT polymers:

The transfer of electron from D to A forms an intermolecular D-A bond, possibly together with various other types of interaction, including dipole-dipole, polarization and also van der Waals forces. [96] Mostly, the studies often dedicated to high electrical conductivity or superconductivity emerging from organic CT salts. In recent times, D-A supramolecular cocrystals [101-103] have displayed to be worthy contenders for organic ferroelectrics because of the promising long-range alignment of their CT dipoles present in highly ordered complexes. Nevertheless, CT complexes have numerous distinctive features that are valuable for dynamic supramolecular assemblies, molecular switches, self-healing, and responsive materials, organic electronics, [104] host-guest complexes [105] and sensing, [106] which is due to their low extinction coefficients. As CT complexes normally absorb in the Vis region of the absorption spectrum, CT sensors can be detected by the naked eye. Further, colors of these complexes

are susceptible to the electronic properties of the D and A molecules and their relative geometry. Therefore, binding interactions that make modifications in the structure can be easily examined by variations in their colors.

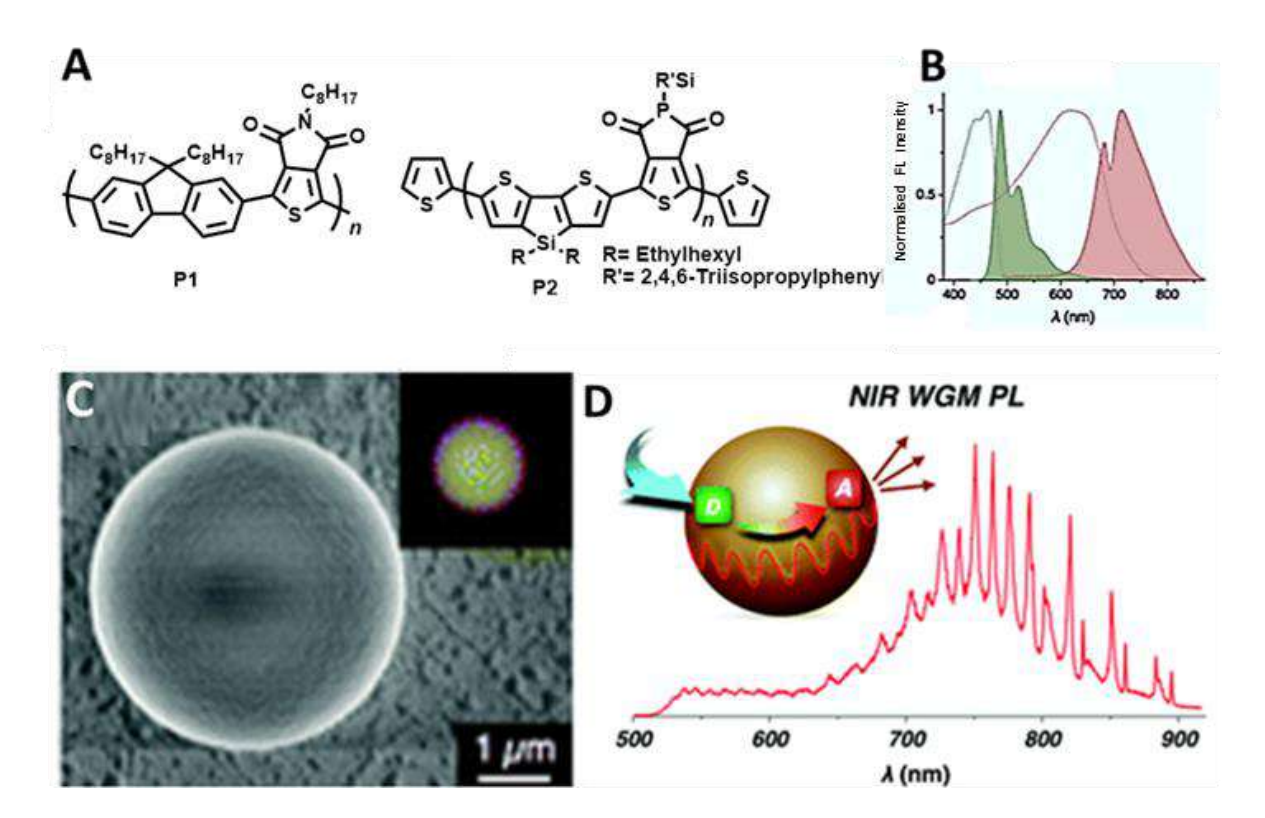


Figure 1.14: A) Chemical structures of **P1** and **P2.** Absorption (broken lines) and FL (solid lines) spectra of **P1** (green) and **P2** (red) in CHCl₃. C) FESEM micrographs of the self-assembled precipitates of **P1** and **P2** Insets show FL micrographs of the precipitates. D) WGMs in NIR region from FRET mediated CT polymer.^[109]

In general, NIR emitting CT molecules have low Φ_{FL} due to the small energy gap between HOMO and LUMO, causing non-radiative thermal deactivation. These NIR emitting molecular materials have been extensively used in bio-sensing and bio-imaging owing to high transparency. In 2017, Yamamoto and his co-workers have made a NIR emitting CT polymer blend containing π -conjugated donor polymer namely, (poly[(9,9-dioctylfluorene-2,7-diyl)-alt-(5-octylthieno[3,4-c]pyrrole-4,6-dione-1,3-diyl)] (P1) with $\overline{M_n}$ of 24 kg mol-1 and acceptor polymer (poly[(5-(2,4,6-triisopropylphenyl)thieno[3,4-c]phosphole-4,6-dione)-alt-(4,4-bis(2-ethylhexyl)-silolo-[3,2-b:4,5-b]dithiophene)] (P2) with $\overline{M_n}$ of 24 kg mol-1 (Fig. 1.14 A). In solid-state, this polymer blend hardly fluoresces due to aggregation-induced quenching. However, in the CHCl₃ the FL band of P1 overlaps with the absorption band of P2, thereby

facilitating considerable fluorescence resonance energy transfer (FRET)^[108] from **P1** to **P2** (**Fig. 1.14 B**). **P1** and **P2** coassembled into micro-structures in CHCl₃/MeOH solvent mixture. FESEM analysis revealed a well-defined spherical geometry of the micro-structures with a typical size of 5 µm (**Fig. 1.14 C**). Micro-spheres displayed WGM FL in the NIR region due to FRET phenomenon from **P1** to **P2** (**Fig. 1.14 D**).

1.1.2.9. WGMRs from chiral molecules:

Generally, chiral materials (molecules and structures) exhibit weak chiro-optical properties. Further, enhancing the circular dichroism (CD) effect (i.e., the differential absorption of the left and right circularly polarized lights by the chiral medium.) in the NLO regime is a challenging effort. CD effect in NLO emissions is important in potential applications in fieldsranging from biomedical to nanophotonic applications.^[111] Both experimental and theoretical advancements in NLO-CD afford new opportunities in understanding the structural and conformational properties of the optically active chemical systems. The CD effect in the NLO signal that can be calculated from the following equation.

$$CD (NLO) = \frac{I(RCP) - I(LCP)}{I(RCP) + (LCP)} \qquad ----- (1.13)$$

where *I*(RCP) and *I*(LCP) are the intensity of NLO signal under the right and left circularly polarized light, LCP, and RCP, respectively. A brief introduction to NLO properties is given in sec 1.2.

Recently, Chandrasekar et al. have demonstrated an original technique to increase the CD-NLO resonantly using chiral organic micro-resonators (**Fig. 1.15**). They have made *R*- and *S*-type micro-spherical WGMRs through self-assembling the D-π-A systems, namely, *R*- and *S*-4-[2,2'-diethoxy-6'-(4-formylphenyl)-[1,1'-binaphthalen]-6-yl]benzaldehyde, **1-***R* and **1-***S* (**Fig. 1.15 A**), respectively, in CHCl₃/MeOH mixtures. Confocal optical microscopy analysis of micro-particles exhibited the formation of micro-structures of different sizes (**Fig. 1.15 B**). Further, FESEM examination established the spherical geometry of the micro-particles (**Fig. 1.15 C**). ^[68] Single-particle spectroscopy studies revealed optical WGMs in the FL spectra of a single micro-particle. The *Q*-factor lies between 100 to 770 for the micro-spherical WGMR with a size of 6 μm (**Fig. 1.15 D**). Both **1-***R* and **1-***S* WGMRs displayed constant CD-NLO values of about 10% with the opposite CD signs due to better light-matter interactions (**Fig. 1.15 E** and **F**).

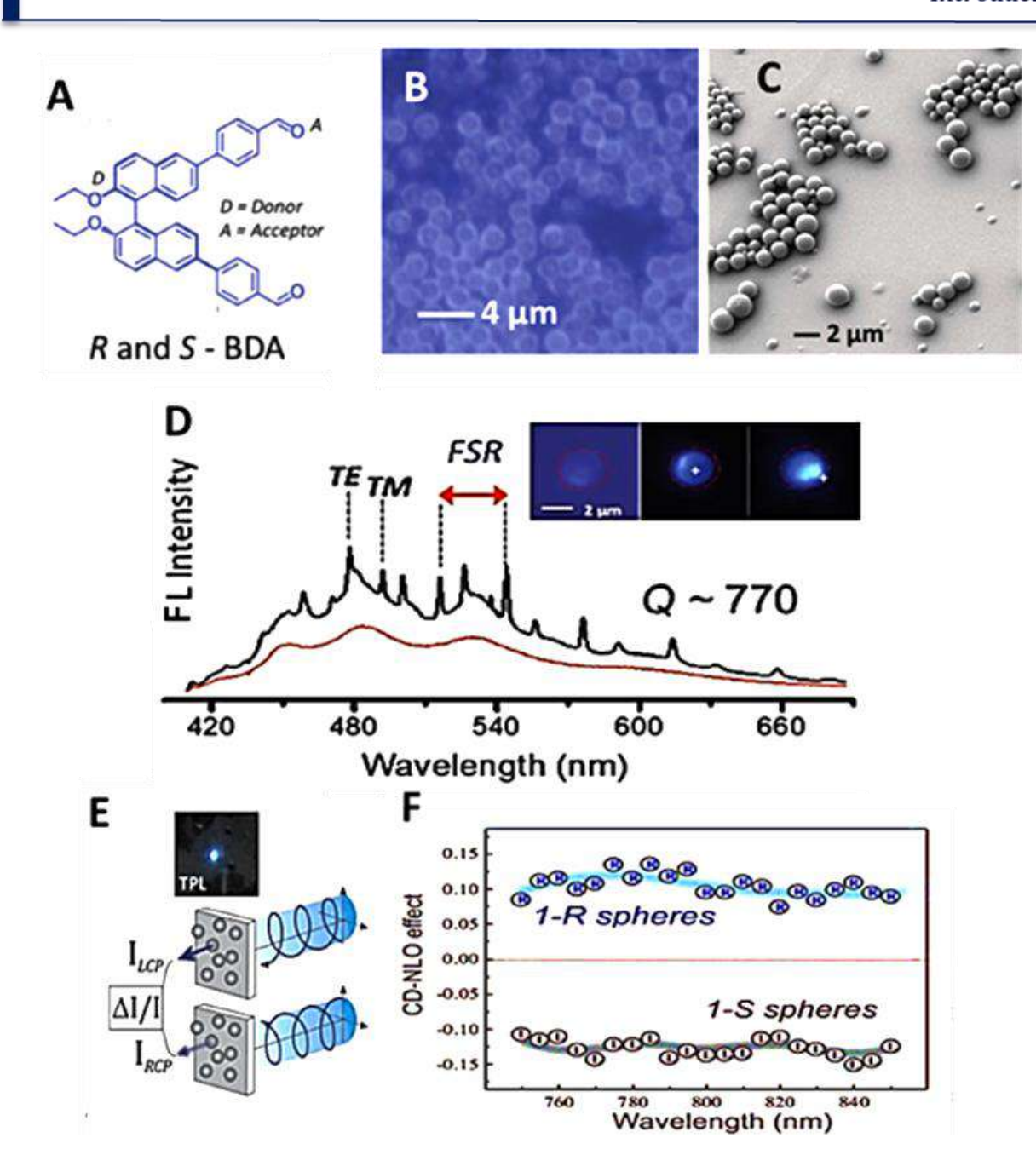


Figure 1.15: A) Chemical structure of *R*- and *S*-4-[2,2'-diethoxy-6'-(4-formylphenyl)-[1,1'-binaphthalen]-6-yl]benzaldehyde (**1-***R* and **1-***S*). B) Confocal microscopy images of micro-spheres self-assembled from **1-***R* and **1-***S*. C) FESEM image of **1-***R* and **1-***S* micro-spheres. D) Single-particle FL spectra of **1-***R* and **1-***S* exhibiting WGMs. The black and red lines of the spectra show excitation of the particle edge and centre, respectively. E) Cartoon representation of the experiment on the CD effect in the TPL response of **1-***R* and **1-***S* WGMR micro-spheres excited by LCP and RCP. The top inset shows TPL from the sample. F) Spectral dependencies of the CD-NLO indicating opposite signs for the LCP and RCP in the case of **1-***R* and **1-***S* micro-spheres. [110]

1.2. NLO properties:

The term "nonlinear" depicts that the NLO phenomena, which take place when a material reacts in a nonlinear fashion to the time-dependent applied intense electric field E(t). When an E(t) is applied to an NLO active medium, the nuclei and the accompanying electrons in the medium generate strong electric dipoles and hence become polarized. [112] Generally, the photon interaction with matter is very weak. The electric field $E(t) \sim 600 \text{ V/m}$ associated with light beams from traditional sources is below that of the strength of the atomic field (E_a) ~10¹¹ V/m (optical intensity, $I_a \sim 10^{20}$ W/m²). Therefore, polarization is not strong enough to produce a measurable NLO effect.[113,114] After the advent of the laser, which provided energy (intensities I $>10^8$ W/m²) is comparable or even higher to that of characteristic E_a and facilitated the observation of NLO process from NLO materials. [114] If the E(t) is very intense, the response of the medium is no longer linear and the relation between radiation intensity and the vibration amplitude turn out to be nonlinear. Finally, it leads to the production of frequencies which are dissimilar from those of incident light. Therefore, second and higher harmonic generation occurs. The interpretation of the NLO process lies in a manner in which a beam of light propagates through the NLO solid. Here, time-dependent electric polarization P(t) (polarization density or the dipole moment/unit volume or induced polarization) of the medium is dealt as a nonlinear function of the E(t) of the light.

$$P(t) = N\mu \qquad ----- \blacktriangleright (1.14)$$

Where μ = electric dipole of each atom in the solid, N = no of atoms per _nit volume. In conventional linear optical properties where the P(t) varies linearly with the E(t) in such a way, which can be defined by the following equation.

$$P(t) = \varepsilon_0 \chi^{(1)} E(t) \qquad ----- \blacktriangleright (1.15)$$

Where $\chi^{(1)}$ is known as the linear electric susceptibility and ε_0 is the permittivity of free space. Unlike linear optical properties, in NLO process on a macroscopic level, the P(t) must be extended in a power series with respect to E(t) as follows.

$$P(t) = \varepsilon_0[\chi^{(1)} E(t) + \chi^{(2)} E^2(t) + \chi^{(3)} E^3(t) + \dots] \qquad ------ \blacktriangleright (1.16)$$

$$P(t) = P^{(1)}(t) + P^{(2)}(t) + P^{(3)}(t) + \dots$$
 ------(1.17)

Where $\chi^{(2)}$ and $\chi^{(3)}$ are second- and third-order NLO electric susceptibilities, respectively. Normally these susceptibilities depend on the frequencies of the applied field, but at this point, generally, it is presumed that the NLO medium reacts immediately (lossless and dispersionless

medium), therefore NLO susceptibilities are taken as constants. For convenience, P(t) and E(t) are considered to be scalar quantities in the above equations. This thesis mainly focuses on the third-order NLO process, involving nonlinear polarization $P^{(3)}(t)$,

$$P^{(3)}(t) = \varepsilon_0 \chi^{(3)} E^3(t)$$
 ------ (1.18)

Different processes can be used to explain the association between the material response and the applied electric field amplitude. In non-resonant excitation conditions, $\chi^{(2)}$ will be the order of $\chi^{(1)}/E_a$. As $\chi^{(1)}$ is the order of unity for condensed matter, therefore, $\chi^{(2)} = {}^{1}/E_a \cong 1.94 \times 10^{-12} \, \text{m/V}$. In the same way, it is anticipated that $\chi^{(3)}$ to be the order of $\chi^{(1)}/(E_a)^2 \cong 3.78 \times 10^{-24} \, \text{m}^2/\text{V}^2$. [112] In this thesis, the results of one of the NLO phenomena such as two-photon luminescence (TPL)[115] from organic CT compounds is presented, therefore a short introduction to TPL will be given in the next section.

1.2.1. Two-photon absorption (TPA) and emission:

TPA is an optical process in which a material or molecule absorbs two photons (from laser source typically in NIR region) simultaneously to reach an excited state via virtual state followed by optical emission. Theoretically, TPA was first predicted by Göppert-Mayer (GM)^[116] and was later proved by Kaiser and Garrett. [117-119] Depending on the energies of the two photons, TPA can be categorized as degenerate or nondegenerate, respectively. However, for real applications, the degeneration of TPA is very advantageous. TPA is largely weaker than

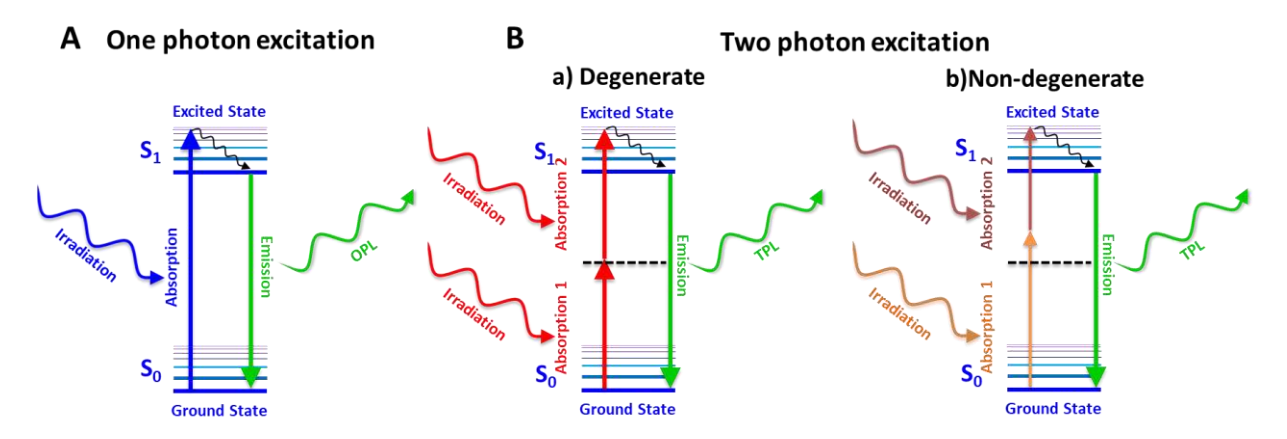


Figure 1.16: Jablonski diagram for one-photon A) and two-photon B) excitations.[120]

one-photon absorption (OPA). In OPA the molecule absorbs one photon with energy (ΔE) equal to the difference in energy between the ground (E_g) and excited state (E_e) to reach the excited state (Fig. 1.16 A).

$$E_e$$
- E_g = hv (OPA) ------ (1.19)

While in TPA, the molecule captures two photons of the same wavelength or different wavelength (Fig. 1.16 B) with their combined wavelength matching with the energy difference between E_a and E_e states as

$$E_e$$
- E_g = 2hv (TPA) ------ (1.20)

Evidently, in TPA the two transitions take place in femtosecond (fs) time interval. In TPA, the molecule absorbs low-energy photon having longer wavelengths that can pass deeper into the sample compared to OPA, thus letting two-photon excitation to proceed deeper into the sample. The main difference between OPA and TPA is that TPA involves the concurrent interaction of two photons and hence it shows quadratic dependence of intensity of incident light, whereas OPA shows linear dependence. Therefore, TPA is observed mainly with ultrafast pulse lasers. Like Beer-Lambert law for OPA, the decrease in the intensity of the laser beam resulting exclusively from TPA is given by the following expression: [121-123]

$$-\frac{dI(z)}{dz} = \alpha I(z) + \beta I^{2}(z) \qquad \qquad ----- \blacktriangleright (1.21)$$

Where *I* is the intensity of the propagating laser beam along the *z*-axis, and α and β are one-and TPA *co-efficient* of the transmitting medium. In non-linear phenomenon, the imaginary part of the third-order nonlinear susceptibility, $Im(\chi^{(3)})^{[124,125]}$ is associated with β as

$$\beta = \frac{48\pi^3}{n^2c\lambda} \operatorname{Im} (\chi^{(3)}) (\text{in esu}) \qquad ----- \blacktriangleright (1.22)$$

For clarity, here it is taken that the time-independent incident light has a uniform transverse intensity distribution. When there is no OPA (α =0) at the wavelength range of the incident laser beam, TPA appears alone at that excitation wavelength

$$-\frac{\mathrm{dI}(z)}{\mathrm{d}z} = \beta \ \mathrm{I}^{2}(z) \qquad \qquad ----- \blacktriangleright (1.23)$$

Equation 1.23 illustrates the probability of TPA transition primarily depends on the square of the photon flux or square of the light intensity.

$$I(x,\lambda) = \frac{I_0}{1+\beta(\lambda)I_0cx} \text{(TPA)} \qquad ----- \blacktriangleright (1.24)$$

where $I(x,\lambda)$ is the intensity of TPA light, which is a function of path length or cross-section (x) and wavelength (λ) of the incident light. I_0 is the intensity of the incident light with a top-hat

pulse shape, c is the concentration of the sample and β is a material parameter which depends on λ of the incident light.

The TPL signal intensity would be modified appropriately by changing the light incidence angle and polarization. Therefore, β can be calculated by the expression given below:

$$\beta = \frac{\sigma_2 N}{hv} = \frac{\frac{cm^4 \cdot sec \ molecule}{molecule \ cm^3}}{J} = \frac{cm}{W} \qquad ----- \blacktriangleright (1.25)$$

Where N [molecules/cm³] is the molecular concentration and $h\upsilon$ is the photon energy (measured in J). By solving the above equation, it was found that units of β are expressed in $\frac{cm}{W}$. Furthermore, the probability of TPA (N₂) rises with the square of the absorbed light intensity I as follows:^[126,127]

$$N_2 \propto \sigma_2 (\lambda) I^2$$
 ----- (1.26)

$$\frac{dN_{TPA}}{dt} = \frac{1}{2} \sigma_2 N_{gs} I^2 \qquad ----- \blacktriangleright (1.27)$$

Where $\sigma_2(\lambda)$ is the TPA cross-section, N_{gs} and N_{TPA} are the number of molecules per unit volume in the ground state and excited state due to TPA, respectively. This equation elucidates the probability of TPA transition primarily depends on the square of the photon flux. $\sigma_2(\lambda)$ defines the strength of the TPA process and is generally expressed in GM unit (1 GM = 10^{-50} cm⁴ s photon⁻¹ molecule⁻¹).

$$\sigma_2 = \frac{\beta E}{N} = \frac{\text{cm/W. J}}{\text{molecule/cm}^3} = \frac{\text{cm}^4 \cdot \text{sec}}{\text{molecule}}$$
 -----\(\blacktriangle (1.28)

Where E is the photon energy (J) and N is the number density, which is equivalent to the number of molecules per unit volume (molecule/cm³). It is very evident that in order to get the σ_2 (λ) from any measurement, a cross-sectional variation of the beam and time must be known. The NLO transmission $T(I_0)$ of a material absorbing two-photons varies as a function of the intensity of the laser beam I_0 with cross-section x used for excitation can be expressed as:

$$T(I_0) = \frac{I}{I_0} = \frac{1}{1 + \beta I_0 cx} \text{(TPA)}$$
 ----- (1.29)

Selection rules for TPA vary entirely from that of OPA, which is dependent on $\chi^{(1)}$. In the case of molecules with centre of inversion, allowed transitions are mutually exclusive for OPA and TPA. This variance results from the condition to conserve the angular momentum quantum

mechanical point of view. As photon has a spin of ± 1 , the one-photon transition involves an electron altering its molecular orbital to one with an angular momentum changed by ± 1 , whereas for two-photon transition a change of ± 2 , 0, or ± 2 is required. TPA transition is allowed between two states having the same parity i.e.; from gerade to gerade ($g \leftrightarrow g$) and from ungerade to ungerade ($u \leftrightarrow u$), whereas in OPA transition is possible between states having different parity, i.e.; from $g \leftrightarrow u$ and vice versa. [127] Nevertheless, for high symmetrical molecules, a few transitions are forbidden for both OPA and TPA. For non-centrosymmetric molecules, certain transitions are allowed for both one and two-photon transitions. Therefore, molecules devoid of inversion centre do not show exclusivity in selection rules for OPA and TPA. Finally, in these molecules the excited states can be attained by OPA or TPA, even though, depending on the symmetry, a few states may be forbidden, for OPA or TPA or both.

1.2.2. Molecules for TPL:

The main driving force for the optical nonlinearity is the intramolecular CT (ICT) phenomenon from an electron D to electron A. According to Webb's model, [128] the basic structural units for the active two-photon chromophores are: (i) strong electron-rich unit (D) or strong electron-withdrawing component (A) at one end; (ii) π -conjugated bridge and (iii) another D or another A at opposite end (Fig. 1.17).

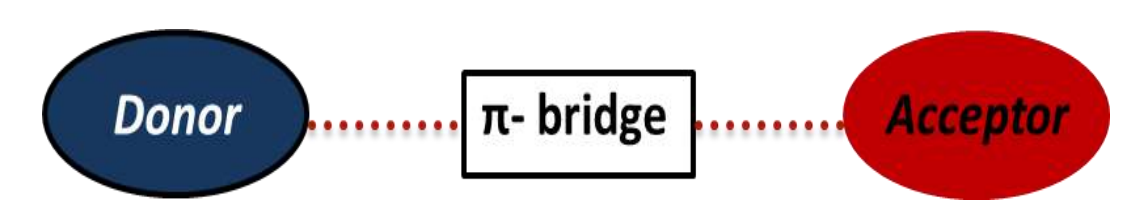


Figure 1.17: Basic structural units of TPA molecules in Webb's model.

 π -conjugated molecules with considerable alterations of quadrupole moment upon optical excitation are beneficial to obtain large $\sigma_2(\lambda)$. The main strategic design for the TPA compounds having large $\sigma_2(\lambda)$, was proven using the idea of symmetric CT from the terminals of a conjugated system to the centre, or vice versa. The molecules exhibiting a combination of high Φ_{FL} and large $\sigma_2(\lambda)$ values have been developed for providing extraordinary brightness in TPL imaging. Elongated π -conjugating structures such as conjugated polymers^[115] are interesting compounds to study as TPA materials as they can stimulate strong optical nonlinearities. However, when compared to dendritic and linear molecules, the polymers having hyperbranched structures^[129] display supremacy for the simple one-pot synthetic access

and the processability into large scale devices. Moreover, hyperbranched polymers display some exceptional secondary properties, such as disordered intra- and inter-molecular CT processes, low viscosity and high solubility, which are beneficial in designing TPA materials, organic light-emitting diodes and organic solar cells applications.^[130]

For example, red laser dye 4-(dicyanomethylene)-2-methyl-6-(4-dimethylaminostyryl)-4 H-pyran (**DCM**) is a D- π -A type molecule, which exhibits FL through ICT mechanism (**Fig. 1.18 A**). [131,132] DCM dye self-assembled into micro-spheres with the size ranging from 2 to 11 μ m in acetonitrile (**Fig. 1.18 B**). The FL and TPL spectra collected from a bunch of spheres exhibited no WGMs (**Fig. 1.18 C**). It was ascribed to averaging over single micro-spheres spectra with modes at various frequencies. However, a similar experiment of single micro-resonators of the diameter of 9 μ m, revealed WGM in the TPL spectrum when the excitation and collection points were at the periphery of the spherical structures, but no WGMs were observed at the centre (**Figure. 1.18 D**). The WGM spectrum also revealed the TE- and TM-polarized modes. The *Q*-factors of micro-spheres are in the range of several hundred, example, $Q\sim200$ for the micro-resonator with a size of 9 μ m.

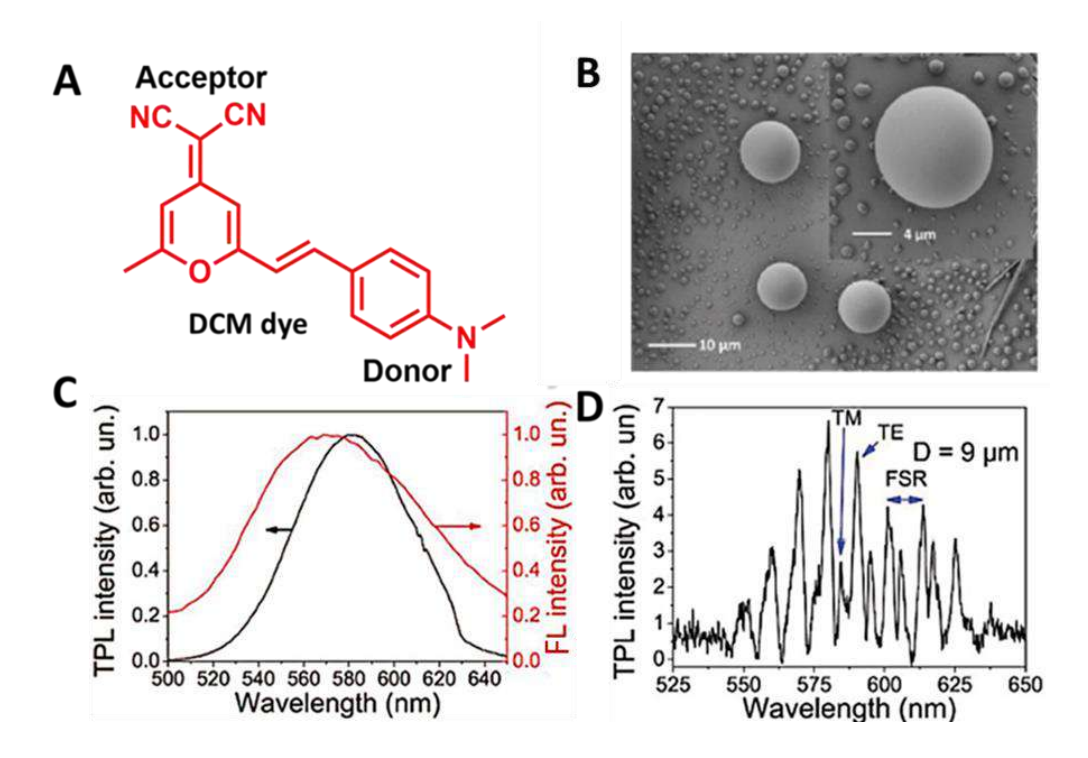


Figure 1.18: A) Structure of **DCM** dye. B) FESEM image of the self-assembled **DCM** dye into microspheres. C) One and TPL spectra of micro-spheres. D) WGMs in the TPL spectrum of micro-sphere diameter 9 μm.^[133]

Furthermore, π -conjugation length^[134] of the organic moieties has a great effect on the magnitude of (χ^3) whose imaginary part is accountable for TPA. As molecules contain high Φ_{FL} and large $\sigma_2(\lambda)$ values, TPA has significant benefits over conventional OPA. This leads to a lot of applications in material science, microfabrication,^[135] TPL imaging,^[136-138] photonics (optical power limiting,^[139] up-converted lasing), medicine (photodynamic therapy,^[140] photoactivation and drug delivery) and three-dimensional optical memory.^[141]

1.3. Self-assembly:

The controlled synthesis of micro and nanostructures from organic molecules and polymer macromolecules is a quite challenging task. In the contemporary research, functional organic molecular and polymer systems with distinct morphologies and structures obtained through self-assembly, have gained significant importance owing to their potential applications in different fields such as molecular electronics, catalysis, photovoltaics, [142] light-emitting diodes, [143] NLO, [144] photonic bandgap materials, [145] sensors [146] and optical microresonators. [147] Self-assembly is one of the bottom-up approaches for the synthesis of well-organized structures from the disordered precursor molecules. Self-assembly is a spontaneous process forming well-defined structures via non-covalent interactions at suitable temperatures and appropriate solvents. The non-bonding interactions such as electrostatic, [148] π - π stacking, [149] van der Waals interactions, [150] hydrophobic, [151] halogen bonding and hydrogen bonding strongly influence the ultimate morphology in the self-assembly process. Along with these interactions, liquid-solid or liquid-liquid interfaces and chemical reactions between the particles can also affect the formation of ordered molecular aggregates. [154,155]

Mainly ICT compounds can be organized into relatively discrete solid superstructures governed by supramolecular interactions, namely symmetric dipole and asymmetric dipole interactions and axial interactions.^[156] These supramolecular interactions are the driving force for the self-organization of molecular assemblies with various links showing noticeably diverse self-assembly behaviour. Employing solvent-vapour techniques^[157] and phase transfer methodologies, these molecular assemblies can be organized into numerous structures such as hallow nano-spheres, micro-ribbon like structures, micro-rhombic architecture.^[157,158] The most important aspects like the concentration of precursor sample, growth period, temperature and other operating factors considerably affect the shape or structure of the molecular aggregates by controlling the nucleation rate, nucleation sites and crystal growth in different chemical environments owing to various interactions among them.^[159] The structure of the

predecessor crystal seed influences the eventual morphology in self-assembly phenomenon. The other distinguishing property to almost all self-assembled structures is their thermodynamic equilibrium, which is attained by decreasing the Gibbs free energy (ΔG°). It ensures the stable and defect-free self-assembled structures, compared to their single, unassembled moieties.

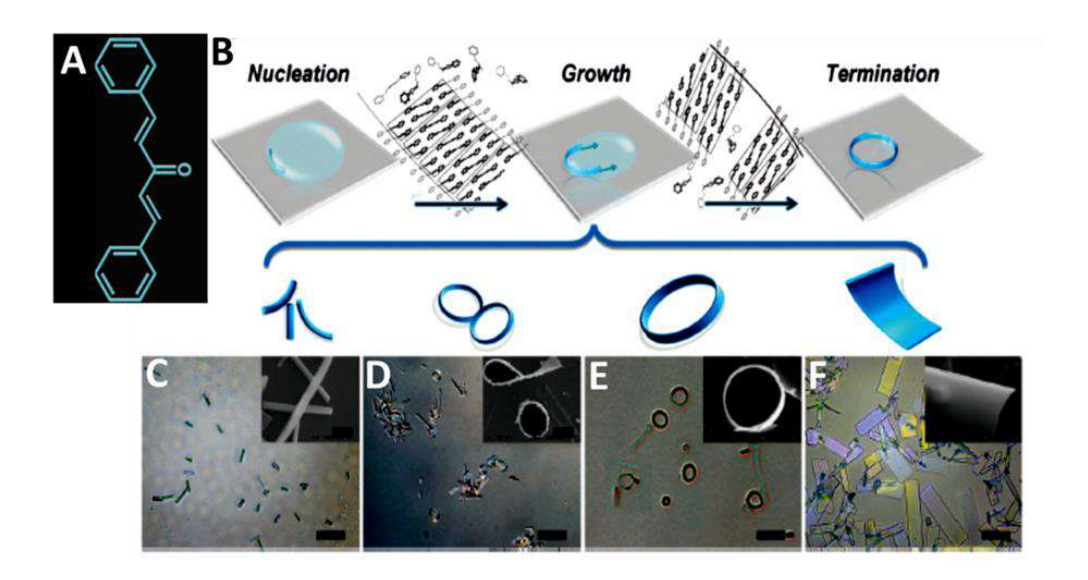


Figure 1.19: A) Molecular structure of 1,5-diphenyl-1,4-pentadien-3-one (**DPPDO**). (B) Illustration of the formation mechanism of the self-assembled micro-rings driven by the interfacial tension of liquid droplets. By this means, typical products (wires, rings, tiles) could be obtained by controlling the solution concentration. (C-F) Optical microscopy images of wires, small/large rings and tiles obtained by using **DPPDO** solutions with different concentrations of 2 mmol L⁻¹, 4 mmol L⁻¹, 6 mmol L⁻¹ and 10 mmol L⁻¹. Scale bars are 25 μm. Insets: corresponding SEM images. Scale bars are 2 μm. [132]

Zhao and his group have reported the different morphologies transformation of 1,5-diphenyl-1,4-pentadien-3-one (DPPDO) during self-assembly (**Fig. 1.19 A**). Upon varying the concentration of 2 mmol L⁻¹, 4 mmol L⁻¹, 6 mmol L⁻¹ and 10 mmol L⁻¹, they observed microwires, micro-rings (small/large) and micro-tiles, respectively (**Fig. 1.19 C-F**). [132] It would be possible to alter the shape and size of the assembled aggregates by merely tuning the factors mentioned above. Micro-spheres (capillary interaction is the driving force which arises from the deformation of the surface of liquid), nano-wires, nano-fibers, and nano-rods (the highest surface energy existing among all of the facets of the 1D aggregate, resulting in the rod-like geometry) [160] are the commonly formed geometries among the self-assembled structures. A few π -conjugated organic molecules can self-assemble into well-ordered structures like nano-

wires and nano-disks, which may serve as optical micro-resonators to subsidize feedback and mode selection for the stimulated emission.^[161] Usually, the unidirectional intermolecular force would turn the molecules to assemble in to1D geometries like micro-rods, micro-wires, which can be used as F-P^[25] type micro-resonators. It would be possible also to fabricate WGM^[162] micro-rings by joining the ends of the flexible 1D structure. Furthermore, two types of equivalent intermolecular forces along various directions would induce 2D molecular assembling to form micro-disks, which support WGM resonance.

1.4. Aggregation of conjugated polymers:

The energetically suitable interactions among many closely spaced conjugated polymers (CPs) chains increase the chromophore density and lead to the creation of aggregates. These aggregates may be H- or J-types (H- and J-stands for hypsochromic and Jelley), excimers, or exciplexes. [163-165] Besides the aggregates mentioned above, conformational irregularity initiated upon chain folding (e.g. bending/entanglement of the polymer backbone) lead to the disruption of polymer main chain π -conjugation. Aggregate type produces alterations in the optical emission characteristics of CP in contrast to polymer in a suitable solvent. Both types can be distinguished by comparing their spectral shifts (that emerge from the alignment of coupled transition dipoles), and FL lifetimes ($\tau_{\rm FL}$). Whereas

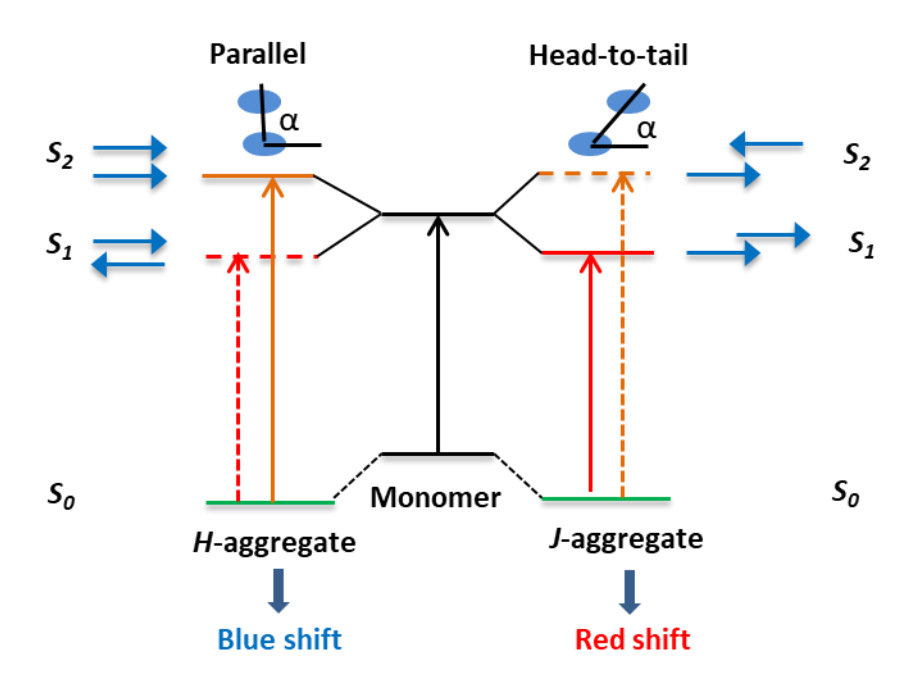


Figure 1.20: Schematic representation of the relationship between chromophore arrangement and spectral shift based on the molecular exciton theory.

directional dependence of transition dipole is understood in the Frenkel model, recent studies on these aggregates favour to discourse direction dependence arising from the structural arrangement of the interacting chromophores, identified as the "slippage angle (α)." α is defined as the angle between the molecular long axis and the line joining the centres of the chromophores. When α < 54.7°, the transition dipoles are oriented in a head-to-tail manner, that results in *J*-type aggregation. However, when α > 54.7° the transition dipoles are in head-to-head alignment, generating *H*-type and in aggregates (Fig. 1.20). [166] In *H*-type aggregates, the electronic absorption and emission spectra moved to lower wavelength (blue-shifted or hypsochromic shift) with the spectral broadening. Their τ_{FL} are also either comparable to or higher than the monomer. [167-169] Whereas, in *J*-type bathochromic shift, with a reduction of the FL bandwidth, a surge in Φ_{FL} , and a considerable decrease in τ_{FL} are observed in comparison to monomer.

The energies of the H- and J-type aggregates shift with the formation exciton amongst the aggregated molecules. This leads to Davydov splitting (high and low energy states) in aggregates comparative to the degenerate monomers. As a result, the transition dipole moment for the lower and higher energy levels in each aggregate type governs whether the transition is allowed or forbidden. The vector sum of transition dipole moment is non zero for allowed transition (i.e. face-to-face for H and head-to-tail for J) and zero for forbidden transition in both aggregates developing dark exciton states.[170,171] Transitions to lower and higher energy state are allowed for J- and H-type, respectively. The electronic coupling of chromophores and aggregation of CPs play an important role in the interpretation of absorption and spectra. Spano et al. have proposed a theoretical model to understand the coupling mechanisms in single molecules in the solution state. [172] Figure 1.21 A illustrates three different types of aggregates: H-type, J-type, and the non-advent of coherent coupling in CP aggregates, and the anticipated role of alkyl side chains. The following hypothesis can be stated if one assumes dissimilar morphologies at the nanoscale level to be accountable for Htype and J-type aggregates. For significant J-type aggregation to occur, high ordering in intrachain should be there to arrange the transition dipole moments (TDMs) of adjacent repeating monomers in a head-to-tail manner, as illustrated in the middle and left section of Fig. 1.21 A. Moreover, a high-level interchain ordering among adjacent chains is critical for Htype aggregation to takes place, as described in Fig. 1.21 A left side. Hence, interchanging between these two types of aggregations becomes possible if morphology is directed by changing the molecular structure of the side chain of CPs.

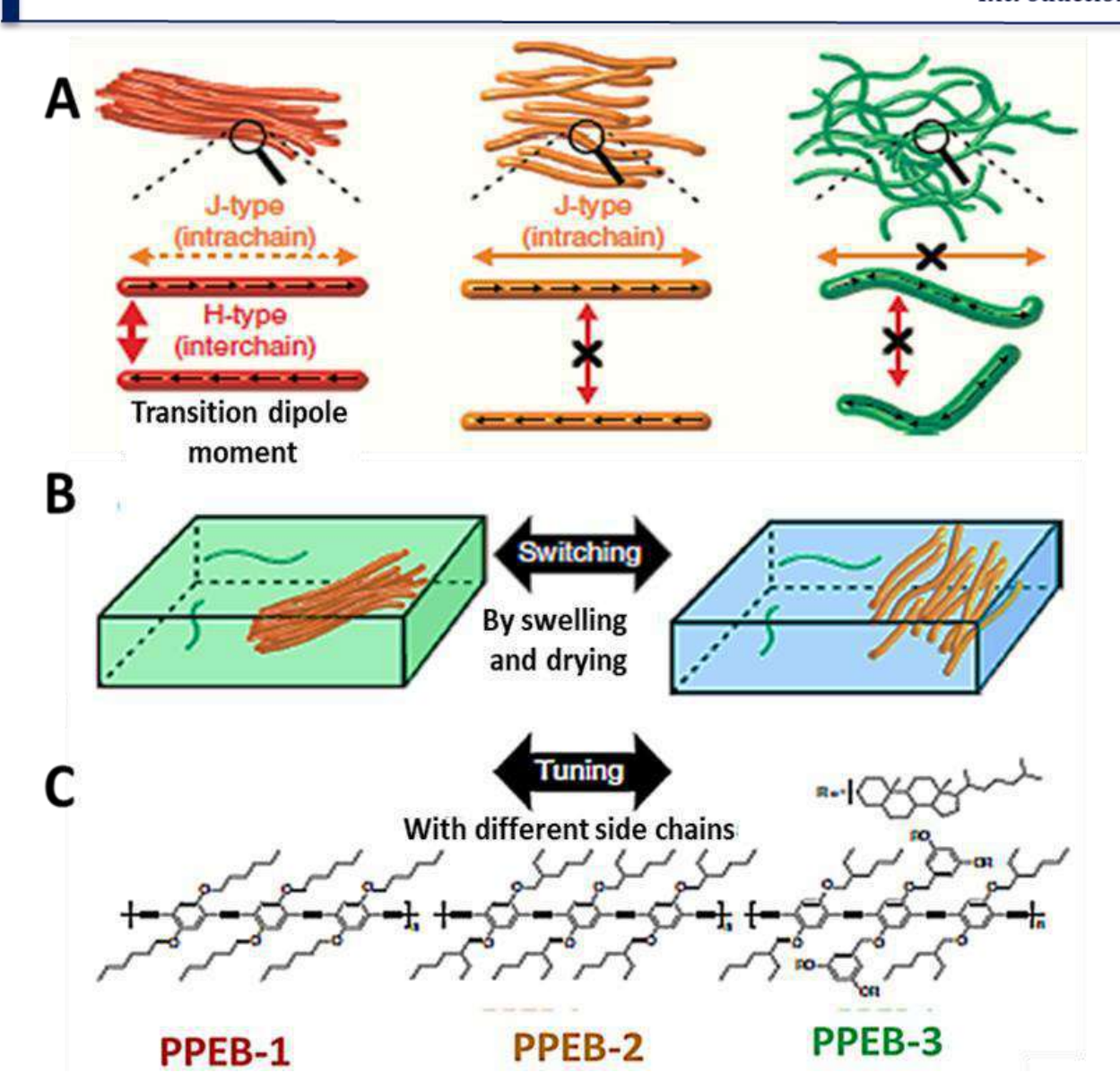


Figure 1.21: Transition between different types of electronic coupling. A) Mechanisms of *H*-type and *J*-type coupling and the suppression of interactions and their expected relationship with aggregate morphology. B) Switching between *H*-type and *J*-type coupling by drying (green box) and swelling (blue box) the aggregate embedded inside a polymer matrix by solvent vapour annealing. C) Structures of samples used to tune between *H*-type (PPEB-1), *J*-type (PPEB-2), and suppressed coupling (PPEB-3) by changing the side chains.^[173]

Jan Vogelsang group have tested the above postulate by interchanging transition between *J*-type and *H*-type coupling in luminescent CP polymer aggregates embedded in non-luminescent PMMA matrix by solvent vapour annealing (SVA) Fig. 1.21 B.^[173] They have fine-tuned the SVA method to partly swell the polymer aggregates preventing the collapse of

aggregate into single CP chains. Swelling terminates the interchain H-type aggregation. Eventually, it was confirmed that by varying the morphology of the side chains of poly(paraphenylene-ethynylenebutadiynylene) (PPEB) having hexyloxy group (PPEB-1), 2-ethylhexyloxy group (PPEB-2) and cholestenol substituted benzyloxy group (PPEB-3) as depicted in Fig. 1.21 C, the transition between H-coupling (PPEB-1), J-coupling (PPEB-2), and annihilated coupling (PPEB-3) can be studied. The *J*-type is recognized by a decrease in τ_{FL} , narrowing of red-shifted FL band, increased vibronic peak ratio 0-0 to 0-1 in FL spectrum. On the other hand, broadening of hypsochromic shifted FL with a decline in 0-0 to 0-1 peak ratio in FL spectrum and increased τ_{FL} is observed in *H*-type aggregates. Figure 1.22 A depicts transient FL decay of a dry aggregate (H-aggregate) as a broad red band and is associated with a swollen aggregate (J-aggregate) as narrowing orange curve. Both H- and J-aggregates FL decay accompany a mono exponential decay with τ_{FL} of 3.51 and 0.47 ns, respectively (Fig. 1.22 B). It is interpreted that high level of ordering i.e., inter and intrachain order, along with the improved lifetimes, will assist energy transfer in neighbouring polymeric chains in H-coupling. Contrary to J-aggregates, mainly energy transfer and interaction takes place in the same polymeric chain. The transition from H-aggregation to J-aggregation in chiral polymers will be discussed in Chapter-5 of the thesis.

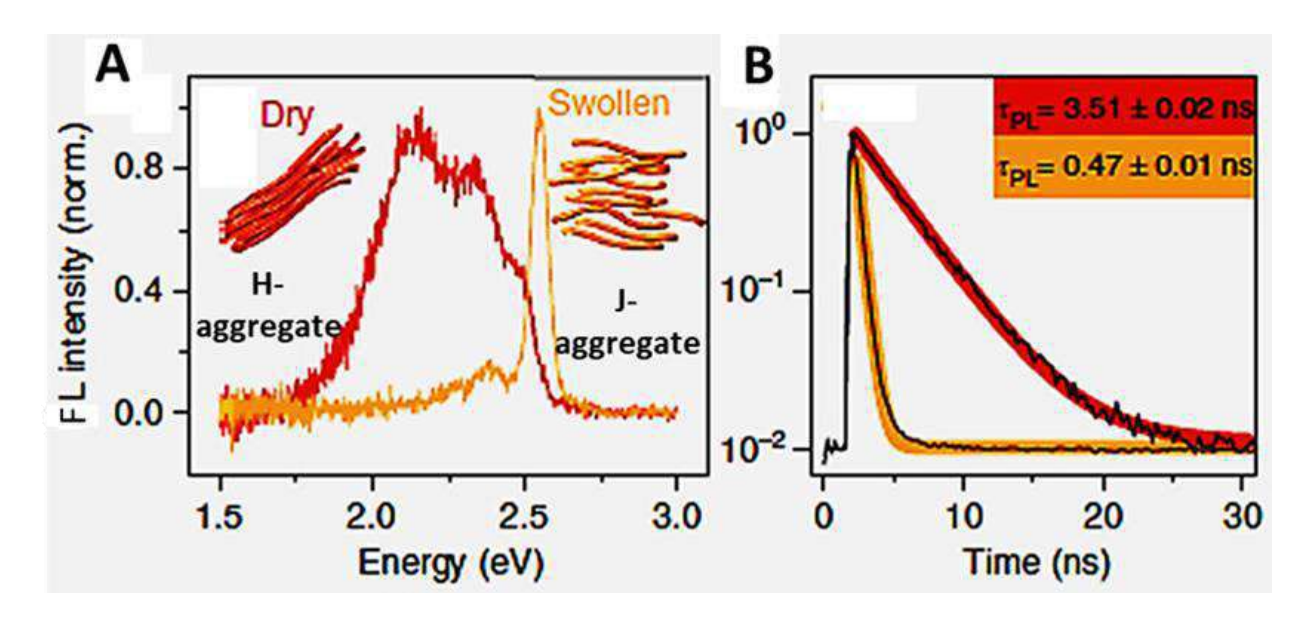


Figure 1.22: Normalized FL spectra and transient FL decays of a single aggregate in a dry (red) and swollen state (orange). The FL decays are fitted by a single exponential function with an offset to extract the FL lifetime. [173]

1.5. Carbon dots (CDs):

CDs are a novel type of carbon-based nano-materials with discrete quasi-spherical nano-particles whose dimensions lower than 10 nm.^[174-178] CDs were by chance found in the electrophoretic purification of single-wall carbon nanotubes (SWCNTs) by Xu et al., in 2004.^[179] CDs have gained importance in recent years, due to their small size, superior PL properties and availability of economical starting materials. CDs are known as *fluorescent carbon* due to their strong FL. The as-prepared CDs display quantum effects with a diameter < 10 nm, which is the size-dependent optical properties

Interestingly, CDs display intriguing features such as versatile surface chemistry, high optical absorptivity, water-solubility, low-toxicity, good chemical stability, biocompatibility and resistance to photobleaching.^[180] Specifically, along with down-converted FL, CDs exhibits outstanding up-converted FL (UCFL), which facilitates the design of high-performance CDs for

effective utilization of the full spectrum of sunlight.[181,182] Depending on the synthetic methods and dopant elements, structure of CDs varies. In contrast to nano-diamonds, CDs have more sp² character, which indicates the graphitic nature of CDs. Transmission electron microscopy (TEM) is used to investigate the size, micro-structure and morphology of the N-doped CDs. TEM images showed that the N-doped CDs have a nearly spherical shape with a narrow size distribution with an average size of ≈ 5 nm (Fig. 1.23 A). High Resolution -TEM images clearly showed the details of the structure and the atomic lattice fringes (Fig. 1.23 B, C and D). As shown in Fig.

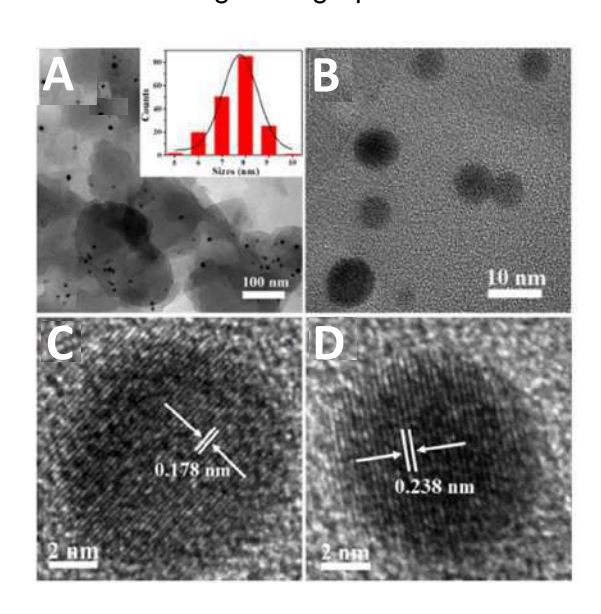


Figure 1.23: A) Low-resolution (LR)-TEM image of N-doped CDs. The inset shows the particle size distribution histogram and B, C and D) High-resolution (HR)-TEM images of the as-synthesized N-doped CDs. [183]

1.23 C and **D**, the interatomic lattice spacing ≈ 0.178 and 0.238 nm of N-CDs are close to the (004) interlayer spacing and (100) in-plane lattice spacing of graphite, [184,185] respectively demonstrating their crystalline nature and graphite-like structure.

1.5.1. Optical properties of CDs:

One of the interesting characteristics of the FL of CDs is the dependency of the emission on the excitation wavelength. Here the supposition is that core states (sp²- hybridized graphene flakes or carbon nano-domains) are the basis for the absorption property and a variation of surface states (are oxygen (O)-, nitrogen (N)-, or sulfur (S)- containing functional groups and defects in the amorphous matrix) are responsible for the excitation wavelengthdependent emission.[176] Both surface states and particles of different sizes influence the excited states of CDs in excitation wavelength-dependent FL.[174-178] One more objective for the excitation-dependent FL is the nature of the surface of the CDs. The existence of different functional groups such as -OH, -NH2, sulfates, epoxy, ether, carbonyl, and -COOH on the surface of the CDs may create a series of emissive traps. Upon excitation of CDs at a particular wavelength, a particular surface energy trap governs the FL. If there is a change in the excitation wavelength, another equivalent surface emissive traps turn into dominant. Sun et al., have reported multicolor broad FL extending the whole visible region, upon excitation of CDs solution with suitable wavelength.[186] They have described that the multicolor FL is due to photo selection of luminescence centres of definite energy levels by the selected excitation wavelength. By using different excitation wavelengths, different fractions of CDs will show the emission of different colors.

of Remarkably, some the CDs show excitation wavelength-independent emissions.[187,188] Yin and his coworkers[189] have assumed that surface groups provide different vibration relaxation for their excitation independent emission. [190-192] Although they observed excitation wavelength-dependent emission from raw CDs, the two fractions obtained from sizeexclusion chromatography (SEC) gave their excitation independent emission (Fig. 1.24). However, the different π -conjugation systems and structure of CDs directed the photon absorption, various functional groups located at the surface provided different vibration relaxation for their excitation independent emission. The surface self-trapping for vibration relaxation caused their large Stokes shift. Because of extraordinary chemical stability, biocompatibility, excellent optical absorptivity, CDs have been extensively used in various fields. The FL CDs are alternate to regular fluorescent materials as they display efficient FL properties, good solubility and biocompatibility. Compared to SQDs and fluorescent organic dyes, luminescent CDs are better in terms of easy functionalization, chemical inertness and high resistance to photobleaching and low toxicity. There have been many applications of CDs such as bio-imaging, optoelectronics, sensors, surface-enhanced Raman scattering (SERS),

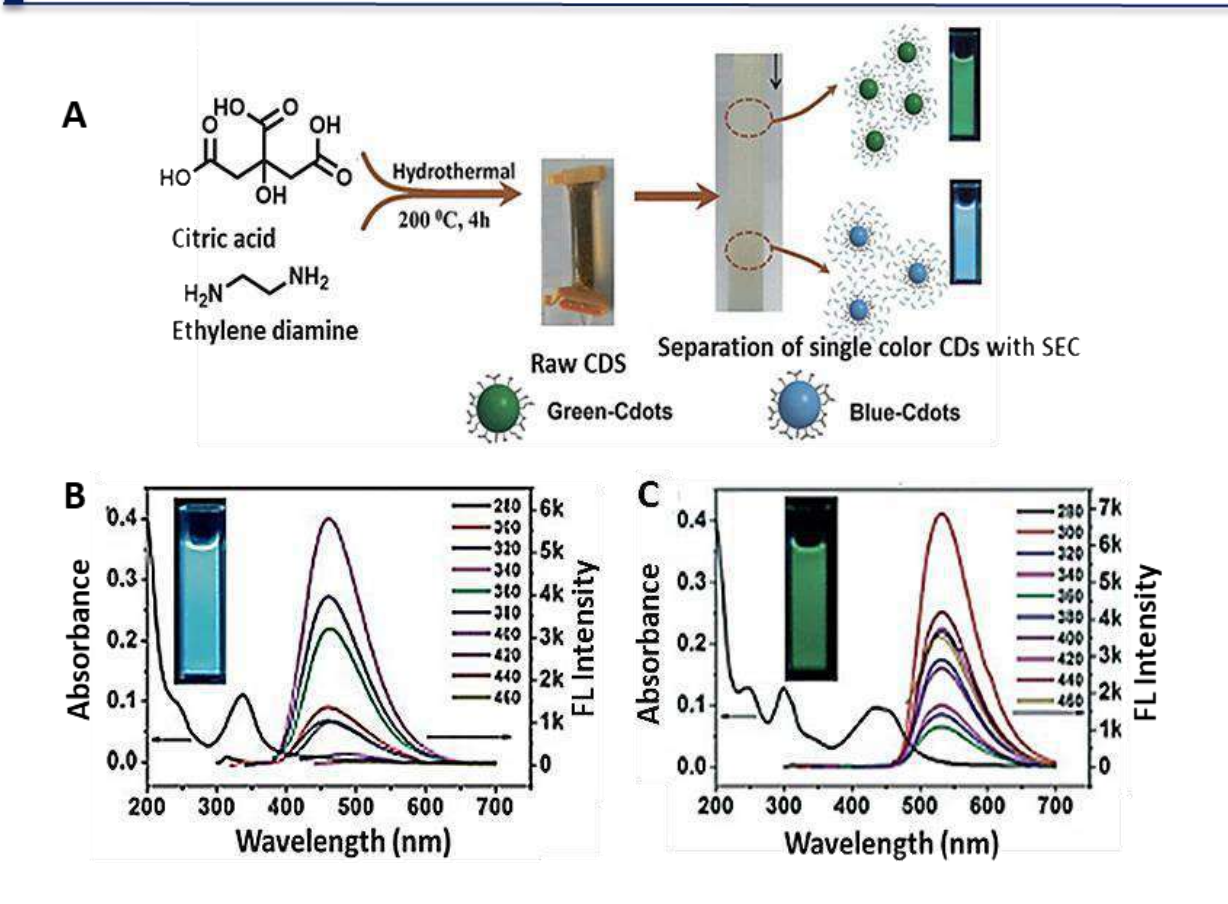


Figure 1.24: A) The synthesis of the raw-CDs from citric acid and ethylenediamine and separation with SEC to isolate blue and green CDs. The UV-Vis and excitation wavelength, independent FL spectra of (B) Blue-CDs and (C) Green-CDs. Inset: photographs of Blue-CDs (left) and Green-CDs (right) solutions under the excitation with UV light.^[189]

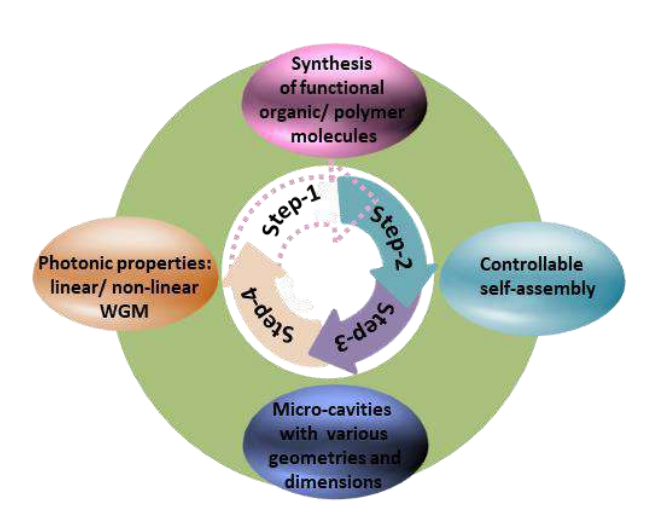
photocatalysis, biological labelling, drug delivery, medical diagnosis, and photovoltaic devices.^[193-200] Successfully, the excitation-dependent FL phenomenon is advantageous in multicolour imaging applications. There have been no reports on the CDs doped polymer to date. In this thesis, CDs doped PS matrix has been used for micro-resonator application and it will be discussed in detail in **Chapter-4** of the thesis.

1.6. Overview of thesis:

This interdisciplinary thesis summarizes several important findings in one of the emerging sub-fields of organic/polymer nanophotonics, namely, optical micro-resonators. The main objective of the thesis is to fabricate self-assembled micro-structures from organic/polymer molecules to be used as linear and NLO micro-resonators, which are

operating in different regions of the EM spectrum. Realizing the objective necessitated a multidisciplinary approach at the interface between chemistry and physics. The general approach followed in this thesis is presented in **Scheme 1.1**.

Flexible micro-resonators emitting in the Vis-NIR range are one of the important criteria for photonic device applications. Though a large number of reported organic fluorophores emit FL in the Vis region, those emitting NIR in the solid-state is still less common. Generally, substituted chalcones derivatives belonging to the class of push-pull molecules. which display strongly stokes-shifted FL in the Vis region. Thus, in this thesis work, it was envisioned that boron-complexes of



Scheme 1.1: Multi-disciplinary approach of thesis.

chalcones would increase the push-pull character of the molecule, thereby decreasing the HOMO-LUMO gap, and might impart NIR emission. Therefore, novel π -conjugated chalcone type D-A molecule and its boron complex, namely, (2E,4E)-1-(2-hydroxyphenyl)-5-(pyren-1-yl)penta-2,4dien-1-one (HPPD) and 2,2-difluoro-4-((1E,3E)-4-(pyren-1-yl)buta-1,3-dienyl)-2H-benzo[d][1,3,2]dioxaborinin-3-ium-2-uide (HPPD-BF) are synthesized. A single crystal x-ray structure of HPPD is obtained to examine the intermolecular forces involved in the aggregation of molecules. The optical properties of these molecules are thoroughly investigated both in solution and solid states to investigate their NIR emission characteristics. To investigate their photonic attributes, HPPD and HPPD-BF are used to fabricate Vis and NIR emitting flexible micro-ribbons and rigid micro-rods, respectively through solvent-assisted self-assembly technique. Single-particle micro-FL spectroscopy studies reveal that micro-ribbons and micro-rods act as the F-P resonators.

There are various fluorescent organic compounds reported to enhance FL intensity by various mechanisms. For example, CDs are well-known for their high quantum yield and their cost-effective synthesis. However, the drawback of as-prepared CDs is that they undergo aerial oxidation which leads to quenching of FL. To overcome this problem, the polymer coating of CDs by doping with polymer matrices like PMMA, **PS** and PVA is an effective solution. Further,

polymer-stabilized CDs can be self-assembled into micro-resonators to protect CDs from degradation, additionally, to enhance CDs FL. Therefore, in this thesis, novel nitrogen-rich luminescent crystalline CDs are prepared from pyridine diamine (PDA) by solvothermal method. Taking advantage of the optical transparency of **PS**, the CDs are doped in the **PS** matrix to prepare **PS-CDs** composite micro-resonators. Single-particle micro-FL experiment unveiled the WGM radiation from the micro-spheres with a high Q-value up to $\approx 2 \times 10^3$. Excitation of a thin film of **PS-CDS** with 800 nm fs pulse laser shows the TPL band with a second-order increase of the signal intensity as a function of pump fluence. These **PS-CDs** micro-spheres exhibit about 40 times enhancement in one photon luminescence (OPL) compare to their corresponding **PS-CDs** homogeneous films.

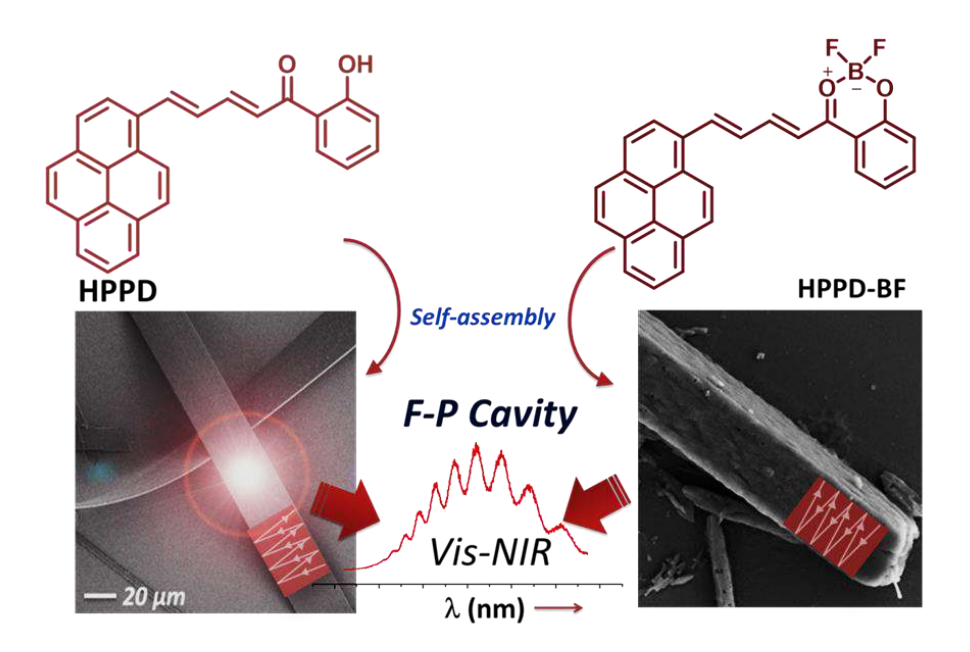
The optical bandgap is tuned to fall in the Vis region using numerous approaches including the variation of polarity, substitution position on the conjugated polymer backbone, conjugation length control, copolymerization with dyes, crystal polymorphism, crystalline-amorphous phase changes, host-guest interactions, particle size effects, π -conjugation length and CT complex formation. However, tuning the bandwidth from Vis to NIR is still challenging in non-conjugated polymers. One of the robust approaches to realize the bandgap shift is to design polymers with D and use them to make CT complexes with various small organic A molecules so that the colour tuning is possible. In this thesis, it was envisioned to prepare high-Q micro-resonators from cross-linked polymer (**PN**) micro-particles using styrene, divinylbenzene and blue-emitting 1-(4-vinylphenyl)-pyrene monomers. As expected, incorporation of TCNQ and TCNB shifts the emission colour of **PN-TCNB** and **PN-TCNQ** micro-resonators from blue to orange and red, respectively. Due to CT nature, these micro-resonators also emit TPL from Vis to NIR. Moreover, the trapped light increases the lightmatter interaction in micro-resonators and therefore enhances the FL intensity, as well as the TPL intensity.

One of the major challenging tasks in chiral-optics or photonics is the enhancement of the chiro-optical signal, for instance, circular dichroism (CD) signal of chiral molecules and chiral π -conjugated polymers. Nevertheless, the enhancement of CD responses in the naturally weak NLO signals is an important task. As a result, until now, the majority of the experiments on chiro-optical effects from chiral molecular/polymer materials were carried out only in the linear optical regime as NLO signals are also usually very weak. Although no theoretical basis relating the chiro-optical effect and optical resonators are available, in this thesis, the study of

NLO-WGM micro-resonator on the CD intensity is intended. The hypothesis for the intention was the light confinement will allow the increase of NLO conversion efficiency of the molecules. eventually enhancing the CD effects. Therefore, two chiral, conjugated copolymers, R- and S-**BP** are synthesized by copolymerizing of *R*- and *S*-6,6'-dibromo-2,2'-diethoxy-1,1'-binaphthyl (R- and S-BINOL derivatives) with 1,4-diethynyl-2,5-bis(octyloxy)benzene by Sonogashira coupling reactions. These R- and S-BP self-assemble into micro-spherical structures exhibiting WGM resonances in the one and TPL (500-720 nm) with a Q of up to ~700. Unexpectedly, at high laser power (≥10 mW), the TPL spectral features of micro-spheres changed significantly, hinting the alteration in the polymer main and side-chain packing. Similar spectroscopic changes were observed for micro-spheres heated thermally or with high power continuouswave laser confirming the laser-triggered heat. FLIM studies down to a single micro-sphere level unambiguously confirm the transformation of polymer packing from a homogeneous J type to a heterogeneous mixture of J, H and H-like types. Additionally, due to their chiral nature, the TPL signals of the enantiomeric polymers also display a CD effect of about 6% with opposite signs. This original work demonstrates the tremendous potential of laser-driven shifting of electronic coupling tunability of conjugated polymers useful for many applications.



Flexible Micro-Ribbons and Rigid Micro-Rods from Self-Assembly of Chalcone-Type Push-Pull Dye Molecules for Vis/NIR Range F-P Micro-Resonators



^{*}This chapter is adapted from:

2.1. Abstract:

This chapter presents the syntheses and self-assembly of chalcone type dye molecule, (2E,4E)-1-(2-hydroxyphenyl)-5-(pyren-1-yl)penta-2,4dien-1-one (HPPD) and its boron complex, namely, 2,2-difluoro-4-((1E,3E)-4-(pyren-1-yl)buta-1,3-dienyl)-2H-benzo[d][1,3,2]dioxaborinin-3-ium-2-uide (HPPD-BF) for Vis/NIR range photonic resonator applications. The single-crystal X-ray structure of HPPD and its solid-state optical studies point towards J-type molecular aggregation. The structure-property relationship studies using single-particle micro-spectroscopy disclose the occurrence of F-P optical resonance from the flexible micro-ribbons and rigid micro-rods. The concentration of the optical field is mainly along the lateral walls of micro-resonator.

2.2. Introduction:

Self-assembly is a simple and inexpensive method to obtain photonic organic particles with different geometries such as rods, [201,25] tubes, [202-204] spheres, [61,71] rings, [205] hemispheres^[51,95,206] and fibers.^[207] Moreover, the geometry of organic particles plays an important role in realizing numerous photonic materials, waveguides, [202,204,208-210] modulators, [201] resonators, [71,203,206,207] lasers [25,51,61,95] and circuits. [110,207] Self-assembled organic structures are evolving as promising materials that improve our fundamental understanding light-matter interactions and facilitate miniaturized of applications. [25,201-204,208-212] Even though numerous reports on self-assembled organic molecules, only a few studies have revealed single-particle-level light-matter interaction properties. FL organic molecules with supramolecular interactions (van der Waals, hydrogen bond, π - π interactions, etc.) act as key building blocks for the creation of shapedefined organic assemblies by solution processing techniques. To our knowledge, till now there have been no reports on elongated flexible micro-ribbons with F-P resonator characteristics.

To fabricate self-assembled photonic particles/structures with an easily tunable bandwidth and high Φ_{FL} , organic D and A type FL molecular systems are the best candidates. Chalcone type D-A push-pull dye molecules with π - π stacking units are helpful to attain supramolecular interactions through long-range ordering in the solid-state. The boron complexes of chalcone derivatives, due to their improved push-pull character, should exhibit larger Stokes shift, reduced optical band gap and solution-/solid-state emission in the NIR range. [213] Therefore, this chapter describes the syntheses, crystal structure, and optical properties of a new chalcone type molecule, namely **HPPD** and its boron complex

HPPD-BF (**Scheme 2.1**). Further, self-assembly of **HPPD** and **HPPD-BF** into flexible microribbons and rigid micro-rods, respectively, via slow solvent evaporation method is described. Finally, single-particle micro-FL spectroscopy studies of micro-structures supporting F-P optical modes in the Vis/NIR region of the EM spectrum are presented.

2.3. Results and Discussion:

2.3.1. Syntheses:

Scheme 2.1: Syntheses of push-pull type **HPPD** and its BF₂ (**HPPD-BF**) complex.

Synthesis of (*E*)-3-(Pyren-1-yl)acryl aldehyde:

This compound was synthesized according to the literature procedure. ^[214] 1-Bromopyrene (0.117 g, 0.5 mmol), tetrabutylammonium acetate (0.302 g, 1.0 mmol), K_2CO_3 (0.104 g, 0.75 mmol), KCl (0.037 g, 0.5 mmol) and $Pd(OAc)_2$ (0.003 g, 0.015 mmol) were taken in a clean and dry 100 mL two neck round bottom flask. The flask was put under a freeze-pump-thaw cycle three times. To this, acrolein diethyl acetal (0.229 mL, 1.5 mmol) and dry DMF of 2.0 mL were added. The resultant solution was heated to reflux at 90 °C for

1.5 h. It was then cooled to rt and 2N HCl was slowly added to it and left for stirring for an additional 10 min. Then, the mixture was diluted with Et_2O , followed by washing with H_2O . The solution was dried over anhydrous Na_2SO_4 and evaporated in vacuo. The obtained crude compound was further purified by chromatography (silica gel) with n-hexane/ethyl acetate 90:10 as eluent to give 0.071 g (88% yield) of (*E*)-3-(Pyren-1-yl)acryl aldehyde. ¹H-NMR (400 MHz, CDCl₃, 298 K) δ /ppm: 9.94-9.93 (d, 1H), 8.66-8.62 (d, 1H), 8.50-8.48 (d, 1H), 8.18-8.33 (m, 6H), 8.1-8.05 (m, 2H), 7.00-7.06 (dd, 1H).

Synthesis of (2*E*,4*E*)-1-(2-hydroxyphenyl)-5-(pyren-1-yl)penta-2,4dien-1-one (HPPD):

A mixture of (E)-3-(Pyren-1-yl)acryl aldehyde (188 mg, 0.73 mmol) and 2hydroxyacetophenone (2-HAP) (100 mg, 0.73 mmol) were placed in a clean and dry 100 mL two neck round bottom flask containing a solution of EtOH/MeOH. Then NaOH solution (73 mg, 1.8 mmol) in H_2O (1 mL) was added to the reaction mixture. The reaction was continued with stirring for 16 h at 60 °C. After cooling to rt, the mixture was neutralized with 1N HCl and extracted with EtOAc. The organic fraction was treated over Na₂SO₄ and evaporated in vacuo. The resulting solid was purified by column chromatography on silica gel (EtOAc/hexane, 5:95) to get red color solid of HPPD. Yield: 150 mg (54%). 1H-NMR (400 MHz, DMSO-d₆, 298 K) δ/ppm: 12.5 (s, 1H), 8.77-8.74 (d, 1H), 8.60-8.54 (t, 2H), 8.37-8.35 (m, 4H), 8.25-8.24 (m,2H), 8.14-8.11 (t, 1H), 8.07-8.05 (d, 1H), 8.02-8.00 (t, 1H), 7.96 (s, 1H), 7.68-7.64 (m, 1H), 7.60-7.57 (t, 1H), 7.04-7.02 (d, 1H). ¹³C-NMR (100 MHz, DMSOd₆, 298 K) δ/ppm: 193, 163, 145, 139, 136, 132, 131, 130, 129.6, 129.3, 129, 128.8, 128.3, 128.2, 127, 126, 125.8, 125.5, 124.9, 124.6, 124.5, 123.5, 123.3, 122, 119,118.6, 118.4. FTIR (KBr; $\bar{\vartheta}$ cm⁻¹): 1632, 1556, 1487, 1437, 1380, 1302, 1261, 1237, 1187, 1152, 1023, 993, 837, 801, 747, 712. ESI-TOF MS (*m/z*): Calculated (M+K): 413.228, Found: 413.265. Elemental analysis (%) C₂₇H₁₈O₂: Calculated: C, 86.61; H, 4.85; Found: C, 86.52; H, 4.91.

Synthesis of HPPD-BF:

HPPD (20 mg, 0.05 mmol) and BF₃·Et₂O (0.1 mL, 0.06 mmol) were taken in a clean and dry 100 mL two neck round bottom flask equipped with a magnetic pellet. To this, CH₂Cl₂ (10 mL) was added and the reaction mixture was heated to reflux at 60 °C for 2 h. After that, solvent was removed in vacuo followed by cooling to get the black color precipitate. The obtained precipitate was filtered off, washed with Et₂O, and air dried at ambient temperature to get **HPPD-BF** as a black solid with 38% Yield (12 mg). ¹H-NMR (400 MHz, DMSO- d_6 , 298 K) δ/ppm: 8.76-8.74 (d, 1H), 8.59-8.56 (m, 2H), 8.337- 8.35 (m, 4H), 8.27-8.24. (m, 2H) 8.14-8.12 (d, 1H), 7.99-7.96 (dd, 1H), 7.67-7.64 (d, 1H), 7.63-7.60

(m, 1H), 7.58-7.56 (dd, 1H), 7.04-7.02 (d, 2H). 11 B-NMR (160 MHz, DMSO- d_6 , 298 K) δ /ppm: -0.54. 19 F-NMR (470 MHz, DMSO- d_6 , 298 K) δ /ppm: -148.07, -148.12 ppm; FTIR (KBr; $\bar{\vartheta}$ cm⁻¹): 1630, 1618, 1588, 1555, 1472, 1404, 1286, 1188, 1123, 1072, 982, 844, 758, 638, 610. Elemental analysis (%) $C_{27}H_{17}BF_2O_2$: Calculated: C, 76.80; H, 4.06; Found: C, 76.69; H, 4.12.

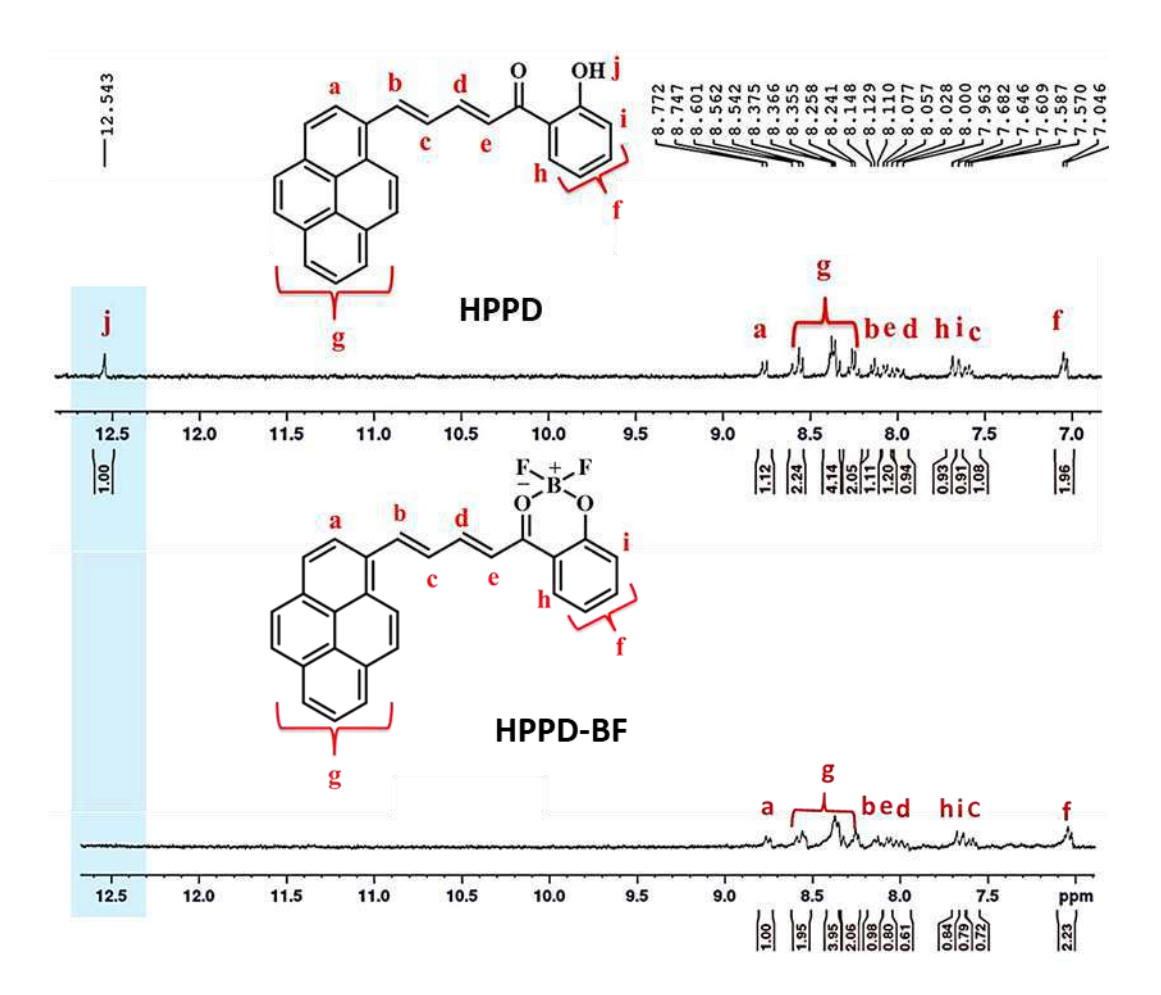


Figure 2.1: ¹H-NMR (400 MHz) spectra of HPPD and HPPD-BF in DMSO-d₆.

The D-A unit **HPPD** and its boron complex were prepared in four steps (**Scheme 2.1**). First, pyrene was converted into 1-Bromopyrene by using N-bromosuccinimide (NBS) and 1-Bromopyrene was transformed into the corresponding pyreneacryl aldehyde. Subsequently, pyreneacryl aldehyde was condensed with 2-hydroxyacetophenone through Claisen–Schmidt reaction to obtain the red **HPPD** dye in 54% yield (**Scheme 2.1**). The 1 H- and 13 C-NMR spectra (in CDCl₃) exhibited chemical shift (δ) values of 12.09 ppm for the -OH proton, and 193.5 ppm for the carbonyl carbon, respectively. The downfield shifted -OH peak is indicative of the intramolecular hydrogen bond in the solution state. Furthermore,

ESI-TOF-MS analysis clearly confirmed the formation of HPPD molecule (m/z 413.228 [M+K]).

In order to reduce the HOMO-LUMO gap, HPPD-BF was synthesized as a black solid from the HPPD ligand by using BF₃-Et₂O in dichloromethane (DCM). In the ¹H-NMR spectrum (in DMSO-d₆) of **HPPD**, the -OH proton peak appeared at 12.54 ppm, and after the addition of BF₃.Et₂O, the proton of -OH is replaced by boron atom. [213] Therefore, the peak at 12.54 ppm completely disappeared in HPPD-BF ¹H-NMR spectrum (Fig. 2.1). In **HPPD-BF**, the ¹¹B-NMR spectrum the peak at 0 ppm corresponds to the BF₃.Et₂O standard, whereas the peak at -0.54 ppm corresponds to the boron atom of HPPD-BF (Fig. 2.2). Even though the boron is supposed to exhibit triplet, it displayed singlet (single peak) in the spectrum, which is comparable with reported literature. [215] This is due to rapid relaxation of ¹¹B-nucleus, which hinders the observation of ¹¹B coupling constant (*J*) of other nuclei like H, O and F. Due to more sensitivity and better resolution at external magnetic field, broad signal (background signal) in the spectrum originated from NMR tube between 30 and -30 ppm, stated as a boron hump. 19F-NMR spectrum of HPPD-BF displayed two peaks at -148.07 and -148.12 ppm (Fig. 2.2). Though F-atom is assumed to exhibit 4 peaks; it displayed two sharp peaks (high sensitivity of F), which is consistent with reported literature.[216]

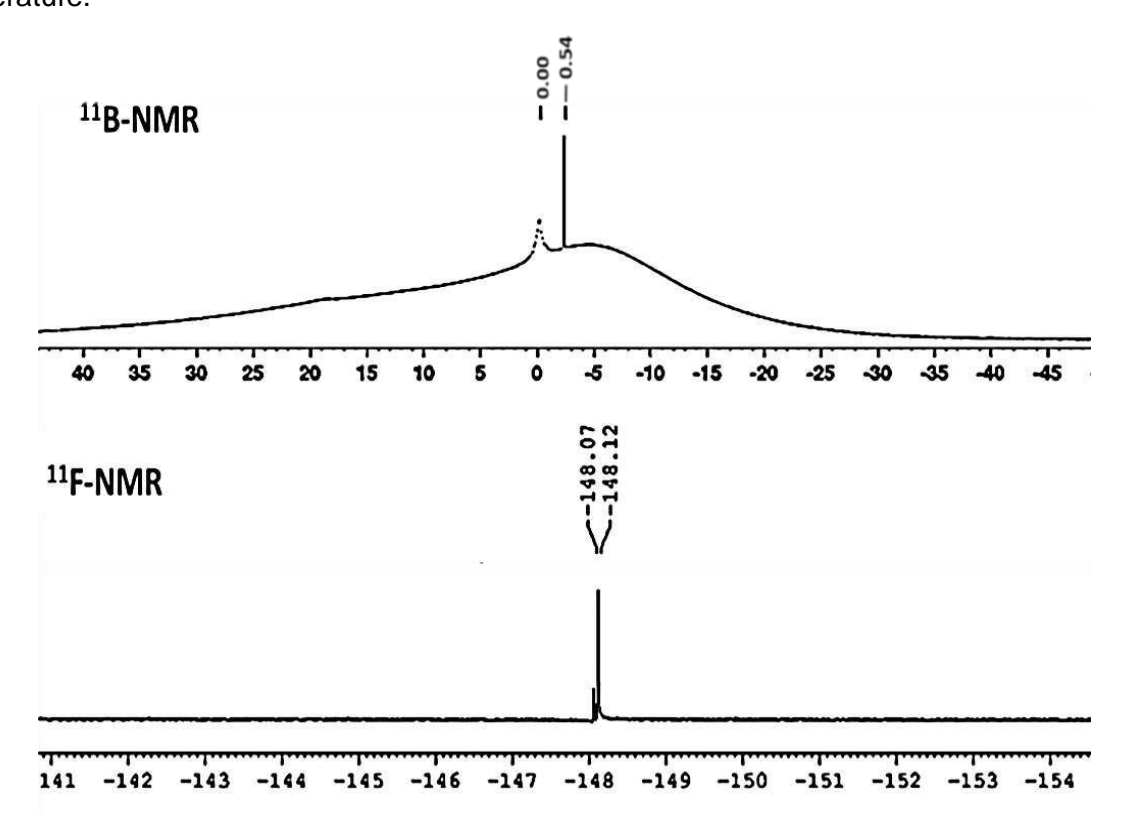


Figure 2.2: ¹¹B-NMR (160 MHz) and ¹⁹F-NMR (470 MHz) spectra of HPPD-BF in DMSO-d₆..

2.3.2. FTIR and Raman spectroscopic studies:

In the FTIR spectra, the -OH and >C=O stretching frequencies of **HPPD** appeared at 3450 cm⁻¹ (broad) and 1630 cm⁻¹ (sharp), respectively. In comparison to **HPPD**, the FTIR spectrum of **HPPD-BF** displayed a reduction of the >C=O stretching band (1630 cm⁻¹) intensity, which signifies the formation of a B-O bond. Here, it is expected that in **HPPD-BF**, the reduced >C=O dipolar character due to the donation of lone pair of electrons to the B-atom. Additionally, **HPPD-BF** exhibited a sharp peak at 609 cm⁻¹ correspondings to the B-F deformation and the peak at 1406 cm⁻¹associated to B-O stretching frequency (**Fig. 2.3 A**). [217] The Raman spectrum (He-Ne: 785 laser) of **HPPD** exhibited two intense peaks at 1063 and 1244 cm⁻¹ (**Fig. 2.3 B**) in addition to other low-intensity bands. As the solid-state absorption band covered the entire visible region up to 800 nm and highly fluorescent even in the NIR region excitation, Raman spectrum could not be recorded in **HPPD-BF** complex.

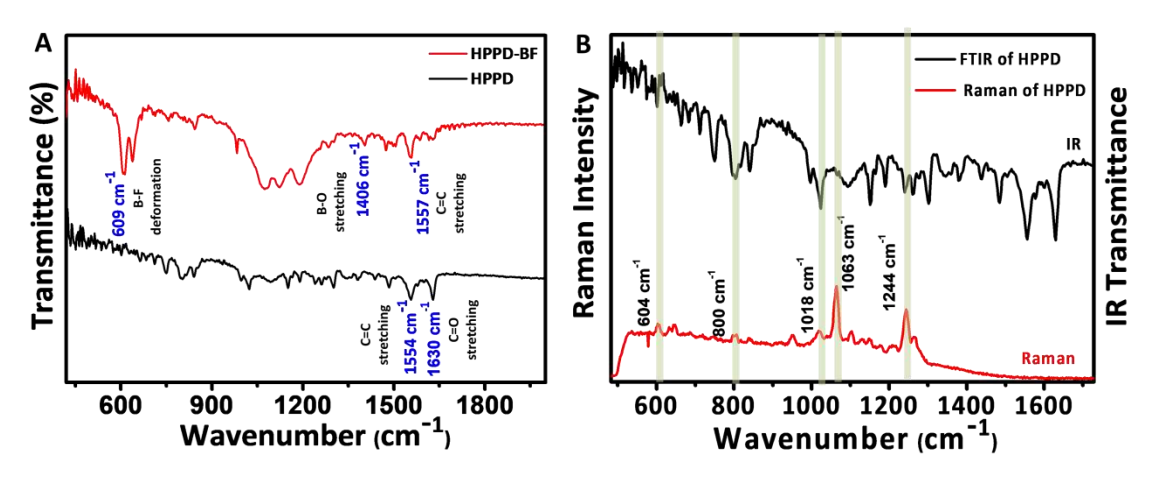


Figure 2.3: A) FTIR spectra of **HPPD** and **HPPD-BF**. B) Comparison of Raman and FTIR spectra of **HPPD**.

2.3.3. Optical properties of HPPD and HPPD-BF:

The optical absorption and emission properties of **HPPD** and **HPPD-BF** in DMF and spin-coated solid-state films are presented in **Fig. 2.4** and **Table 2.1**. In DMF solution ($c \approx 1.0 \times 10^{-5}$ M), **HPPD** exhibited multiple absorbance maxima at 276/326/432 nm (**Fig. 2.4 C**). For the interpretation of these peaks, it is essential to understand the structure of **HPPD**. The molecular structure of **HPPD** consists of an electron-withdrawing 2-HAP type unit coupled to a pyrene entity through a 1,3-butadiene π -conjugated coupler. Intramolecular hydrogen bond also assists in enhancing the π -conjugation of the aromatic π -systems by restricting the rotation of the C21 and C22 bond, forming a planar structure (see **Fig. 2.7 A**). Moreover, pyrene acts as either A or D depending upon the substituents. [218] The high

intensity broad band appeared at 432 nm (with a shoulder at 402 nm) in the absorbance spectrum of **HPPD** suggests towards its origin as a result of ICT. The FL band (λ_{ex} = 432 nm) of **HPPD** showed a broad emission with a peak maximum located at 607 nm with a Stokes shift of 172 nm (Fig. 2.4 C).

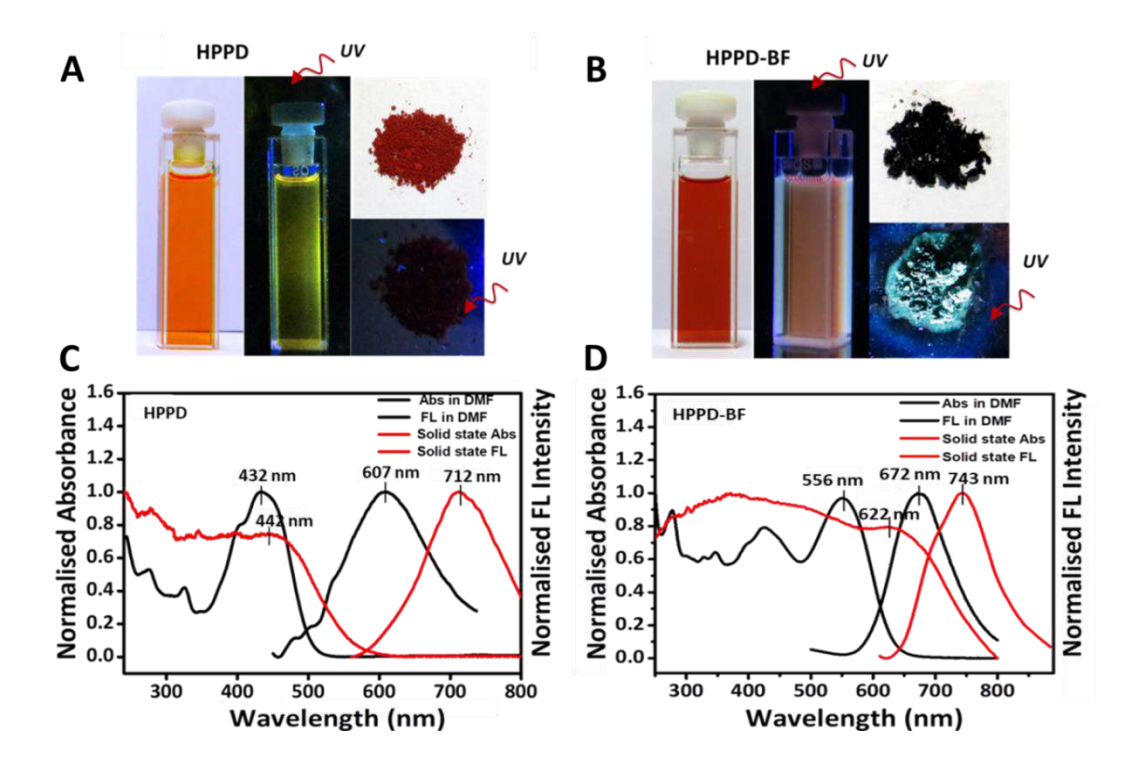


Figure 2.4: A and B) Photographs of the **HPPD** and **HPPD-BF** in solution and solid-state at ambient temperature and under UV light irradiation. C and D) Solution (in DMF, black lines) and solid-state (red lines) absorbance and FL spectra of **HPPD** and **HPPD-BF** complex, respectively.

Further, solvents of different polarities from nonpolar to polar aprotic [hexane, diethyl ether, THF, ethyl acetate, acetone, acetonitrile] were used to investigate the solvatochromic effects in the electronic spectra (Fig. 2.5). Though the absorption band moved a little to the low energy side, the emission band displayed a strong redshift (ca. 100 nm) upon varying the solvent from hexane to acetonitrile indicating the existence of the ICT process in HPPD. In contrast to solution-state, the HPPD in solid-state exhibited absorbance maximum centered at 442 nm and emission at 712 nm with a large Stokes shift of 270 nm. Because of very weak electronic coupling between the molecules, from the spectral data, it was not possible to recognize the typical *J*-band anticipated from the solid-state packing of HPPD.

Moreover, the solution state absorbance spectrum of **HPPD-BF** showed pyrene spectral features (242, 278, 349 nm) and two new broadbands in the visible region, one at 421 nm, followed by a second band at 556 nm. Further, **HPPD-BF** displayed FL maximum

at 672 nm with a Stokes shift of 122 nm (**Fig. 2.4 D**). The significant Stokes shift pointing out the strong dipolar character of the BF₂-complex. Compared to the solution-state, solid-state **HPPD-BF** showed a bathochromic shift in absorbance and emission spectra. The later spectral band appeared in the range of ca. 620 to 950 nm, covering most of the NIR region indicating possible *J*-aggregated state.

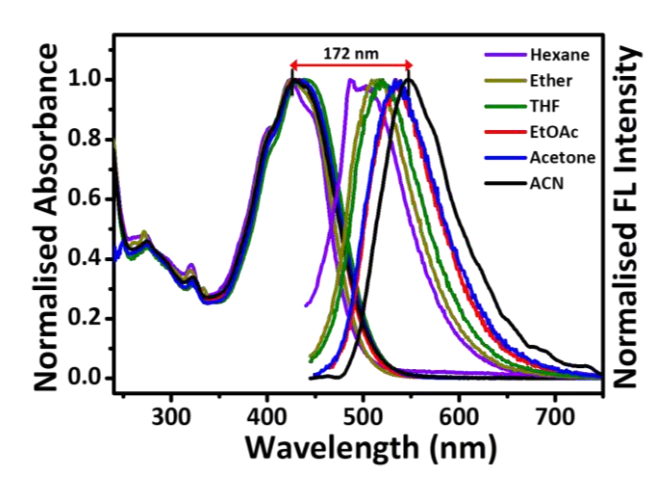


Figure 2.5: Absorbance and FL spectra of HPPD in different solvents.

Table 2.1: UV-Visible absorbance and emission spectroscopy data of HPPD and HPPD-BF.

Compound	Solution-state (DMF)		Solid-state	
	Absorbance	FL	Absorbance	FL
HPPD	432 nm, shoulder 402 nm	607 nm	442 nm	712 nm
HPPD-BF	421 nm, 556 nm	672 nm	622 nm	743 nm

2.3.3.1. FL lifetime studies:

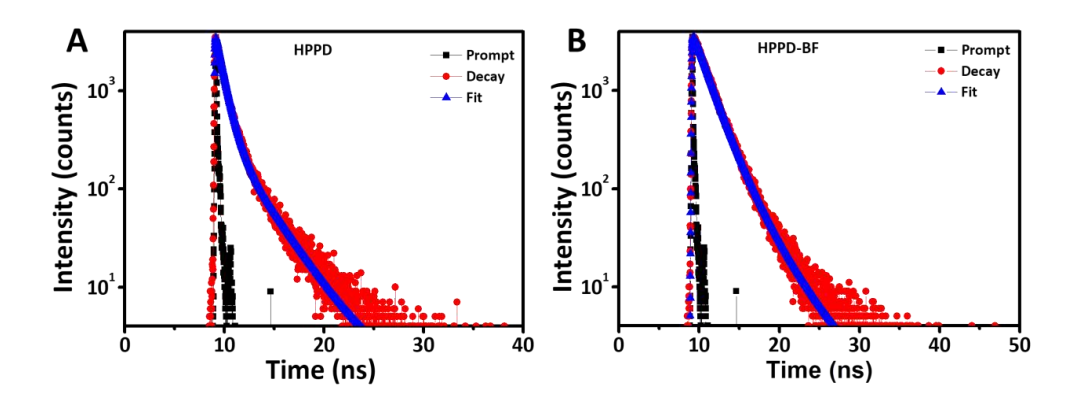


Figure 2.6: Steady-state lifetime measurements of HPPD A) and HPPD-BF B).

Both **HPPD** and **HPPD-BF** molecules in DMF exhibited monoexponential FL decay with lifetime (τ_{FL}) of 0.97 and 1.97 ns, respectively (**Fig. 2.6**), which suggest the fast excited state dynamics of the **HPPD** molecule compared with that of **HPPD-BF**.^[219,220]

2.3.4. Self-assembly of HPPD and HPPD-BF:

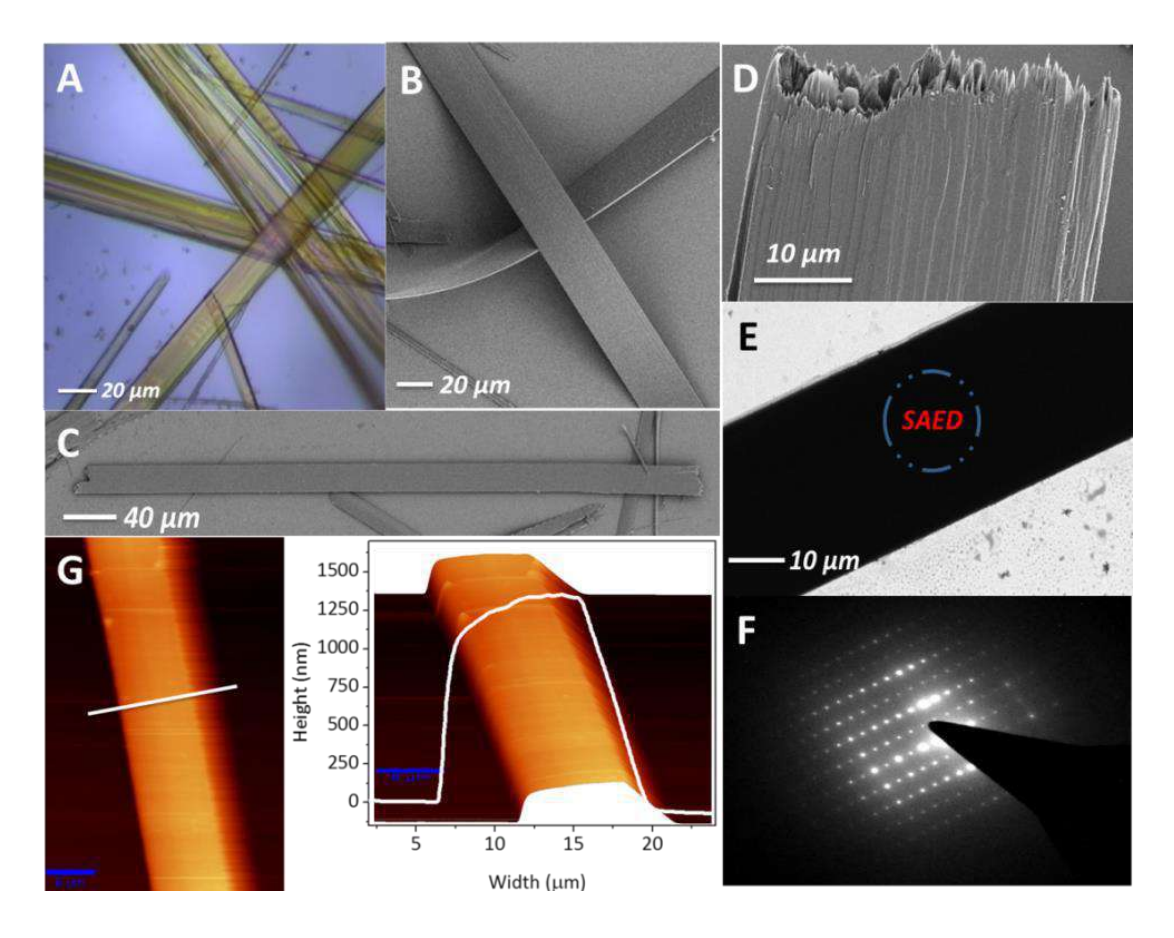


Figure 2.7: A) Confocal microscopic image of **HPPD** micro-ribbons. B) and C) FESEM image of flexible and straight micro-ribbons. D) Expanded view of the ribbon tip (shown in red box in C) displaying the presence of individual nanofibers along its growth axis. E) TEM image of a single crystalline micro-ribbon and F) its corresponding SAED pattern. G) AFM image of a single micro-ribbon displaying its thickness (T) and width (W) profiles.

The bottom-up self-assembly approach was followed to get micro-scale aggregates of **HPPD** and **HPPD-BF**. At first, 1 mg of **HPPD** was dissolved in a mixture of CHCl₃/EtOH (2:1), followed by placing the solution at 0 °C for a day to obtain micro-crystals. Later, 2-3 drops of solution from mother liquor (100 mL) having single crystals were drop casted on a clean glass cover-slip and the solvents were allowed to evaporate slowly. Investigation of the sample under a confocal optical microscope showed the presence of micro-ribbon type structures with linear and bent geometries, which specify their flexible nature (**Fig. 2.7 A**).

FESEM Moreover. analysis revealed the formation of flexible microribbons of variable lengths (L), widths (W), and thicknesses (T) (Fig. 2.7 B, C). A close examination of the ends of a single micro-ribbon revealed that every ribbon consists of several anisotropically stacked nanofibers (Fig. 2.7 D). Further, TEM investigation of a selected micro-ribbon displayed a dark its considerable contrast due to thickness (Fig. 2.7 E). AFM topography images of a selected micro-ribbon showed T \sim 1.2 μm and W \sim 20 μm confirming the ribbon-like structure (Fig. **2.7 G**). The selected area electron diffraction (SAED) (Fig. 2.7 F) showed a clear, bright diffraction spot, indicating the single-crystalline nature of the

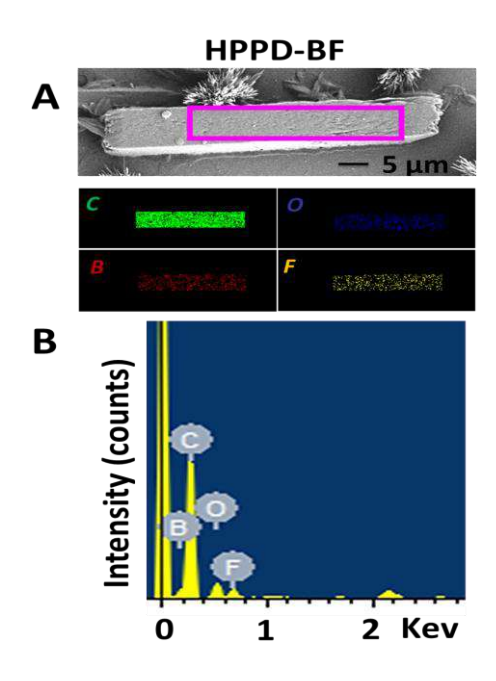


Figure 2.8: A) FESEM image of a single crystalline **HPPD-BF** micro-rod and its EDS elemental map. B) EDS data exhibiting distribution of B, C, O, and F elements in the micro-rod.

micro-ribbonsTo unveil the photonic behavior of **HPPD-BF**, it was self-assembled (1 mg mL⁻¹) in CHCl₃ by drop-casting the dispersion on a coverslip to generate micro-structures. Analysis of the micro-structures under FESEM revealed the rectangular feature of the micro-particles (micro-rods) (**Fig. 2.8 A**). Further energy dispersive X-ray (EDS) investigation performed on micro-rod, showed the presence of B, O, C, and F elements, which prove the chemical composition of the micro-rods (**Fig. 2.8 B**).

2.3.5. Disassembly study of micro-ribbons:

The formation of micro-ribbons are probably due to π - π stacking interactions (as shown by the single X-ray structure of **HPPD**; see **Fig. 2.10 B**) between adjacent molecules of pyrene units forming nano-fibers, which consequently aggregate into flexible micro-ribbon-like structures. To investigate the formation mechanism of micro-ribbons, they were slowly dissolved or disassembled and this process was followed by the confocal microscope as a function of time. In the dissolution process, the addition of a few drops of acetonitrile/EtOH or acetonitrile to micro-ribbons revealed the disassembly of the micro-ribbons to produce numerous brush-like nano-fibers structures through intermediate

structures. This mechanistic study revealed that the micro-ribbons are possibly superstructures that are formed due to several stacked nano-fibers (Fig. 2.9).

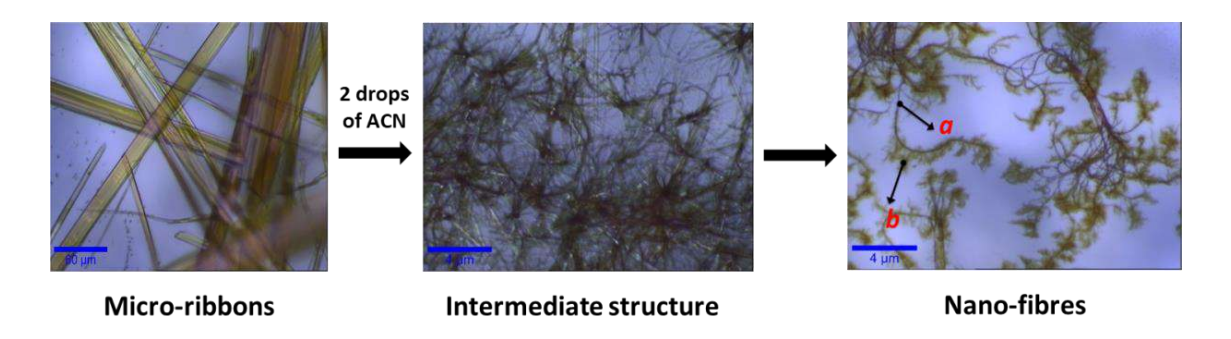


Figure 2.9: Confocal optical microscopy images of disintegrating micro-ribbons (see label a) into nano-fibres (see label b).

2.3.6. Crystal structure of HPPD:

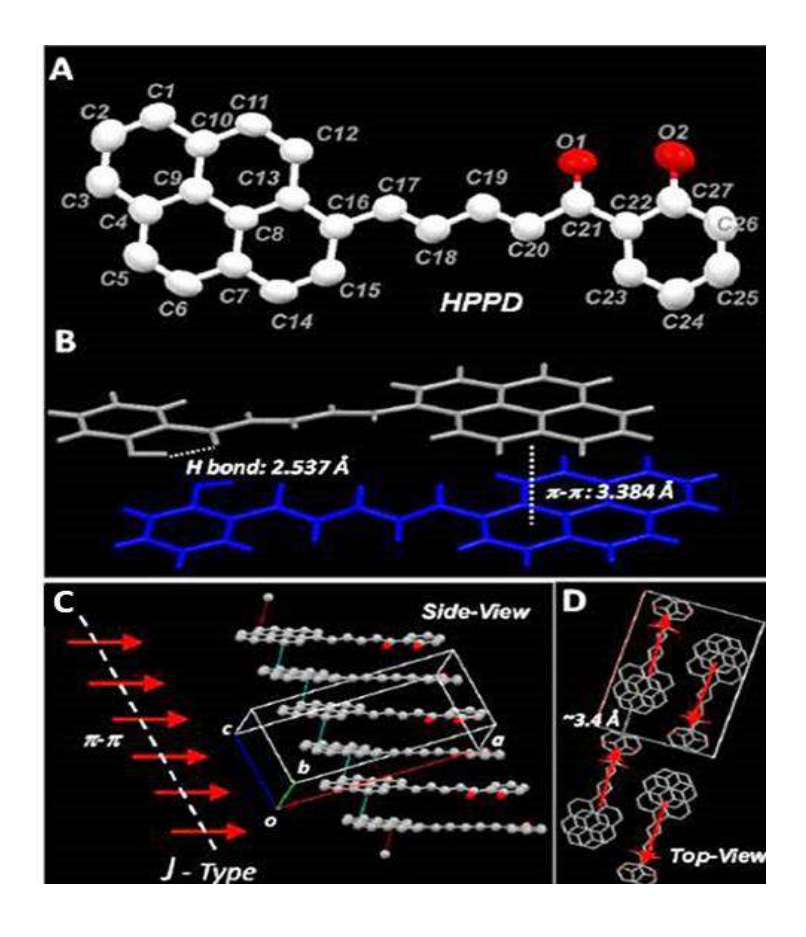


Figure 2.10: A) Single-crystal structure of **HPPD**. B) **HPPD** dimer displaying π - π stacking and intramolecular H-bond. C and D) Packing of π - π stacked molecules along the crystallographic c-axis.

HPPD molecules formed single crystals in a mixture of $C_2H_5OH/CHCl_3$ (1:2). Investigation of the single-crystal X-ray structure (monoclinic; P21/c; CCDC 1479670) (Fig.

2.10 A) showed the existence of supramolecular interactions required for the aggregation to occur. The solid-state packing of **HPPD** exhibited an intramolecular hydrogen bond interaction between the carbonyl oxygen and the hydroxyl group $[O(1)\cdots H\ (24)=2.537\ Å]$ and intermolecular π - π stacking of pyrene units $C(9)\cdots C(18)\approx 3.384\ Å$ (**Fig. 2.10 B**). Moreover, the *trans*-configured 1,3-butadiene fragment connecting the pyrene donor and acceptor units retain the entire molecule in an in-plane configuration. The molecular packing specified a slipped ladder-type *J*-type aggregation of **HPPD** in solid-state (**Fig. 2.10 C**). The one dimensional (1D) π - π stacks are nearly 45° to the crystallographic *b*-axis and they propagate alongside the crystallographic *c*-axis. Unfortunately, attempts to acquire the crystal structure of **HPPD-BF** were not successful.

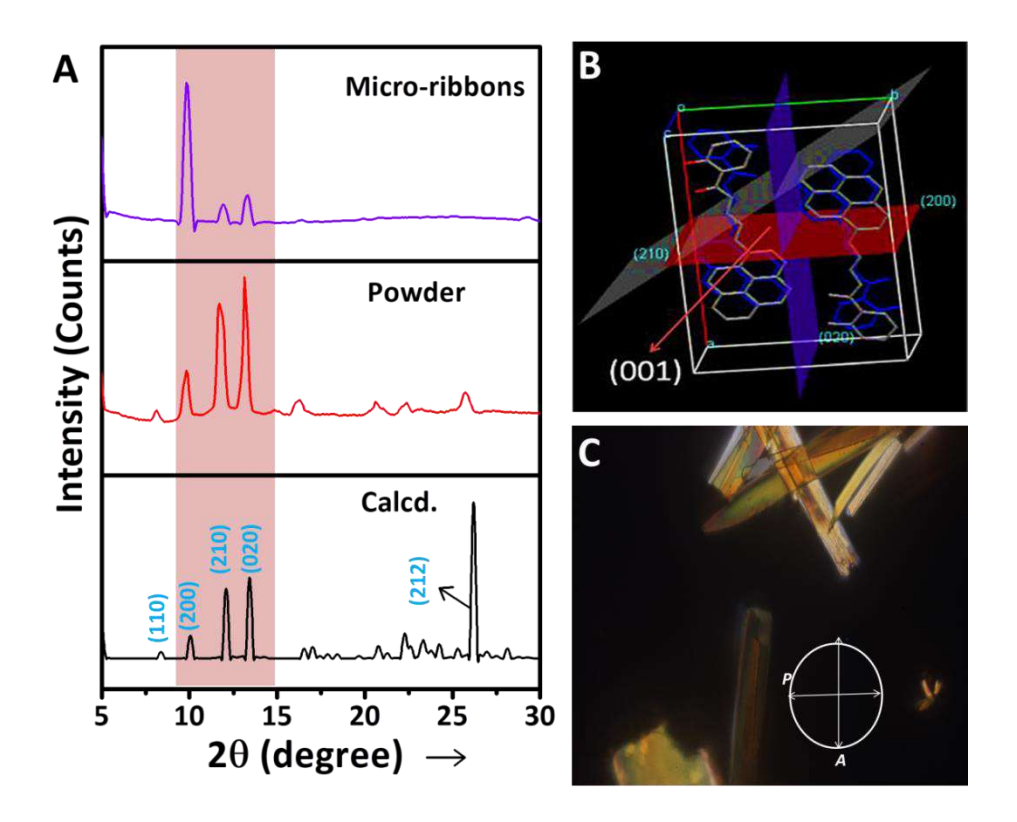


Figure 2.11: A) Powder XRD data of micro-ribbons, powder **HPPD**, and calculated spectrum from the single-crystal data. B) Packing of **HPPD** molecules within the unit cell. C) Polarized optical microscopy images of **HPPD** micro-ribbons (white crossed arrow illustrate the crossed polarizers).

Moreover, a comparison of the calculated powder XRD of micro-ribbons with its single-crystal XRD data revealed three intense as well as matching diffraction peaks at 2θ (hkl) values 10.04° (200), 12.16° (210), and 13.5° (020). The intensity of (200) peak in micro-ribbon was found to be higher than the calculated value. Further, the powder sample displayed approximately equivalent peak positions and intensities with the calculated data (**Fig. 2.11 A**). This outcome proves the presence of equivalent molecular packing both in

single crystals and micro-ribbons. The growth direction of the micro-ribbon is probably in the π - π stacking direction of pyrene units, which is the crystallographic *c*-axis (001 plane) (**Fig. 2.11 B**). In order to check optical anisotropy and intrinsic molecular ordering in single-crystalline micro-ribbon, the polarized optical microscopic study was carried out. In cross-polarizer set-up, the micro-ribbons that are oriented 0°, 90°, 180°, 270° to the polarizer/analyzer appeared dark. Whereas, maximum brightness was observed when the micro-ribbons aligned almost 45°, 135°, 225° to the polarizer/analyzer suggesting the direction of the optical axis (a direction in which a ray of transmitted light suffers no birefringence) (**Fig. 2.11 C**).

2.3.7. Single-particle micro-spectroscopy studies of HPPD:

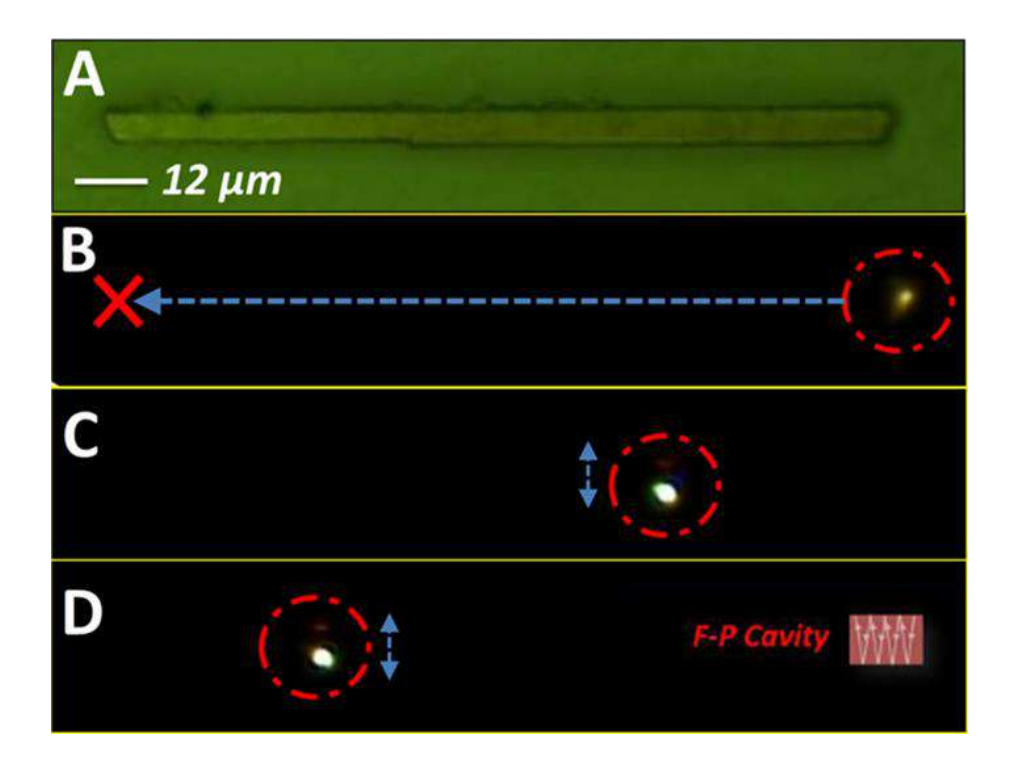


Figure 2.12: A) Bright-field and FL confocal optical micrographs of a single micro-ribbon. B) Excitation of a micro-ribbon tip with 488 nm Ar⁺ laser shows no light propagation along the fiber axis. C and D) Excitation along the corners shows light propagation in the transverse direction. The inset shows a cartoon depicting the F-P type resonator.

To verify the resonator characteristics of the micro-ribbon single-particle micro-FL experiment was performed on a Laser Confocal Microscope (LCM) set-up. At first, the center of a single micro-ribbon (Fig. 2.12 A) was optically excited with a CW laser (488 Ar⁺, objective: 150x; NA: 0.95). Though this excitation produced red FL at the excitation point, no waveguiding of the FL was detected along the growth axis of the ribbon (Fig. 2.12 B).

However, FL waveguiding was recorded in the lateral direction, indicating the effect of the optical anisotropy of the micro-crystalline ribbon (Fig. 2.12 C, D). Remarkably the corresponding single-particle spectrum (collected in a reflection mode) exhibited FL band together with series of wavelength-dependent intensity-modulated peaks. These intensity-modulations indicate the resonator action of the single micro-ribbon. The separation between peaks FSR periodically increased towards the higher wavelength region (up to 850 nm). This result shows the mirror-like reflection action of micro-ribbon surfaces, which allow multiple FL wave interferences.

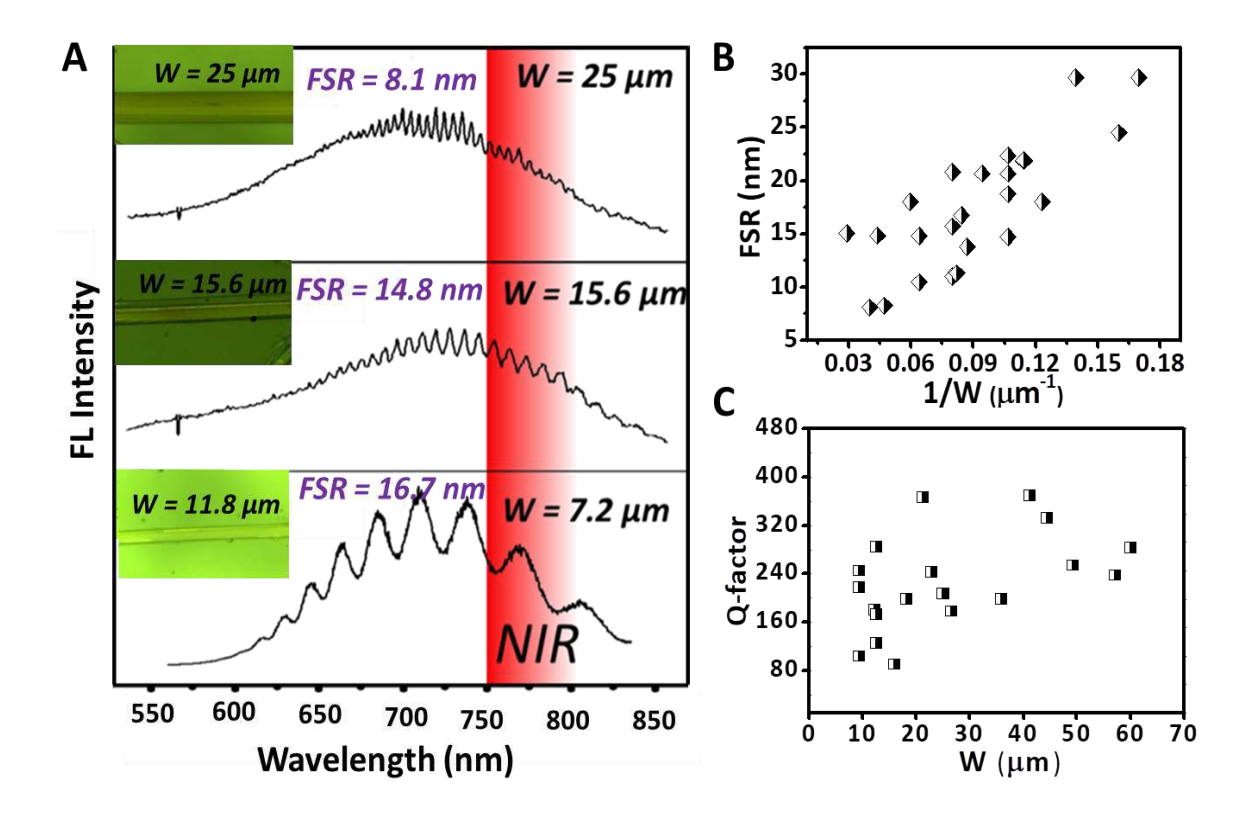


Figure 2.13: A) Single-particle FL spectra of three micro-ribbons of varying widths. B) A plot of FSR versus 1/W. C) A plot of *Q*-factor versus W.

To confirm the resonator type of micro-ribbons, the above experiments were carried out on several micro-ribbons with varying widths. Three different micro-ribbons and their FSR values are presented in **Figure 2.13 A**. When the W of the micro-ribbons decreased from 25, 15.6 to 7.2 µm, FSR values increased to 8.1, 14.8, and 29.7 nm, respectively as per equation 1.7 of Chapter-1 (**Fig. 2.13 A**). Moreover fitting a plot of spacing of optical modes (FSR) against inverse resonator width (1/W) showed nearly a linear relationship (**Fig. 2.13 B**), which further proves the F-P type resonance action of individual micro-ribbon, in which the two opposite lateral facets function as light mirrors by reflecting the FL waves.

The micro-ribbons exhibited a *Q*-factor of up to 400 (**Fig. 2.13 C**). The *Q*-factors in the plot **Fig. 2.13 C** specify the differences in the optical quality of different micro-ribbons. It is also imperative to mention here that sharp resonance lines produced by the micro-ribbons covered both Vis and NIR regions of the EM spectrum.

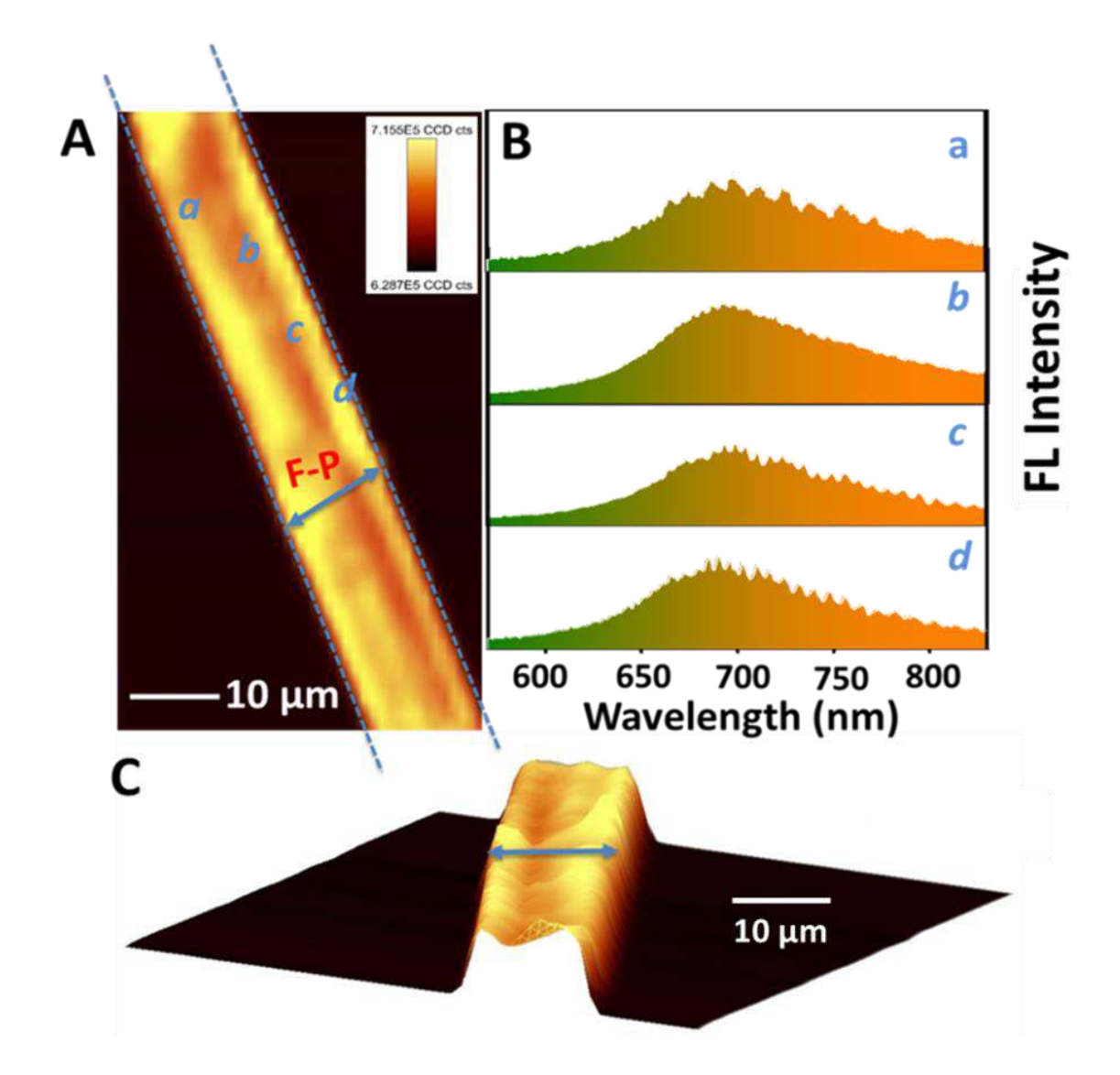


Figure 2.14: A and C) 2D and 3D FL intensity maps of the micro-ribbon. The dotted lines indicate mirror-like surfaces that support F-P resonance. B) The excitation position-dependent F-P modes of the micro-ribbon.

Additionally, FL imaging was performed on a selected micro-ribbon segment to verify the electric field enhancement and its distribution indirectly within the micro-ribbons. The resultant 2D and 3D FL intensity maps of the selected micro-ribbon are presented in Fig. 2.14 A and C. Remarkably, the 3D map unveiled an improved FL signal intensity along the mirror-like walls of micro-ribbon compared with other areas. It indicated that electric field

is highly concentrated along lateral side of the resonator (Fig. 2.14 A). The number of modes and mode spacing in the FL spectrum of a resonator is dependent on excitation positions. The 2D FL image collected in reflection mode configuration demonstrated strong lateral position (a-d) dependent spectral patterns (number of modes) owing to disparity of the density of modes per unit volume at different places of the micro-ribbons (Fig. 2.14 B).

2.3.8. Single-particle microscopic studies of HPPD-BF:

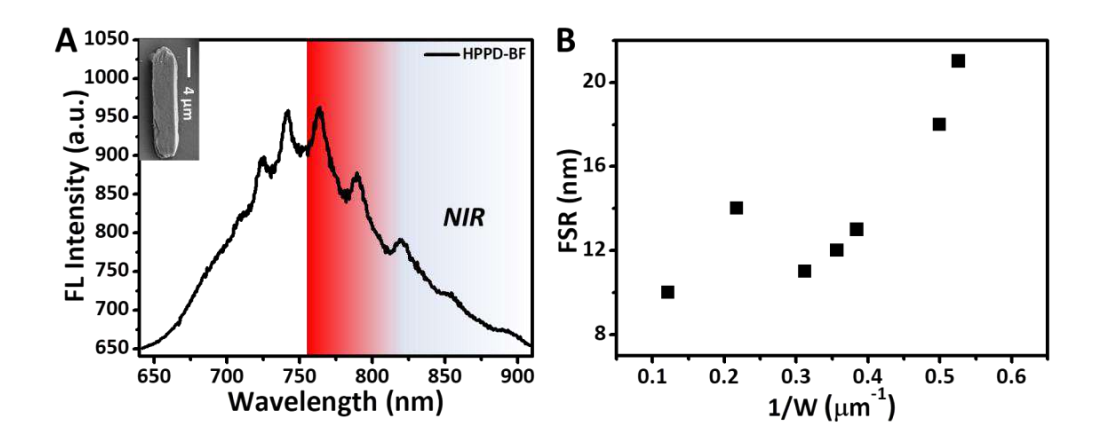


Figure 2.15: A) Single-particle FL spectrum of a selected micro-rod displaying F-P type resonance (Inset: FESEM image of a single crystalline **HPPD-BF** micro-rod). B) FSR versus 1/W plot of **HPPD-BF** micro-rod.

Single-particle micro-FL spectroscopy studies were also performed on **HPPD-BF** micro-rods. Compared to its solid-state emission, the **HPPD-BF** micro-rods displayed a redshift of the FL bandwidth (650–900 nm) covering most of the NIR region of the EM spectrum (**Fig. 2.15 A**). Interestingly, the FL band also comprised of several wavelength-dependent intensity-modulated resonance peaks. The FWHM of the resonance peaks were rather broad compared with those of **HPPD** micro-ribbons, which represents a weak optical confinement (more optical loss) within these rods. A plot of FSR values of selected micro-rods of varying cross-sections showed the increase of the FSR value upon decreasing width, confirming that the micro-rods act as F-P type resonator (**Fig. 2.15 B**). However, the *Q*-factor was very low due to rough surface of the micro-rods facilitating optical loss due to scattering (Q_{scat}) (see **Fig. 2.15 A inset**).

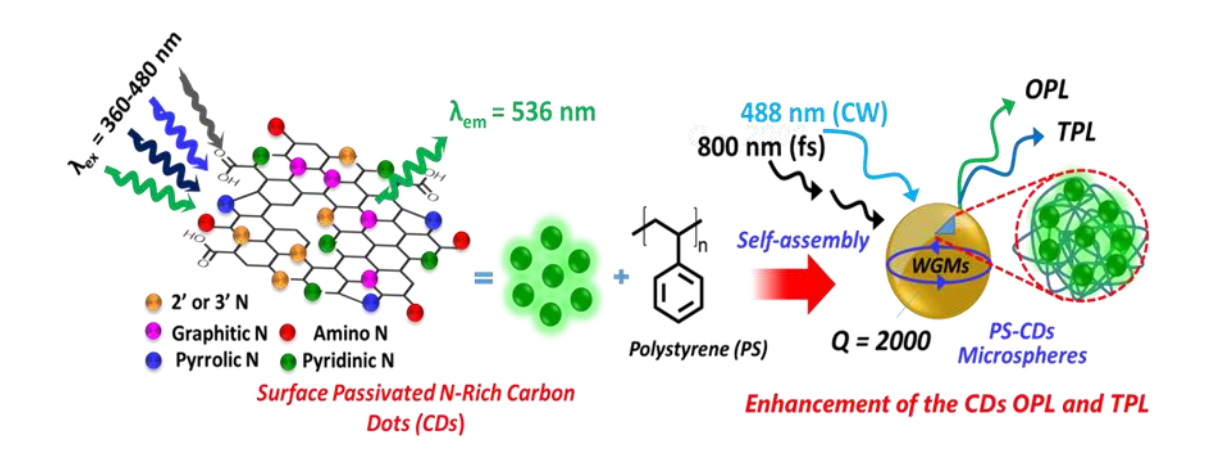
2.4. Summary:

This chapter presented the syntheses of novel push-pull type chalcone ligand, **HPPD**, and its BF₂ complex, **HPPD-BF**. In the crystalline state, **HPPD** molecules aggregate in *J*-type via intermolecular π - π stacking (ca. 3.384 Å) of pyrene units. During self-

assembly, ligand **HPPD** and its boron complex **HPPD-BF** produced visible emitting microribbons and NIR emitting micro-rods, respectively. The solid-state FL of **HPPD** was weaker than that of the **HPPD-BF** complex. Single-particle micro-FL spectroscopy revealed both **HPPD** micro-ribbon and **HPPD-BF** micro-rods act as F-P resonators. The presented **HPPD** micro-ribbon and **HPPD-BF** micro-rods are the first of its kind in organic crystalline photonic resonators.



2D Arrangement of Polymer Micro-Spheres Photonic Cavities Doped with Novel N-Rich CDs Display Enhanced Oneand TPL Driven by Optical Resonances



3.1 Abstract:

Luminescent CDs are evolving as a potential eco-friendly substitute to standard metal-based semiconductor inorganic quantum dots. This chapter presents a novel, N-rich, amine-functionalized, rare excitation wavelength-independent green-emitting ($\lambda_{max} \approx 522$ nm in solution and 536 nm in solid) crystalline CDs obtained from a pyridine diamine precursor in ethanol (EtOH) by solvatothermal method. In contrast to a neat thin film of CDs, a thin film of CDs doped PS micro-spheres (**PS-CDs**) shows a significant enhancement of the PL emission intensity facilitated by their light-trapping capacity or optical resonator effect. The FL lifetime imaging microscopy (FLIM) images of a thin film of **PS-CDs** exhibit an increase of the PL lifetime for bigger micro-spheres (~10.5 μ m; 4.5 ns) compared to the smaller ones (~2.3 μ m; 1.87 ns), thus revealing their size-dependent light trapping tendency. Further, upon excitation with an 800 nm femtosecond (fs) pulse laser both the CDs and **PS-CDs** display enhanced up-conversion TPL compared to neat CD thin film.

3.2 Introduction:

Following the outline which is given in Sec. 1.5 on CDs, it also should be noted that although numerous articles report the synthesis of CDs from a variety of sources, there is no information available on their reproducibility. Hence in our case, the synthesis was performed multiple times under identical preparative conditions. To our surprise, the obtained CDs showed varying absorbance bands, indicating the sensitivity of CD formation to slight environmental fluctuations. Interestingly, the FL band of the CDs showed nearly same emission energy, which is very important as far as usefulness of CDs is concerned. In this context, Kim et al. have reported on the size and shape/edge-state effect on the absorbance and FL spectra of graphene quantum dots (GQDs). [221] They showed that the absorbance spectra varied drastically with respect to particle size/shape, while the FL band did not exhibit any shifts for GQDs of average sizes in the range of 25–35 nm, smaller dots (12–22 nm) exhibited FL shifts due to quantum confinement effect (QCE). Hence in our case, the observed diverse absorbance spectral features/shifts and similar FL energy can be attributed to a slight variation of the CDs sizes/surface states beyond QCE limit.

In contrast to mechanism of FL in inorganic and organic molecules, there is no well-defined mechanism is established to interpret the origin of FL in CDs due to their multi-exponential FL decay lifetimes. [222-224] The FL of CDs is known to be dependent on various factors like size of CDs, surface-states, defects and edge shapes. [174-178] Till now, two mechanisms have been suggested, such as 1) intrinsic-state FL by electron-hole recombination and size effect and 2) defect-state FL by surface energy traps. The majority

of CDs exhibit excitation wavelength-dependent FL and excitation-independent FL is very rarely achieved. Moreover CDs show low Φ_{FL} , which is a barrier for practical application purposes. To address these two major issues simultaneously, starting materials containing amine and sulfur groups are used to make N, S-doped CDs, showing effective surface passivation, which leads to high Φ_{FL} and excitation independent emission of CDs. The FL intensity of CDs can be enhanced by surface passivation, cooperativity of N, S-CDs^[185] and enhancing the excited life time^[225] methods. Apart from the abovementioned methods, an alternative and yet unexplored method to achieve enhanced FL (either up or down conversion) and even lasing from an ultra-low concentration of CD are by confining the FL via photonic cavity effect. To our knowledge, there have been few reports are available on the upconversion FL (TPL) of CDs.^[181,182]

Therefore, this chapter presents the fabrication of a novel N-rich, crystalline CDs with amine as surface passivation groups from PDA by solvatothermal method. The X-ray photoelectron spectroscopy (XPS) analysis of as-prepared CDs unveils the N-doping (pyridinic structure) and the presence of surface amine groups. The CDs show remarkable excitation-wavelength independent FL. It was found that CD-doped PS self-assemble into photonic grade thin film consists of **PS-CDs** micro-spheres. Surprisingly, the PS-CD photonic quality thin-film displays enhancement of the FL intensity (both FL and TPL) of CDs in comparison with a simple **PS-CD** thin film. This enhancement is due to the efficient light trapping tendency of micro-spheres via WGM resonance. Additionally, FLIM investigations exemplify the unique relationship between **PS-CD** particle size and photon lifetime values.

3.3. Results and Discussion:

3.3.1. Synthesis of CDs:

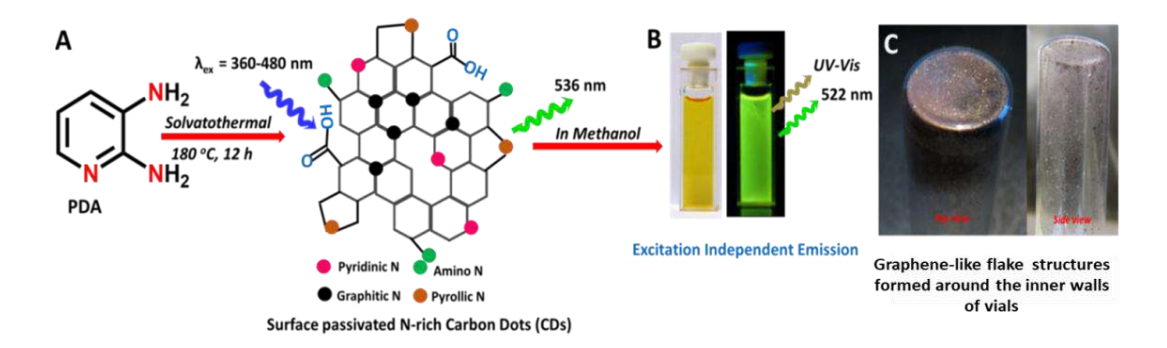


Figure 3.1: A) Preparation of green-emitting N-doped amine-functionalized CDs from PDA via solvatothermal reaction. B) Solution-state optical properties of N-rich CDs. C) Pictures of graphene-like flake structures formed in the vials.

PDA was chosen as a starting material for the synthesis of new and surface passivated crystalline CDs. The precursor was dissolved in C₂H₅OH and treated successively by solvatothermal method at 180 °C for 12 h (Fig. 3.1). Eventually, the solution converted to black color and displayed a strong green emission when exposed to UV light (365 nm). Because of hydrothermal treatment, different fragments of CDs were formed. Along with green-emitting CDs, cyan emitting CDs were formed due to less conjugation. The acquired crude product was purified by column chromatography on silica (Eluents: CH₂Cl₂:CH₃OH; 5:1 ratio) to remove remnants of cyan-emitting CDs from the green-emitting ones. Notably, after the slow evaporation of solvents, graphene-like sheets/flakes were formed around the inner walls of the vials (Fig. 3.1 C). Moreover, the graphene-like sheets and the morphology of these CDs were confirmed by TEM and the details will be provided in section 3.3.3. The obtained CDs are soluble in H₂O, CH₃OH, C₂H₅OH and THF and showed a long-standing homogeneous phase devoid of any substantial aggregation/precipitation at ambient temperature (Fig. 3.1 B).

3.3.2. Optical properties of CDs:

The photophysical properties of a methanolic solution of CDs were probed by UV-

Vis absorption and FL The spectroscopy. absorbance spectrum of CDs in solution state exhibited a sharp peak at 333 nm (associated with n- π^* transition of C=O bond) accompanied by weak broadband in the range of 400-510 nm owing to the π conjugated structure CDs (Fig. 3.2 left). The FL spectrum of CDs exhibited a green emission with a

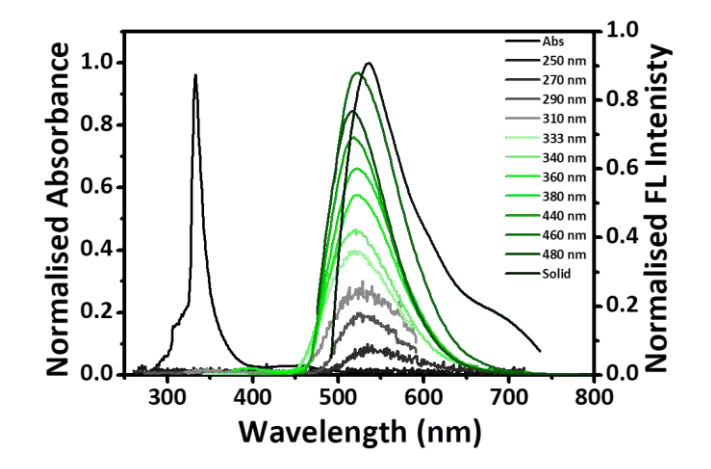


Figure 3.2: Solution-state UV-Vis and FL spectra of N-rich CDs at different excitation wavelength. The solid black line illustrates the solid-state FL spectrum.

peak maximum centered at 522 nm (**Fig. 3.2 right**). Remarkably, the excitation wavelength (360-480 nm) dependent FL spectral studies of N-rich CDs disclosed no significant shift of the emission maxima (**Fig. 3.2**), specifying the non-existence of any trapped surface-states and surface in-homogeneity. In the thin-film state ($\lambda_{ex} = 488$ nm), CDs exhibited a slightly circa 14 nm bathochromic-shifted FL maximum with a shoulder around ca. 600 nm and ca.

700 nm (Fig. 3.2 solid black line), which is probably due to aggregated states in the solid-state.

3.3.3. Structural analysis of CDs:

To study the structure of CDs, Raman spectroscopy was carried out and results

were compared with graphite powder (Fig. 3.3). The powder sample of CDs displayed two equally intense Raman peaks at 1342 cm⁻¹ (D band) and 1585 cm⁻¹ (G band; in-phase vibration of the graphite lattice) equivalent to E_{2q} and A_{1q} stretching modes, respectively, which are almost comparable with graphite D and bands. suggesting the graphene-like structure of CDs. **FTIR** discrete spectroscopy showed the existence of NH₂ (3363 and 3385 cm⁻¹; N-H stretch and 747

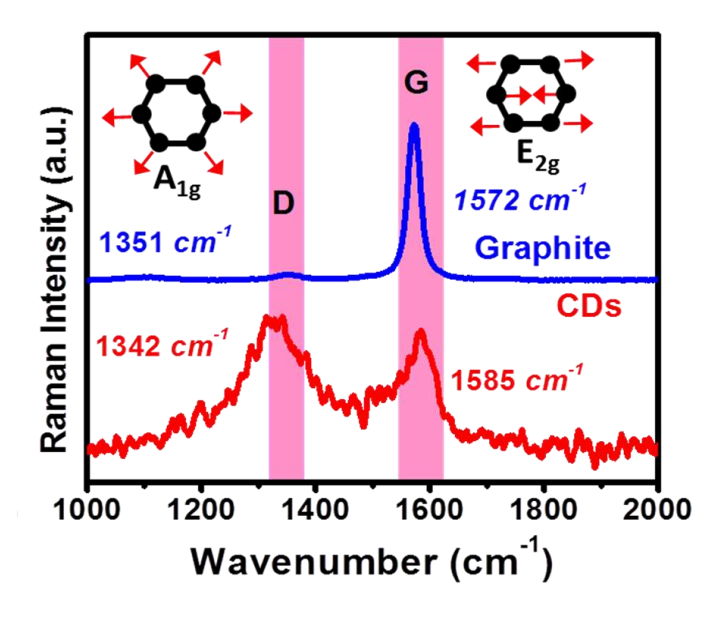


Figure 3.3: Raman spectra of CDs in comparsion with graphite. The insets display the streching modes.

cm⁻¹; NH2 wagging) and carbonyl (1721 cm⁻¹) functional groups in the CDs (Fig. 3.4).

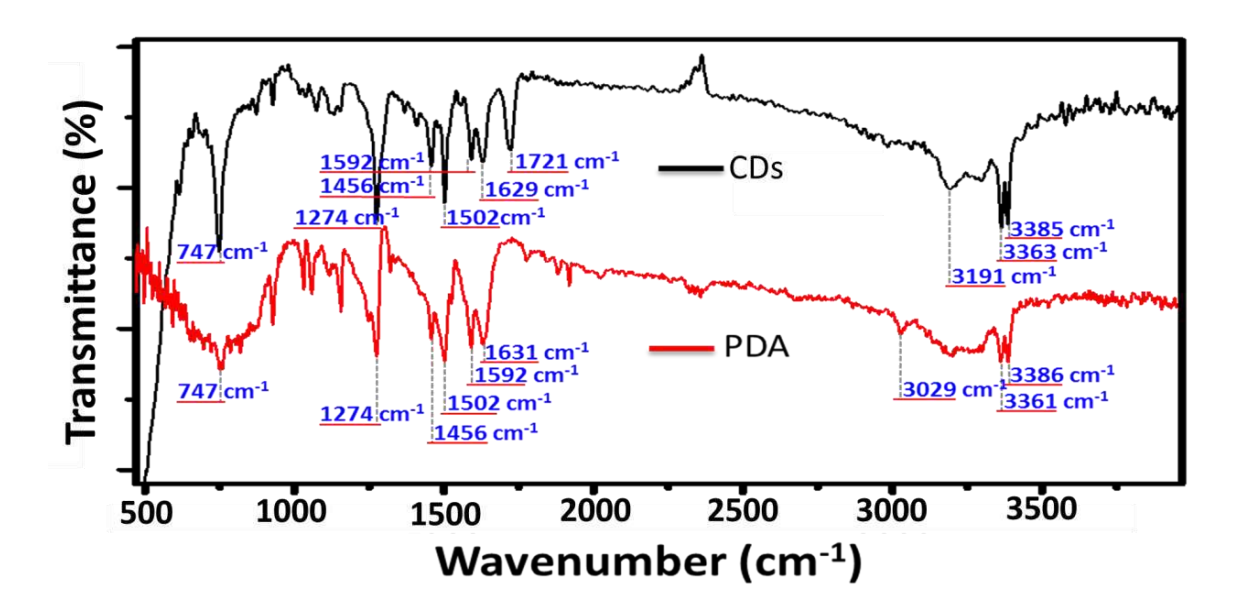


Figure 3.4: FTIR spectra of PDA and CDs.

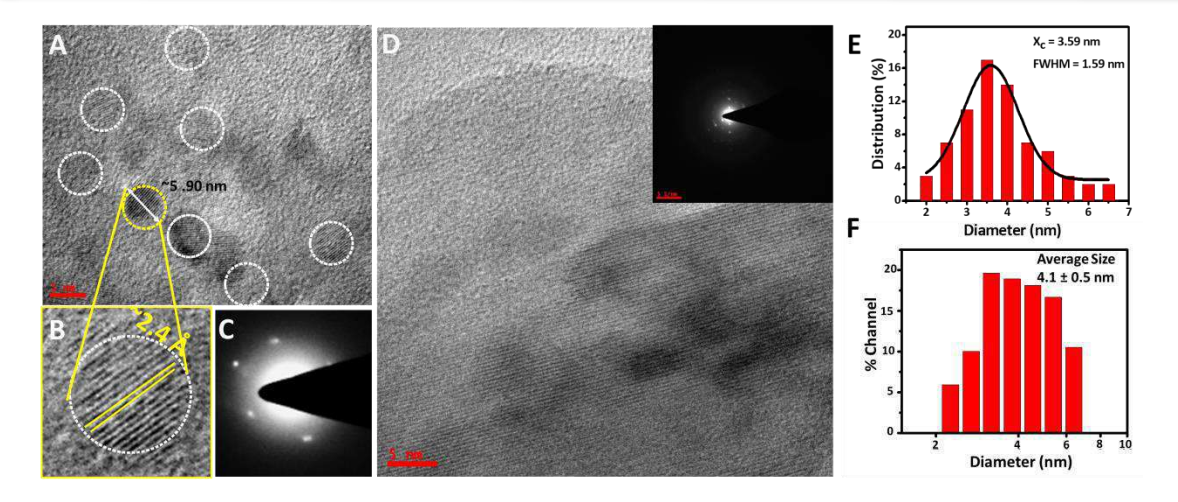


Figure 3.5: TEM image of A) CDs shown within the white dotted circles. B) Close-up view of a single CD. C) SAED pattern of a single CD. D) HR-TEM images of graphene-like sheets. The inset shows their SAED pattern. CDs size distribution from E) TEM and F) DLS histogram.

TEM analysis of the sample proved the existence of CDs and graphene-like sheets in the sample (Fig. 3.5 A and D). From the TEM data, it was evaluated that the diameter of the CDs varied from 2-6.5 nm, with a broader distribution of CDs with size of \approx 3.6 nm (Fig. 3.5 E). With the help of dynamic light scattering (DLS) technique, the hydrodynamic radius of the CDs was found to be 4.1 \pm 0.5 nm (Fig. 3.5 F). HR-TEM images of single CD

displayed lattice spacing of ~0.24 nm equivalent graphene-like to arrangements (Fig. 3.5 B). Furthermore, in agreement with the TEM and Raman spectroscopy analyses, the SAED pattern of a single CD showed clear bright diffraction patterns with a six-fold symmetry supporting the graphene-like structure of CDs (Fig. 3.5 C). The powder x-ray diffraction (PXRD) pattern of CDs displayed two broad peaks correspond to (002) and (100) hkl planes (Fig. 3.6).

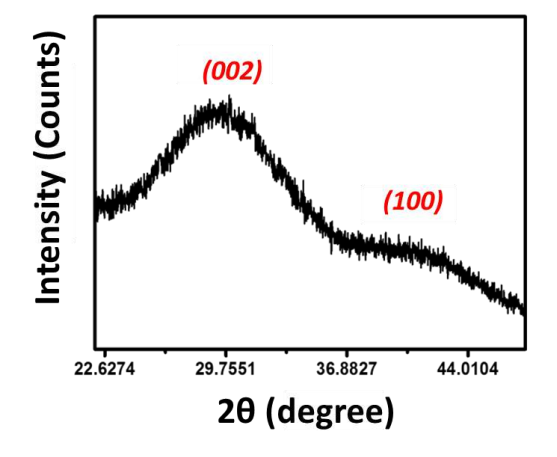


Figure 3.6: Powder XRD pattern of CDs.

Similarly, analysis of the TEM images of the graphene-like sheets (acquired after solvent evaporation) exhibited existence of single-, bi- and multi-layers of graphene sheets (Fig. 3.5 D). SAED data of these sheets showed bright diffraction with an overlap of many spots with six-fold symmetries specifying the layered-structure of graphene-like sheets (Inset of Fig. 3.5 D).

Furthermore, to identify the elemental composition, surface functional groups, chemical bonds and binding energies XPS investigation was performed for CDs. The XPS survey spectra indicated the presence of carbon, nitrogen, and oxygen in the CDs (Fig. 3.7 A). The high-resolution spectrum of C1s displayed four characteristic peaks (Fig. 3.7 B). The peak position at 284.0 eV and 284.8 eV supported the graphitic structure (C=C) and (sp² C-C) of CDs.[226] The peak at 285.7 eV directed the presence of C-N bond. The other two peaks at 286.6 eV and 287.4 eV were assigned to C-O and C=O functional groups, respectively. The ¹³C-NMR spectra also confirmed the presence of (C=O) group in CDs by revealing a peak at 172 ppm (Fig. 3.8). The N1s spectrum displayed the presence of both pyridinic N (398.9 eV), amino N (400.1 eV) pyrollic N (400.9 eV) and graphitic N (402.1 eV) in the CDs (Fig. 3.7 C) which is in agreement with previous reports.[226,227]

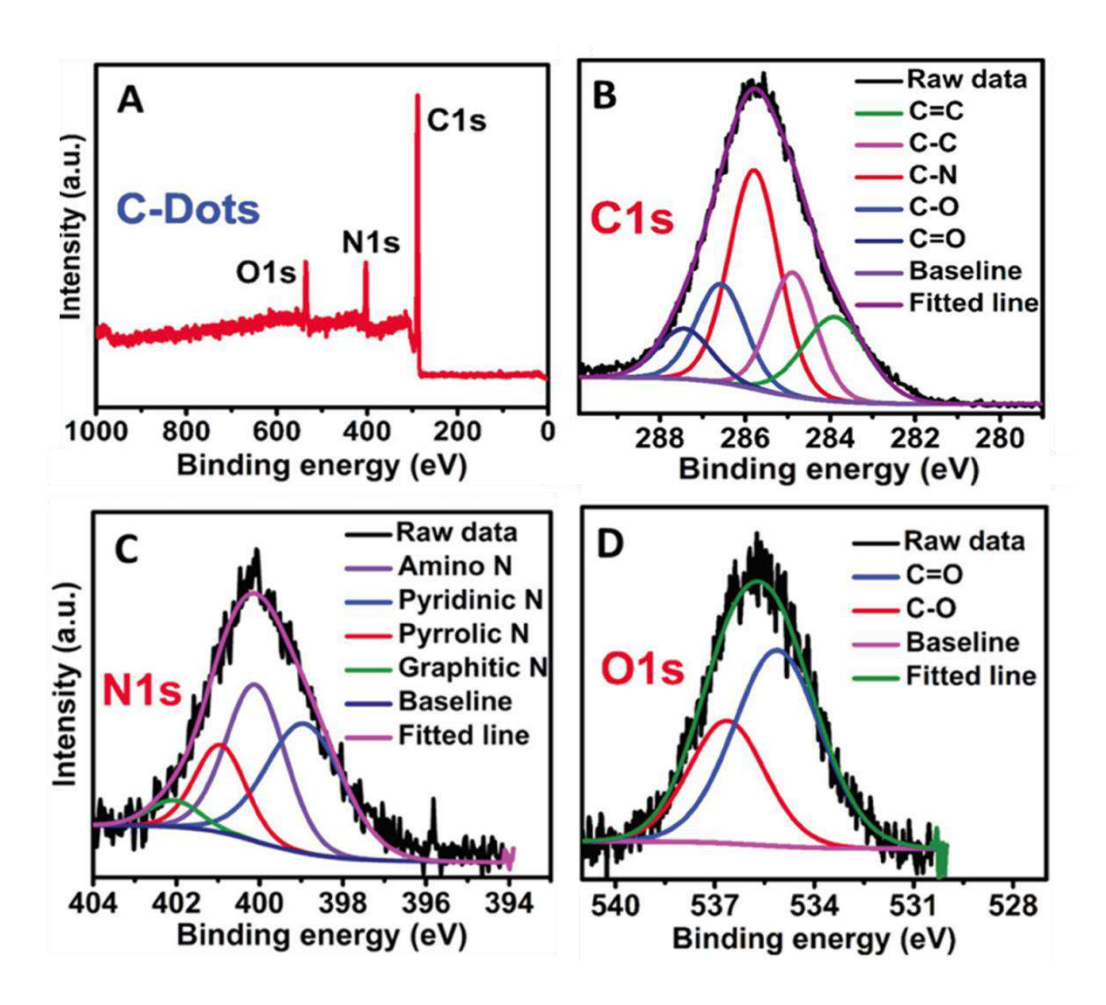


Figure 3.7: A) XPS survey spectrum of N-rich CDs. The high-resolution (XPS) binding energy survey spectra of B) C1s, C) N1s and D) O1s.

The O1s spectrum (Fig. 3.7 D) of CDs could be disintegrated into two peaks such as OH/C-O (532.83 eV) and COO (534.35 eV). The molecular precursor consists of only carbon and nitrogen elements, however, after solvatothermal treatment, it produced CDs,

which contain C, N and O. This result clearly proved that the starting material is oxidized and generated N-doped CDs having N and O containing functional groups on the surface.

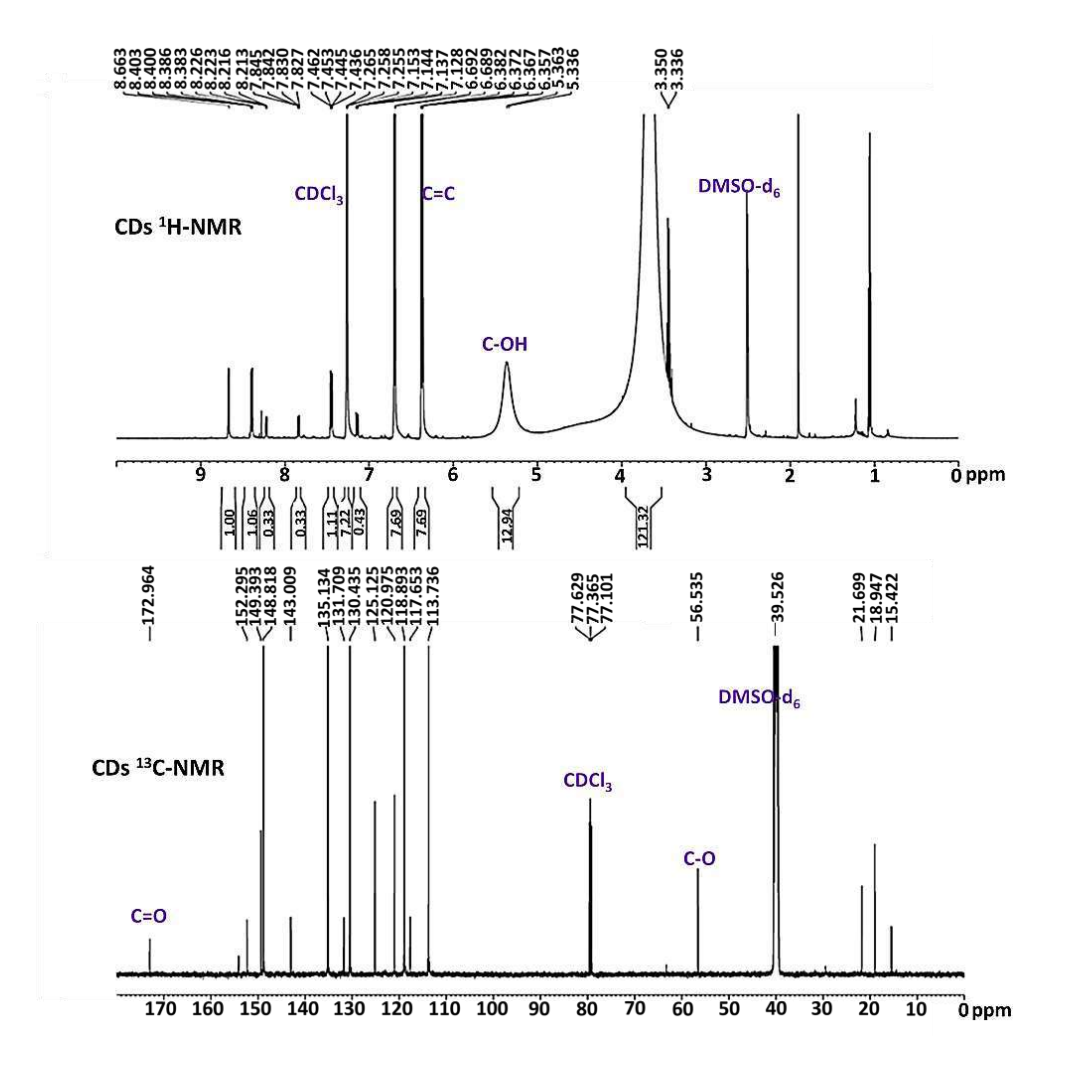
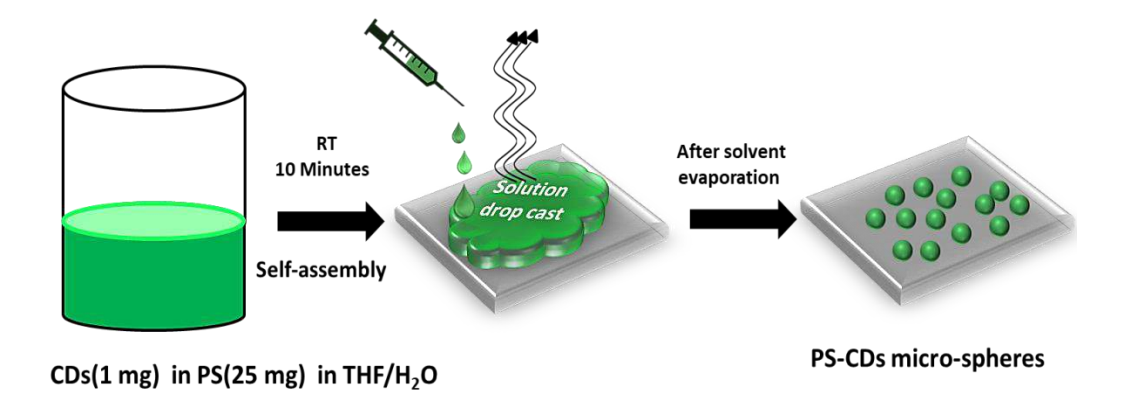


Figure 3.8: ¹H (400 MHz) and ¹³C-NMR (100 MHz) spectra of CDs recorded in CDCI₃ (with 2 drops of DMSO).

3.3.4. Preparation of PS-CDs micro-spheres:

Most of the CDs show FL with low Φ_{FL} as the nonsurface passivated CDs is not a single species and it contains various kinds of nano graphenes. Due to internal quenching, recombination, deactivation of excited molecules, reversing of primary photochemical reaction and insufficient excitation energy, they exhibit low Φ_{FL} . To enhance the solid-state emission of CDs for lighting/imaging applications polymer/CDs composite resonator was prepared. For the preparation CDs (1 mg) were doped with PS (25 mg) in THF (4 mL) and subsequently, H_2O (1 mL) was added to this mixture. Finally, the solution was kept undisturbed for 10 min to grow photonic-grade PS micro-spheres doped with N-rich CDs. Afterwards, two drops of the solution were drop-casted on a clean cover-slip to form a thin

film of numerous **PS-CDs** micro-spheres after the evaporation of solvent at rt. (**Scheme 3.1**).



Scheme 3.1: Self-assembly of CDs doped PS into micro-spheres.

3.3.5. Microscopic studies of PS-CDs micro-spheres:

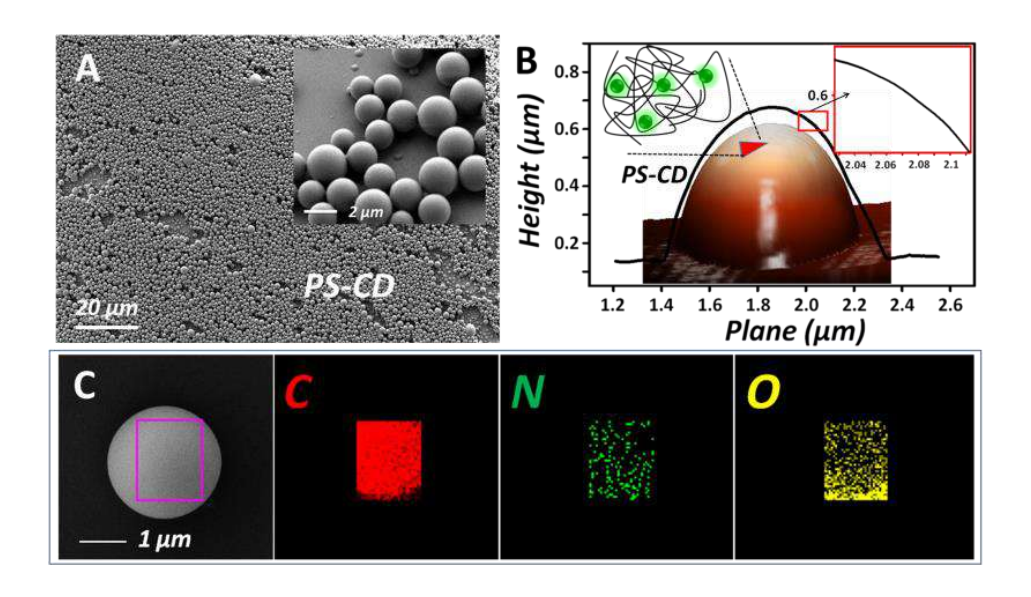


Figure 3.9: A) FESEM images of a film of **PS-CDs** micro-spheres. The inset shows the close-up view of the micro-spheres. B) 3D AFM topography image of micro-spheres. The right and left insets show the smoothness profile and cartoon representing **PS-CDs** composite. C) EDAX elemental map of **PS-CD** micro-sphere.

Investigation of the PS/CDs composite sample prepared by self-assembly under confocal microscopy demonstrated the presence of circular particles with an average diameter in the range of $\approx 2\text{-}12~\mu\text{m}$. FESEM images established the spherical shape of the **PS-CDs** micro-particles and their extensive coverage area (**Fig. 3.9 A**). The AFM analysis of a selected **PS-CDs** micro-sphere confirmed its surface smoothness, which is essential for the achievement of optical cavity effect and high optical gain (**Fig. 3.9 B**, **right inset**).

The EDAX elemental mapping evidently displayed the presence of CDs within the PS spheres by unveiling N and O signals (Fig. 3.9 C).

3.3.6. Single-Particle microscopic studies of PS-CDs micro-spheres:

To verify the resonator characteristics of **PS-CDs** micro-spheres, the single-particle micro-FL experiment was carried out on LCM set-up. CW laser excitation (488 nm Ar⁺) of a single **PS-CDs** micro-sphere exhibited enhanced FL emission band covering 480 nm to 700 nm range of the EM spectrum. The spectrum corresponding to FL emission contains a series of wavelength-dependent periodic intensity-modulated sharp peaks, clearly demonstrating the WGM resonance emanating from a single **PS-CDs** micro-sphere due to tight confinement of FL photons and successive FL wave interference (**Fig. 3.10** A). [44,51,69,71,74,95,201,203,207] In each single particle FL spectrum, multiple pairs of peaks were detected all over the spectral region. These pairs of peaks were known to be TM and TE modes, generally identified for WGM cavities. [228] According to the equation 1.7 given in

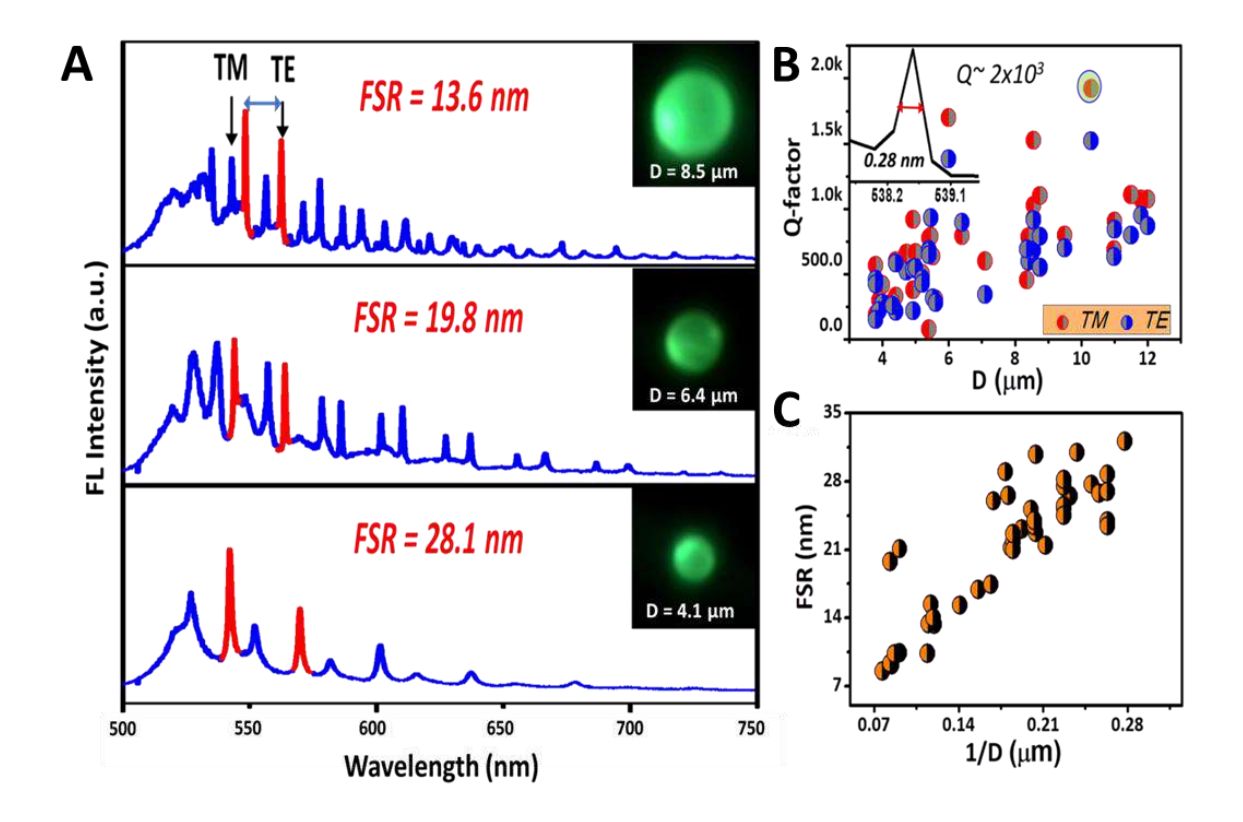


Figure 3.10: A) Size-dependent WGM spectra of **PS-CDs** micro-spheres displaying different FSR values as per FSR~1/D relationship. B) A plot of *Q*-factor versus micro-sphere D. C) A plot of FSR versus 1/D.

Chapter-1, particles with diameters of 8.5 μm, 6.4 μm, and 4.0 μm showed an apparent increase of the FSR values of 13.6 nm, 19.8 nm and 28.1 nm, respectively (Fig. 3.10 A

and C). The *Q*-factor increased with an increase in the size of micro-spheres up to the value of 2000, due to better light confinement within larger micro-spheres (Fig. 3.10 B).^[162,229] This result specified that the *Q*-factor and FSR values exclusively depend upon the size of the micro-spheres. To compare the magnitude of FL enhancement from the thin film of **PS-CDs** micro-spheres with the spin-coated **PS-CDs** thin film (of same CDs concentration), FL spectra were collected for a selected area under the same experimental conditions, such as laser power, 150× objective and integration time (Fig. 3.11).

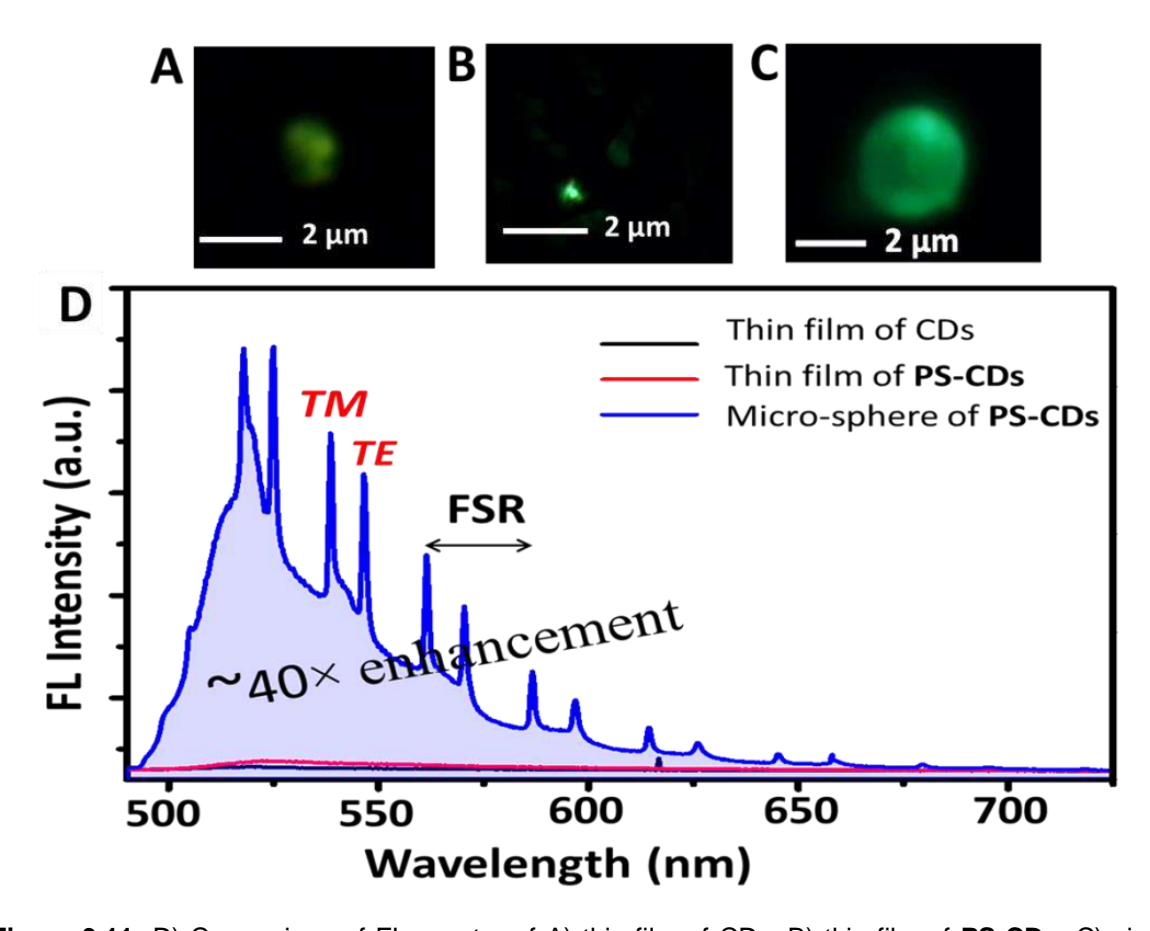


Figure 3.11: D) Comparison of FL spectra of A) thin film of CDs, B) thin film of **PS-CDs**, C) single micro-sphere of **PS-CDs**.

For a reasonable estimation of the FL enhancement, thin films of CDs PS-CDs with same height were compared with a single micro-sphere displaying WGMs. Interestingly, the integrated FL intensity of photonic grade thin film of PS-CDs micro-sphere was about 40-fold higher than the CDs, PS-CDs film under the same experimental condition. It should be noted that the FL enhancement order of the thin film of PS-CDs micro-sphere different from one area to another (though always higher than the spin-coated PS-CDs thin film), because of the disparity of the average size/surface coverage of the micro-spheres in a given area.

3.3.7. FL lifetime studies of PS-CDs micro-spheres:

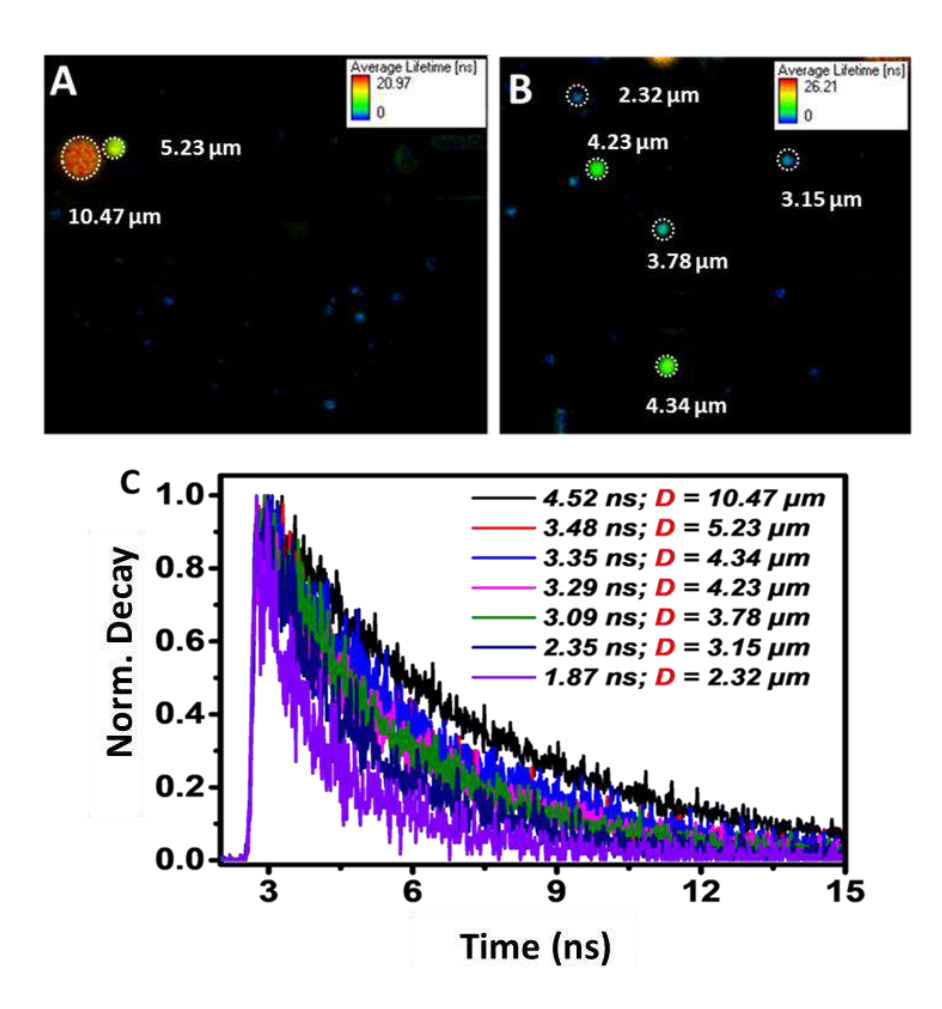


Figure 3.12: A) and B) FLIM images of **PS-CDs** micro-spheres. C) Size-dependent photon lifetime values of **PS-CDs** micro-spheres.

FL lifetime decays and FLIM images of **PS-CDs** micro-sphere were recorded using TCSPC on a Micro-Time 200 confocal FLIM setup (Pico Quant). A selected area of the sample surface was excited with a 405 nm ps pulse diode laser and the resultant FLIM images are shown in **Fig. 3.12 A and B**. Surprisingly, the larger micro-spheres showed longer lifetime (red color-coded), however, the lifetime of smallest micro-spheres dropped (blue color-coded) considerably. The variation of lifetime decay profile for several micro-spheres of different sizes is plotted in **Fig. 3.12 C**. For example, the biggest (10.47 μm), medium (4.23 μm) and smallest (2.32 μm) particles exhibited lifetime values of 4.52 ns, 3.29 ns, and 1.87 ns, respectively. To verify the influence of photonic properties of microspheres on the particle size-dependent lifetime, for comparison, FLIM experiment was carried out on a neat **PS-CDs** homogeneous thin film (i.e. without micro-spheres) and the result showed a very short lifetime value of 1.31 ns. Here, the observed particle size-dependent lifetime can be explained using quantum electrodynamics theory, which states

that the spontaneous emission rate of an emitter can be modified when the emission frequency couples to the resonator frequency as per Fermi's golden rule. The suppression or enhancement of radiative optical modes also depends upon the mode density $M(\vartheta)$ (the number of modes per unit volume of the resonator per unit bandwidth surrounding the frequency (ϑ) and optical field fluctuations inside the cavities. The $M(\vartheta)$ of biggest particles is higher compared to smaller ones thereby possess superior light-trapping tendency and subsequently exhibiting longer FL lifetime (Fig. 3.12).

3.3.8. NLO studies of PS-CDs micro-spheres:

To examine the NLO property of **PS-CDs** samples, a Ti: Sapphire 800 nm fs pulse laser (pulse width 100 fs, repetition rate 1 kHz) was used. The experiment was done by placing the sample at focal volume having the spot size of 101.8 µm and is exposed by linearly polarized light with various input powers. To investigate pump power-dependence of TPL signal, the intensity at the focus is increased from 12.3 to 39.2 mJ/cm² by changing the wave plate and the equivalent TPL spectra are shown in **Fig. 3.13 C**. The spectra showed that the TPL band intensity of **PS-CDs** micro-spheres surged very sharply after certain pump fluence (**Fig. 3.13 C**).

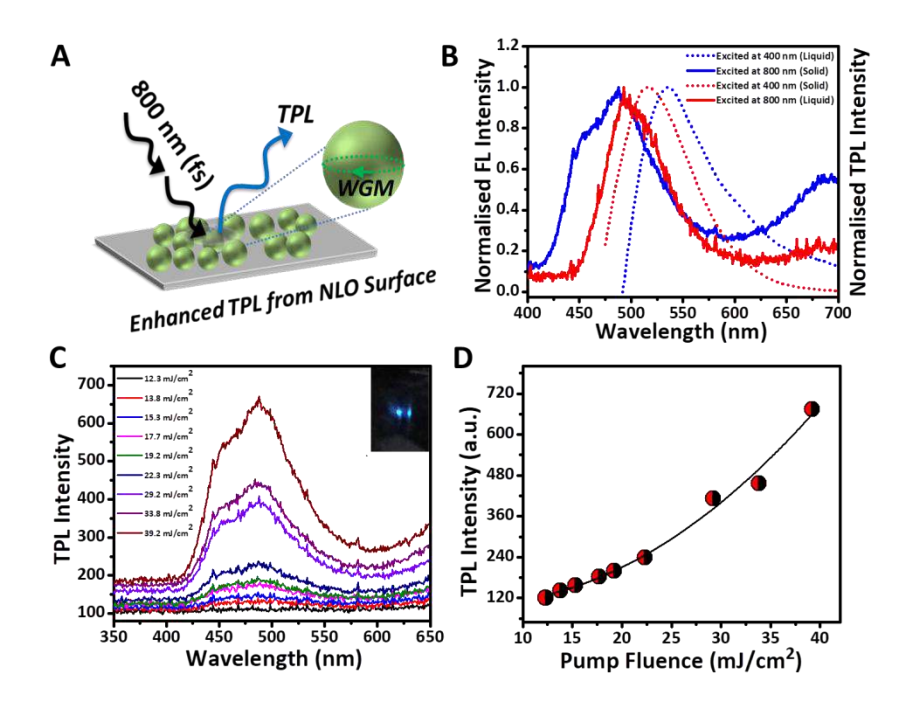


Figure 3.13: A) Graphical representation of the emergence of enhanced TPL from organic NLO surface containing **PS-CDs** WGM micro-resonators. B) One-photon (400 nm) and two-photon (800 nm) emission spectra of CDs (in liquid state; dotted lines) and **PS-CDs** micro-spheres (solid lines). C) TPL spectra of **PS-CDs** micro-spheres at different pump-fluence. The inset picture shows the emergence of TPL from the sample. D) A plot of laser pump-fluence versus TPL intensity.

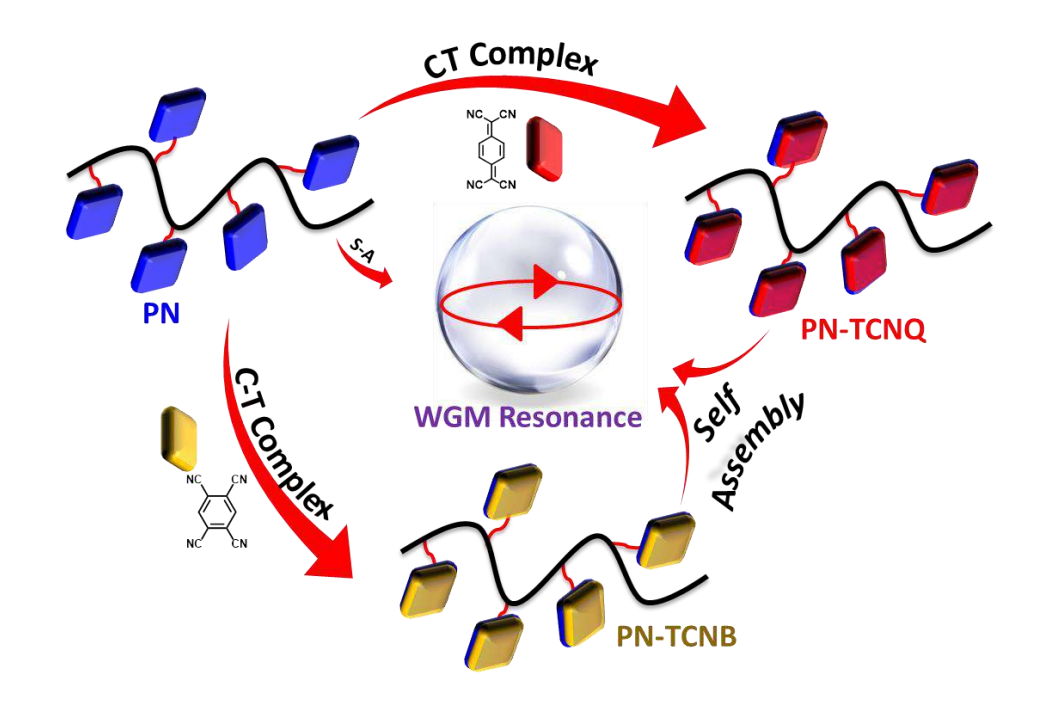
Interestingly, beyond $\approx 25 \text{ mJ/cm}^2$ laser fluence, the TPL band clearly exhibited an increase of the $\approx 489 \text{ nm}$ signal and presence of a shoulder at $\approx 459 \text{ nm}$. A plot of $\approx 489 \text{ nm}$ TPL band intensity with pump fluence demonstrated a second-order increase of the signal intensity of the random particles, thus confirming the TPA process. (Fig. 3.13 D). In contrast to FL, the TPL of CDs in CH₃OH exhibited about 21nm hypsochromic shifted band with a maximum intensity at $\approx 496 \text{ nm}$, demonstrating their different excited-state emission processes (Fig. 3.13 B). Similar to FL, the average TPL intensity of PS-CDs micro-spheres was much higher than the weak signal exhibited by the PS-CDs thin film ($\approx 4 \text{ }\mu\text{m}$ thickness) under the same experimental conditions due to the cavity confinement effect of the WGM micro-spheres.

3.4. Summary:

This chapter presented the first successful preparation of N-rich CDs with efficient surface passivation by using solvatothermal technique. The obtained CDs exhibited a rare excitation wavelength-independent green FL. Moreover, for the first time, simple, high performance and an inexpensive method were developed to enhance the emission intensity of CD film by trapping the FL and TPL within the PS micro-spherical cavities. The resultant photonic grade **PS-CDs** micro-sphere film displayed about 40 times enhancement in FL contrast to their corresponding pure **PS-CDs**. Moreover, CDs films due to better light confinement or energy storage capacity of **PS-CDs** micro-spheres having Q value up to $\approx 2 \times 10^3$. Further, FLIM experiments on the surface covered with **PS-CDs** composite microsphere unravelled resonator size-dependent FL lifetime, as a result of QED effect. Our technique is very useful to get photonic-grade polymer-CDs composite with brilliant green FL appropriate for one and two-photon bio-imaging, deep tissue sensing, light-emitting and lasing devices.



Micro-Resonators from CT in Polymer Particles - toward Enhanced and Tunable Two-Photon Emission



*This chapter is adapted from:

V. Radhika, D. Venkatakrishnarao, C. Sahoo,

S. R. G. Naraharisetty, D. Narayana Rao,

K. Müllen and R. Chandrasekar*

ACS Appl. Mater. Interfaces. **2018**, 10, 16723-16730.

4.1. Abstract:

This chapter presents bandgap tunability and enhancement of one- and two-photon pumped optical emission intensities (blue, orange and red) of polymer micro-resonators. These resonators are formed through self-assembly of novel blue-emitting cross-linked copolymer poly(styrene-co-4-(1-pyrene)styrene-co-divinylbenzene) (PN) and orange and red-emitting CT polymer complexes such as PN-TCNB, and PN-TCNQ with the acceptor molecules like 1,2,4,5-tetracyanobenzene (TCNB) and 7,7,8,8-tetracyanoquinodimethane (TCNQ), respectively. FLIM studies show the decrease of PN decay lifetime from 1.7 ps to 1.24 ps and 1.48 ps, for PN-TCNQ and PN-TCNB, respectively. Single-particle excitation of all the polymer particles with CW lasers reveals WGM resonator action through tight optical confinement with a Q-value of up to 1000. Moreover, the trapped light enhances the lightmatter interaction and thus increases the FL intensity, including the TPL. In solution-state PN, PN-TCNB and PN-TCNQ display TPA and exhibit β values of 4.4×10^{-10} , 3.18×10^{-10} , and 3.28×10^{-10} cm/W, respectively. This distinctive combination of properties is beneficial for many upconversion based NLO applications.

4.2. Introduction:

Optical band gap tunability is imperative for applications such as micro-lasers, [34,44,230-233] on-chip optical communications, [234] micro-resonators, [69,206,207] lighting, [235] electronics [236] and sensors. [237] So far, tuning the bandgap is achieved by concepts such as π -conjugation length, [238,239] crystal polymorphism, [240] crystalline-amorphous phase changes, [241] particle size effects, [242] host-guest interactions, [243] CT complex formation. [230,244] However, broadband tunability from Vis to NIR remains challenging. [245-247] Moreover, most of the potential applications of organic materials are limited to OPL and a little work has been performed on their NLO properties. A majority of the organic and polymeric NLO molecules exhibit weaker TPL than the OPL. Thus, polymers can be self-assembled into micro-spherical particles, which can enhance the optical emission since they can act as high Q WGM resonators by confining high electric field intensity.

Surprisingly, there have been no reports presented, which address both issues: (i) tuning the band gap in the linear and NLO systems and (ii) amplification of the optical emissions by means of self-assembled micro-resonators. Hence, novel micro-resonators were prepared from macromolecules with supra-molecular CT type pendant groups displaying both tunable and enhanced OPL and TPL. For this, pyrene was selected as a D unit as it forms D-A complexes with many A molecules like TCNQ and TCNB. They exhibit CT emissions at different wavelengths depending upon the strength of interaction within the

D-A pair.^[248] To attach pyrene as a pendant group to the macromolecular chain, polymerization of PS and 1-(4-vinylphenyl) pyrene with DVB as a cross-linker is anticipated to be an ideal choice. Because it provides cross-linked micro-spherical particles with a smooth surface in the case of poly(styrene-co-divinylbenzene).^[249] This approach provided easy synthetic accessibility, widely tunable optical emissions, optical nonlinearity and excellent solution processability for bottom-up and top-down technologies. ^[230,250-252] This chapter presents a novel *blue*-emitting cross-linked polymer network namely, **PN** in which the pyrene act as a D is directly linked to PS (**Scheme 4.1**). **PN** forms *orange*- and *red*-emitting CT complexes, **PN-TCNB** and **PN-TCNQ** with acceptor molecules like TCNB and TCNQ, respectively and in DMF/H₂O mixtures they convert into well-defined micro-spherical particles exhibiting WGM resonance. Owing to increased light-matter interaction time, these WGM micro-resonators exhibit one- and two-photon pumped optical emissions with increased intensity than their corresponding thin films.

4.3. Results and Discussion:

4.3.1. Synthesis of 1-(4-vinylphenyl)-pyrene (1) monomer, copolymer (PN) and preparation of PN-TCNB and PN-TCNB CT complexes:

Synthesis of 1: This compound was prepared by Suzuki coupling reaction according to the reported procedure.^[253]

First, a THF solution (40 mL) was added to a degassed aqueous solution of 2M K_2CO_3 (1.47 g, 10.5 mmol). 1-bromopyrene (1 g, 3.5 mmol) and 4-vinylphenylboronicacid (0.52 g, 3.5 mmol) were dissolved in the prepared solution and N_2 bubbling was carried out for 15 min. To the above solution, $Pd(PPh_3)_4$ (0.200g, 0.17 mmol) was added and the reaction mixture was heated to reflux for 24 hrs at 100 °C. After completion of the reaction, the reaction mixture was cooled to rt and the solvent was evaporated under reduced pressure. The residue was extracted with CH_2Cl_2/H_2O (1:2 v/v) for 2 times. The organic layer was dried over Na_2SO_4 . The crude solid was then purified by column chromatography on silica gel using n-hexane/EtOAc (95:5 v/v). Then target product was obtained as yellow powder with (0.920 g) 86% yield. R_f value ~0.40.

¹H-NMR (400 MHz, CDCl₃, 298 K) δ/ppm: 7.99-8.21 (m, CH₂CHC₆H₄C₁₆H₉, 9H), 7.6 (d, CH₂CHC₆H₄C₁₆H₉, 4H), 6.9 (dd, CH₂CHC₆H₄C₁₆H₉, 1H), 5.3(d, CH₂CHC₆H₄C₁₆H₉, 1H) and 5.9 (d, CH₂CHC₆H₄C₁₆H₉, 1H).

¹³C-NMR (100 MHz, CDCl₃, 298 K) δ/ppm: 140, 137, 136, 131.5, 131.2, 131, 130, 128, 127.56, 127.51, 127.48, 127.45, 126.3, 126, 125.9, 125.2, 125.1, 125.05, 125.01, 124.97, 124.91, 124.73, 114.22.

ESI-TOF MS (*m/z*): Calculated: 304.13, Found: 304.12.

FTIR (KBr; $\bar{\vartheta}$ cm⁻¹): 3036 (C-H stretching vibration of substituted benzene ring), 2921 (C-H stretching vibration of vinyl group), 1599 (C=C stretching vibration of aromatic ring), 905 (C-H bending vibration of vinyl group) and 836 (C-H bending vibration of para di-substituted benzene).

Scheme 4.1: Synthesis of cross-linked polymer (PN) and its CT complexes, PN-TCNQ and PN-TCNB.

Synthesis of PN:

A mixture of azobisisobutyronitrile (AIBN) (30 mg, 0.16 mmol) and (1) (500 mg, 1.64 mmol) was placed in a 250 mL two-neck round-bottomed flask equipped with magnetic pellet and was purged with N₂ for 10 min. Then, THF (45 mL), styrene (2) (0.2 mL, 1.64 mmol), DVB (3) (0.18 mL, 1.28 mmol) were added to the reaction mixture and stirred at 60 °C for 24 hrs (Scheme 4.1). After cooling to rt, the generated sticky green semi-solid (gel + sol) was poured into a beaker having a large excess of CH₃OH. The green color precipitate was separated (through a Büchner funnel) and washed with CH₃OH for 3 times to remove unreacted monomers and sol at rt. The gel product (PN) was dried out under vacuum overnight. Yield (0.92 g) 74%. The product was subjected to Soxhlet extraction (ACN, CHCl₃ and finally with THF).

¹H-NMR (400 MHz, CDCl₃, 298 K) δ/ppm: 7.6-8.3(CH₂CHC₆H₄C₁₆H₉, where C₁₆H₉ = phenyl pyrene), 6.3-7.2(CH₂CHC₆H₅, CH₂CHC₆H₄CHCH₂, CH₂CHC₆H₄C₁₆H₉), 1.2–2.2 (CH₂CHC₆H₅, CH₂CHC₆H₄ CH CH₂, CH₂CHC₆H₄ C₁₆H₉). ¹³C-NMR (100 MHz, CDCl₃, 298 K)

Charge transfer

δ/ppm: 145, 131.50, 131.02, 130.24, 128.04, 127.67, 127.44, 125.63, 124.97, 124.71, 40.57, 37.11, 32.77, 31.93, 30.04, 29.71, 29.36, 27.10, 22.70, 19.73, and 14.11.

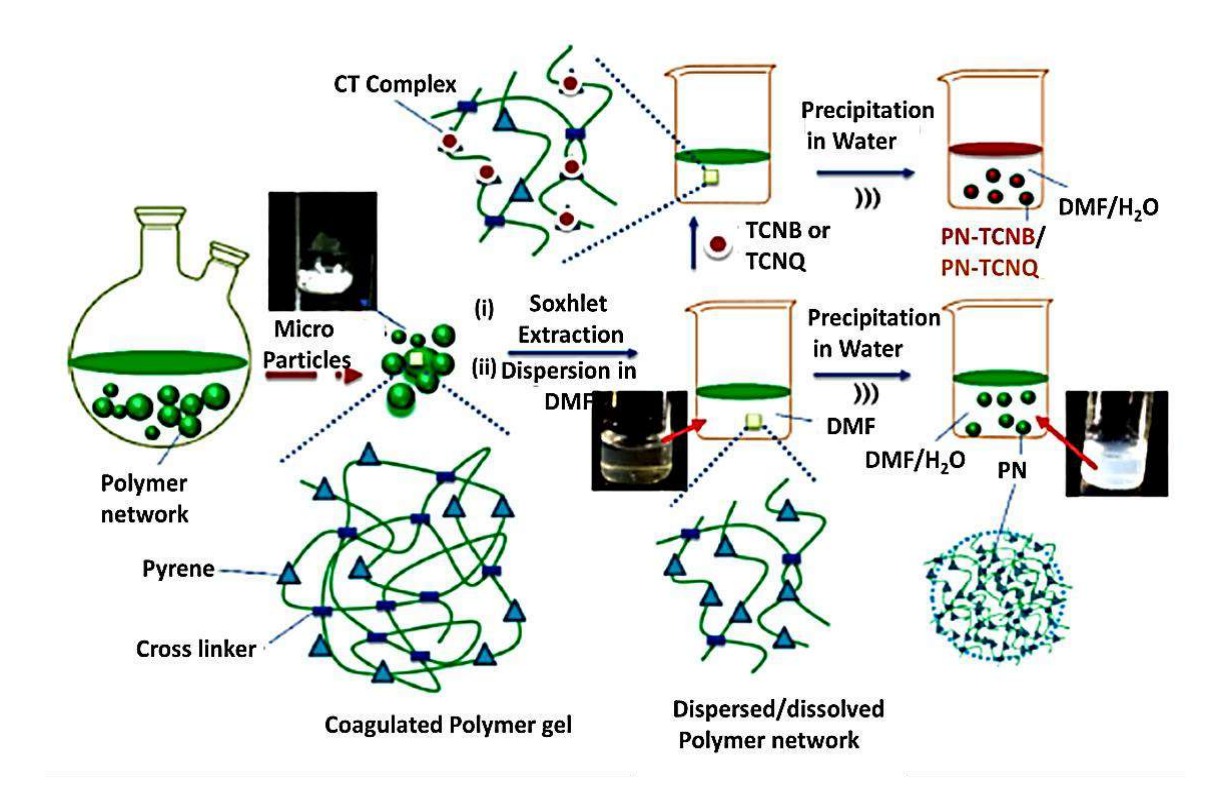
FTIR (KBr; $\bar{\vartheta}$ cm⁻¹): 3024 (C-H stretching vibration of aromatic group), 2920 (C-H stretching vibration of methylene (-CH₂) group), 1600 (C=C stretching vibration of aromatic group), 1494 (C-H bending vibration of methylene (-CH₂) group), 1452 (C-H bending vibration of methylene (-CH₂) group, 1260 (C-C stretching vibration of (-H₂C-CH) group), 804 (C-H bending vibration of para di-substituted aromatic group) and 698 (C-H bending vibration of aromatic group).

Synthesis of PN-TCNB and PN-TCNQ:

For the preparation of CT polymer particles, three routes were considered: (1) Primarily A-units were directly integrated into D-units during polymerization. But it was not successful due to the decomposition of AIBN initiator in the presence of TCNQ[254] causing no particle formation. (2) Polymerization was done without the addition of A-units. Nevertheless, FESEM analysis of the precipitated **PN** powder after washing with CH₃OH disclosed the formation of a combination of coalesced micro-particles and isolated particles. Even though the cross-linking density was not measured, the coalesced particles indicated the low degree of polymer cross-linking. [255,256] Moreover, post-polymerization incorporation of A-units into D-units became challenging due to poor dispersibility of the PN microparticles in THF and DMF. The two above methods evidently had shown a complex overlay between reality (trouble in filling A-units into the particles, coalescence of particles and poor dispersibility) and the necessity (CT particles, spherical micro-particles and cross-linked particles with the smooth surface). (3) lastly, the best guid pro quo is using the sol part having lightly cross-linked **PN**. [256] Hence, the sol was Soxhlet extracted at high temperature from the PN powder. The acquired portion was dispersed and partially dissolved in DMF to facilitate A-units could be easily integrated into D-units (Scheme 4.2 and Fig. 4.1 to 4.3).

Further, the last approach was chosen as the sol part in DMF readily precipitates as spherical micro-particles upon the addition of H₂O and subsequent ultrasonication. Moreover, these micro-particles are still superior to linear chain PS particles in terms of surface smoothness and mechanical stability, which are important for tight light confinement. The mechanism of micro-particles formation is maybe relatively comparable to that of PS micro-spherical particles in THF/H₂O under ultrasonication.^[35,71] CT polymers were prepared by dissolving **PN** (1 mg) and TCNB or TCNQ (0.5 mg) in DMF solvent and stirred at rt for 2 days under dark conditions to acquire brown- and black-colored solutions

respectively. After solvent evaporation, the yields of CT polymers **PN-TCNB** and **PN-TCNQ** were found to be 47% and 78%, respectively.



Scheme 4.2: Schematic representation of methods used for the preparation of **PN**, **PN-TCNB** and **PN-TCNQ** micro-spheres.

4.3.2. NMR spectroscopy analysis:

The accomplishment of polymerization reaction was confirmed by the 1 H-NMR spectrum which revealed three broad resonance peaks (8.01, 7.09 and 6.68 ppm) devoid of vinylene peaks of the **1** (**Fig. 4.1**). After soxhlet extraction, $\overline{M_n}$ of **PN** was found to be in the range of 7.6 kDa against the PS standard in gel permeation chromatography (GPC) study. The 13 C-NMR spectra evidently confirmed the stability of the CT complexes even in the solution state (**Fig. 4.2** and **4.3**). The respective TCNB peaks observed at 137.45, 120.60 and 112.30 ppm were shifted to up-fields to the values of 136.54, 119.70 and 112.20 ppm in **PN-TCNB**. Similarly, the 150.83 and 111.4 ppm peaks of TCNQ were also correspondingly shifted to 152.04 and 114.2 ppm in **PN-TCNQ**.

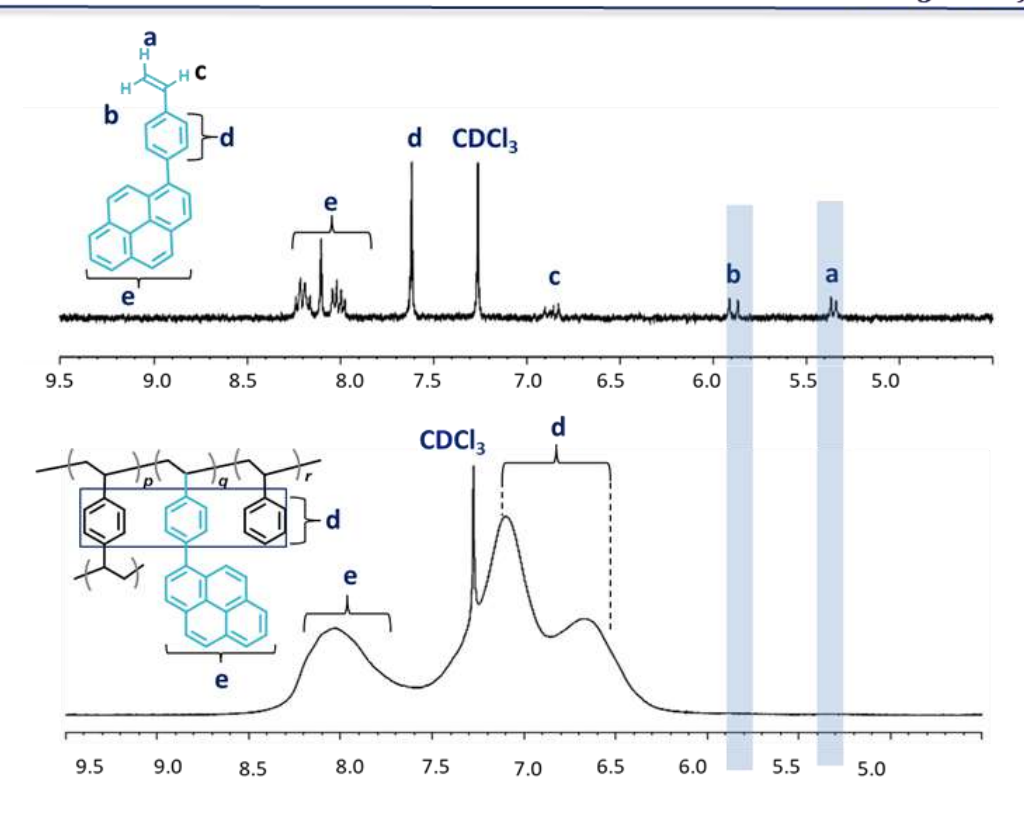


Figure 4.1: ¹H-NMR (CDCl₃) spectra of 1-(4-vinylphenyl)pyrene (1) and polymer (PN).

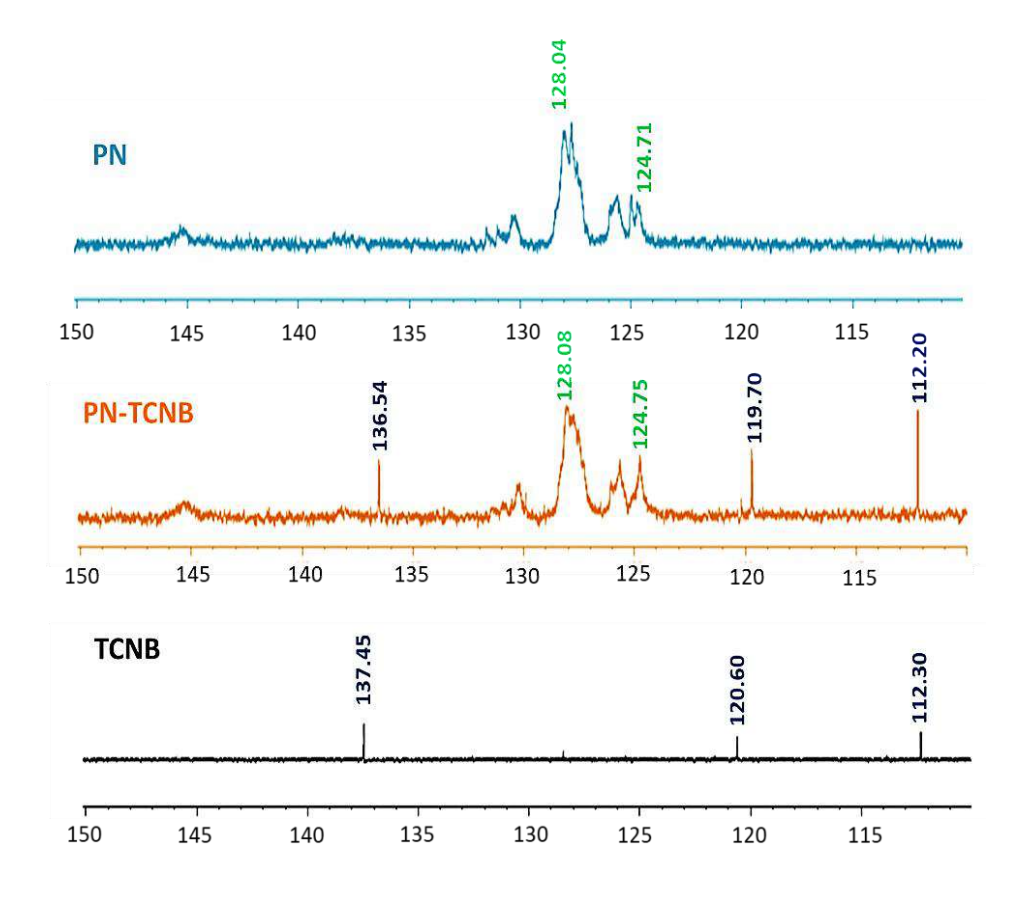


Figure 4.2: ¹³C-NMR (CDCl₃) spectra of PN, PN-TCNB and TCNB.

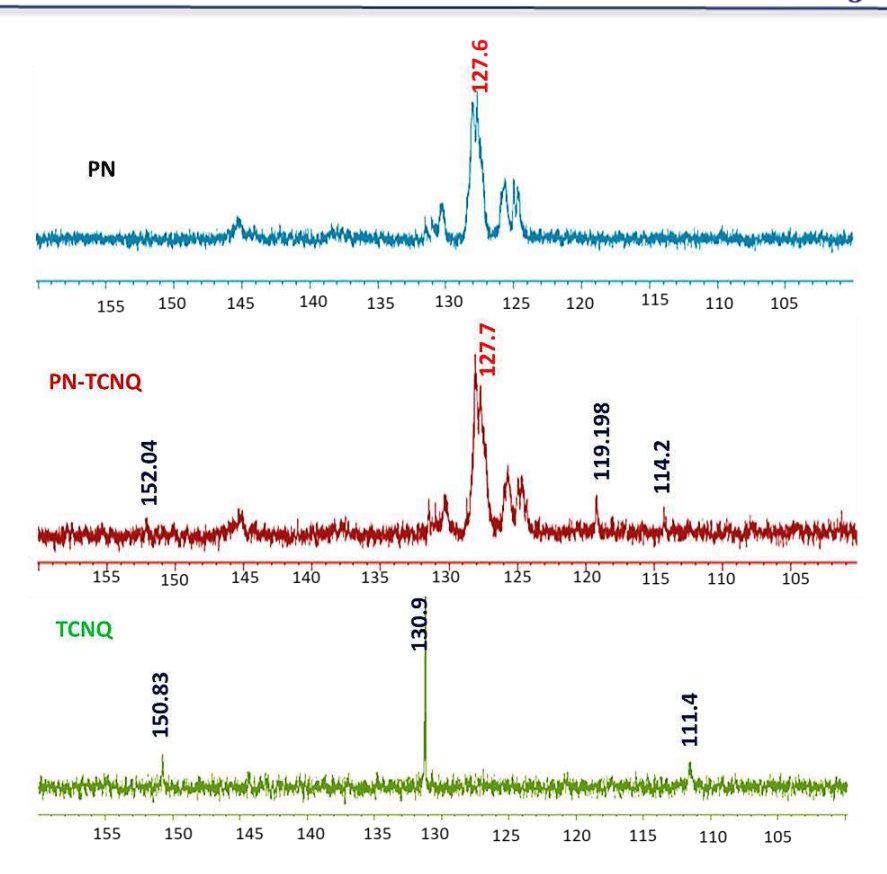


Figure 4.3: ¹³C-NMR (CDCl₃) spectra of PN, PN-TCNQ and TCNQ.

4.3.3. FTIR spectroscopy analysis of PN, PN-TCNB and PN-TCNQ:

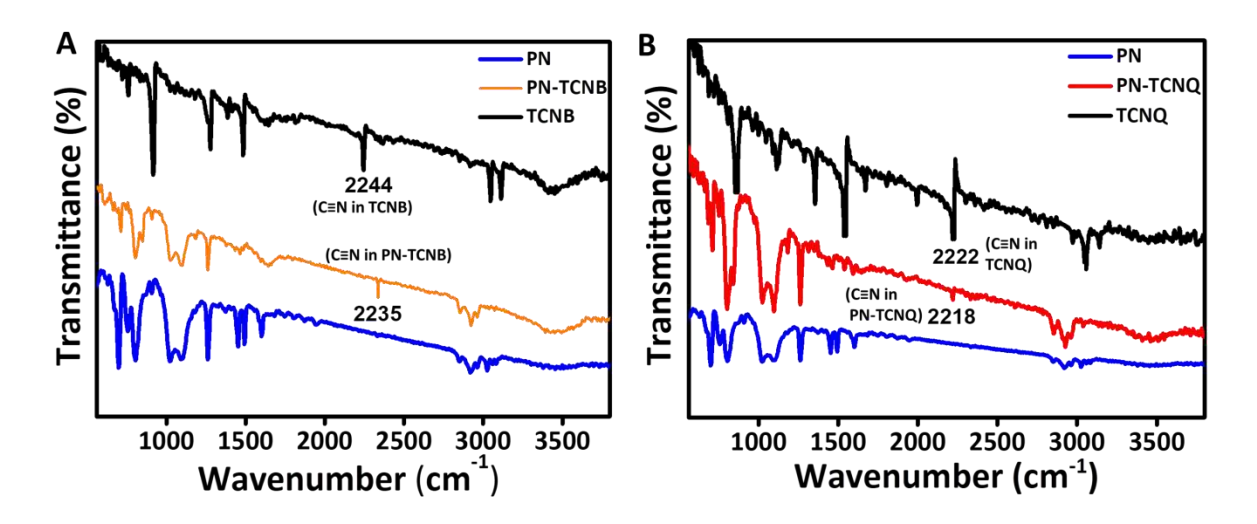


Figure 4.4: FTIR spectra of (A) PN, TCNB and PN-TCNB and (B) PN, TCNQ and PN-TCNQ.

The FTIR spectra of **PN-TCNB** and **PN-TCNQ** exhibited shifts of the C \equiv N stretching vibration ($\bar{\vartheta}_{(C\equiv N)}$) to 2335 cm⁻¹ and 2218 cm⁻¹, respectively in comparison to neutral TCNB (2244 cm⁻¹) and TCNQ (2222 cm⁻¹) molecules, proving the formation of CT complexes (**Fig. 4.4 A** and **4.4 B**). TCNQ is a good acceptor molecule with neutral quinonoid form, which

undergoes a one-electron reduction during CT process forming a stable radical monoanion TCNQ⁻. Thus triple bond character is reduced to double bond.^[257,258] Eventually, the value of stretching frequency of CN group decreased with decrease in the bond strength. Like **PN-TCNQ**, in **PN-TCNB** also, TCNB⁻ formation leads to change in the stretching frequency of CN group.

4.3.4. Thermal properties of PN, PN-TCNB and PN-TCNQ:

The thermal stability (the ability of a compound to resist decomposing when heated) of **PN**, **PN-TCNB** and **PN-TCNQ** was probed by TGA analysis. **PN** exhibited degradation

that began almost at 385 °C and continued rapidly till 426 °C, pointing to the bulk decomposition of PN. Whereas, PN-TCNB degradation takes place in two steps beginning the first step at 234 $^{\circ}C$ terminating at 263 °C indicating the TCNB molecules decomposition in the CT complex, while the second step started at 383 °C and closed at 421 °C for the degradation of polymeric chains in the CT complex (Fig. 4.5). Like in the previous case, PN-TCNQ too underwent decomposition in two steps. In the

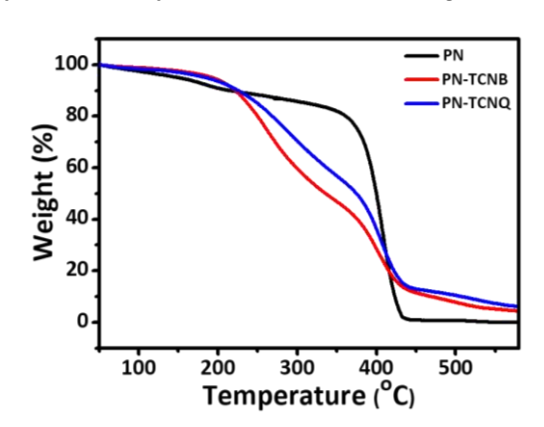


Figure 4.5: Thermogravimetric analysis (TGA) curves of **PN**, **PN-TCNB** and **PN-TCNQ**.

first step, it suffered weight loss in the temperature range of 274 °C to 309 °C equivalent to degradation of TCNQ molecules in the CT complex and in the second step it decomposed in the range of 386 °C to 426 °C due to loss of polymeric chains in the CT complexes.

4.3.5. Optical properties of PN, PN-TCNB and PN-TCNQ in DMF solvent:

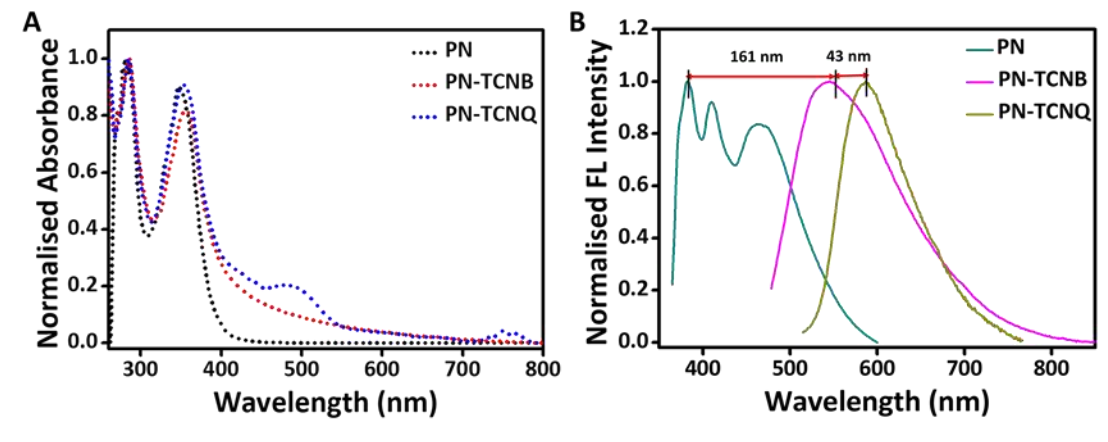


Figure 4.6: UV-Vis absorbance A) and FL spectra B) of PN, PN-TCNB and PN-TCNQ in DMF solvent.

The absorption and emission properties of **PN**, **PN-TCNB** and **PN-TCNQ** in DMF solvent (**Fig. 4.6**) were evaluated by UV-Vis absorption and FL spectroscopy. Two absorption features at 278 and 347 nm were observed for **PN** owing to π - π * transitions. While **PN-TCNQ** absorption spectrum comprised of two bands with maxima at 284 and 353

nm attributed to π - π * transitions and two weak absorption features that extend through Vis (460-540 nm) and NIR (720-780 nm) regions specifying the association of **TCNQ** with pyrene unit of PN making a CT complex (Fig. **A**). 4.6 absorption bands were found at 285/355 nm for PN-TCNB besides

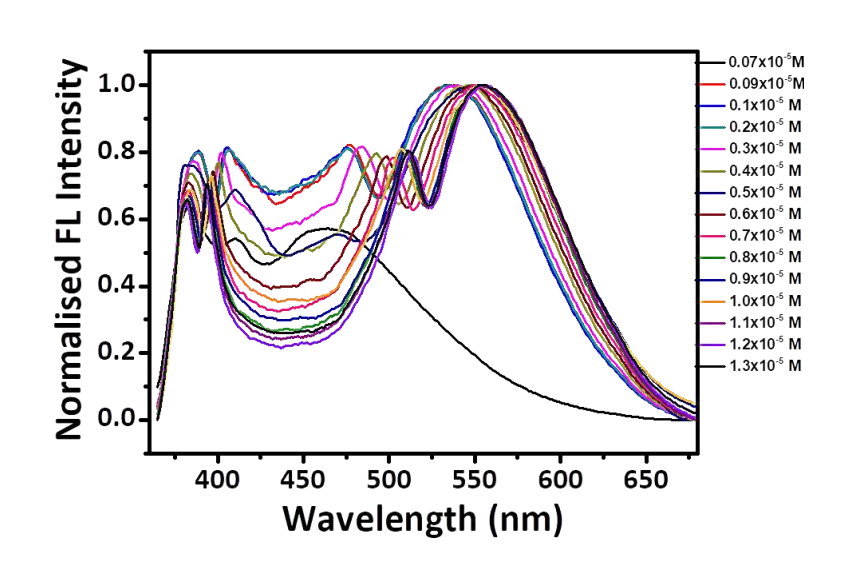


Figure 4.7: PN concentration (in DMF) dependent FL spectra.

shoulder in the range of 400-600 nm can be credited to π - π^* and CT transitions, respectively. **PN** emission spectrum showed multiple bands at 381, 410 nm in the blue region of EM spectrum. It should be noted that Bardeen et al. observed no measurable FL from pure pyrene/TCNQ in the solution state, [259] but in the case of **PN-TCNB** and **PN-TCNQ**, two distinct broad emission bands centered at 542 nm (orange) and 587 nm (red), respectively were found (**Fig. 4.6 B**). This reason is because of PS, which serves as a matrix and assists deliberate charge recombination, henceforth suppressing non-radiative relaxation and FL quenching. The FL spectrum of **PN** displayed bands at 381 and 410 for the pyrene derivative and an additional concentration sensitive broadband at ~464 nm for the excimer species (**Fig. 4.7**).

In solution state, the Φ_{FL} of **PN**, **PN-TCNB** and **PN-TCNQ** are measured to be 46%, 3% and 8.4%, respectively. The longer wavelength absorbance peaks demonstrated substantial shifts depending upon the solvent polarity indicating the polar ground state of **PN-TCNB** and **PN-TCNQ** (**Fig. 4.8 A and 4.8 C**). Further, the emission maxima of **PN-TCNB** and **PN-TCNQ** showed apparent shifts in solvents of different polarity, indicating the involvement of sizeable excited-state molecular dipole moment and different solvation dynamics involved in the excited-state of **PN-TCNB** and **PN-TCNQ** (**Fig. 4.8 B and 4.8 D**).

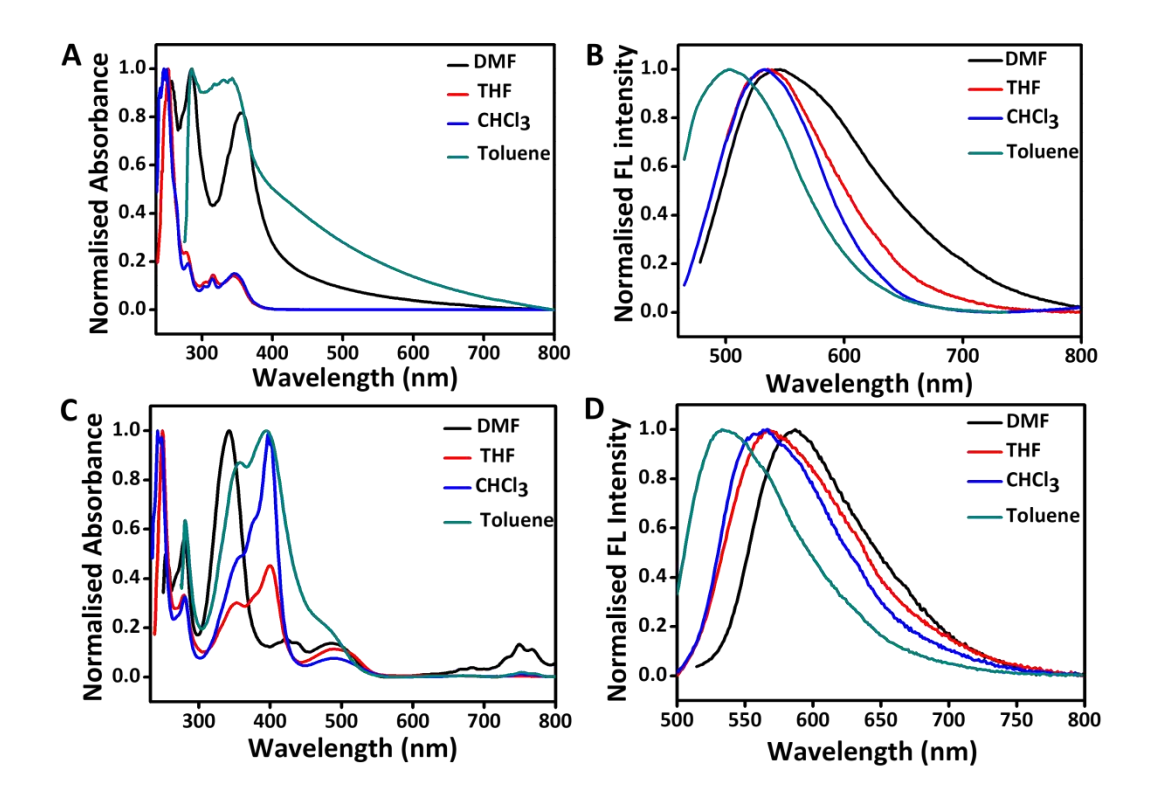


Figure 4.8: UV-Vis absorbance and FL spectra of **PN-TCNB** (A and B) and **PN-TCNQ** (C and D) in different solvents.

4.3.6. Optical properties of PN, PN-TCNB and PN-TCNQ in solid state:

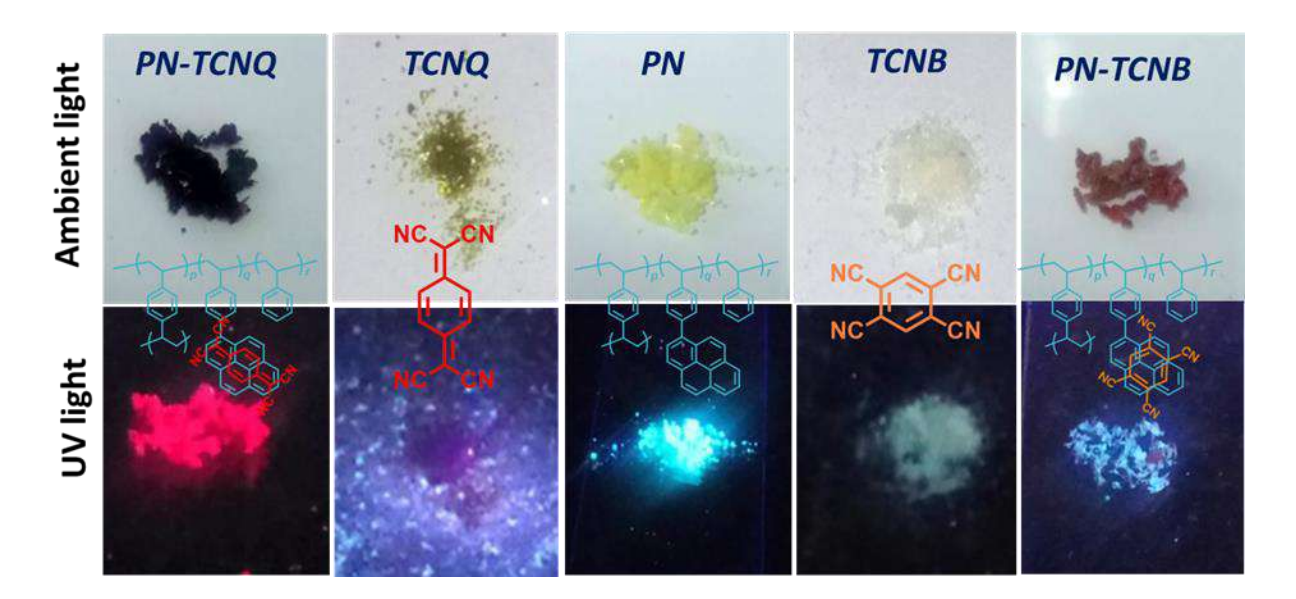


Figure 4.9: Photographs of compounds under ambient conditions and UV light (365 nm).

In contrast to the solution, solid-state samples (Fig. 4.9 and 4.10) revealed a bathochromic shift in the absorption and FL spectra. PN exhibited bands at 266, 333 and 374 nm, whereas PN-TCNB showed two maxima at 306 and 382 nm in their corresponding

absorbance spectrum. **PN-TCNQ** displayed multiple absorption bands corresponding to π - π */CT transitions in visible and NIR regions (**Fig. 4.10**). Remarkably, in comparison to **PN**

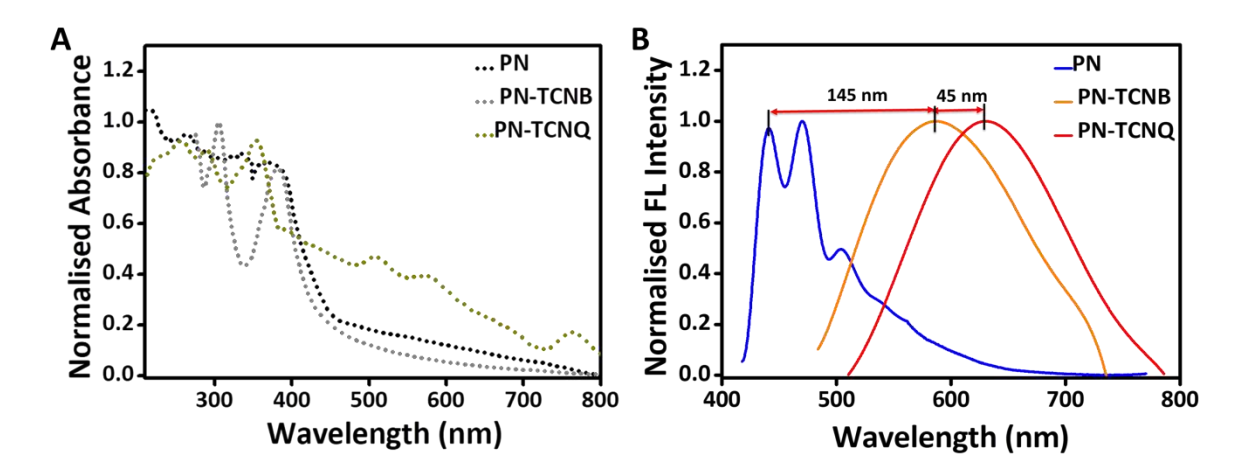


Figure 4.10: UV-Vis absorbance (A) and FL spectra (B) of **PN**, **PN-TCNB** and **PN-TCNQ** in solid state.

emission at *cyan*-colored region ((λ_{max} ~440-540 nm), **PN-TCNB**, and **PN-TCNQ** FL spectra displayed massive redshifts of nearly 140 nm to 190 nm, respectively and observed in the *orange* (λ_{max} ~587 nm) and *red* (λ_{max} ~632 nm) part of the EM spectrum. The optical

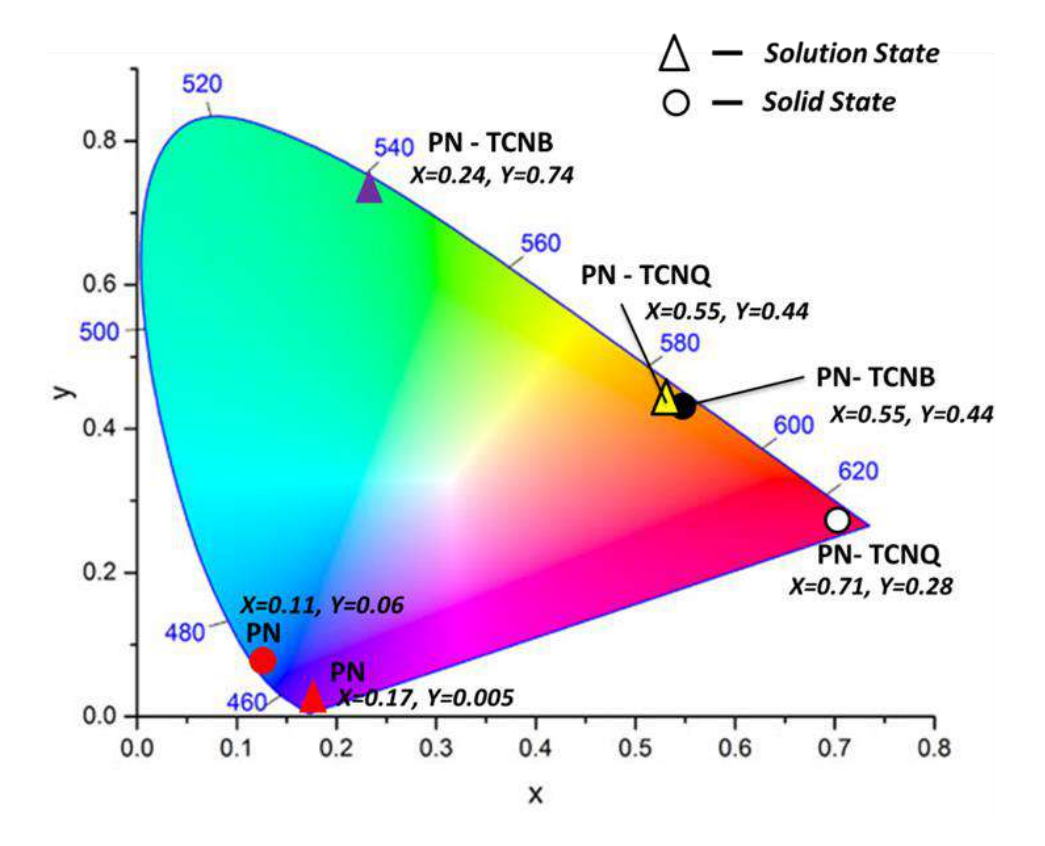
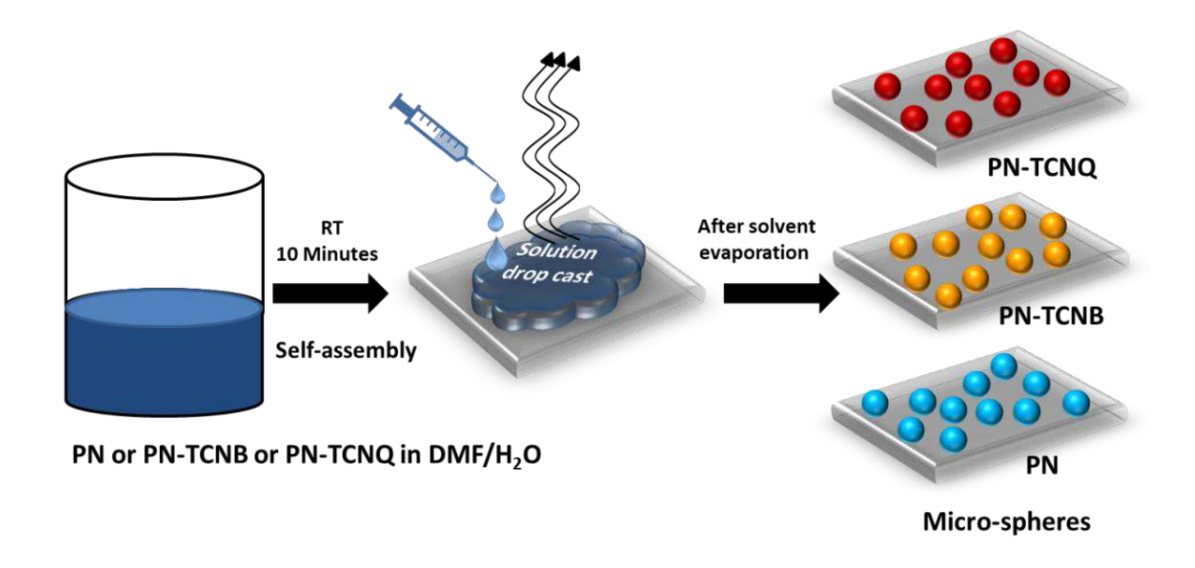


Figure 4.11: Emission colors of **PN**, **PN-TCNB** and **PN-TCNQ** in solution and solid states in a CIE standard observer chromaticity diagram.

spectroscopy results specify that the CT interaction from pyrene to TCNQ is stronger than that of TCNB, therefore decreasing the optical bandgap of the former complex. Further, comparative Commission Internationale de l'Eclairage (CIE) color coordinate values of all polymers in the solution and the solid state shown in Fig. 4.11 prominently illustrate emission shifts.

4.3.7. Self-assembly of PN, PN-TCNB and PN-TCNQ into micro-spheres:

To a solution of **PN** (1 mg of **PN**/1 mL of DMF), millipore water (15 μ L) was added, ultra-sonicated for 30 s and left undisturbed for 10 min at rt. Afterward, two drops of the solution was spread on a clean glass coverslip and allowed to evaporate slowly at rt to produce self-assembled particles. In case of **PN-TCNB** and **PN-TCNQ**, millipore water (15 μ L) was added directly into the reaction solutions and similar procedure was followed as in the case of **PN** to make spherical micro-structures (**Scheme 4.2**).



Scheme 4.2: Self-assembly of PN, PN-TCNB and PN-TCNQ into micro-spheres.

4.3.8. Microscopic studies of PN, PN-TCNB and PN-TCNQ micro-spheres:

Investigation of micro-particles of **PN**, **PN-TCNB** and **PN-TCNQ** by using FESEM showed the formation of micro-spheres of almost similar size (**Fig. 4.12 A** and **4.12 B**). Micro-particles surface smoothness is a crucial factor that governs the quality of the resonator. Particles which have rough surfaces (> $^{\lambda}/_{2}$) generally decrease the *Q*-factor of a resonator caused by light scattering and in extreme situations^[260] (surface irregularity) even do not generate the WGMs. AFM was performed to probe the surface smoothness of the micro-spheres. As one can see in the inset of **Fig. 4.12 C**, the roughness of a representative micro-sphere is lower than the detection limit signifying the suitability of the

particle for photonic studies. TEM studies presented dark contrast indicating the dense packing of the polymer chains within the micro-spheres (Fig. 4.12 D). Expectedly, the SAED unveiled no diffraction spots showing the amorphous nature of the micro-particles (Fig. 4.12 E). For CT micro-spheres EDS analysis confirmed the incorporation of A-units within PN by proving the nitrogen (N) element distribution (Fig. 4.12 F).

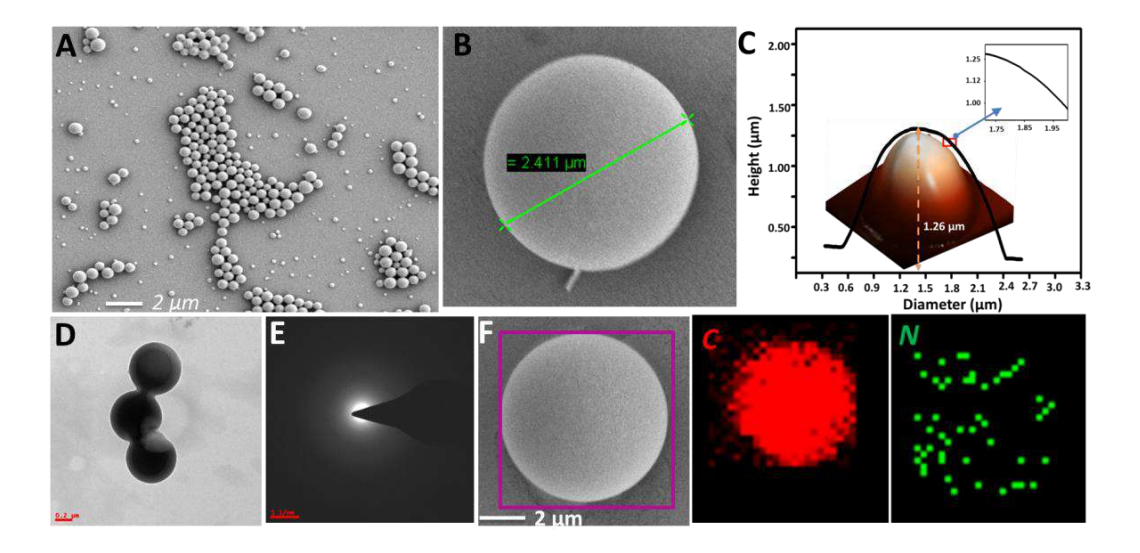


Figure 4.12: A) and B) FESEM images of **PN** micro-spheres. C) AFM image of a single **PN** micro-sphere. The right inset shows the surface smoothness. D) TEM image of **PN** micro-spheres. E) SAED pattern of micro-spheres. F) EDAX elemental (*C* and *N*) map of **PN-TCNQ** micro-sphere.

4.3.9. Raman spectra of PN-TCNB and PN-TCNQ:

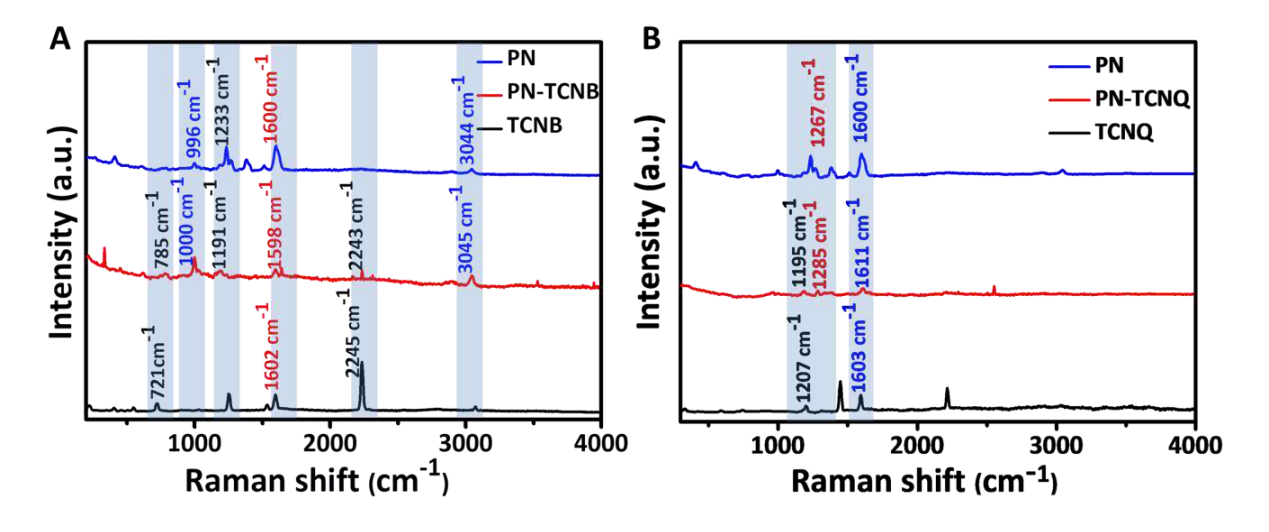


Figure 4.13: Raman spectra of (A) PN, PN-TCNB and TCNB and (B) PN, PN-TCNQ and TCNQ.

To further confirm the composition of the CT complexes Raman spectra were recorded. It was observed that the Raman peaks originating from TCNB molecules, were seen in the

spectrum of the **PN-TCNB** CT complex (**Fig. 4.13 A**). However, these peaks shifted from those of the TCNB single-crystal relative to each other. In the **PN-TCNB** CT complex, -C=N, -C=C- stretching vibration modes were shifted to 2243 cm⁻¹ and 1598 cm⁻¹, respectively, compared to that of TCNB stretching vibration modes (-C=N 2,245 cm⁻¹, -C=C- bonds 1602 cm⁻¹). **Figure 4.13 B** shows the Raman spectra of the **PN-TCNQ** CT complex obtained from **PN** and TCNQ. A shred of strong evidence to prove the formation of the CT complexes is the shift of the TCNQ -C=C- ring stretching frequency and a bending vibration mode of C-H bond. The -C=C- ring stretching band and C-H bending vibration band were observed at 1603 cm⁻¹ and 1,207 cm⁻¹, respectively for TCNQ, while those bands were shifted to 1611 cm⁻¹, 1195 cm⁻¹ for the **PN-TCNQ**. Besides, new peaks which do not belong to TCNQ appeared in the **PN-TCNQ** CT complex.

4.3.10. Lifetime imaging of PN, PN-TCNB and PN-TCNQ micro-spheres:

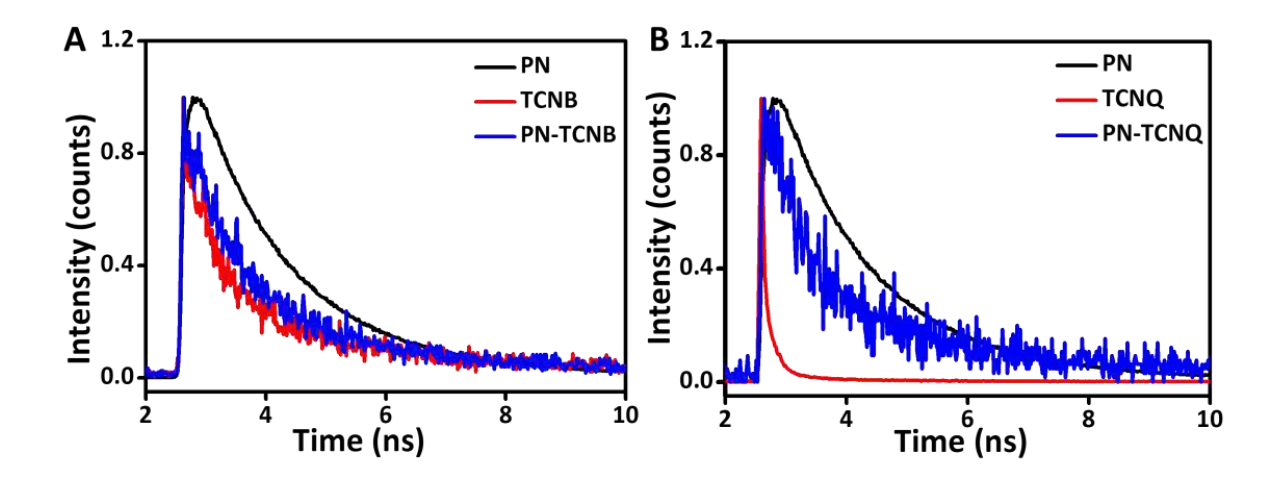


Figure 4.14: Lifetime decay profiles of (A) **PN**, TCNB and **PN-TCNB** and (B) **PN**, TCNQ and **PN-TCNQ**.

To examine the FL lifetime properties of **PN**, **PN-TCNB** and **PN-TCNQ** in DMF solvent, FLIM studies were performed. A picosecond (ps) pulse laser (λ = 405 nm) was used for the excitation and the decay profile was acquired through a time-correlated single-photon counting (TCSPC) technique. All compounds showed bi-exponential decay with varying lifetime values. FL lifetime measurements (**Fig. 4.14**) displayed FL lifetime (τ_{FL}) value of 1.7 ns for **PN**. The measured τ_{FL} values of **PN-TCNB** and **PN-TCNQ** are 1.48 and 1.24 ns, respectively which are dissimilar from pure TCNB (1.43 ns) and TCNQ (0.41 ns). This finding indicates that **PN-TCNB** and **PN-TCNQ** complexes have fast excited-state dynamics compared to pure **PN**.

4.3.11. Single-particle microscopic studies of PN, PN-TCNB and PN-TCNQ microspheres:

To examine the light-trapping capacity of **PN**, **PN-TCNB** and **PN-TCNQ** microspheres, single-particle FL spectroscopy studies were performed on LCM set-up in reflection geometry. For excitation, CW (Ar⁺ 488 nm and diode 405 nm) lasers were employed. Single **PN** micro-sphere was illuminated at the middle using a 405 nm laser (objective 150x; NA 0.95) displayed an intense blue emission spectrum. Remarkably, while tangential excitation of micro-sphere generated a blue ring-like pattern and its corresponding FL spectrum revealed a series of multiple pairs of sharp lines or optical modes signifying WGM resonance (**Fig. 4.15**). The obtained frequency-dependent optical modes specify tight confinement of circulating FL photons within the micro-resonator via

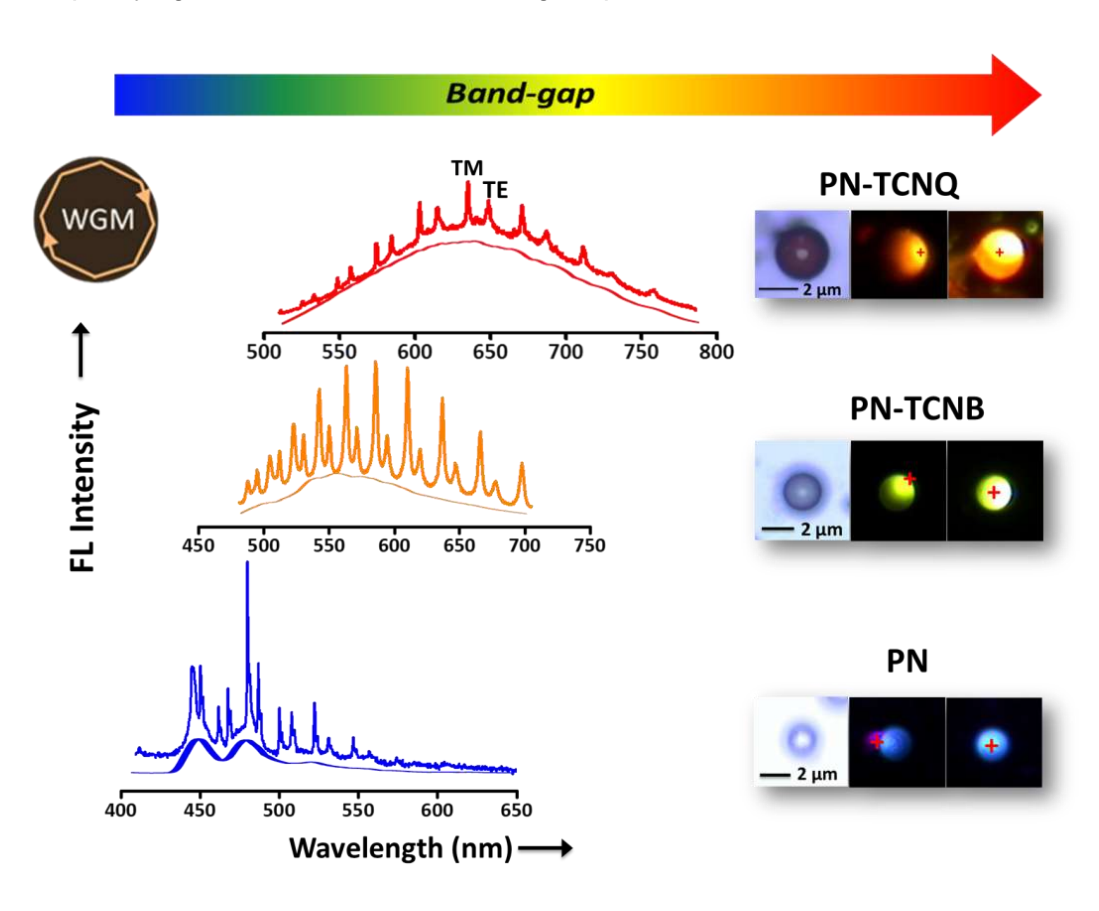


Figure 4.15: Single-particle FL spectra of **PN**, **PN-TCNB** and **PN-TCNQ** exhibiting WGMs. The insets show the corresponding WGMs emissions shown by the micro-spheres.

repeated TIR at the air-resonator surface boundary. These resonator modes originate as a result of constructive wave interference of the circulating FL and their number surge with the increase of the resonator size. These resonance modes can be noticed only if the FL frequencies equivalent to the frequencies of the resonator allowed modes, as termed by the

so-called Purcell effect.^[261] In the same way, **PN-TCNB** and **PN-TCNQ** micro-spheres upon illumination with 488 nm laser showed *orange* and *red* color emissions, respectively accompanied by WGMs. A pair of periodic sharp peaks correspond to TE and TM WGMs (**Fig. 4.15**), which generally show up due to breakdown of TE/TM degeneracy. Further, the spacing between modes or FSR and the number of observed modes are very much sensitive to the size of the micro-sphere.

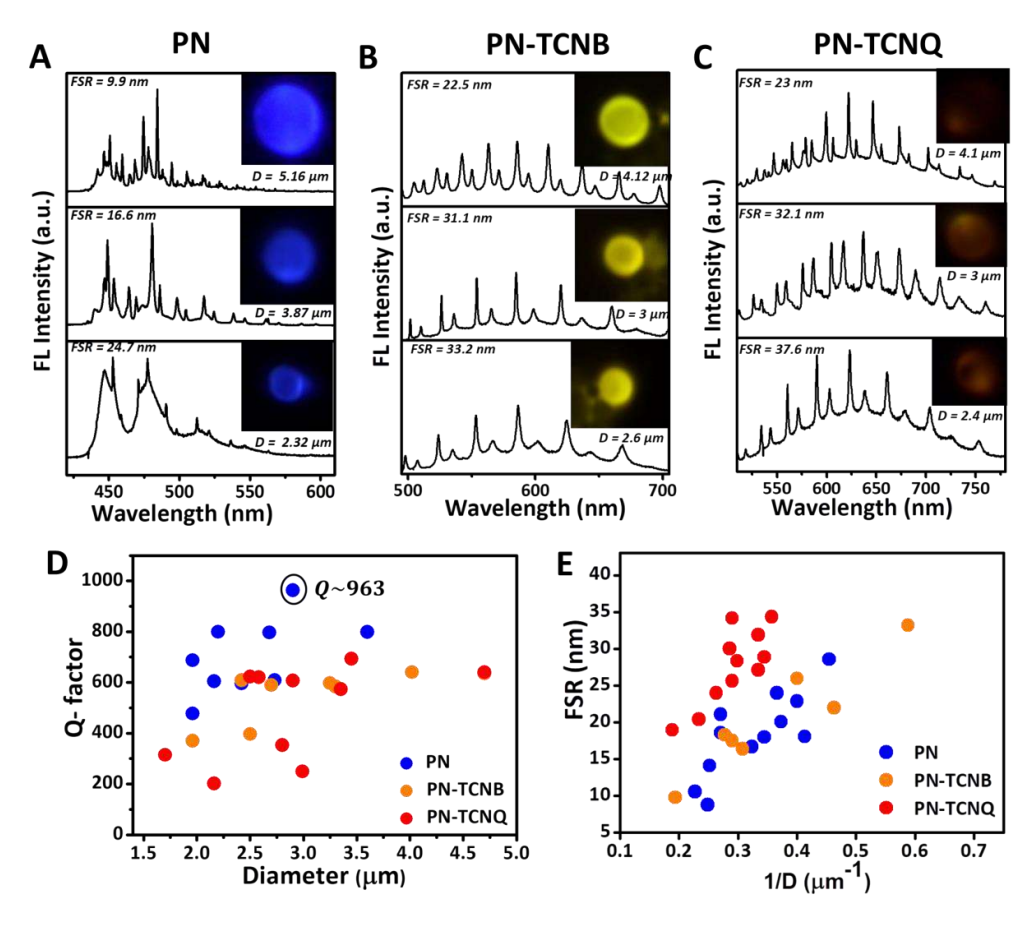


Figure 4.16: Single-particle FL spectra of micro-spheres of **PN** (A), **PN-TCNB** (B), and **PN-TCNQ** (C) displaying particle size-dependent WGM resonance. The insets show the corresponding FL images. D) The *Q*-factor versus D plot is shown at the left-bottom. E) FSR vs 1/D plots of different sizes micro-spheres.

To study the particle size-dependent photonic effects, three representative microspheres of varying diameters were identified. FSR values increase upon decreasing the diameter of micro-spheres valued from the confocal microscope images (Fig. 4.16 A, B and C). A plot of FSR versus 1/D was evidently in line with the relation of FSR and 1/D (Fig. 4.16 E), which further confirms the WGM type resonating action of each micro-sphere, through TIR. In case of PN, PN-TCNB and PN-TCNQ, the *Q*-factor of the micro-resonators are in the range of 600-1000, which is a better value for a polymer-based optical resonator^[10] (Fig. 4.16 D). For the OPL enhancement, thin films of PN, PN-TCNB and PN-

TCNQ were compared with a thin film of micro-spheres displaying WGMs. Interestingly, the average OPL intensities of **PN**, **PN-TCNB** and **PN-TCNQ** micro-spheres were found to be nearly 10 times higher than the corresponding thin films under identical experimental conditions (**Fig. 4.17**). It should be noted that the OPL enhancement order of the thin film of micro-spheres varied from one area to another (though always higher than the spin-coated thin film). The above single-particle experiments make evident the potential usage of self-assembled polymer CT complexes to achieve bandgap tunable micro-resonators generating enhanced optical emissions.

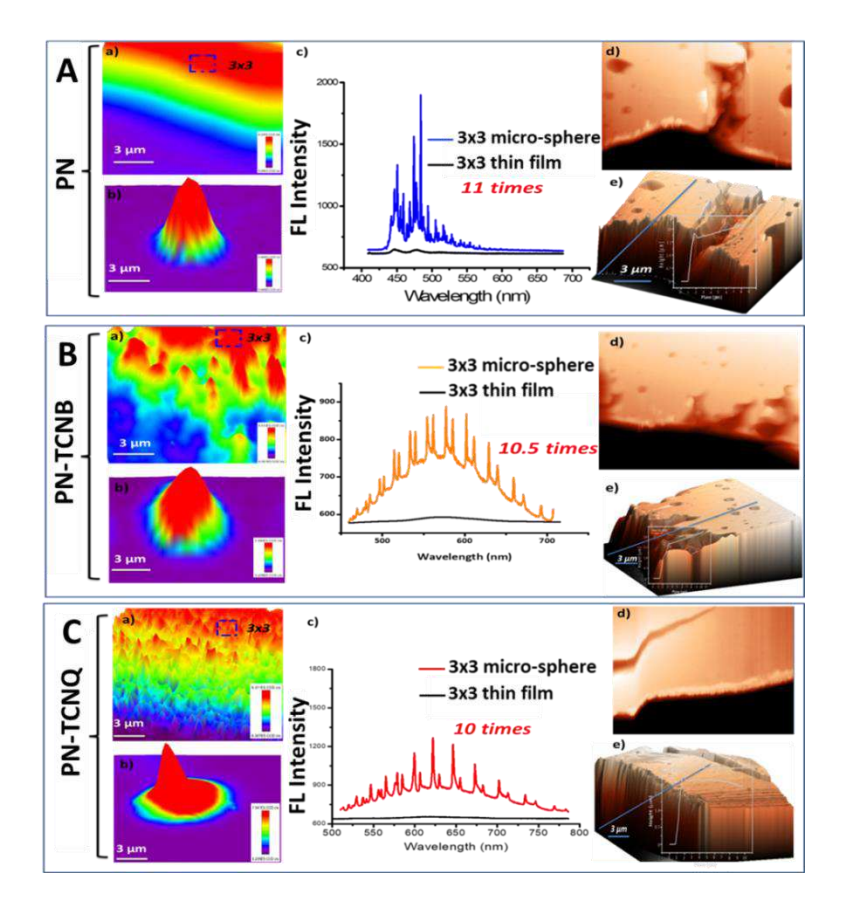


Figure 4.17: Comparative FL intensity of thin-film and micro-spheres of **PN** (A), **PN-TCNB** (B), and **PN-TCNQ** (C). a) and b) 3D FL images of thin film of selected area $(3\times3 \ \mu\text{m}^2)$ and micro-sphere of 3 μ m D, respectively. Their corresponding spectra are shown in c. d) AFM 3D topography thin film with 3 μ m height together with their corresponding height profile plots.

4.3.12: Nonlinear absorption coefficient (β) measurements:

As stated earlier, CT complexes are familiar to display NLO properties when irradiated with high energy lasers, since the applied electric field intensities are equivalent to internuclear atomic fields. The nonlinear optical absorption measurements were done by Z-scan technique with 100 fs pulse width and 1 kHz repetition rate, 800 nm Ti: sapphire

laser. β of the **PN**, **PN-TCNB** and **PN-TCNQ** in solution were determined by performing the open aperture Z-scan experiment. Concisely, in a distinctive Z-scan experimental method, a single laser beam with a Gaussian profile is concentrated by using a lens. The sample in a 1 mm thick cell was then translated along the path of the focused beam. At the focal point,

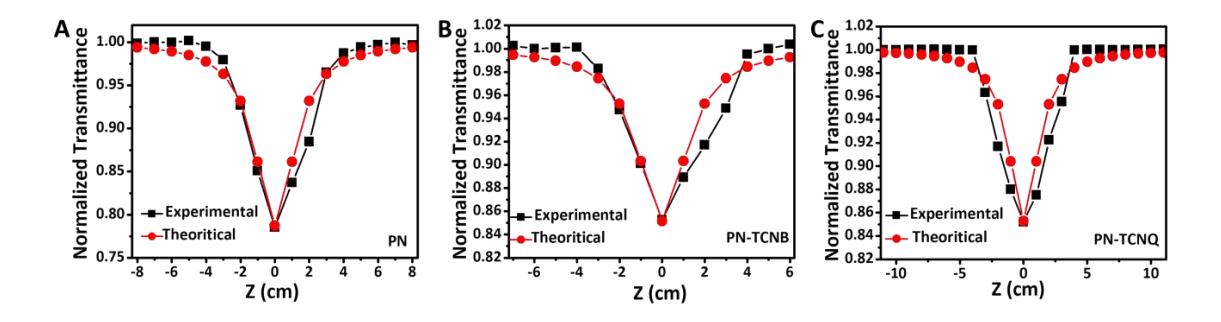


Figure 4.18: Open aperture Z-scan curves of PN, PN-TCNB and PN-TCNQ.

the sample encounters maximum intensity, which slowly declines in both directions from the focus. The thickness of the sample was taken such that it was smaller than the Rayleigh range of the focused beam, which is approximately 1 mm, well-calibrated neutral density filters were used to regulate the laser intensity. The data is then collected by scanning the cell across the focus and the β is acquired by fitting the nonlinear transmission expression for an open aperture Z-scan curve.

$$T = 1 - \frac{\beta L_{eff} I_o}{\frac{3}{2^{\frac{3}{2}} [1 + (\frac{z}{z_o})^2]}} - - - - + (1.30)$$

where z is the sample position, $z_o = \pi \omega_o^2/\lambda$ is the Rayleigh range, ω_o is the beam waist at the focal point (z = 0), λ is the laser excitation wavelength, I_o is the intensity on the sample at focus, β is the effective nonlinear absorption coefficient, effective optical path length in the sample of length L is given as $L_{eff} = 1 - e^{-\alpha L/\alpha}$, and α is the linear absorption coefficient. Figure 4.18 illustrates the open aperture Z-scan curve for PN, PN-TCNB and PN-TCNQ, solid lines indicate the theoretical fit achieved using the above equation. The open aperture Z-scan curve displayed TPA process. The β assessed from the theoretical fitting is 4.4×10^{-10} cm/W, 3.18×10^{-10} cm/W, and 3.28×10^{-10} cm/W for PN, PN-TCNB and PN-TCNQ, respectively having intensity at the focus $1.9 \times 10^{12} \frac{W}{cm^2}$ (Fig. 4.18).

4.3.13: TPL Studies of PN, PN-TCNB and PN-TCNQ:

As stated earlier, CT complexes are familiar to display NLO properties when irradiated with high energy lasers, since the applied electric field intensities are equivalent

Charge transfer

to internuclear atomic fields. Hence, to probe the NLO properties of a thin-film of **PN**, **PN-TCNB** and **PN-TCNQ** micro-spheres, each sample was illuminated by Ti: Sapphire 800 nm fs pulse laser (pulse width 100 fs, repetition rate 1 kHz). The experiment was done by placing the sample at focal volume having spot size of 101.8 µm wrapping a dozen of particles and is exposed by linearly polarized light with different input powers. The intensity at the focus was varied by adjusting the wave plate. According to our anticipation, a thin film of **PN** has shown a TPL band at ~ 488 nm, almost matching with its OPL (**Fig. 4.19 B**) by emitting intense blue light. In the same way **PN-TCNB** and **PN-TCNQ** thin films containing micro-spheres also exhibited TPL spectra at ~ 580 nm and ~ 602 nm, respectively corresponding to their OPL bands. The observed narrower FWHM of the TPL spectra in comparison to the OPL spectra is attributed to reabsorbance effect of the samples. [115] Further, upon increasing the pump power, the TPL intensity of the micro-spheres showed square dependence with the pump energy, suggesting the TPA process (**Fig. 4.19 C**).

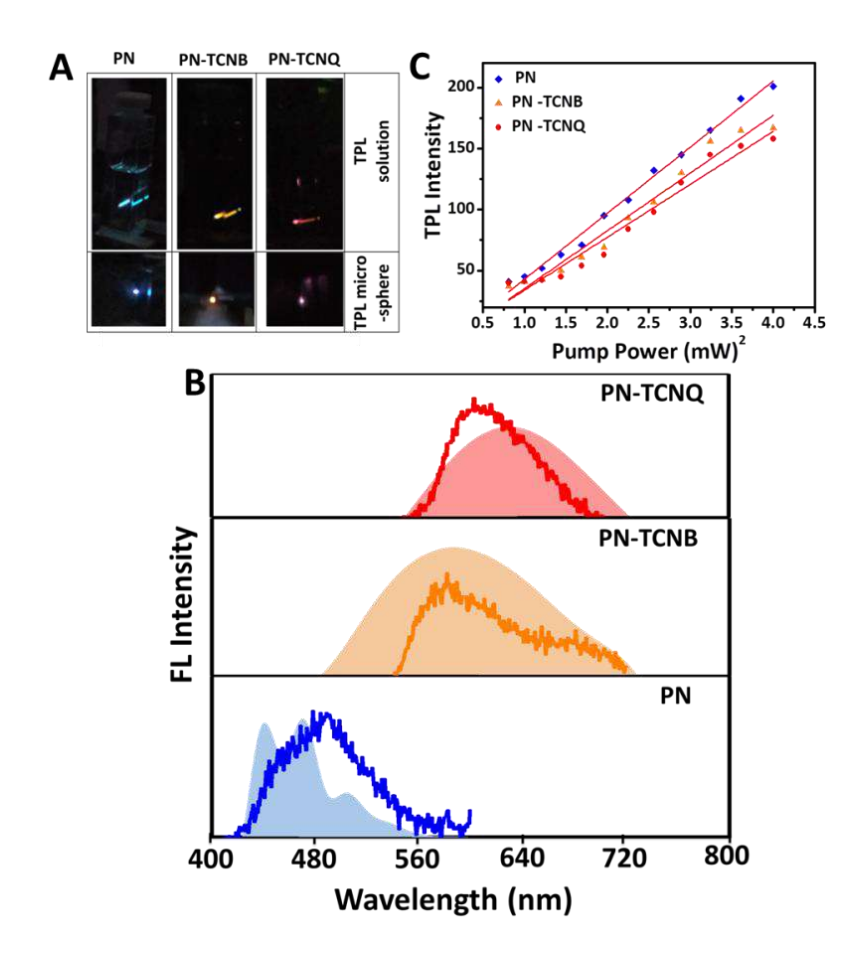


Figure 4.19: A) TPL photographs from solution and micro-spheres of **PN**, **PN-TCNB** and **PN-TCNQ**. B) TPL spectra (solid line) of **PN**, **PN-TCNB** and **PN-TCNQ** micro-spheres together with their OPL (solid fill). and C) The corresponding linear relationship between TPL intensity and excitation power in (mW)² unit. The blue, orange and red dotted lines correspond to **PN**, **PN-TCNB** and **PN-TCNQ**.

In order to observe the TPL enhancement, homogeneous thin films of PN, PN-TCNB and PN-TCNQ were compared with the corresponding micro-spheres exhibiting WGMs. Interestingly, the TPL intensities (collected at different areas) of PN, PN-TCNB and PN-TCNQ micro-spheres were found to be several orders of magnitude higher than the corresponding thin films owing to the optical-resonator effect of the former (Fig. 4.20). Most of the areas of thin films did not display any measurable TPL signal. It should be noted that the TPL enhancement order of the thin film of micro-spheres different from one area to another (although always higher than the spin-coated thin film). As per the stability is concerned PN-TCNB is more stable than PN-TCNQ since the former showed strong TPL even after several months compared to the latter (only a week stable).

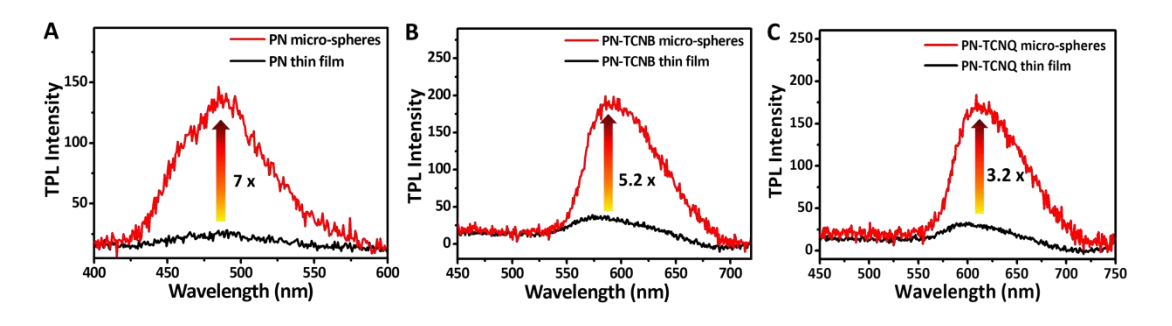


Figure 4.20: Comparative TPL intensity of thin-film and micro-spheres of **PN**, **PN-TCNB**, and **PN-TCNQ**.

4.4. Summary:

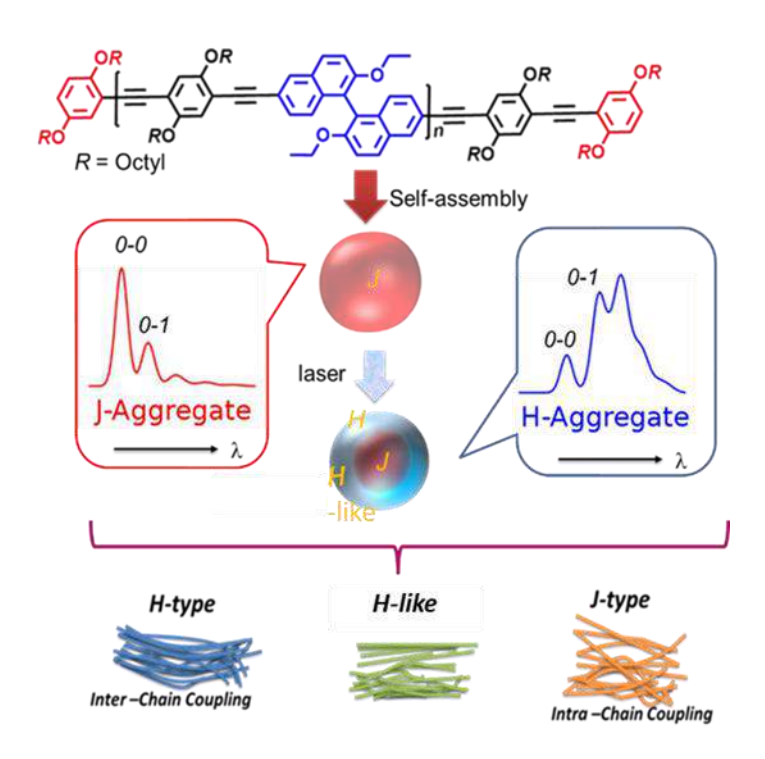
This chapter presented the successful synthesis of CT-type polymer particle microresonators via the principle of supramolecular CT interactions. For this, at first, a new cross-linked macromolecule (**PN**) with pyrene as pendant D-group was made to incorporate acceptors A-molecules like TCNB and TCNQ. Nevertheless, very low dispersability of the polymer particles turn into one of the restrictions, inhibiting solution state incorporation of A-units into D-components of **PN**. Alternatively, to prepare mechanically stable particles with good surface smoothness, polymer cross-linking was needed. Hence, the sol part of the **PN** having lightly cross-linked polymer was isolated and dispersed in DMF to integrate TCNB and TCNQ acceptors successfully. Later, the obtained cross-linked polymer and its CT complexes were precipitated as micro-particles by the addition of H₂O and successive ultrasonication. The mechanism of formation of polymer particles from **PN** is maybe somewhat comparable to the dye-incorporated PS micro-particle formation. The resulting micro-particles consisted of **PN**, **PN-TCNB** and **PN-TCNQ** emit *blue*, *orange* and *red* colors upon one-photon excitation due to CT interactions. The single-particle photonic experiment was performed on these CT micro-spheres showed multimodal WGM emissions in the vis-

Charge transfer

NIR range with a *Q*-factor as high as 1000 indicating increased photon residence time within the resonators. Two-photon pumped (800 nm) NLO spectroscopy studies of micro-resonators displayed TPL almost comparable with their OPL bands. Moreover, the high *Q*-micro-spheres exhibited improved emissions in both linear and NLO systems in contrast to their analogous homogenous thin films proving improved light-matter interaction. Our method evidently proves the efficiency of supramolecular CT micro-resonators to get diverse Vis-NIR range up-conversion CT emissions appropriate for numerous NLO applications.

5

Laser-Driven Shifting of *H*-Type Electronic Coupling to *J*-Type in NLO Chiral Polymer Micro-Resonators - A Single-Particle Investigation



V. Radhika, M. Annadhasan, J. Ravi, M. Durga Prasad, N. Mitetelo, K. Zhdanova, E. Mamonov, K. Müllen, T. V. Murzina and R. Chandrasekar* (manuscript is to be communicated)

^{*}This chapter is adapted from:

5.1. Abstract:

Two novel, green-emitting, chiral, conjugated copolymers abbreviated as R- and S-BP are synthesized by copolymerizing of R- and S-6.6'-dibromo-2,2'-diethoxy-1,1'binaphthyl (R- and S-BINOL derivatives) with 1,4-diethynyl-2,5-bis(octyloxy)benzene by Sonogashira coupling reactions. $\overline{M_n}$ of **R-** and **S-BP** are 15 and 13 kDa, respectively. Moreover, these R- and S-BP self-assemble in THF/H₂O/EtOH mixture generates microspherical structures. The depiction of intra- and inter-polymer structural changes in the selfassembly are explored by CD and UV-Vis spectroscopy studies. The former technique demonstrates the surge of the ellipticity of the optical response of the chiral component and its conversion from cisoid to transoid conformation during polymer aggregation. In contrast, the latter technique shows the lowering of the conjugation between diethynyl benzene and 1,1'-binaphthyl unit along the chain during the self-assembly procedure. Remarkably, these micro-spheres exhibit WGM resonances (500-720 nm) in the one- and TPL with a Q of up to ~700. Nevertheless, at high laser power (≥10 mW), the TPL spectral features of microspheres changed significantly with the increase in the ratio of $I_{0-0}^{TPL}/I_{0-1}^{TPL}$, broadening of the linewidth and red-shift hinting transformation of polymer packing. Similar spectroscopic changes were observed for micro-spheres heated thermally (range: 60 °C-160 °C) or with high power (≥10 mW) continuous-wave laser confirming the laser-triggered heat. FLIM studies using a TCSPC unambiguously confirm the transformation of polymer packing from a homogeneous J type to heterogeneous (J, H and H-like). The TPL-CD value averaged over the whole spectral range for R- and S-BP micro-spheres is 6% with the opposite sign. This original work demonstrates the tremendous potential of laser-triggered heat in introducing polymer packing heterogeneity to achieve multi-color emitting conjugated polymer structures useful for many applications.

5.2. Introduction:

Recently, π -conjugated polymers (CPs)^[230,262,263] with multi-functional properties such as chirality, NLO, and electronic coupling tunability (ECT, for example, aggregation-dependent optical emission shifts)^[173] have gained vital importance. The presence of chiral groups in the donor-acceptor type CP facilitates the production of the chiro-optical effect and NLO emissions, respectively. For example, CD is one such chiro-optical effects that arises from the different absorption of left and right-handed circularly polarized light by the enantiomeric chiral materials.^[264] The envisaged applications of the above-mentioned multifunctional CP materials include biomedical sciences, quantum information technology, chiral optical-tweezers, and quantum networks, ^[110,265] to name a few. Hence, the creation of

multi-functional CPs with chirality, NLO, and ECT properties is a challenging endeavor. Notably, compared to the former two properties, there is no design principle available for the latter.

Further, the practical applicability of (any) chiral NLO materials is limited by two critical features: (i) weak NLO signals and (ii) weak chiro-optical responses. Thus, so far, most of the experiments on chiro-optical effects from small chiral molecules or polymers were recorded only in the linear optical regime. [110,266,267] Alternatively, to increase the strengths of NLO and chiro-optical signals, effects suitable for confining or trapping the incident light have been created in plasmonic nanostructures, metamaterials, nanoantennae, and optical resonators.[111,268-274] For example, in an optical resonator, the increased residence time or photon lifetime (τ_p) of the trapped incident photons is expected to increase the light-matter interaction, thereby amplifying the signal strength. [59,111,274-276] In this regard, spherical NLO resonators obtained via solvent-assisted self-assembly chiral polymers are advantageous.^[276] The reason is that these resonators are prone of trapping light via WGM resonance [49,51,59,72,206,276] and of improving NLO and related CD-NLO signals. Additional advantages of polymer-based resonators are that they can be obtained defectfree and with a smooth surface due to tightly packed polymer chains. These features are essential to realizing high Q polymer resonators (high light storage) by minimizing scattering induced optical losses.[59]

ECT is observed in CPs as a function of temperature in the solution state. $^{[69,277,278]}$ The temperature-dependent emission shift is usually attributed to various inter and intra polymer chain coupling mechanisms such as H- and J-aggregations $^{[279]}$ or excimer formation, $^{[280]}$ and backbone planarization. $^{[281]}$ Spano et al. have proposed a theoretical model that distinguishes H and J-type aggregates based on the ratio of the first two vibronic peaks (0-0 and 0-1) of the FL spectrum. $^{[279,282]}$ In J-type polymer aggregates, the *head-to-tail* arrangement of chains favors intra-chain electronic coupling and the 0-0 vibronic transition is dipole allowed. Further, in J-type compared to the uncoupled system, the $I_{0-0}^{FL}/I_{0-1}^{FL}$ (where, I_{0-0}^{FL} and I_{0-1}^{FL} are FL intensity of 0-0 and 0-1 peaks, respectively) ratio increases, τ_{FL} reduces, and emission shifts to the red side of the electromagnetic spectrum. $^{[173,279,282]}$ In contrast, the H-type aggregate requires a *face-to-face* arrangement of polymer chains, thereby facilitating inter-chain electronic coupling. Here, the 0-0 transition is dipole forbidden, and the FL spectroscopic changes are opposite to those of J-type aggregate. Recently, Eder et al. have elegantly demonstrated the reversible switching of electronic coupling (H-type and J-type) in nanoscopic isolated CP aggregates by partially

swelling and drying the aggregates embedded inside a non-fluorescent polymer matrix. [173,279,282]

Typically, laser-based spectroscopy studies on organic or polymer samples involve the interaction of ultrafast pulse CW laser beam with the sample. However, above a specific pump power, the produced local heat might induce morphological or phase changes within the polymer and thus shift the optical emission wavelength (depending upon the polymer structure and molecular weight). However, to the best of our knowledge, there exists no literature either on ultrafast laser- or CW-induced changes in polymer chain packing and subsequent shifts of the polymer electronic coupling. We believe that these overlooked spectral outcomes from micro-spectroscopy experiments treating polymer samples at high laser intensities are worth a detailed investigation and report.

This chapter presents chiral micro-resonators made from self-assembly of enantiomeric π -conjugated NLO copolymers, namely, R- and S-2,2'-diethoxy-1,1'binaphthyl-co-1,4-diethynyl-2,5-dioctyloxy benzene (R-BP and S-BP). These tailor-made polymers prepared via Sonogashira coupling reaction are made of (i) enantiomeric 1,1'binaphthyl with electron-donating ethoxy groups substituted at the 2,2' positions; (ii) moderately electron-withdrawing 1,4-diethynyl phenyl units provide ECT to the polymer^[281] and (iii) flexible *n*-octyloxy polymer side chains to attain solution processability (Scheme 5. 1). As the enantiomeric copolymers are hydrophobic, their self-assembly in THF solution by adding antisolvents (water/ethanol) produced corresponding micro-spheres. The diameter of the obtained R- and S-BP micro-spheres ranged from ~3-8 µm as evident from the confocal- and electron-microscopy techniques. In conjugated polymers, their order is related to alkyl side-chain positions, chain length/shape, molecular weight, and backbone curvature. The spectroscopic snapshots of the self-assembly process were obtained by adding the antisolvent mixture in portions (0-70%) to the THF solution of the polymers. A comparative analysis of these mixed solutions in various ratios using optical absorption, FLand CD-spectroscopy techniques revealed weakening of the π -conjugation along the polymer chain (blue shift of the optical emission) and change of the ellipticity of the polymer (dramatic changes of the CD signals), respectively.

Remarkably, each R- and S-BP polymer micro-sphere upon one- and two-photon (low-power: <2 mW) pumping perform as WGM micro-resonator exhibiting high Q-factor. TPL of R- and S-BP polymer micro-spheres displayed an intense band at ~466 nm (0-0 transition) and a relatively broad low-intensity sideband at ~502 nm (0-1 transition) with a $I_{0-0}^{TPL}/I_{0-1}^{TPL}$ ratio of 1.8. However, at high laser pump powers (>10 mW), we could detect a

dramatic change in the emission spectra intensity with the decrease of the $I_{0-0}^{TPL}/I_{0-1}^{TPL}$ ratio and broadening of the 0-1 peak together with the red-shift (up to 100 nm). Intuitively, these dramatic spectral transformations, directly hint at changes in the polymer electronic coupling as a result of the alteration of the polymer nanoscopic morphologies (packing type, H or J) triggered by the heat produced by the high power laser beam. In line with above-findings, upon increasing the temperature (up to 120 °C) CW laser power (up to 15 mW) the micro-spheres exhibited nearly similar broadening and redshifts of the emission spectra confirming the ultrafast laser-induced heating hypothesis.

Generally, during single micro-sphere TPL or FL spectroscopy experiments, the spot-size or the exposure area of the laser beam is kept smaller than the micro-sphere size (down to a spot size of <1 µm). However, ultrafast laser pulses trigger more *localized* heating (a lower heat-affected region and greater heat) in samples compared to CW laser (higher heated affected region and lower heat) for the same average power. [286,287] Therefore, to find the answer to the question, whether the transformation of polymer chain packing within the micro-sphere is homogeneous or heterogeneous, we have carried out FL lifetime imaging experiments. The latter experiments revealed the heterogeneous distribution of polymer chain packing within the micro-spheres or in other words existence of both *H, H-like*[291] and *J*-type electronic coupling, after exposure to high power CW laser. These light-trapping micro-spheres exhibited a much sought after CD effect in the TPL with different signs at low pump powers. Finally, these results enhance our understanding of laser-triggered ECT in CP polymers, which has ongoing relevance to polymer based nano-photonic structures, and optical meta materials useful from opto-electronics and to quantum information processes.

5.3. Results and Discussion:

5.3.1. Syntheses of monomers and polymers:

The syntheses of **R-** and **S-BP** polymers are outlined in **Scheme 5.1**. Compounds 2-iodo-1,4-dioctyloxybenzene (**M1**), 1,4-diethynyl-2,5-bis(octyloxy)benzene (**M2**) and **R-** and S-6,6'-dibromo-2,2'-diethoxy-1,1'-binaphthyl (**M3**) were synthesized according to reported procedure. [281-283]

Synthesis of 2-iodo-1, 4-dioctyloxybenzene (M1):

1,4-dioctyloxybenzene (1 g, 2.98 mmol, 1 eq.) was taken in a round-bottomed flask containing acetic acid (10 mL) and H_2SO_4 (0.1 mL). To this reaction mixture, a

solution containing KIO₃ (127 mg, 0.6 mmol, 0.2 eq.), I_2 (378 mg, 0.2 eq.), two drops of conc. H_2SO_4 and H_2O (1 mL) were added by drop-wise. The reaction was heated to reflux for 5 h. The progress of the reaction was examined by TLC to check the formation of the mono iodinated product. The reaction was quenched by addition of aqueous $Na_2S_2O_3$ solution to quench excess I_2 . The precipitate formed was collected by filtration and extracted with CHCl₃, dried over Na_2SO_4 and evaporated in vacuo. The obtained crude compound was refined by column chromatography on silica gel with n-hexane/ EtOAc (95:5 v/v) as eluents to get **M1** (0.23 g, 82%) ¹H-NMR (400 MHz, CDCl₃, 298K) δ /ppm: 6.83 (dd,1H), 6.72 (d,1H) 7.34 (d, 1H), 3.93 (t, 2H), 3.87 (t, 2H), 1.84-0.90 (m, 24H), 0.88 (t, 6H). ¹³C-NMR (100 MHz, CDCl₃, 298K) δ /ppm: 153.69, 152.07, 125.32, 115.36, 113.09, 87.00, 70.24, 68.89, 31.99, 29.66, 29.42, 29.38, 26.19, 26.09, 22.76, 14.19.

Synthesis of 1,4-diethynyl-2,5-bis(octyloxy)benzene (M2):

A mixture of 2,5-diiodo-1, 4-dioctyloxybenzene (5 g, 8.5 mmol, 1 eq.), Cul (150 mg, 0.789 mmol, 0.1 eq.) and $Pd(PPh_3)_2Cl_2$ (300 mg, 0.427 mmol, 0.05 eq.) were added to a clean and dry two neck round-bottomed flask and was subjected to a freeze-pump-thaw cycle for three times. To this mixture, dry Et₃N (60 mL) was added under N₂ condition. Further, trimethylsilylacetylene (3.5 mL, 25.5 mmol, 3 eq.) was added dropwise to the reaction mixture. The reaction was continued with stirring for 12 hrs at 70 °C. Afterwards cooling the mixture to rt, the solvent was removed in vacuo and the crude product was refined by chromatography on a short plug of silica gel with n-hexane/ ethyl acetate (95:5 v/v) as eluent to afford golden coloured oil (4.7 g, 83%) that solidified slowly upon storing at rt. Then, the as-obtained product was dissolved in THF (35 mL) and methanol (CH₃OH) (50 mL). Later, an aqueous NaOH (2.5 N, 7.5 mL) was added to the reaction mixture. The deproduction reaction was continued with stirring at rt for 5 h. The solvent was evaporated under reduced pressure. To the crude porduct was added H₂O (20 mL) and extracted the organic layer with DCM (20 mL). The solvent was concentrated under reduced pressure to get the target compound **M2** as yellow solid (3.4 g, 97%). ¹H-NMR (CDCl₃, 400 MHz, 298K) δ /ppm: 6.94 (s, 2H, Ph-H), 3.98 (t, 4H, O-CH₂), 3.33 (s, 2H, ≡C-H), 1.78 (m, 4H), 1.54-1.28 (m, 20H), 0.9 (t, 6H, CH₃). ¹³C-NMR (CDCl₃, 100 MHz, 298K) δ/ppm: 151.3, 117.4, 109.2, 81.9, 78.7, 68.1, 31.9, 29.7, 29.3, 25.9,22.6, 14.1.

Synthesis of *R*- and S-6,6'-dibromo-2,2'-diethoxy-1,1'-binaphthyl (M3):

A suspension of R- and S- 1,1'-binaphthol (2.0 g, 7 mmol) in acetonitrile (20 mL) was stirred under N₂ atmosphere, later K₂CO₃ (3.8 g, 28 mmol) and C₂H₅Br (1.5 mL, 21 mmol) were added to it and the mixture was heated to reflux at 85 °C for 24 h. The solvent was removed in vacuo, and the mixture was diluted with CH₂Cl₂ (30 mL). The organic layer was further washed with H₂O and brine and dried over anhydrous Na₂SO₄. After removal of solvent, the crude product was refined by column chromatography (silica gel, hexane/EtOAc, 95:5) to give 2,2'-diethoxy-1,1'-binaphthalene as a viscous liquid. Yield (1.86 g, 78%). ¹H-NMR (400 MHz, CDCl₃, 298K) δ/ppm: 7.93 (d, 2 H), 7.85 (d, 2 H), 7.42 (d, 2 H), 7.42 (d, 2 H), 7.30 (dd, 2 H), 7.20 (dd, 2 H), 7.13 (br d, 2 H), 4.04 (m, 4 H), 1.05 (t, 6H). ¹³C-NMR (100 MHz, CDCl₃ 298K) δ/ppm: 154.22, 134.08, 129.15, 128.97, 127.68, 125.93, 125.40, 123.31, 120.58, 115.77, 65.10, 14.88, 2,2'-diethoxy-1,1'-binaphthalene (2 g, 5.8 mmol) was dissolved in CH₂Cl₂ (50 mL) and cooled to 0 °C. Br₂ was added to it in increments, starting with 1.8 eq. until the reaction went to completion. The reaction mixture was then extracted with 10% NaHSO₃ and brine. After drying over Na₂SO₄ and filtering, the solvent was removed to yield the product R- and S-6,6'-dibromo-2,2'-diethoxy-1,1'-binaphthalene in the form of oil (2.14 g, 74%). ¹H-NMR (400 MHz, CDCl₃) δ/ppm: 8.00 (d, 2H), 7.84 (d, 2H), 7.42 (d, 2H), 7.26 (dd, 2H), 6.95 (d, 2H), 4.03 (m, 4H), 1.06 (t, 6H), ¹³C-NMR (100 MHz, CDCl₃, 298K) δ/ppm: 154.42, 132.41, 130.11, 129.68, 129.34, 128.32, 126.98, 119.93, 117.16, 116.35, 64.96, 14.89.

Syntheses of *R*- and *S*-BP polymers:

R- and *S*-M3 (178 mg, 0.35 mmol), M2 (136 mg, 0.356 mmol), Pd(PPh₃)₄ (41 mg, 0.03 mmol) and CuI (7 mg, 0.03 mmol) were added to a mixture of solvents of THF (8 mL) and Et₃N (4 mL) under N₂ atmosphere. The mixture was stirred at 70 °C under N₂. End group molecule, M1 (32 mg, 0.03 mmol, 0.2 eq.) was added to the reaction mixture after 15 min of starting the reaction. After 72 h, the mixture was brought to rt, and the solvent was evaporated. Then the residue was washed with CH₃OH to take away any small molecular impurities. The product was dried under vacuum overnight. The yields of *R*- and *S*-BP are 0.066 g and 0.064 g, respectively. The product was submitted to Soxhlet extraction (acetonitrile, CHCl₃ and lastly with THF) to discard low molecular weight fraction and isolate soluble high molecular weight polymer fractions. *S*-BP: ¹H-NMR (400 MHz, CDCl₃ 298K) δ/ppm: 8.02 (s, 20H), 7.82–7.85 (d, 22H), 7.72 (s, 9H), 7.64-7.69 (m, 52H), 7.53-7.56 (m, 30H), 7.44-7.48 (m, 58H), 7.40-7.42 (m, 26H), 7.33-7.35 (m, 3H), 7.31-7.32 (m, 6H), 6.90-6.95 (m, 39H), 6.81-6.83 (d, 2H), 6.70-6.73 (d, 2H), 4.02-4.04 (m, 70H), 3.95-3.97 (m, 32H),

3.91-3.92 (m,8H), 3.85-3.88 (m, 10H), 1.04-1.09 (m, 113H), 0.86-0.88 (m, 174H). *R***-BP**: ¹H-NMR (400 MHz, CDCl₃, 298K) δ/ppm: 8.02 (s, 14H), 7.83–7.85 (d, 14H), 7.72 (s, 3H), 7.65-7.68 (m, 23H), 7.53-7.55 (m, 12H), 7.45-7.48 (m, 25H), 7.41-7.42 (m, 16H), 7.31-7.33 (m, 3H), .24-7.2 6(m, 3H),6.94-6.95 (m, 18H), 6.81-6.83 (d, 2H), 6.71-6.73 (d, 2H), 4.04-4.06

Scheme 5.1: Syntheses of *R*- and *S*-2,2'-diethoxy-1,1'-binaphthyl-*co*-1,4-diethynyl-2,5-dioctyloxy benzene (*R*- and *S*-BP).

(m, 36H), 3.95-3.97 (m, 6H), 3.91-3.92 (m,6H), 3.85-3.88 (m, 6H), 1.04-1.07 (m, 77H), 0.86-0.88 (m, 151 H). $\overline{M_n}$ [by ¹H-NMR] \approx 6.3 KDa and 7.8 KDa for **R-** and **S-BP** polymers, respectively. ¹³C-NMR (100 MHz, CDCl₃, 298K) δ /ppm: 154.54, 132.52, 132.22, 132.12, 132.04, 131.90, 130.34, 130.23, 129.85, 129.77, 129.65, 129.45, 129.29, 128.75, 128.52, 128.42, 127.54, 127.08, 125.37, 120.07, 117.27, 116.48, 115.45, 113.16, 70.22, 69.78, 68.87, 65.07, 37.08, 32.73, 31.90, 31.78, 30.31, 30.01, 29.67, 29.63, 29.33, 29.30, 29.26, 29.21, 29.05, 27.06, 26.07, 26.04, and 25.97.

5.3.2. NMR spectroscopy analysis of *R*- and S-BP polymers:

The *R*- and *S*-2,2'-diethoxy-1,1'-binaphthyl-*co*-1,4-diethynyl-2,5-dioctyloxy benzene copolymers end-capped with **M1** were synthesized by copolymerizing diethynyl benzene linker (**M2**) and chiral monomers (*R*- and *S*-M3) via a palladium-catalyzed Sonogashira cross-coupling reaction (Scheme 5.1).^[282-284] The obtained polymers were washed via

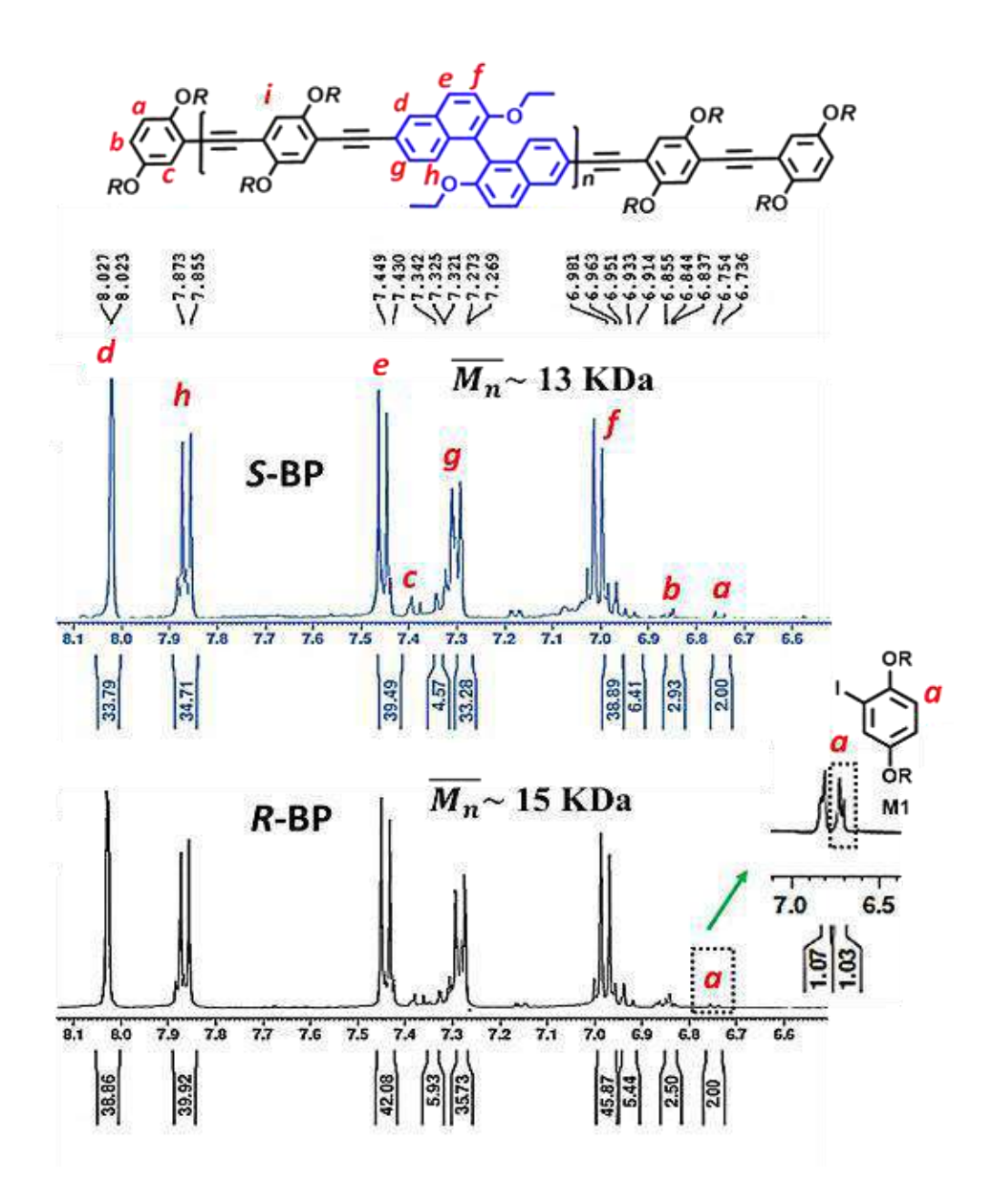


Figure 5.1: ¹H-NMR (DMSO-*d*₆) spectra of *R*- and *S*-BP polymers.

Soxhlet extraction to remove low molecular weight oligomers with solvents like hexane, MeOH, ACN, CHCl₃ and finally with THF. The polymers (yield 48-52%) were soluble in common organic solvents (THF, DCM and toluene) due to the presence of flexible noctyloxy group substituent in the polymer side chain. The THF insoluble high molecular

weight *R*- and *S*-BP polymer fractions (yield 19-23%) were partially soluble in DMSO. The remaining very high molecular weight *R*- and *S*-BP polymers (yield 16-18%) were insoluble in any solvents. In the ¹H-NMR spectra (in DMSO-*d*₆) of *R*-and *S*-BP, the disappearance of a peak at 3.33 ppm, which corresponds to the ethynyl proton (-C≡C-H) hint at the formation of polymers. The aromatic proton (see label "*a*") of the end-capping unit appeared as doublet around 6.72−6.75 ppm (Fig. 5.1). In the ¹³C-NMR spectra of *R*-and *S*-BP, the acetylenic carbon peaks appeared in the deshielded regions at 87.9 and 87.0 ppm (Fig. 5.2). The chemical shifts values of these deshielded peaks are different from the polymer obtained from the homocoupling of M2 (as the buta-1,3-diyne carbon peaks of the homocoupled product appear at 89.2 and 79 ppm), [290] which confirms the formation of *R*-and *S*-BP polymers.

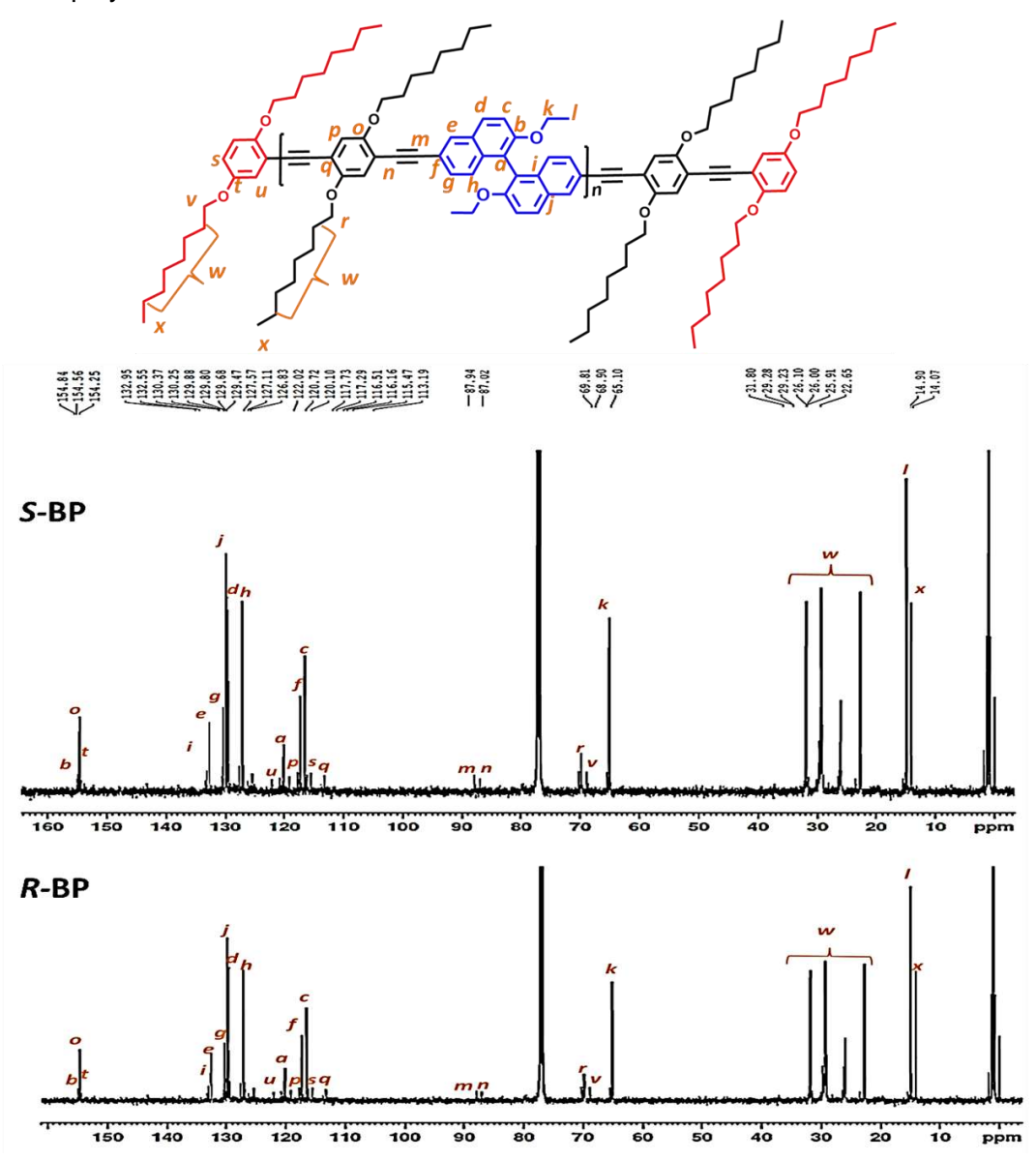


Figure 5.2: ¹³C-NMR (CDCl₃) spectra of *R*- and S-BP polymers.

5.3.3. Number average molecular weight $(\overline{M_n})$ of R- and S-BP polymers:

With the assumption that the majority of the polymer chain ends have been end-capped, the $\overline{M_n}$ was estimated from the ¹H-NMR spectra (**Fig. 5.1**). For **S-BP**, the relative signal intensities of binol proton (marked as "d") to protons of 1,4-dioctyloxybenzene of end group (marked as "a") was 34:2. This ratio suggested degrees of polymerization ($\overline{X_n}$) of 17 corresponding to $\overline{M_n}$ of about 13 kDa. A similar analysis revealed $\overline{X_n}$ value of about 19.5 for **R-BP** with $\overline{M_n}$ of ~15 kDa. The above results show that the molecular weight of the insoluble polymers obtained during the Soxhlet extraction is much higher than the DMSO soluble ones. As THF is convenient for solution processability polymers, we have used the THF soluble polymer fractions [**R-BP**: $\overline{M_n}$ ~6.3 kDa and **S-BP**: $\overline{M_n}$ ~7.8 kDa] for further studies).

5.3.4. FTIR spectroscopy analysis of R- and S-BP polymers:

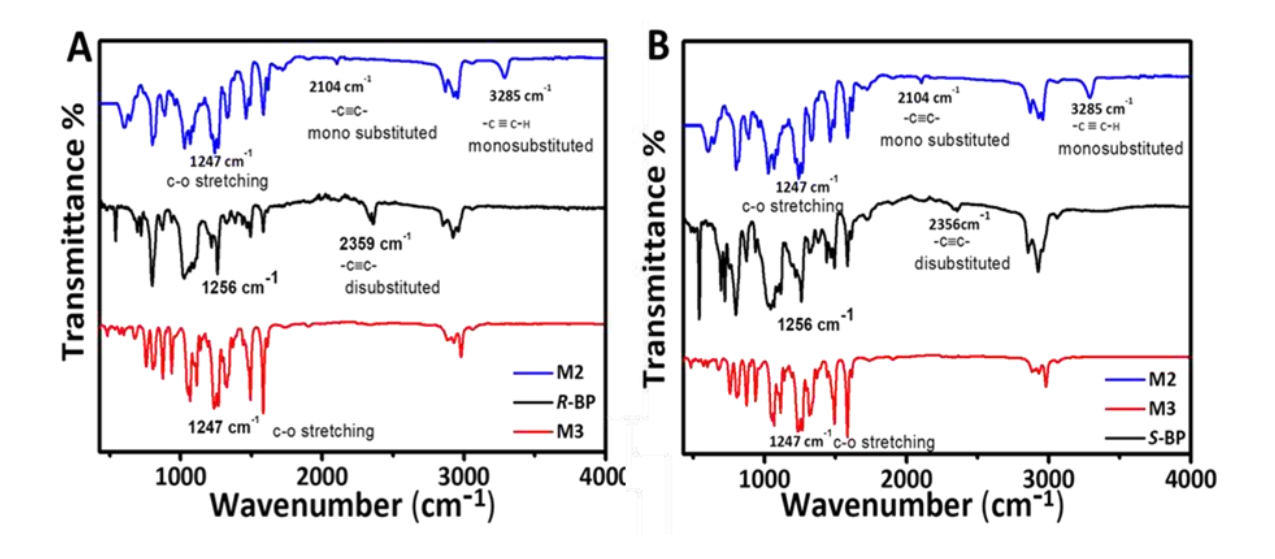


Figure 5.3: FTIR spectra of A) M2, R-BP and M3 and B) M2, S-BP and M3.

The FTIR spectra of R- and S-BP displayed shifts of the C \equiv C stretching vibration ($\bar{\vartheta}_{C\equiv C}$) to 2359 cm⁻¹ and 2356 cm⁻¹, respectively in comparison to C \equiv C stretching vibration ($\bar{\vartheta}_{C\equiv C}$) \approx 2104 cm⁻¹ of M2 proving the formation of enantiomeric polymers (Fig. 5.3 A and B).

5.3.5. Differential scanning calorimetry (DSC) of R- and S-BP polymers:

The glass transition temperature (T_g) (the range of temperature in which glassy state transforms to to viscous rubbery state) and melting temperature (T_m)

(endothermic peak) of $\it R$ - and $\it S$ -BP were determined by DSC in the temperature range of 25 to 230 °C under N₂ atmosphere (heating rate of 10 °C/min) (Fig. 5.4). The $\it T_g$ values of $\it R$ - and $\it S$ -BP were found to be in the range of 85-90 °C specifying the amorphous nature of enantiomeric polymers. Moreover, $\it R$ - and $\it S$ -BP exhibited $\it T_m$ at 129 and 128 °C, respectively (Fig. 5.4). From the above results, it can be anticipated that the chiral polymers are semi-crystalline in nature.

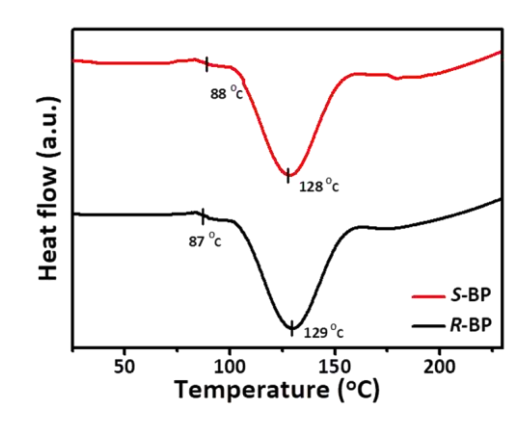


Figure 5.4: DSC curves of chiral polymers **R**-and **S-BP**.

5.3.6. Optical properties of *R*- and S-BP polymers:

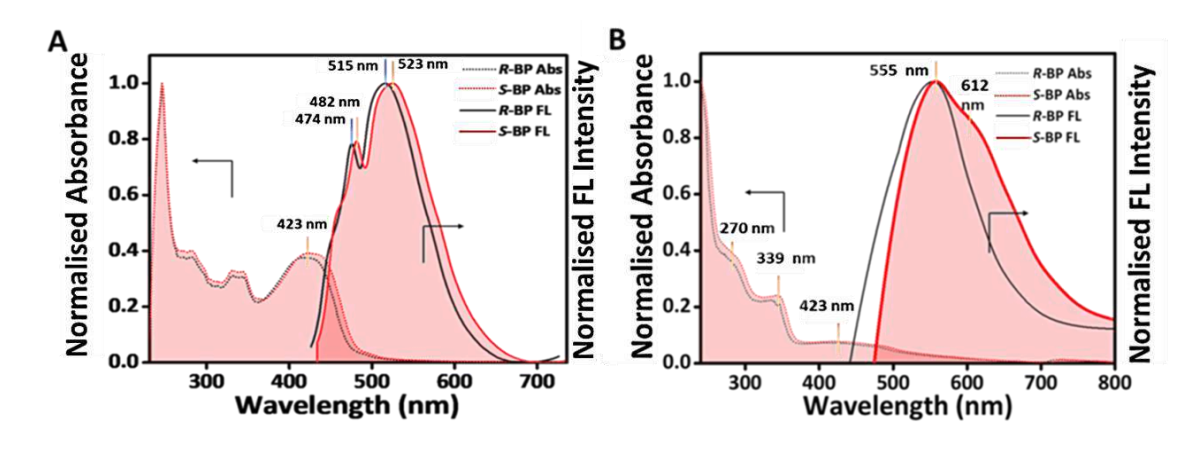


Figure 5.5: UV-Vis absorbance and FL spectra of chiral polymers **R-** and **S-BP** in A) THF and B) thin-film state, respectively.

The photophysical properties of R- and S-BP are presented in Figure 5.5. The UV spectra of R- and S-BP in THF solution ($c \approx 1.0 \times 10^{-5}$ mol/L) displayed multiple absorption maxima at 248/278/337 nm which can be allocated to the π - π * transition of the M3 unit (Fig. 5.5 A). A new low energy absorption band situated at ~423 nm exhibited by both R- and S-BP (which is not present in case of binol monomers (R- and S-M3)) directs the conjugated structure connecting binol units and diethynyl benzene unit. The intensity variation and redshifts shown by this ~423 nm band in solvents of low dielectric constants point towards its CT nature (Fig. 5.7 A and B). The solution state FL bands of R- and S-BP appeared very similar with peak maxima at 474/512 and 482/523 nm, respectively (Fig. 5.5 A). Here, the red-

shifted (~8 nm) emission band showed by R-BP polymer points to better π -conjugation along the longer polymer chains. The solid-state absorption spectrum of R- and S-BP showed numerous absorption maxima for both polymers at ~270/339/423 nm. Contrary, to solution state, the solid state FL bands of R- and S-BP looked broad with maxima at ~555 nm with a shoulder at 612 nm (Fig. 5.5 B). The electronic CD spectra are shown in Fig. 5.6. displayed mirror image CD bands in THF solution owing to different

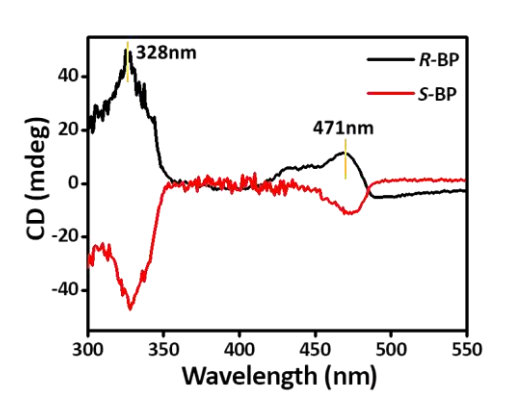


Figure 5.6: Solution-state (in THF) CD spectra of *R*- and *S*-BP polymers.

handedness of **R-** and **S-BP**. The **R-** and **S-BP** exhibited bands of opposite signs at ~328 and 469 nm demonstrating their opposite chiral handedness.

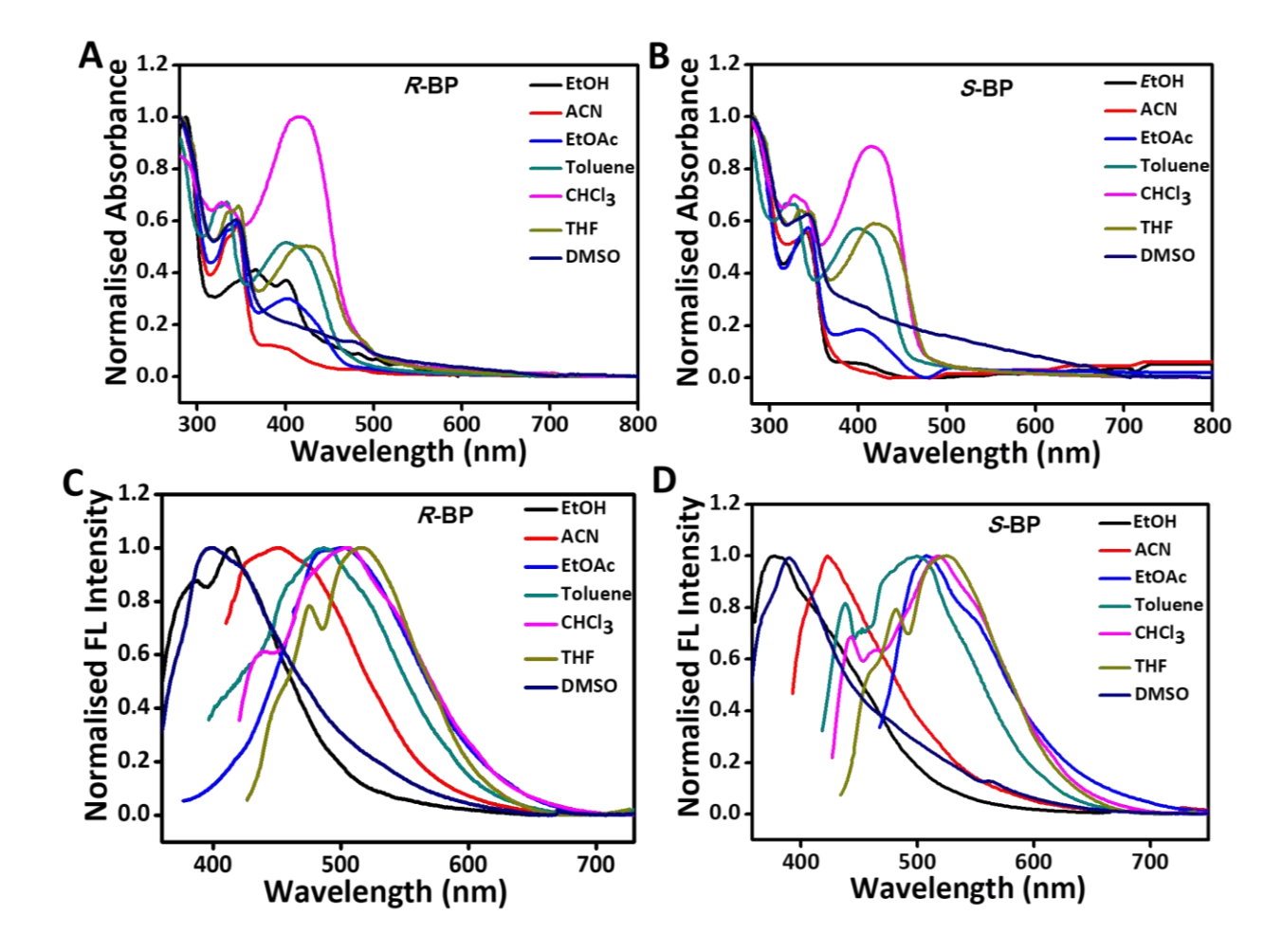
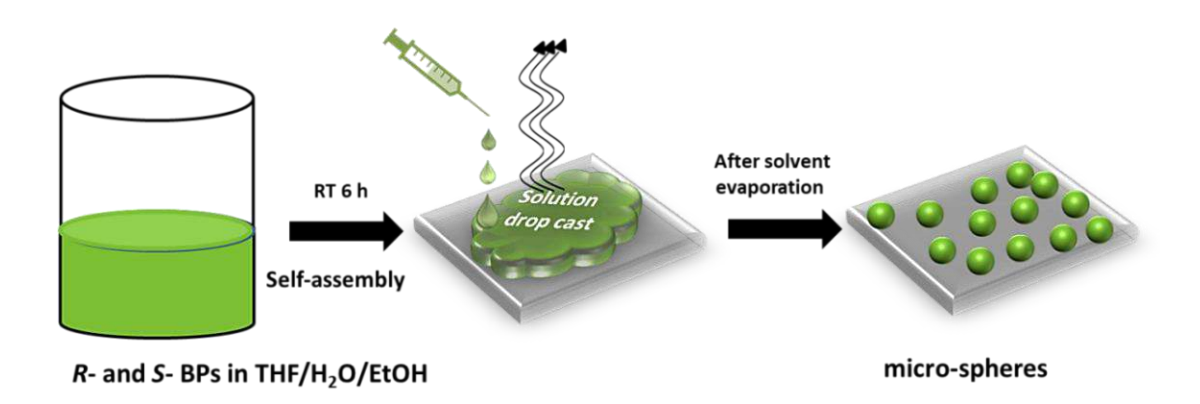


Figure 5.7: A and B) UV-Vis absorbance spectra of **R-** and **S-BP** polymers in various solvents. C and D) FL spectra of **R-** and **S-BP** polymers in various solvents.

5.3.7. Self-assembly of *R*- and S-BP polymers:

Hydrophobic **R-** and **S-BP** were transformed into micro-structures through self-assembly method. In short, in a vial 1 mg of hydrophobic **R-** and **S-BP** were dissolved in 1 mL of THF, and the obtained solution was transferred gently alongside the walls of a vial consisting of a mixture of 2 mL of H₂O/EtOH (7:1). The obtained turbid solution was left uninterrupted for 6 hrs to sustain the development of the micro-particles. Then, 2 drops of the solution were drop casted on a coverslip, followed by slow evaporation of solvent under ambient conditions to acquire several micro-spheres wrapping a huge surface area of the coverslip (**Scheme 5.2**).



Scheme 5.2: Self-assembly of *R*- and *S*- BP polymers into micro-spheres.

5.3.8. Microscopic studies of *R*- and S-BP:

R- and **S-BP** were self-assembled into micro-spherical particles in THF/H₂O/EtOH mixture (**Scheme 5.2**). It is assumed that the generation of microspheres through aggregation is driven by the poor solvent i.e; water.^[72,276] Investigation of the sample under confocal microscopy displayed the formation of circularly-shaped micro-particles (**Fig. 5.8 A**). Moreover, FESEM analysis established the spherical geometry of the micro-particles with comparatively narrow size-distribution with a diameter ~3-8 μ m (**Fig. 5.8 E**). TEM studies showed dark contrast for the micro-spheres directing tight packing of the polymer chains within the micro-structures (**Fig. 5.8 B**). SAED pattern of a single micro-sphere showed no noticeable diffraction spots from micro-particles (**Fig. 5.8 C**). AFM examination of a selected micro-sphere confirmed the smooth surface of the micro-sphere, which is important to minimize the light scattering loss and increase the *Q*-factor of optical micro-resonators (**Fig. 5.8 D**).

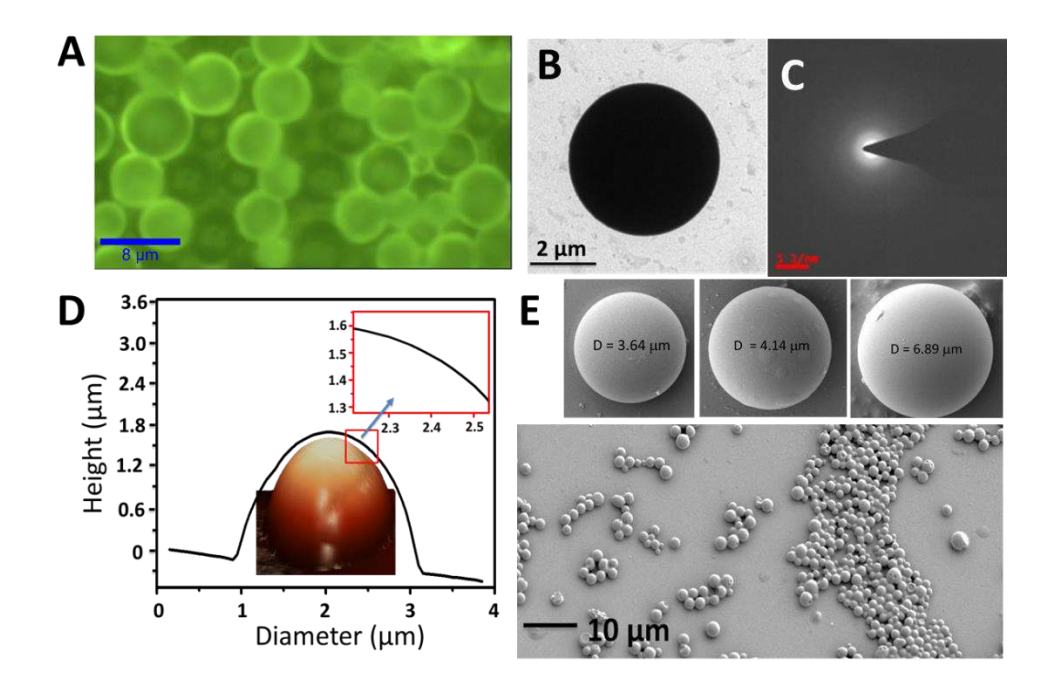


Figure 5.8: Confocal optical microscope image of micro-spheres. B and C) TEM image of a single chiral polymer micro-sphere and its SAED image, respectively. D) AFM topography image of a micro-sphere with its dimension profile. The right inset shows the surface smoothness and E) FESEM images of micro-spheres. The top three figures show a close-up view of a single micro-sphere of varying diameters.

5.3.9. Aggregation studies of *R*- and S-BP polymers:

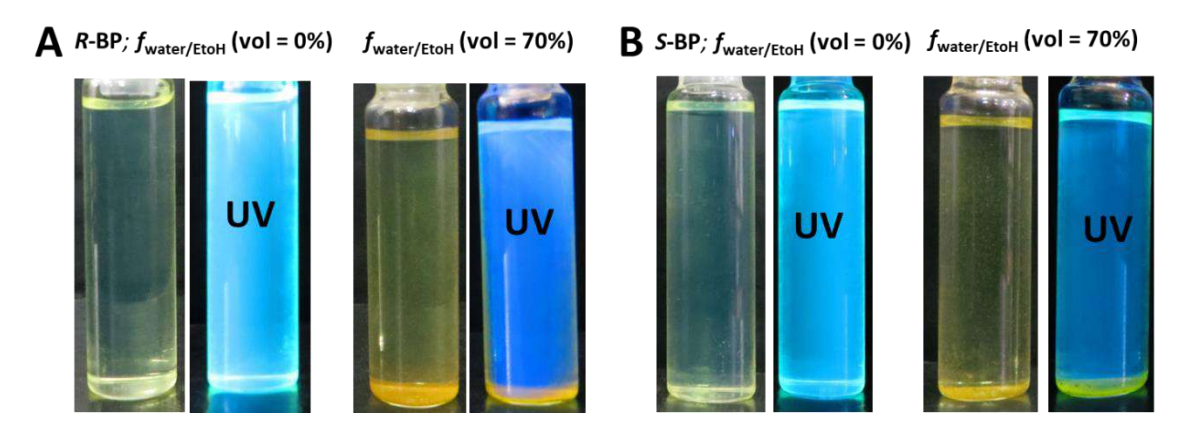


Figure 5.9: A and B) Photographs of R- and **S-BP** polymer solutions with 0% and 70% $H_2O+EtOH$.

To understand the influence of polymer conformation/packing in self-assembled micro-spheres, the evolution of absorption, emission, and CD spectroscopic signatures of THF solution of R- and S-BP polymers with different volume fractions ($f_{\text{water:EtOH (7:1)}} = 0-70\%$) of the antisolvent mixture (Fig. 5.9). Here, the gradual change of the composition of a mixed solvent decreases the solubility of the polymer in a controlled manner to induce inter and

intra chain interactions and provide the snapshots of molecular-level structural changes during polymer self-assembly (**Fig. 5.10**). Upon increasing the fraction of the non-solvent mixture in the THF solution of polymers, the optical absorption (**Fig. 5.10 A, B**) and $I_{0-0}^{FL}/I_{0-1}^{FL}$ ratio (**Fig. 5.19 B**) did not reveal any significant changes. However, the FL spectra of both polymers showed slight blue shifts along with FL quenching. To correlate how the conformational changes of 1,1'-binaphthyl affect polymer backbone and subsequent electronic coupling, we have also recorded the CD spectra of the same solutions used for the absorption and emission measurements (**Fig. 5.11 A, B**). In CD spectroscopy the

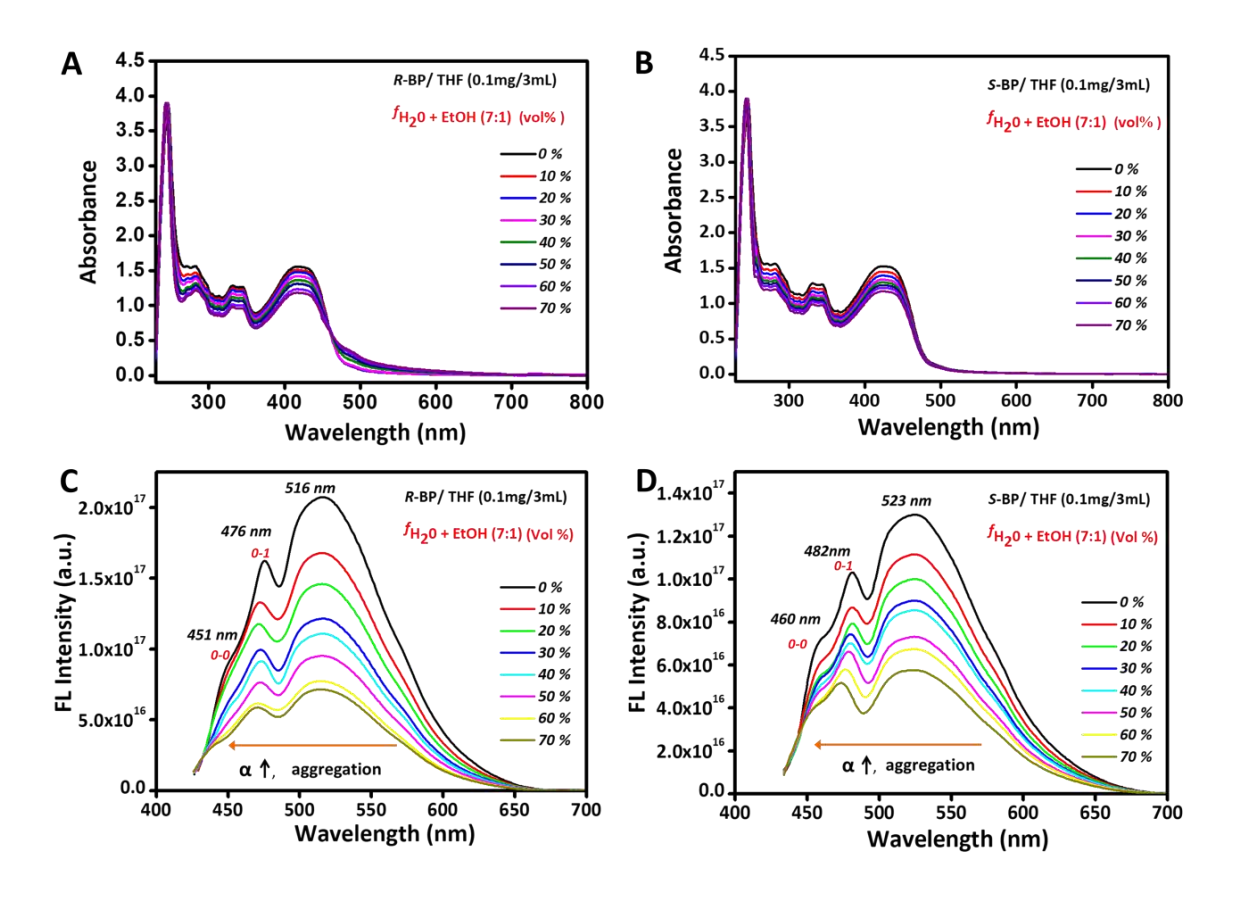


Figure 5.10: A and B) UV-Vis absorbance spectra of **R-** and **S-BP** polymers in THF with different vol% ratios of water/EtOH. C and D) FL spectra of **R-** and **S-BP** polymers in THF with different vol% of water/EtOH mixture.

magnitude of CD peaks and their shift provides structural information of the polymer chains during their self-assembly. Both *R*- and *S-BP* in THF exhibited well pronounced positive and negative CD peaks at 470 and 473 nm, respectively Fig. 5.11 A, B). Upon addition of water, the intensity of the ~470 nm peak decreased, and a new peak at ~319/326 nm emerged from *R*- and *S-BP* polymer solution. Zhang et al. have computationally demonstrated that for the structurally analogous conjugated polymer, [285] the torsion angle

(Θ) of 1,1'-binaphthyl increases with the water content of the solvent mixture due to its transformation from *cisoid* to a *transoid* conformation (**Fig. 5.12 A, B**).^[286]

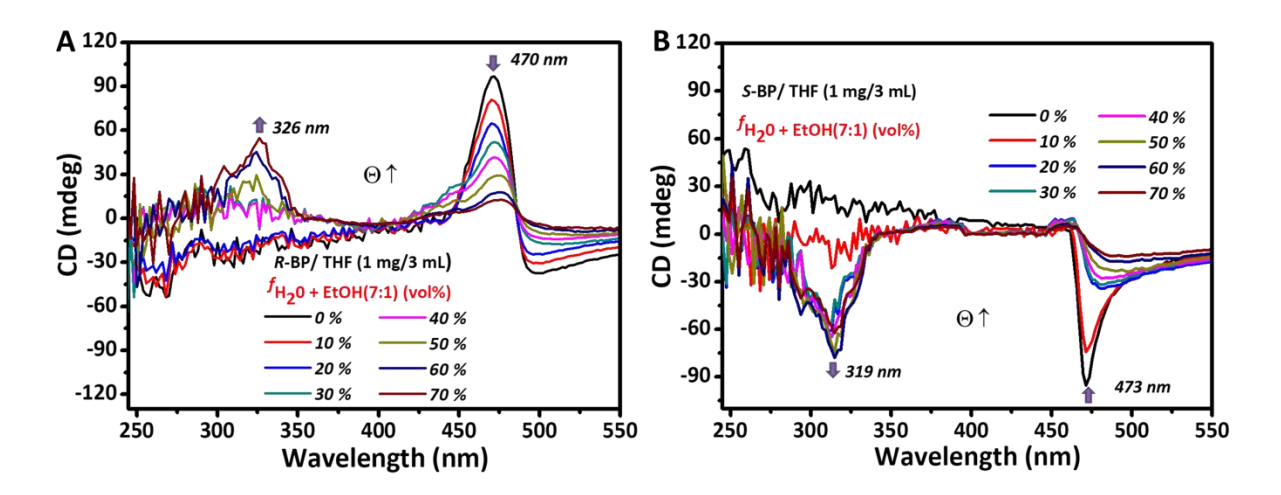


Figure 5.11: A and B) CD spectra of **R**- and **S-BP** polymers in THF with different vol% of water/EtOH mixture.

It is clear from the CD data that the reason for the FL blue shifts presented by Rand S-BP polymers is the increase of the Θ -value, which weakens the π -conjugation
through the 1,1'-binaphthyl units. Therefore, in the case of R- and S-BP polymers a *cisoid*to a *transoid* conformation change of the 1,1'-binaphthyl is expected during the selfassembly process (Fig. 5.12 A, B). It is interesting to note here that the absorption spectra
of both R- and S-BP polymers (see Fig. 5.10 A, B) showed nearly no peak shifts in
response to the Θ value change exhibited by CD spectra. Nevertheless, it is clear from the
CD data that the reason for the FL blue shift presented by R- and S-BP polymers is the
increase of the Θ values, which causes weakening of the conjugation through 1,1'-bond
connecting the biphenyl units (Fig. 5.12 A, B).



Figure 5.12: A) Repeating unit of **BP** polymer. B) From *cisoid* to the *transoid* conversion of the 1,1'-bond of binol unit of the polymer.

5.3.10. Single-particle microscopic studies of *R*- and S-BP micro-spheres:

Single-particle micro-FL experiments were carried out on a confocal microscopy (back scattering mode) was used to examine the light-trapping ability of micro-spheres. Upon electronic excitation of an edge of a single micro-sphere with

CW 488 nm (Ar⁺) laser (power: 5 mW) exhibited a broad green emission spectrum (from 500-750 nm) with multiple pairs of sharp peaks identified as WGMs (Fig. 5.13 A and B). These pairs of peaks equivalent to TE and TM modes. One can conclude from the FL spectrum that the wavelength-dependent periodic intensity variation of the peaks is a function of micro-resonator diameter. To investigate the size-dependency on the number of optical modes, and FSR values, micro-particels of different sizes were studied. The FSR values of three representative S-BP micro-particles of different diameters are presented in the Figure 5.13 B. In line with the relation: FSR ~1/D (see equation 1.7 in Chapter-1) the three representative micro-spheres of diameters ~7.6, 6.2 and 3.9 µm (diameters calculated from LCRM images) displayed reduction in the number of modes from 38 to 18 and increase in FSR values from 10.1, 14.1 to 20.4 nm, respectively (Fig. 5.13 B).

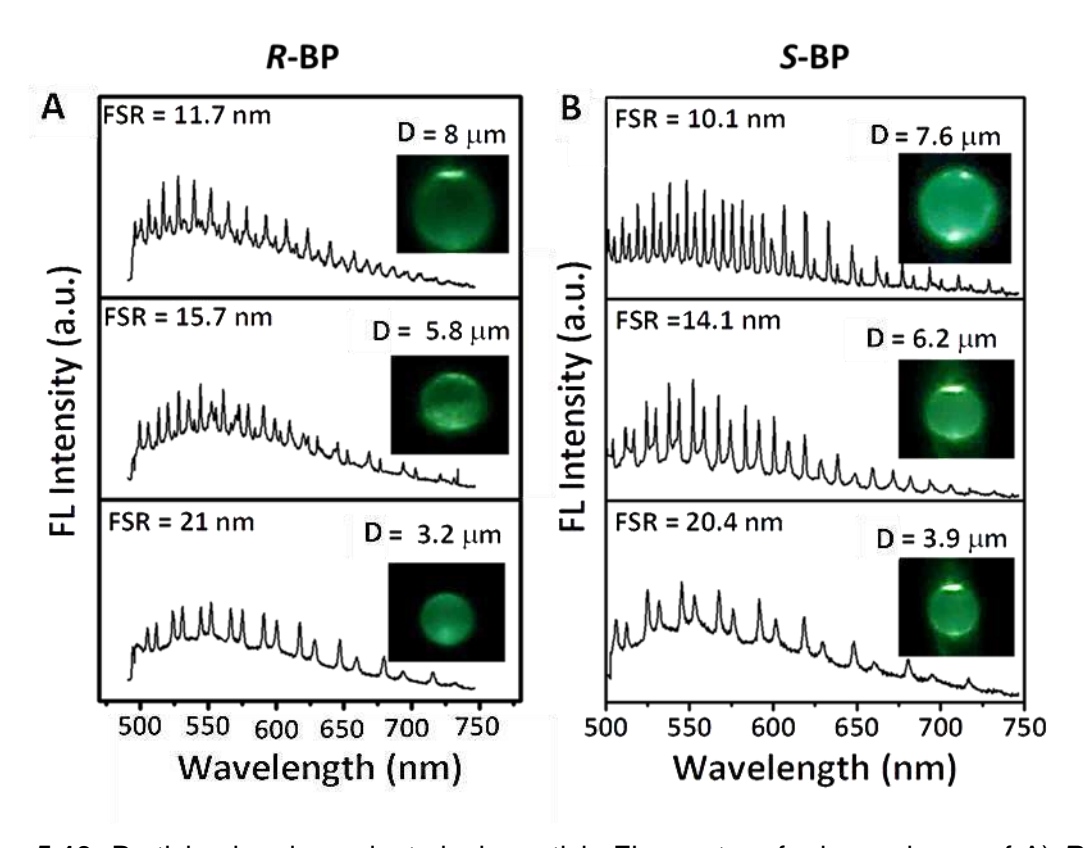


Figure 5.13: Particle size-dependent single-particle FL spectra of micro-spheres of A) *R*-BP and B) **S-BP** exhibiting WGM resonances. The insets show the FL images of micro-resonator during excitation with CW laser (488 nm, Ar⁺).

Further, fitting a plot of FSR Versus inverse of micro-resonator size presented approximately a linear relationship within the limits of experimental errors as per the equation 1.7 given in **Chapter-1** (**Fig. 5.14 A**). These experimental results found that the spherical micro-particle acts as a WGM resonator by reflecting the FL photons

within the boundary multiple times via TIR. Likewise, *R*-BP micro-spheres displayed particle size-dependent resonance behaviour (Fig. 5.13 A and 5.14 A). The *Q*-factor of *S*- and *R*-BP micro-spheres increased linearly with the diameter to the value of ~680 and 610, respectively (Fig. 5.14 B).

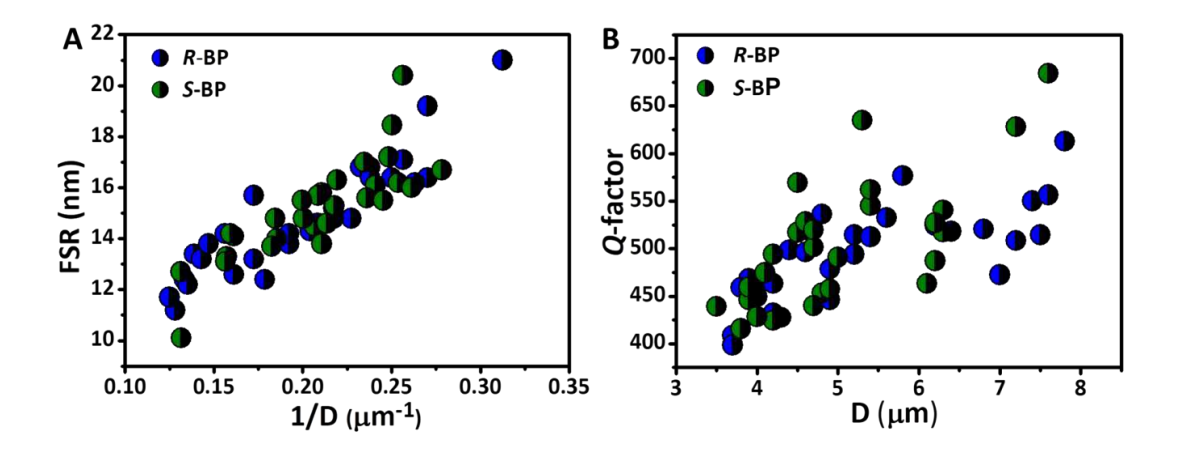


Figure 5.14: A) A plot of FSR versus 1/D for **R-** and **S-BP** micro-spheres. B) A plot of Q-factor versus particle D for **R-** and **S-BP** micro-spheres.

5.3.11. NLO microscopy studies of *R*- and S-BP micro-spheres:

As these R- and S-BP polymers in solution state exhibited sizable β -values, we have explored the NLO properties of micro-resonators as well. Open aperture Z-

experiment (Fundamental scan wavelength: 800 nm) was performed to evaluate the β of **R-** and **S-BP**. The estimated β -values of R- and S-BP are 0.124×10^{-11} and 0.155×10^{-11} cm/W, respectively, which confirm their NLO properties (Fig. **5.15**). microscopy studies were carried out by exciting a single micro-resonator using a Ti:Sapphire femtosecond pulse laser (wavelength 740 nm, pulse width 60 fs, repetition rate 80 MHz). Interestingly,

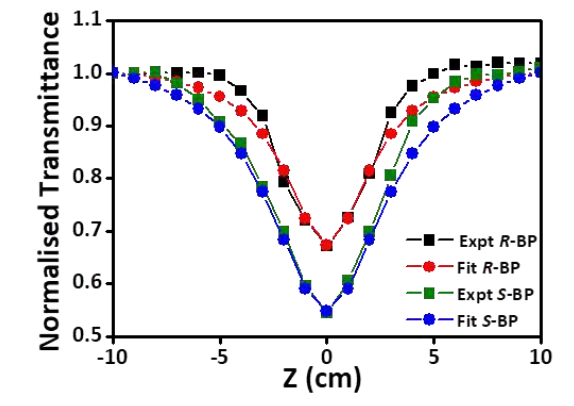


Figure 5.15: Open aperture Z-scan data of **R-** and **S-BP** polymers.

at low power (4 mW), both R- and S-BP micro-resonators (D ~13 μ m and 9 μ m, respectively) revealed WGMs signatures in TPL spectra (Fig. 5.16 A, B).

The TPL spectra of **R**- and **S-BP** micro-resonator comprised of a high-intensity 466 nm peak and a relatively broad low-intensity ~502 nm peak. As expected, here, the increase of the pump power of the fundamental excitation beam increased the intensity of both peaks. Interestingly, at high pump powers, an unexpected result was obtained when we analyzed the TPL spectra. The profile of the TPL spectra changed drastically with selective amplification of ~502 nm (0-1) peak (with a red-shift of about 100 nm) relative to high energy (0-0) peak and displayed several vibronic structures (**Fig. 5.17 A, B**).

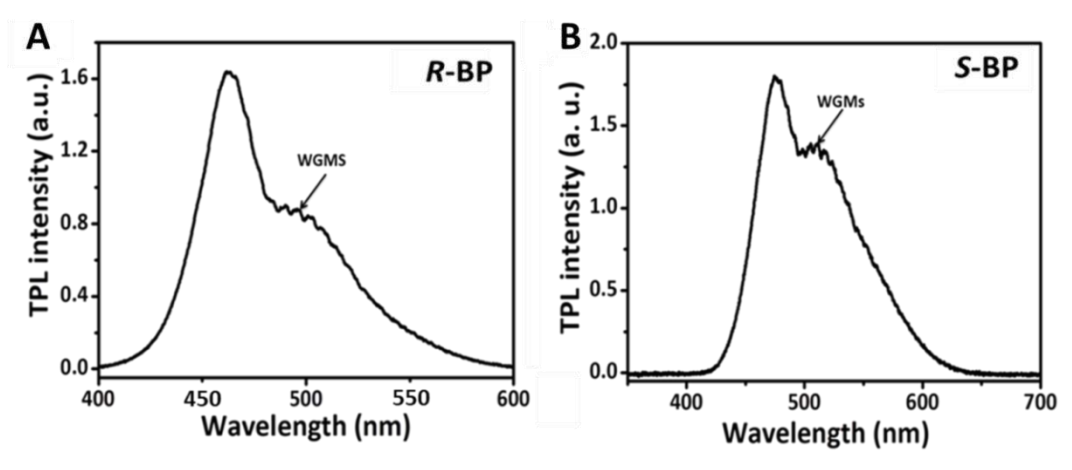


Figure 5.16: A and B) TPL spectra revealing WGMs excitation for single **R-BP** and **S-BP** microresonators.

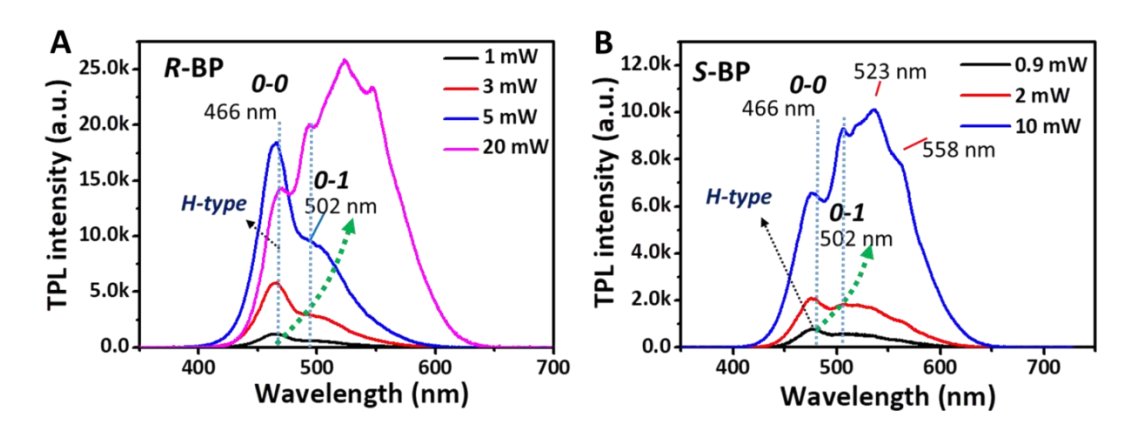


Figure 5.17: A and B) Shape of the TPL spectra **R-BP** and **S-BP** micro-resonators as a function of pump power.

5.3.11.1. Polymer chain packing dependent electronic coupling of *R*- and *S*-BP micro-spheres:

In general, the electronic coupling in conjugated polymer is sensitive to its conformation and chain packing. The amplification of 0-1 peak compared to 0-0 peak

in the TPL spectra at high laser power indicates a dramatic change of the polymer packing within the micro-resonators. Earlier reports have established that ultrafast laser pulses trigger more *localized* heating (a lower heat-affected region) in samples compared to CW laser. [288,289] Further, the short-pulse laser increases the sample temperature greater than the CW laser of the same average power. [288] It is possible that the ultrafast laser triggered a *local* temperature increase within the micro-resonators, prompting a transformation of polymer packing. In order to validate the "*laser-induced heating*" hypothesis, we have heated the coverslip (20 to 160 °C) containing the *R*- and *S*-BP polymer micro-resonators and collected the temperature-dependent FL spectra by exciting them with a continuous wave CW laser (405 nm; 5 mW power) (Fig. 5.18 A, B). The spectra recorded at high-temperatures (40-160 °C)

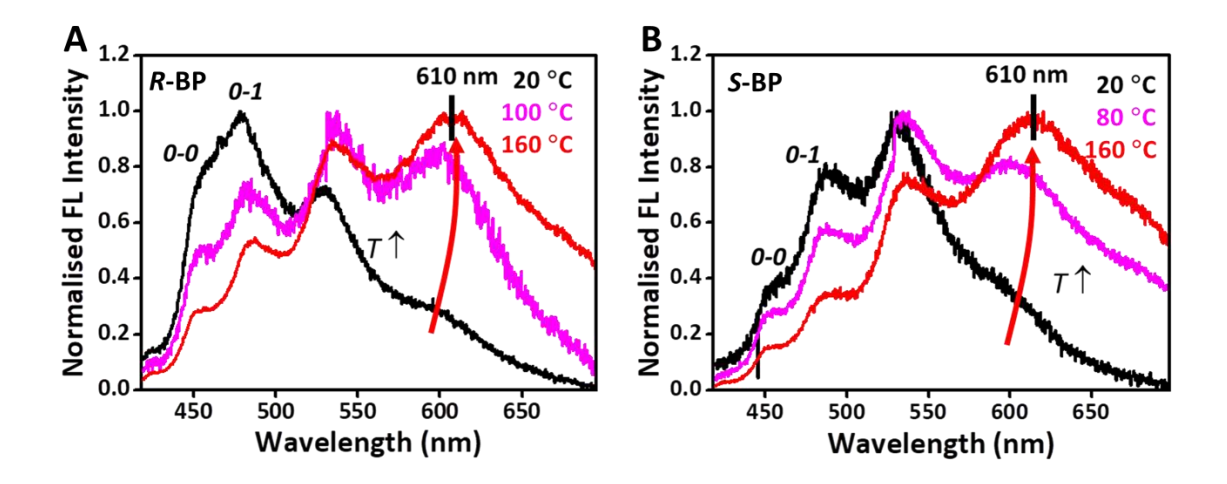


Figure 5.18: A and B) Temperature-dependent one-photon pumped FL spectra of *R*- and *S*-BP micro-resonators.

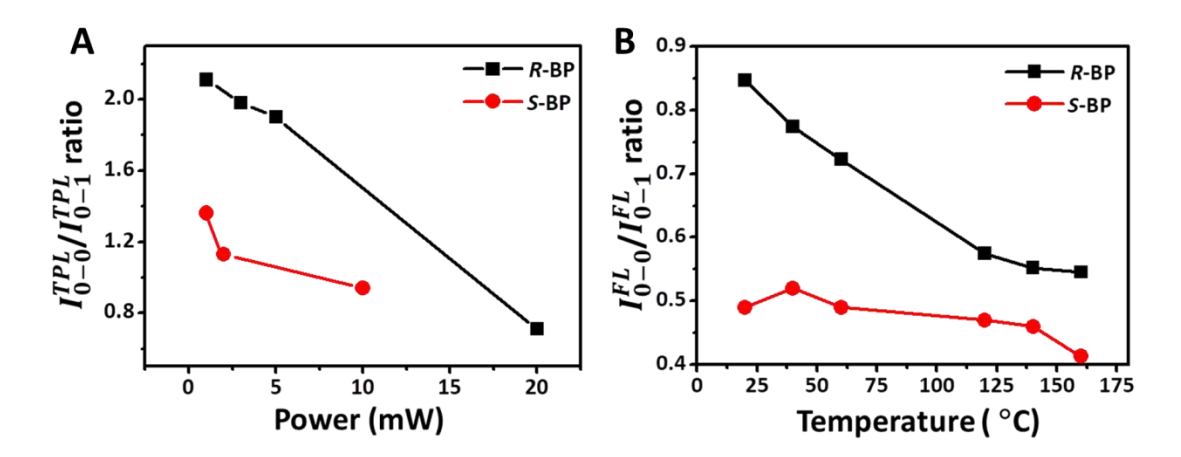


Figure 5.19: The ratio 0-0/0-1 optical emission peak intensities as a function of A) fs laser power and B) thermal heating for *R*- and *S*-BP micro-spheres.

exhibited an intensification of the 610 nm peak accompanied by red-shift with rising temperature in comparison to low-temperature (20 °C) spectrum. Overall, the above experiments confirm the premise that heat-induced spectral changes in polymer microresonators occur due to the absorption of ultra-fast laser light. However, the FL spectra of thermally heated samples cannot be entirely matched with TPL spectra as the latter samples were heated by fs laser and arises due to TPA Interestingly, at high pump powers, an unexpected result was obtained when we analyzed the TPL spectra.

In order to explain the temperature-dependent optical spectral shifts, it is essential to understand the polymer chain packing-dependent electronic coupling using Spano's model. However, this model is directly applicable to polymer systems with a homogeneous distribution of polymer chain packing type (either H or J), not for heterogeneous type. Notably, during the TPL experiments using high power ultrafast laser, the centre of the micro-particle was subjected to light irradiation. Therefore the question that remains unanswered is whether the polymer packing distribution within the micro-sphere is homogeneous or heterogeneous. In the case of latter distribution, correlating pump-power-dependent TPL spectra with polymer packing type is not straight forward. However, it is expected that the micro-spheres with heterogeneous polymer chain packing should reveal aggregation-type dependent τ_{FL} values. Thus, we have probed τ_{FL} down to a single microsphere level by FLIM technique using a TCSPC. For a fair comparison of results, we have used the *same* micro-particle before and after a high power laser (CW 405 nm) irradiation or thermal heating (Fig. 5.20).

We have investigated R- and S-BP micro-spheres before treating them with high power CW laser (15 mW), which exhibited a single exponential FL decay with a nearly uniformly distributed average τ_{FL} values of 0.54-0.61 ns (Fig. 5.20 A, D). However, the same micro-spheres after laser treatment revealed dramatic changes and heterogeneous distribution in the τ_{FL} values, a shorter radiation time at the center (core) of the particle (pump area) and moderate radiation around the core (<1 ns) and a much longer radiation time (up to ~10 ns) exhibited by their circular periphery (Fig. 5.20 B, E). Here, the regions with higher and lower τ_{FL} values point to H (inter-chain electronic coupling) and J (intrachain electronic coupling) type polymer chain packing, respectively. [278,280,288] The regions with intermediate τ_{FL} possibly arise due to polymer chain packing much H-like but with disordered octyl side chains. The increase of τ_{FL} in the micro-spheres from the core to periphery validates the heterogeneous transformation of polymer chain packing at different

regions due to laser-induced heating. The τ_{FL} also indicates that the polymer chains are tightly packed at the periphery of the micro-spheres compared to its core.

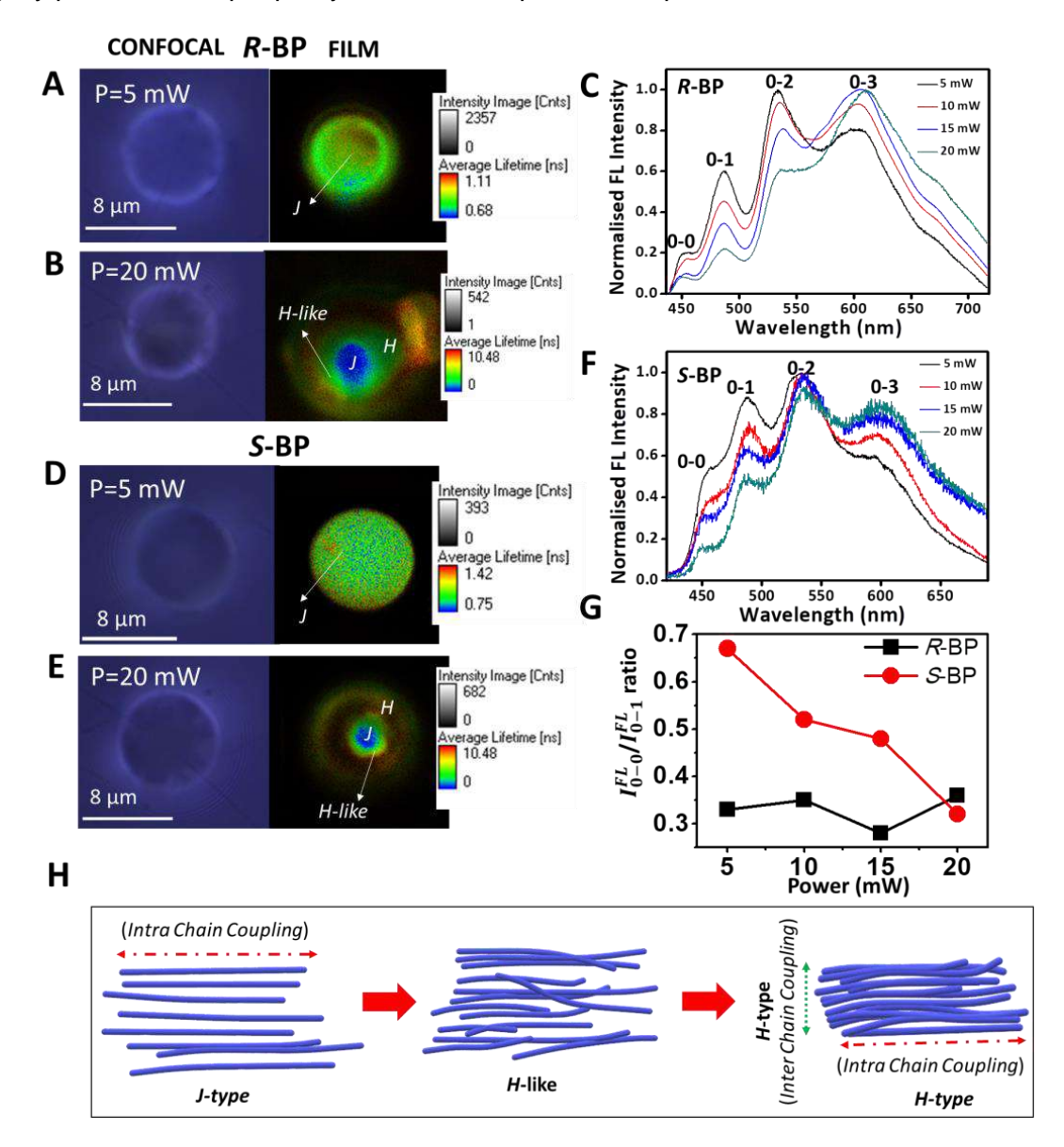


Figure 5.20. Confocal microscopy (left) and the corresponding FLIM-TCSPC (right) images of **R-** and **S-BP** micro-spheres A and B) before and D and E) after laser-induced heating. C and F) FL spectra of **R-** and **S-BP** micro-spheres (used in FLIM experiments) at different CW laser (450 nm) pump powers. G) H) The ratio 0-0/0-1 optical emission peak intensities as a function of CW laser power for **R-** and **S-BP** micro-spheres. H) Schematic illustrating the mechanisms of *H*-type and *J*-type coupling in **R-** and **S-BP** polymer chains.

The $I_{0-0}^{TPL}/I_{0-1}^{TPL}$ ratios of **R-** and **S-BP** polymer micro-spheres excited with fs laser at low pump power (<1 mW) was about 1.8 (**Fig. 5.19 A**), which is close to *J*-type polymer packing (with a homogeneous distribution of τ_{FL}) but may not be the predominant one. For

example, in the case of trans-polydiacetylene polymer chains, the ratio goes up to severalhundreds[69,277] due to an effective long-range J-coupling. However, at high fs laser power (>10 mW) these micro-spheres show a decrease in $I_{0-0}^{FL}/I_{0-1}^{FL}$ ratio (Fig. 5.20 G) due to a substantial reduction of the 0-0 peak intensity. This result confirms the H-type coupling observed in the micro-sphere peripheral regions by the τ_{FL} measurements. The R- and S-BP polymer micro-spheres heated either thermally (>80 °C) or CW laser (>10 mW) showed lessening trend of the $I_{0-0}^{FL}/I_{0-1}^{FL}$ ratio (Fig. 5.19 B and Fig. 5.20 G). Nevertheless, both 0-0 and 0-1 peak intensities reduced considerably (Fig. 5.18 A, B and Fig. 5.20 C, F). This result is not surprising as the FLIM experiments demonstrated the heterogeneous distribution of polymer chain packing in the R- and S-BP polymer micro-spheres. Further, the manifestation of slightly broadened and red-shifted emission spectra (0-3 vibronic peak) with high intensity (Fig. 5.19 A, B and Fig. 5.20 C, F) arises possibly due to intra-chain level planarization of the aromatic backbone in the core region of the micro-sphere (more J character),^[288] and excimer like-transition^[281] from the peripheral regions the micro-sphere. One of the unprecedented applications of the above experiments is that these lasertriggered aggregation changes can be effectively used to control the electronic coupling in conjugated polymers.

5.3.11.2. CD-TPL studies of *R*- and S-BP micro-resonators:

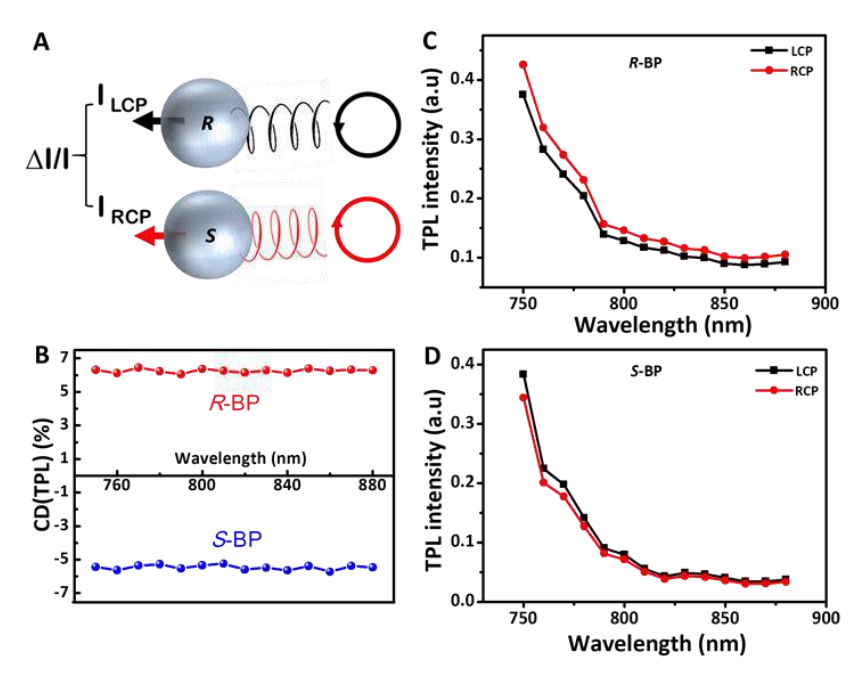


Figure 5.21: A) Schematic view of the experiment on the CD effect in the TPL response of **R**-and **S-BP** micro-spheres excited by left- and right-polarized light. B) TPL-CD signal of **R**- and **S-BP** as a function of pump wavelength. C and D) TPL intensity of **R**- and **S-BP** microspheres as a function of pump wavelength.

Enantiomeric NLO micro-spheres are presumed to exhibit CD effects in the TPL signal owing to different handedness. It has been described by the coefficient CD(TPL) equation 1.13 in Chapter-1. The scheme of the experiment is given in Figure 5.21 A. To examine this CD(TPL) effect in R- and S-BP micro-spheres, experiments were carried out by exciting the single micro-sphere with RCP and LCP fundamental lights of wavelength (λ) from 750 to 880 nm [power: 7 mW; 0.4 GW/cm²]. It is worth mentioning that in this excitation power, degradation of the micro-spheres was not observed. The TPL spectra for R- and S-BP micro-spheres at various fundamental excitation wavelengths are shown in Figure 5.21 C and D. The TPL intensity of a single micro-sphere when excited with LCP and RCP fundamental lights of different wavelengths showed that the TPL intensity variation is prominent at the region of maximum TPA, i.e., at 750 nm. Further, a noticeable TPL intensity difference for **R**- and **S-BP** micro-resonators upon excitation with light of matching handedness was observed (Figure 5.21 B). The CD (TPL) spectra of R and S-BP micro-spheres displayed nearly constant CD values of about ~6% (with opposite signs) without any apparent spectral dependence. As mentioned earlier, both CD and TPL signals are usually feeble. [263,266,276] However, the remarkable manifestation of CD effect in the TPL signal from a single microresonator (R or S-BP) point at the increased light-polymer interaction due to light confinement.

5.4. Summary and Conclusions:

Two novel chiral-NLO-CPs, abbreviated as $\it R-$ and $\it S-BP$ via Sonogashira cross-coupling reaction with $\it M_n$ = 13 and 15 kDa, respectively were synthesized. The obtained polymers self-assemble into micro-spheres (diameter ~3-8 μ m) in THF/EtOH/H₂O mixture. Individual micro-spheres displayed FL spectra with WGMs with a $\it Q$ -factor of up to 700. This result confirms the potential of $\it R-$ and $\it S-BP$ polymer micro-spheres in nanophotonic device applications in the form of micro-resonators. Remarkably, due to donor-acceptor nature, these $\it R-$ and $\it S-BP$ polymer micro-resonators, upon two-photon excitation (at low pump power), displayed TPL emission together with WGMs. A noteworthy feature of this chiral $\it R-$ and $\it S-BP$ polymer micro-spheres is that when excited with CPL of different handedness, they exhibited a much sought after CD effect in the TPL signal with values ~6%. The observation of (generally weak) CD effect in the TPL emission of a single micro-resonator confirms amplified light–polymer interaction within the high $\it Q$ -resonator, which is attractive for chiral nanophotonic applications.

Unexpectedly, both R- and S-BP polymer micro-spheres during pump-powerdependent experiments revealed very significant results related to ECT. However, at high two-photon pump power (> 10 mW), due to laser-induced heating, the spectral feature of the TPL band has significantly altered. The spectral alternation include the decrease of the $I_{0-0}^{TPL}/I_{0-1}^{TPL}$ ratio, line broadening and red-shifts. The hypothesis that the spectral transformation is due to ultrafast laser triggered heating was confirmed by heating the micro-sphere samples thermally. Unlike TPL spectra, the R- and S-BP polymer microspheres, when (i) excited with high power CW laser, and (ii) thermal heating revealed reduction of the $I_{0-0}^{FL}/I_{0-1}^{FL}$ ratio. Further, these FL spectra showed similarity with TPL spectra by exhibiting emission line broadening and red-shifts compared to the spectra obtained at low pump powers. As the observed spectral transformation is a direct indicator of the changes in the inter and intra polymer chain electronic coupling, FLIM-TCSPC experiments were carried out down to single micro-sphere level to probe the distribution of τ_{FL} . The obtained τ_{FL} image of **R-** and **S-BP** polymer micro-spheres after exposer to CW laser at high power (≥10 mW) established the existence of *H*-type, *J*-type and *H*-like polymer chain packing in comparison to homogeneous J-type polymer packing showed by the microspheres which were not exposed to high power laser irradiation. Additionally, comparison of the optical emission spectra and τ_{FL} image of **R-** and **S-BP** polymer micro-spheres revealed that the use of Spano's theoretical model based on $I_{0-0}^{TPL}/I_{0-1}^{TPL}$ ratio to polymer samples having severe polymer packing heterogeneity is not straight forward. However, this model is still useful to study the formation of heterogeneous polymer chain packing with the help of τ_{FL} imaging experiments.

Nevertheless, the above studies pinpoint the cautious approach one should take while interpreting the spectral changes observed from organic/polymer micro-resonators at high pump powers. Another very important aspect of this work is the laser-based original approach allows aggregation-dependent ECT in CP useful for the control of charge carrier mobility and optical emissions of electronic and photonic polymer devices.

6

Conclusions

This thesis entitled "Organic and Polymer Nonlinear Optical Micro-Resonators – A Single-Particle Micro-Spectroscopy Investigation" presented the syntheses of D-A type CT organic/polymer molecules and exploration of their self-assembly properties to fabricate micro-ribbons, micro-rods and micro-spheres, having resonating behavior and TPL features. Particularly the beginning part of the thesis, Chapter-1 introduced various types of organic optical micro-resonators and resonator parameters such as FSR, Q-factor, and the relationship between Q-factor and τ_P . An economical approach i.e.; bottom-up technique such as self-assembly and aggregation behavior (H, J, and H-like) in chiral polymer particles were presented. A special attention had been paid to outline of CT complexes, luminescent CDs and their photophysical properties reported in the literature. Finally, a short overview of nonlinear absorption co-efficient, NLO processes such as two-photon absorbance and emission, circular dichroism (CD) in TPL, NLO molecule-design principle is also presented.

Chapter-2 described the synthesis and self-assembly of novel push-pull type organic chalcone derivative and its BF₂ complex for photonic cavity applications. X-ray crystal structure of **HPPD** and its solid state optical studies directed towards *J*-type aggregation. By following bottom-up self-assembly approach flexible micro-ribbons and rigid micro-rods have been prepared from HPPD and HPPD-BF, respectively. The obtained micro-ribbons and micro-rods displayed F-P modes due to optical resonator effect in the Vis-NIR region and enhanced the FL intensity due to increased τ_P as well. Finally, FL imaging performed on these micro-ribbons had shown position-dependent cavity modes, which revealed the presence of

electric field distribution mainly along the lateral walls of the resonator. Application point of view, these micro-scale particles may act as coherent laser sources, and label-free ultrasensitive biosensors for single species (molecule, nanoparticle, virus, DNA, etc.)

Chapter-3 presented the successful preparation of N-rich, crystalline, green emitting CDs form PDA precursor by solvatothermal method in the EtOH solvent. In contrast to mechanism of FL in inorganic and organic molecules, there is no clear mechanism is established to interpret the origin of FL in CDs due to their multi-exponential FL decay life times. Interestingly, the obtained CDs exhibited excitation wavelength independent FL in the green region ($\lambda_{max} \approx 522$ nm in solution and 536 nm in solid) of electromagnetic spectrum. The photonic grade thin film of PS-CDs micro-sphere revealed about 40 times enhancement in OPL contrast to their corresponding pure PS-CDs. Additionally, CDs films due to better light confinement or energy storage capacity of PS-CDs micro-spheres displayed WGM resonance with Q-value up to ≈ 2×103 when excited with CW (488 nm Art) laser. Further, FLIM experiments on surface covered with PS-CDs composite micro-sphere unraveled cavity sizedependent FL life time, as a result of QED effect. Remarkably, upon excitation with 800 nm fs pulse laser both the CDs and PS-CDs display enhanced up-conversion TPL in the range of around 410-580 nm. Our technique is very useful to get photonic-grade polymer-CDs composite with brilliant green FL appropriate for one and two photon bio-imaging, deep tissue sensing, light-emitting and lasing devices.

Later in *Chapter-4*, we have shown band gap tunability and enhancement of optical emission intensities from novel polymer based CT micro-particles. For this, a novel cross-linked blue emitting copolymer poly(styrene-co-4-(1-pyrene)styrene-co-divinylbenzene) (PN) has been prepared using precipitation polymerization. Further, incorporation of acceptors such as TCNB and TCNQ into PN produces orange and red emitting PN-TCNB and PN-TCNQ CT micro-resonators, respectively through self-assembly technique. Moreover, thin films of PN, PN-TCNB and PN-TCNQ micro-spheres have exhibited nearly 10 fold enhancements in OPL intensities compared to their corresponding neat thin film under same experimental conditions. Single-particle microscopic studies were performed on these CT micro-spheres displayed multimodal WGM emissions in the Vis-NIR range with a Q-factor as high as 1000 demonstrating increased photon residence time (τ_P) within the resonators. Two-photon pumped (800 nm) NLO spectroscopy studies of micro-resonators exhibited TPL emission almost comparable with their OPL bands. Our method significantly proves the effectiveness of

supramolecular CT micro-resonators to get various Vis-NIR range up-conversion CT emissions suitable for numerous NLO applications.

Finally, Chapter-5 demonstrated the successful syntheses of green emitting Chiral, conjugated copolymers abbreviated as **R-** and **S-BP** $[\overline{M_n} \sim 15]$ and 13 kDa, respectively] are prepared by copolymerization of R- and S-6,6'-dibromo-2,2'-diethoxy-1,1'-binaphthyl (R- and S-BINOL derivative) with 1,4-diethynyl-2,5-bis(octyloxy)benzene by Sonogashira coupling reaction. The R- and S-BP copolymers self-assemble in a THF/H₂O/EtOH mixture producing micro-spherical structures. CD and UV-Vis spectroscopy titration (THF:EtOH/H₂O at %ratio) reveal the structural snap-shot of the polymer during self-assembly. Remarkably, these R- and S-BP polymer micro-spheres support excitation of WGM resonances in the one- and TPL (500-720 nm) with a Q up to ~700. However, at high laser power (≥10 mW), the TPL spectral features of micro-spheres changed significantly with the increase in the ratio of 0-0/0-1 peaks intensity together with broadening of the linewidth and red-shift hinting alteration in the polymer packing. Similar spectroscopic changes were observed for micro-spheres heated thermally (range: 20 °C-160 °C) or with high power (≥10 mW) continuous-wave laser confirming the laser-triggered heat. FILM studies down to a single micro-sphere level unambiguously confirm the transformation of polymer packing from a homogeneous J type to heterogeneous mixture of J, H and H-like types. Additionally, due to their chiral nature, the TPL signals of the enantiomeric polymers also display a CD effect of about 6% with opposite signs. This original work demonstrates the tremendous potential of laser-triggered electronic coupling tunability in conjugated polymers useful for many applications.

APPENDIX-A

ABBREVIATION FOR CHEMICALS PRESENTED IN THESIS

AIBN	Aldrich, 98%
Pd(OAc) 2	Aldrich, 98%
Pd(PPh ₃) ₄	Aldrich, 99%
Cul	Avra Synthesis Pvt. Ltd. 98%
Pd(PPh ₃) ₂ Cl ₂	Aldrich, 99%
BF ₃ ·Et ₂ O	Aldrich, 98%
DVB	Aldrich, 85%
HIO ₃	Sigma Aldrich, 99.5%
	Finar Reagents, 99.5%
KI	Merck Chemicals Pvt. Ltd. 99%
tetrabutylammonium acetate	Aldrich, 97%
TMSA	Avra Synthesis Pvt. Ltd. 98%
Triethylamine	Aldrich, 99.5%
Pyridine di amine	Aldrich, 95%
Pyrene	Aldrich, 98%
K ₂ CO ₃	Aldrich, 99.99%
KCI	Aldrich, 99%
DMF	Aldrich, 99.8%
HCI	Aldrich, 99%
Et ₂ O	Aldrich, 99%
CDCl ₃	Aldrich, 99.8%
Na ₂ SO ₄	Aldrich, 99%
2-hydroxyacetophenone	Aldrich, 98%
EtŐH	Aldrich, 96%
MeOH	Aldrich, 99.8%
NaOH	Aldrich, 98%
EtOAc	Aldrich, 99.8%
Hexane	Aldrich, 95%
CH ₂ Cl ₂	Aldrich, 99.8%
DMSO-d ₆	Aldrich, 99.9%
THF	Aldrich, 99.9%
Styrene	Aldrich, 99.9%
TCNQ	Aldrich, 98%
TCNB	Aldrich, 97%
Polystyrene	Aldrich, 95%
R- and S-1, 1'-binaphthol	Aldrich, 99%
H ₂ SO ₄	Aldrich, 98%
Acetic acid	Aldrich, 99.8%
C ₂ H ₅ Br	Aldrich, 98%
acetonitrile	Aldrich, 99.8%
КОН	Avra Synthesis Pvt. Ltd. 98%
	1

APPENDIX B

Instrumentation

Nuclear Magnetic Resonance Spectroscopy

¹H- and ¹³C-NMR spectra were recorded on a Bruker 400 & 500 MHz NMR spectrometer. Spectra were recorded using the solvent peaks as the internal standard.

Mass Spectrometry

Shimadzu LC-MS 2010A equipment was used to record the mass spectra of the isolated compounds following atmospheric pressure chemical ionization (APCI) technique.

Elemental Analysis

Elemental analysis was carried out on a Thermo Finnigan Flash EA-1112 series CHNS analyzer.

Infrared Spectroscopy

FT-IR spectra were recorded on a JASCO FT/IR-5300 or Nicolet 5700 FT-IR. Solid samples were recorded as KBr pellets and liquid samples as thin films between NaCl plates.

Optical Absorption Spectroscopy

Absorption spectra were recorded on a Shimadzu UV-3600 UV-Vis-NIR Spectrophotometer or Cary 100 Bio UV-Visible spectrophotometer.

Solid State Optical Absorption Studies

The solid state absorbance spectra were collected from a Shimadzu UV-3600 spectrometer in a diffuse reflectance UV-Visible (DR-UV-Vis) mode. The reflectance spectra were converted to a absorbance spectra using Kubelka-Munk function.

Fluorescence Spectroscopy

Steady-state fluorescence emission and excitation spectra were recorded on a Jobin Yvon Horiba model Fluoromax-3 spectrofluorometer.

Transmission Electron Microscopy (TEM)

TEM images were obtained on a TECNAI G2 FEI F12 TEM at an accelerating voltage of 120 kV. Samples were prepared by placing a drop of the samples on a polymer (polyvinyl formvar) – coated copper grid (200 mesh) and air drying.

Field Emission Scanning Electron Microscopy (FESEM)

FESEM images were recorded on a Philips XL30 ESEM and a HITACHI S-4300SE/N FESEM respectively using beam voltages of 20 kV. The samples were fixed on aluminium platforms using carbon tapes; a conducting connection was made between samples and aluminium platform by silver paint. Samples were coated with a thin layer (3–5 nm) of sputtered gold prior to imaging.

Atomic Force Microscopy (AFM)

AFM imaging was carried out on NT-MDT Model Solver Pro M microscope using a class 2R laser of 650 nm wavelength having maximum output of 1 mW. All calculations and image processing was carried out by a software NOVA 1.0.26.1443 provided by the manufacturer. The images were recorded in a semi-contact mode using a noncontact mode tip purchased from NT-MDT, Moscow. The dimensions of the tip are as follows: Cantilever length = 95 (\pm 5) μ m, Cantilever width 30 (\pm 5) μ m, and Cantilever thickness = 1.5-2.5 μ m, Resonate frequency = 140-390 kHz, Force constant = 3.1-37.6 N/m, Chip size = 3.4×1.6×0.3 mm, Reflective side = Au, Tip height = 14-16 μ m, Tip curvature radius = 10 nm, and Aspect ratio 3:1-5:1.

Confocal Raman Micro Spectroscopy Studies

Single-particle micro-spectroscopy experiment was carried out on a back scattering mode set-up of the Wi-Tec alpha 300 AR laser confocal optical microscope (T-LCOM) facilities equipped with a Peltier-cooled CCD detector. Using a 300 grooves/mm grating BLZ = 750 nm, the accumulation time was typically 10 s and integration time was typically 1.0 s. Ten accumulations were performed for acquiring a single spectrum. A 150x (0.95 NA) objective was used to excite single micro-structures. Argon ion 488 nm CW laser, 405 nm diode laser were used as an excitation source. Laser power was estimated using THOR Labs power meter.

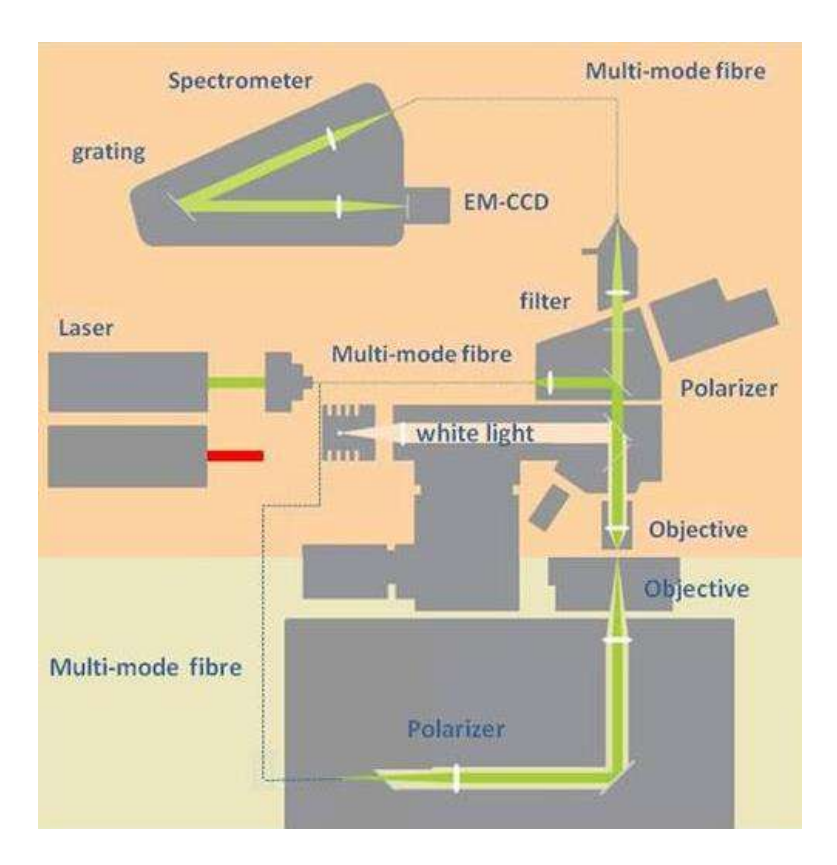


Figure S1: Laser confocal Raman microscopy experimental set up for single particle spectroscopic studies.

Single Crystal X-ray Diffraction: Data Collection, Solution and Refinement

The X-ray intensity data of crystals were collected on a Bruker Nonius SMART APEX CCD area detector system equipped with a graphite monochromator and a MoK α fine-focus sealed tube (λ = 0.71073 Å) (40 kV, 35 mA). The detector was placed at a distance of 6.003 cm from the crystal. The frames were integrated by Bruker SAINT and the structure was solved and refined using the direct method analysis in Bruker SHELXTL Software Package.

Nonlinear Optical (NLO) Spectroscopy Studies

For TPL measurement a home build experimental set up was developed by using a commercial Ti: Sapphire laser having central wavelength 800 nm, pulse width 100 fs, repetition rate 1 kHz. The laser output is directed by a half-wave plate and polarizer combination to control the laser power, a lens having a focal length of 50 cm is used to focus the laser beam on the sample. The reflected beam is filtered by a notch filter to cut down the fundamental excitation wavelength, the filtered beam is collected by a fiber-coupled spectrometer, and the spectrometer output is displayed by a computer. The experiment is performed by keeping the

sample at focal volume having a spot size of $102 \, \mu m$ and is exposed by linearly polarized light with different input powers.

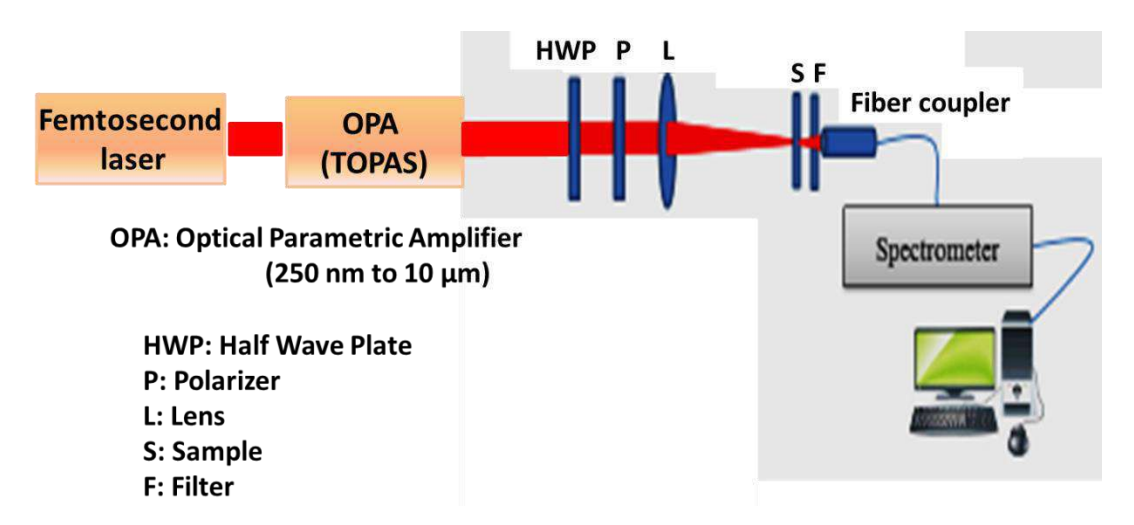


Figure S2: Experimental setup for TPL measurement.

Nonlinear absorption co-efficient (β) Measurements (Z-scan)

The β value can be determined by open aperture Z-scan technique. While doing measurement, sample is dissolved in a suitable solvent taken in 1-mm-thick cell. Experiment is carried out using 800 nm, 100 fs pulse width and 1-kHz repetition rate, Ti:sapphire laser. Normally in Z-scan measurement, a single laser beam with a Gaussian profile is concentrated by means of a lens and then sample is moved along the direction of the focused laser beam and determining the light intensity at the detector as a function of its position along this z-axis. The sample encounters maximal intensity at the focal point, but the intensity falls in both directions starting from the focus point. The sample thickness is selected in such a way that slightly lesser than the Rayleigh range of the focused laser beam, which is approximately 1mm. Even more, intensity of the laser is regulated with well calibrated neutral density filters. Finally, data is collected by scanning the cell across the focus and the β is acquired by fitting the nonlinear transmission equation for an open aperture Z-scan curve.

$$T = 1 - \frac{\beta L_{eff} I_o}{2^{\frac{3}{2}} [1 + (\frac{Z}{Z_o})^2]}$$

where β is the effective nonlinear absorption coefficient, z is the position of the sample, $z_o = \pi \omega_0^2/\lambda$ is the Rayleigh range, ω_0 is the beam waist at the focal point (z = 0), λ is excitation wavelength of the laser, I_o is the intensity on the sample at focus, effective optical path length

in the sample of length L is given as $L_{eff}=1-e^{-\alpha\,L/\alpha}$, and α is the linear absorption coefficient.

Fluorescence Lifetime Imaging Microscopy (FLIM)

FL decays and FL lifetime images were recorded on a time-resolved Micro-Time 200 confocal FLIM setup (PicoQuant) equipped with an inverted microscope (Olympus IX 71). Measurements were performed under ambient conditions, at room temperature, on a microparticles deposited cover-slip. Samples were excited by a 405 nm ps diode pulse laser with a stable repetition rate of 20 MHz (FWHM: 176 ps). The data acquisition was performed with a SymPhoTime software controlled PicoHarp 300 time-correlated single-photon counting (TCSPC) module in a time tagged time-resolved mode. The overall resolution of the setup was 4 ps. The FLIM images of microspheres were recorded using a 60x Nikon objective with a scanned speed of 0.60 ms/pixel. The image pixels for micro-particles are 72x72 and 512x512, respectively.

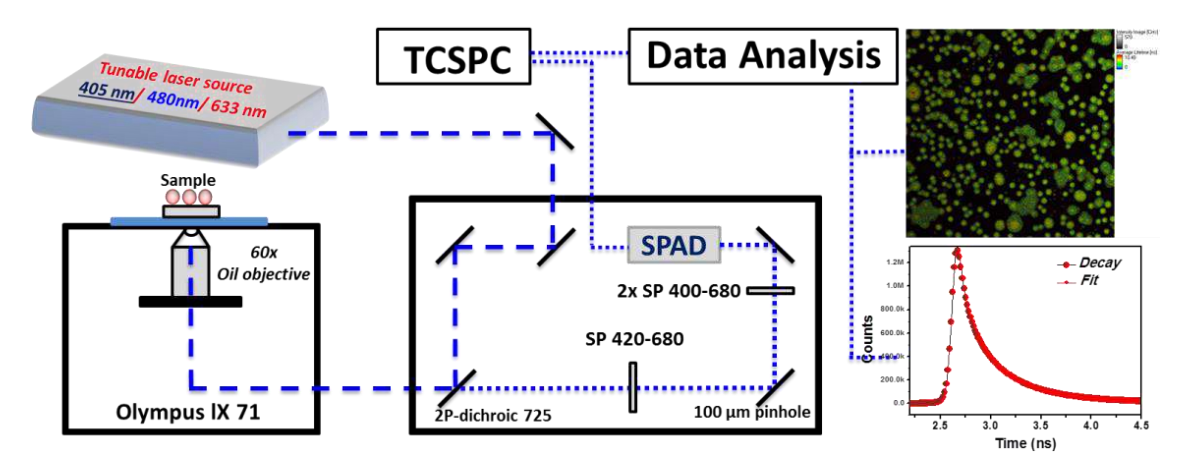


Figure S3: Experimental setup for life time measurement by FLIM set up.

APPENDIX C

Table A1: Crystal data and structure refinement parameters of HPPD (CCDC: 1479670)

X-ray c	crystal structure information
Chemical Formula	C ₂₇ H ₁₈ O ₂
FW	374.13
Color	Red
Crystal System	Monoclinic
Space group	P 21/c
a	17.656 (2)
b	13.1736 (18)
С	8.0101 (10)
α	90.00
β	95.111(11)
γ	90.00
V (Å)	1855.7 (4)
Z	4
ρ	1.324
Т	298 K
λ (Å)	0.71073
F (000)	1705.9
Theta	71. 265
Index Ranges (h, k, l)	21, 16, 8
R1 (Reflections)	0.1095
Goodness of Fit on F ² . S	1.093

RESEARCH PUBLICATIONS FROM THESIS

 V. Radhika, D. Venkatakrishnarao, M. A. Mohiddon and R. Chandrasekar. Self-Assembly of "Chalcone" Type Push-Pull Dye Molecules into Organic Single Crystalline Micro-Ribbons and Rigid Micro-Rods for Vis/NIR Range Photonic Cavity Applications.

Chem. Phys. Chem. 2016, 17, 3435-3441.

2. D. Venkatakrishnarao, C. Sahoo, **V. Radhika**, M. Annadhasan, S. R. G. Naraharisetty and R. Chandrasekar.

2D Arrangement of Polymer Micro-Sphere Photonic Cavities Doped with Novel N-Rich Carbon Quantum Dots Display Enhanced One- and Two-Photon Luminescence Driven by Optical Resonances.

Adv. Opt. Mater. 2017, 5, 1700695.

V. Radhika, D. Venkatakrishnarao, C. Sahoo, S. R. G. Naraharisetty, D. N. Rao, K. Müllen and R. Chandrasekar,

Micro-Resonators from Charge-Transfer in Polymer Particles - toward Enhanced and Tunable Two-Photon Emission.

ACS Appl. Mater. Interfaces. 2018, 10, 16723-16730.

4. V. Radhika, M. Annadhasan, J. Ravi, M. Durga Prasad, N. Mitetelo, K. Zhdanova, E.

Mamonov, K. Müllen, T. V. Murzina and R. Chandrasekar,

Laser-Driven Shifting of Electronic Couplings from H-and J-type in NLO Chiral Polymer Micro-Resonators - A Single Particle Investigation

(Manuscript is to be communicated)

PRESENTATIONS IN CONFERENCES AND SYMPOSIUMS

1. V. Radhika and R. Chandrasekar

Photonic Micro-Resonators from Charge-Transfer in Polymer Particles-toward Enhanced and Tunable Two-Photon Emission.

Poster presented at the Chem-fest-2016, School of Chemistry, UOH, India.

2. V. Radhika and R. Chandrasekar

Flexible and Rigid Micro-Resonators from Chalcone type Push-Pull Molecules and Their Photonic Applications.

Posterpresented at EAS-8-2017, CSIR-NIIST, Thiruvanthapuram, Kerala, India.

3. V. Radhika and R. Chandrasekar

Photonic Micro-Resonators from Charge-Transfer in Polymer Particles-toward Enhanced and Tunable Two-Photon Emission.

Oral presentation at the Chem-fest-2017, School of Chemistry, UOH, India

References:

- 1. H. J. Kimble, *Physica Scripta* **1998**, *76*,127.
- 2. S. Haroche, *Physica Scripta* **1998**, *76*, 159.
- 3. A. Kiraz, P. Michler, C. Becher, B. Gayral, A. Imamoglu, L. Zhang, E. Hu, W. Schoenfeld and P. Petroff, *Appl. Phys. Lett.* **2001**, *78*, 3932.
- 4. P. R. Berman, Cavity Quantum Electrodynamics, Academic Press, San Diego, CA 1993.
- 5. Y. Luo, C. Yuan, J. Xu, Y. Li, H. Liu, S. Semin, T. Rasing, W. Yang and Y. Li, *ACS Appl. Mater. Interfaces* **2017**, *36*, 30862.
- A. E. Fomin, M. L. Gorodetsky, I. S. Grudinin and V. S. Ilchenko, *J. Opt. Soc. Am. B.* 2005, 22, 459.
- J. Pfeifle, V. Brasch, M. Lauermann, Y. Yu, D. Wegner, T. Herr, K. Hartinger, P. Schindler,
 J. Li, D. Hillerkuss, R. Schmogrow, C. Weimann, R. Holzwarth, W. Freude, J. Leuthold, T. J.
 Kippenberg and C. Koss, *Nat. Photonics* 2014, 8, 375.
- 8. S. A. Diddams, T. Udem, J. C. Bergquist, E. A. Curtis, R. E. Drullinger, L. Hollberg, W. M. Itano, W. D.Lee, C. W. Oates, K. R. Vogel and D. J. Wineland, *Science* **2001**, *293*, 825.
- 9. Y. S. Zhao, H. Fu, A. Peng, Y. Ma, Q. Liao and J. Yao, Acc. Chem. Res. 2010, 43, 409.
- 10. I. D. W. Samuel and G. A. Turnbull, Chem. Rev. 2007, 107, 1272.
- 11. I. D. W. Samuel, E. B. Namdas and G. A. Turnbull, Nat. Photonics 2009, 3, 546.
- 12. J. Clark and G. Lanzani, Nat. Photonics 2010, 4, 438.
- 13. C. Zhang, Y. Yan, Y. S. Zhao and J. Yao, Acc. Chem. Res. 2014, 47, 3448.
- 14. W. Zhang, L. Peng, J. Liu, A. Tang, J.-S. Hu, J. Yao and Y. S. Zhao, *Adv. Mater.* **2016**, *28*, 4040.
- S. G. Lipson, H. Lipson and D. S. Tannhauser, *Optical Physics*, 3rd ed., Cambridge University Press, Cambridge, 1995.
- 16. F. Vollmer, S. Arnold and D. Keng, *Proc. Natl. Acad. Sci.* **2008**, *105*, 20701.
- 17. J. Chee, J. Hwu, T. S. Kim, J. Kubby, S. Velicu and N. Gupta, *Proc. SPIE.* **2015**, 9375, 93750K.
- 18. A. R. Ali, A. M. Erian and K. Shokry, *Proc. SPIE.* **2017**, *10246*, 2265814.
- 19. C. Fabry and A. Perot, Ann. Chim. Phys. 1889, 16, 7.
- 20. E. F. Schubert, *Light-Emitting Diodes*, 2nd ed., Cambridge university press, Cambridge, **2006**.
- 21. K. W. Busch, A. Hennequin and M. A. Busch, *In Cavity-Ring down Spectroscopy,* ACS Symposium Series; American Chemical Society: Washington, DC, **1999**.

- J. Kasprzak, M. Richard, S. Kundermann, A. Baas, P. Jeambrun, J. M. J. Keeling, F. M. Marchetti, M. H. Szymaska, R. André, J. L. Staehli, V. Savona, P. B. Littlewood, B. Deveaud and L. S. Dang, *Nature* 2006, 443, 409.
- 23. R. Balili, V. Hartwell, D. Snoke, L. Pfeier and K. West, Science 2007, 316, 1007.
- 24. H. Deng, G. Weihs, C. Santori, J. Bloch and Y. Yamamoto, Science 2002, 298, 199.
- 25. C. Zhang, C.-L. Zou, Y. Yan, R. Hao, F.-W. Sun, Z.-F. Han, Y. S. Zhao and J. Yao, *J. Am. Chem. Soc.* **2011**, *133*, 7276.
- M. P. Zhuo, Y. X. Zhang, Z. Z. Li, Y. L. Shi, X. D. Wang and L. S. Liao, *Nanoscale* 2018, 10, 5140.
- 27. J. C. Knight, N. Dubreuil, V. Sandoghdar, J. Hare, V. Lefèvre-Seguin, J. M. Raimond and S. Haroche, *Opt. Lett.* **1996**, *21*, 698.
- 28. L. Rayleigh, *Phil. Mag.* **1910**, *20*, 1001.
- 29. L. Rayleigh, Proc. R. Soc. London A. 1912, 86, 207.
- 30. M. Gomilšek, Whispering Gallery Modes, University of Ljubljana, 2011.
- 31. X. Peng, F. Song, S. Jiang, N. Peyghambarian, M. K. Gonokami and L. Xu, *Appl. Phys. Lett.* **2003**, *82*, 1497.
- 32. H.-H. Fang, R. Ding, S.-Y. Lu, Y.-D. Yang, Q.-D. Chen, J. Feng, Y.-Z. Huang and H.-B. Sun, *Laser Photonics Rev.* **2013**, *7*, 281.
- 33. Y. Yan and Y. S. Zhao, Chem. Soc. Rev. 2014, 43, 4325.
- 34. W. Zhang, J. Yao and Y. S. Zhao, Acc. Chem. Res. 2016, 49, 1691.
- 35. D. Venkatakrishnarao, C. Sahoo, V. Radhika, M. Annadhasan, S. R. G. Naraharisetty and R. Chandrasekar, *Adv. Opt. Mater.* **2017**, *5*, 1700695.
- 36. J. Zhao, Y. Yan, C. Wei, W. Zhang, Z. Gao and Y. S. Zhao, *Nano Lett.* **2018**, *18*, 1241.
- 37. V. D. Ta, R. Chen, L. Ma, Y. J. Ying and H. D. Sun, Laser Photonics Rev. 2013, 7, 133.
- 38. Y. Wang, V. D. Ta, K. S. Leck, B. H. I. Tan, Z. Wang, T. He, C.-D. Ohl, H. V. Demir and H. Sun, *Nano Lett.* **2017**, *17*, 2640.
- 39. G. C. Righini, Y. Dumeige, P. Féron, M. Ferrari, G. N. Conti, D. Ristic and S. Soria, *Rivista del nuovo cimento* **2011**, *34*, 435.
- 40. V. D. Ta, R. Chen and H. D. Sun, Sci. Rep. 2013, 3, 1362.
- 41. J. Zhao, Y. Yan, C. Wei, W. Zhang, Z. Gao and Y. S. Zhao, *Nano Lett.* **2018**, *18*, 1241.
- 42. H. Chandrahalim and X. Fan, Sci. Rep. 2015, 5, 18310.
- 43. S. K. Vanga and A. A. Bettiol, Nucl. Instrum. Methods Phys. Res. Sect. B 2015, 348, 209.
- 44. D. Venkatakrishnarao, Y. S. L. V. Narayana, M. A. Mohaiddon, E. A. Mamonov, I. A. Kolmychek, A. I. Maydykovskiy, V. B. Novikov, T. V. Murzina and R. Chandrasekar, *Adv.*

- Mater. 2017, 29, 1605260.
- 45. E. A. Mamonov, V. B. Novikov, N. V. Mitetelo, I. A. Kolmychek, A. I. Maydykovskiy, Venkatakrishnarao, Y. S. L. V. Narayana, M. A. Mohaiddon, R. Chandrasekar and T. V. Murzina, *Laser Phys. Lett.* **2017**, *14*, 035403.
- 46. K. J. Vahala, Nature 2003, 424, 839.
- 47. F. Vollmer and S. Arnold, Nat. Methods 2008, 5, 591.
- 48. V. S. Ilchenko and A. B. Matsko, IEEE J. Sel. Top. Quant. Electron. 2006, 12, 15.
- 49. X. Wang, Q. Liao, Q. Kong, Y. Zhang, Z. Xu, X. Lu and H. Fu, *Angew. Chem.* **2014**, *126*, 5973.
- 50. M. C. Collodo, F. Sedlmeir, B. Sprenger, S. Svitlov, L. J. Wang and H. G. L. Schwefel, *Opt. Express* **2014**, *22*, 19277.
- 51. X. Wang, Q. Liao, H. Li, S. Bai, Y. Wu, X. Lu, H. Hu, Q. Shi and H. Fu, *J. Am. Chem. Soc.* **2015**, *137*, 9289.
- 52. S. P. Vyatchanin, M. L. Gorodetsky and V. S. Ilchenko, J. Appl. Spectrosc. 1992, 56, 182.
- 53. G. Schunk, J. U. Furst, M. Fortsch, D. V. Strekalov, U. Vogl, F. Sedlmeir, H. G. L. Schwefel, G. Leuchs and C. Marquardt. *Opt. Exp.* **2014**, *22*, 30795.
- 54. C. Marquardt, D. Strekalov, J. Fürst, M. Förtsch and Gerd Leuchs, *Optics and Photonics News* **2013**, *24*, 38.
- 55. A. N. Oraevsky, Quantum Electron. 2002, 32, 377.
- 56. F. Zhou and W. Du, *J. Opt*, **2018**, *20*, 035401.
- 57. S. Yang, Y. Wang and H. Sun, Adv. Opt. Mater. 2015, 3, 1136.
- 58. M. S. Nawrocka, T. Liu, X. Wang and R. R. Panepucci, *Appl. Phys. Lett.* **2006**, *89*, 071110.
- 59. T. J. A. Kippenberg, *Ph.D. Thesis*, Californialnstitute of Technology, **2004**.
- 60. C. Wei, M. Gao, F. Hu, J. Yao and Y. S. Zhao, Adv. Opt. Mater. 2016, 4, 1009.
- 61. M. Gao, C. Wei, X. Lin, Y. Liu, F. Hu and Y. S. Zhao, Chem. Commun. 2017, 53, 3102.
- 62. Y.-D. Yang, Y.-Z. Huang and Q. Chen, *Phys. Rev. A*, **2007**, *75*, 013817.
- 63. I. Kandas, B. Zhang, C. Daengngam, I. Ashry, C.-Y. Jao, B. Peng, S. K. Ozdemir, H. D. Robinson, J. R. Heflin, L. Yang and Y. Xu, *Opt. Exp.* **2013**, *21*, 18.
- 64. M. Annadhasan, U. Venkataramudu, N. V. Mitetelo, E. A. Mamonov, C. Sahoo, S. R. G. Naraharisetty, T. V. Murzina and R. Chandrasekar, *ACS Appl. Energy Mater.* **2019**, *2*, 428.
- 65. O. Svelto and D. C. Hanna, *Principles of Lasers*. 4th ed., Springer, Berlin, 2009.
- 66. P. Sandeep and P. B. Bisht, Chem. Phys. Lett. 2003, 371, 327.
- 67. H. Fujiwara, K. Sasaki and H. Masuhara, J. Appl. Phys. 1999, 85, 2052.
- 68. D. Venkatakrishnarao, M. A. Mohiddon and R. Chandrasekar, Adv. Opt. Mater. 2016, 5,

- 1600613.
- 69. K. Tabata, D. Braam, S. Kushida, L. Tong, J. Kuwabara, T. Kanbara, A. Beckel, A. Lorke and Y. Yamamoto, *Sci. Rep.* **2014**, *4*, 5902.
- D. V. Strekalov, C. Marquardt, A. B. Matsko, H. G. L. Schwefel and G. Leuchs, *J. Opt.* 2016, 18, 123002.
- Y. S. L. V. Narayana, D. Venkatakrishnarao, A. Biswas, M. A. Mohaiddon, N. Viswanathan and R. Chandrasekar, ACS Appl. Mater. Interfaces 2016, 8, 952.
- 72. V. Radhika, D. Venkatakrishnarao, C. Sahoo, S. R. G. Naraharisetty, D. N. Rao, K. Müllen and R. Chandrasekar, *ACS Appl. Mater. Interfaces* **2018**, *10*, 16723.
- 73. Y. Wei, X. Lin, C. Wei, W. Zhang, Y. Yan and Y. S. Zhao, ACS Nano 2017, 11, 597.
- 74. L. Cerdan, E. Enciso, V. Martin, J. Banuelos, I.- L. Arbeloa, A. Costela and I.-G.Moreno, *Nat. Photonics* **2012**, *6*, 621.
- 75. V. D. Ta, R. Chen and H. D. Sun, Adv. Mater. 2012, 24, 60.
- 76. S. Kushida, S. Okabe, T. D. Dao, S. Ishii, T. Nagao, A. Saeki, M. Kijima and Y. Yamamoto, *RSC Adv.* **2016**, *6*, 52854.
- 77 Y.-Y. Lei, Y. Jin, D.-Y. Zhou, W. Gu, X.-B. Shi, L.-S. Liao and S.-T. Lee, *Adv. Mater.* **2012**, *24*, 5345.
- 78. T. Adachi, L. Tong. J. Kuwabara, T. Kanbara, A. Saeki, S. Seki and Y. Yamamoto, *J. Am. Chem. Soc.* **2013**, *135*, 870.
- 79. Q. Wang, J. Q. Ding, D. G. Ma, Y. X. Cheng, L. X. Wang, X. B. Jing and F. S. Wang, *Adv. Funct. Mater.* **2009**, *19*, 84.
- 80. C. Wei, S.-Y. Liu, C.-L. Zou, Y. Liu, J. Yao and Y. S. Zhao, J. Am. Chem. Soc. 2015, 137,62.
- 81. S. Rakers, L. F. Chi and H. Fuchs, *Langmuir* **1997**, *13*, 7121.
- 82. E. Armstrong and C. O'Dwyer, *J. Mater. Chem. C* **2015**, 3, 6109.
- 83. G. Briegleb, Angew. Chem. Int. Ed. 1964, 3, 617.
- 84. J. Brédas, D. Beljonne, V. Coropceanu and J. Cornil, Chem. Rev. 2004, 104, 4971.
- 85. J. Zyss, I. Ledoux, S. Volkov, V. Chernyak, S. Mukamel, G. P. Bartholomew and G. C. Bazan, *J. Am. Chem. Soc.* **2000**, *122*, 11956.
- 86. Z. R. Grabowski, K. Rotkiewicz and W. Rettig, Chem. Rev. 2003, 103, 3899.
- 87. S. Wang, J. Cai, R. Sadygov and E.C. Lim, J. Phys. Chem. 1995, 99, 7416.
- 88. S.-Y. Kim, Y.-J. Cho, G. F. Jin, W.-S. Han, H.-J. Son, D. W. Cho and S. K. Kang, *Phys. Chem. Chem. Phys.* **2015**, *17*, 15679.
- 89. Y. -J. Cho, S.-Y. Kim, M. Cho, W.-S. Han, H. -J. Son, D. W. Cho and S. O. Kang, *Phys. Chem. Chem. Phys.* **2016**, *18*, 9702.

- 90. N. N. P. Moonen and F. Diederich, Org. Biomol. Chem. 2004, 2, 2263.
- 91. I. Fernández and G. Frenking, Chem. Commun. 2006, 2, 5030.
- 92. M. Rumi, B. Barlow, J. Wang, J. W. Perry and S. R. Marder, Adv. Polym. Sci. 2008, 213, 1.
- 93. M. Szablewski, P. R. Thomas, A. Thornton, D. Bloor, G. H. Cross, J. M. Cole, J. A. K. Howard, M. Malagoli, F. Meyers, J.-L. Brédas, W. Wenseleers and E. Goovaerts J. Am. Chem. Soc. 1997, 119, 3144.
- 94. R. R. Tykwinski, U. Gubler, R. E. Martin, F. Diederich, C. Bosshard and P. Günter, *J. Phys. Chem. B* **1998**, *102*, 4451.
- 95. X. Wang, Q. Liao, X. Lu, H. Li, Z. Xu and H. Fu, Sci. Rep. 2014, 4, 7011.
- 96. E. N. Guryanova and U. Khim, Russ. Chem. Rev. 1968, 37, 1981.
- 97. G. Saito and Y. Yoshida, Bull. Chem. Soc. Jpn. 2007, 80, 1.
- 98. D. Jérome, A. Mazaud, M. Ribault and K. Bechgaard, J. Phys. Lett. 1980, 41, 95.
- 99. D. Jérome, Chem. Rev. 2004, 104, 5565.
- 100. T. Mori and T. Kawamoto, Annu. Rep. Prog. Chem. Sect. C: Phys. Chem. 2007, 103, 134.
- 101. A. S. Tayi, A. K. Shveyd, A. C.-H. Sue, J. M. Szarko, B. S. Rolczynski, D. Cao, T. J. Kennedy, A. A. Sarjeant, C. L. Stern, W. F. Paxton, W. Wu, S. K. Dey, A. C. Fahrenbach, J. R. Guest, H. Mohseni, L. X. Chen, K. L. Wang, J. F. Stoddart and S. I. Stupp, *Nature* 2012, 488, 485.
- 102. a) S. Horiuchi, Y. Okimoto, R. Kumai and Y. Tokura, *Science* 2003, 299, 229; b)
 E. Collet, M. H. Lemée-Cailleau, M. Buron-Le Cointe, H. Cailleau, M. Wulff, T. Luty, S.-Y. Koshihara, M. Meyer, L. Toupet, P. Rabiller and S. Techert, *Science* 2003, 300, 612; c) K. Kobayashi, S. Horiuchi, R. Kumai, F. Kagawa, Y. Murakami and Y. Tokura, *Phys. Rev. Lett.* 2012, 108, 237601.
- 103. F. Kagawa, S. Horiuchi, M. Tokunaga, J. Fujioka and Y.Tokura, Nat. Phys. 2010, 6, 169.
- S. S. Babu, S. Prasanthkumar and A. Ajayaghosh, *Angew. Chem.* 2012, 124, 1800;
 Angew. Chem. Int. Ed. 2012, 51, 1766.
- 105. M. H. Schwartz, J. Inclusion Phenom. Macrocycl. Chem. 1990, 9, 1.
- 106. M. Y. E. Sayed and M. S. Refat, Int. J. Electrochem. Sci, 2014, 9, 608.
- 107. E. A. Owens, M. Henary, G. E. Fakhri and H. S. Choi, Acc. Chem. Res. 2016, 49, 1731.
- 108. a) V. T. Förster, *Ann. Phys.* **1948**, *6*, 55; b) J. P. S. Farinha and J. M. Martinho, *J. Phys. Chem.C* **2008**, *112*, 10591.
- 109. O. Oki, S. Kushida, A. Mikosch, K. Hatanaka, Y. Takeda, S. Minakata, J. Kuwabara, T. Kanbara, T. D. Dao, S. Ishii, T. Nagao, A. J. C. Kuehne, F. Deschler, R. H. Friend and Y. Yamamoto, *Mater. Chem. Front.* 2018, 2, 270.

- D. Venkatakrishnarao, C. Sahoo, E. A. Mamonov, I. A. Kolmychek, A. I. Maydykovskiy,
 V.Mitetelo, V. B. Novikov, S. R. G. Naraharisetty, T. V. Murzina and R. Chandrasekar, *J. Mater. Chem. C* 2017, *5*, 12349.
- 111. a) C. Zhang, C.-L. Zou, Y. Zhao, C.-H. Dong, C. Wei, H. Wang, Y. Liu, G.-C. Guo, J. Yao and Y. S. Zhao, Sci. Adv. 2015, 1, 1500257; b) P. Lodahl, S. Mahmoodian, S. Stobbe, A. Rauschenbeutel, P. Schneeweiss, J. Volz, H. Pichler and P. Zoller, Nature 2017, 541, 473.
- 112. R. W. Boyd, Nonlinear Optics, 3rd ed., Academic, San Diego, CA 2008.
- 113. P. N. Prasad and B. A. Reinhardt, Chem. Mater. 1990, 2, 660.
- 114. Richard S. Quimby, *Photonics and lasers: An introduction*, John Wiley & Sons, Inc. **2006**.
- 115. G. S. He, L.-S. Tan, Q. Zheng and P. N. Prasad, Chem. Rev. 2008, 108, 1245.
- 116. M. Göppert-Mayer, Ann. Phys. 1931, 401, 273.
- 117. M. D. Rahn and T. A. King, *J. Mod. Opt.* **2008**, *45*, 1259.
- 118. A. Argyros, M. A. van Eijkelenborg, S. D. Jackson and R. P. Mildren, *Opt. Lett.* **2004**, *29*, 1882.
- 119. W. Kaiser and C. G. B. Garrett, Phys. Rev. Lett. 1961, 7, 229.
- 120. S. Kulmala and J. Suomi, Analytica Chemica Acta, 2003, 500, 21.
- 121. S. Couris, E. Koudoumas, A. A. Ruth and S. Leach, *J. Phys. B: At., Mol. Opt. Phys.* **1995**, 28, 4537.
- 122. B. Taheri, H. Liu, B. Jassemnejad, D. Appling, R. C. Powell and J. Song, *J. Appl. Phys. Lett.* **1996**, *68*, 1317.
- 123. M. Bass, Handbook of Optics, 2nd ed., McGraw-Hill, 1994.
- 124. M. J. Weber, Handbook of optical materials. 1st ed., CRC Press, 2003.
- 125. A. Dragonmir, J. G. McInerney, D. N. Nikogosyan, Appl. Opt. 2002, 41, 4365.
- 126. H. M. Kim, M. S. Seo, S.-J. Jeon and B. R. Cho, *Chem. Commun.* **2009**, 153, DOI: 10.1039/B916965B.
- 127. M. Pawlicki, H. A. Collins, R. G. Denning and H. L. Anderson, *Angew. Chem. Int. Ed.* **2009**, *48*, 3244.
- 128. M. Albota, D. Beljonne, J.-L. Bredas, J. E. Ehrlich, J.-Y.Fu, A. A. Heikal, S. E. Hess, T. Kogej, M. D. Levin, S. R. Marder, D. McCord-Maughon, J. W. Perry, H. Rockel, M. Rumi, G. Subramaniam, W. W. Webb, X.-L. Wu and C. Xu, *Science* **1998**, *281*, 1653.
- 129. Y. Segawa, T. Higashihara and M. Ueda, J. Am. Chem. Soc. **2010**, 132, 11000.
- 130. H. S. Nalwa and M. Seizō, Nonlinear Optics of Organic Molecules and Polymers,

- CRC Press, 1997.
- 131. P. R. Hammond, Opt. Commun. 1979, 29, 331.
- 132. C. Wei, S.-Y. Liu, C.-L. Zou, Y. Liu, J. Yao and Y. S. Zhao, *J. Am. Chem.Soc.* **2014**, *137*, 62.
- 133. E. A. Mamonov, A. I. Maydykovskiy, N. V. Mitetelo, D. Venkatakrishnarao, R. Chandrasekar and T. V. Murzina, *Laser Phys. Lett.* **2018**, *15*, 035403.
- 134. G. Tsiminis, A. Ruseckas, I. D. W. Samuel and G. A. Turnbull, *Appl. Phys. Lett.* **2009**, *94*, 253304.
- 135. C. N. La Fratta, J. T. Fourkas, T. Baldacchini and R. A. Farrer, *Angew. Chem. Int. Ed.* **2007**, *46*, 6238.
- 136. F. Helmchen and W. Denk, *Nat. Methods.* **2005**, *2*, 932.
- 137. H. M. Kim and B. R. Cho, Acc. Chem. Res. 2009, 42, 863.
- 138. S. Yao and K. D. Belfield, Eur. J. Org. Chem. 2012, 17, 3187.
- 139. C. W. Spangler, *J. Mater. Chem.* **1999**, *9*, 2013.
- 140. W. G. Fisher, W. P. Partridge, C. Dees and E. A. Wachter, *Photochem. Photobiol.* **1997**, 66, 141.
- 141. S. Kawata and Y. Kawata, Chem. Rev. 2000, 100, 1777.
- 142. a) U. Stalmach, B. de Boer, C. Videlot, P. F. van Hutten and G. Hadziioannou, *J. Am. Chem. Soc.* 2000, 122, 5464; b) B. de Boer, U. Stalmach, P.F. van Hutten, C. Melzer, V. V. Krasnikov and G. Hadziioannou, polymer 2001, 42, 9097; c) S.-S. Sun, Solar Energy Mater. Solar Cells. 2003, 79, 257; d) K. Sivula, Z. T. Ball, N. Watanabe and J. M. J. Fréchet, Adv. Mater. 2006, 18, 206; e) Z. T. Ball, K. Sivula and J. M. J. Fréchet, Macromolecules 2006, 39, 70; f) S. Sun, Z. Fan, Y. Wang and J. Haliburton, J. Mater. Sci. 2005, 40, 1429.
- 143. a) A. Kraft, A. C. Grimsdale and A. B. Holmes, *Angew. Chem. Int. Ed.* 1998, 37, 402; b)
 R.M. Tarkka, X. Zhang and S. A. Jenekhe, *J. Am. Chem. Soc.* 1996, 118, 9438; c) X.
 Zhang, A. S. Shetty and S. A. Jenekhe, *Macromolecules* 1999, 32, 7422; d) X. Zhang, A.
 S. Shetty and S. A. Jenekhe, *Acta. Polym.* 1998, 49, 52.
- 144. A. Molinos-Gómes, M. Maymó, X. Vidal, D. Velasco, J. Martorell and F. López-Calahorra, Adv. Mater. 2007, 19, 3814; b) C. J. Yang, S. A. Jenekhe, J. S. Meth and H. Vanherzeele, Ind. Eng. Chem. Res. 1999, 38, 1759.
- 145. a) M. Deutsch, Y. A. Vlasov and D. J. Norris, Adv. Mater. 2000, 12, 1176; b) S. A. Jenekhe, L. Chen, S. A. Jenekhe and X. L. Chen, Science 1998, 279, 1903; c) S. A. Jenekhe and X. L. Chen, Science 1999, 283, 372; d) X. L. Chen and S. A. Jenekhe,

- Langmuir 1999, 15, 8007; e) S. Gottardo, R. Sapienza, P. D. García, A. Blanco, D. S. Wiersma and C. López, *Nat. Photonics* 2008, 2, 429; f) T. Kanai, T. Sawada, A. Toyotama and K. Kitamura, *Adv. Fun. Mater.* 2005, 15, 25.
- 146. B. J. Siwick, O. Kalinina, E. Kumacheva, R. J. D. Miller and J. Noolandi, *J. Appl. Phys.* **2001**, *90*, 5328.
- 147. S. Kushida, D. Braam, C. Pan, T. D. Dao, K. Tabata, K. Sugiyasu, M. Takeuchi, S. Isgii, T. Nagao, A. Lorke and Y. Yamamoto, *Macromolecules* **2015**, *48*, 3928.
- 148. a) A. M. Christofi, P. J. Garratt, G. Hogarth, A. J. Ibbett, Y. F. Ng and J. W. Steed, Tetrahydron 2002, 58, 4543; b) R. Hilgenfeld and W. Saengar, Angew. Chem. Int. Ed. 1981, 20, 1045; c) M. Makinen, M. Nissien, K. Rissanen and P. Vainiotalo, J. Am. Soc. Mass Spec. 2003, 14, 143.
- 149. S. Burattini, H. M. Colquhoun, J. D. Fox, D. Friedmann, B. W. Greenland, P. J. F. Harris, W. Hayes, M. E. Mackay and S. J. Rowan, *Chem. Commun.* **2009**, *7*, 6717.
- 150. J. -M. Lehn, Supramolecular Chemistry: Concepts and Perspectives, John Wiley & Sons, Inc. **1995**.
- 151. J. W. Steed and J. L. Atwood, *Supramolecular Chemistry*, John Wiley & Sons, Inc. **2000**.
- 152. R. Chandrasekar, Z. Qu, O. Fuhr, B. Gopalan, R. Kruk, M. Ghafari and M. Ruben, *Dalton Trans.* **2007**, *32*, 3531.
- G. Armstong and M. Buggy, *J. Mater. Sci.* **2005**, *40*, 547; b) T. Aida, E. W. Meijier and
 S. I. Stupp, *Science* **2012**, *335*, 813.
- 154. A. C. Grimsdale and K. Müllen, Angew. Chem. Int. Ed. 2005, 44, 5592.
- 155. L. C. Palmer and S. I. Stupp, Acc. Chem. Res. 2008, 41, 1674.
- 156. J. Xu, L. Wen, W. Zhou, J. Lv, Y. Guo, M. Zhu, H. Liu, Y. Li and L. Jiang, *J. Phys. Chem. C* **2009**, *113*, 5924.
- 157. D. Jiang, Z. Xue, Y. Li, H. Liu and W. Yang, J. Mater. Chem. C 2013, 1, 5694.
- 158. S. Chen, Z. Qin, T. Liu, X. Wu, Y. Li, H. Liu, Y. Song and Y. Li, *Phys. Chem. Chem. Phys.* **2013**, *15*, 12660.
- 159. T.-Q. Nguyen, R. Martel, M. Bushey, P. Avouris, A. Carlsen, C. Nuckolls and L. Brus, *Phys. Chem. Chem. Phys.* **2007**, *9*, 1515.
- 160. S. Chen, N. Chen, Y. Yan, T. Liu, Y. Yu, Y. Li, H. Liu, Y. Zhao and Y. Li, *Chem. Commun.* **2012**, *48*, 9011.
- 161. W. Zhang, Y. Yan, J. Gu, J. Yao and Y. S. Zhao, *Angew. Chem. Int. Ed.* **2015**, *54*, 7125.
- 162. C. Zhang, C.-L. Zou, Y. Yan, C. Wei, J.-M. Cui, F.-W. Sun, J. Yao, Y. S. Zhao, Adv. Opt.

- Mater. 2013, 1, 357
- 163. A. Hayer, T. Van Regemorter, B. Höfer, C. S. K. Mak, D. Beljonne and A. Köhler, *J. Polym. Sci. Part B: Polym. Phys.* **2012**, *50*, 361.
- 164. E. E. Jelley, *Nature* **1937**, *139*, 631.
- 165. S. A. Jenekhe and J. A. Osaheni, Science 1994, 265, 765.
- 166. F. Wurthner, T. E. Kaiser and C. R. Saha-Moller, Angew. Chem. Int. Ed. 2011, 50, 3376.
- 167. J. Clark, C. Silva, R. H. Friend and F. C. Spano, *Phys. Rev. Lett.* **2007**, *98*, 206406.
- 168. N. C. Maiti, S. Mazumdar and N. Periasamy, J. Phys. Chem. B 1997, 102, 1528.
- D. Chaudhuri, D. Li, Y. Che, E. Shafran, J. M. Gerton, L. Zang and J. M. Lupton, *Nano Lett.* 2011, 11, 488.
- 170. M. Kasha, Rad. Res. 1963, 20, 55.
- 171. A. Köhler and H. Bässler, *Electronic Processes in Organic Semiconductors: An Introduction*; John Wiley & Sons, Inc. **2015**.
- 172. N. J. Hestand and F. C. Spano, *Chem. Rev.* **2018**, *118*, 7069.
- 173. T. Eder, T.Stangl, M. Gmelch, K. Remmerssen, D. Laux, S. Höger, J. M. Lupton and J. Vogelsang, *Nat. Commun.* **2017**, *8*, 1641.
- 174. S. N. Baker and G. A. Baker, Angew. Chem. Int. Ed. 2010, 49, 6726.
- 175. S. Y. Lim, W. Shen and Z. Gao, Chem. Soc. Rev. 2015, 44, 362.
- 176. Y.-P. Sun, B. Zhou, Y. Lin, W. Wang, K. A. S. Fernando, P. Pathak, M. J. Meziani, B. A. Harruff, X. Wang, H. Wang, P. G. Luo, H. Yang, M. E. Kose, B. Chen, M. Veca and S. Y. Xie, *J. Am. Chem. Soc.* **2006**, *128*, 7756.
- 177. L. Cao, M. J. Meziani, S. Sahu and Y.-P. Sun, Acc. Chem. Res. 2013, 46, 171.
- 178. J. G. Zhou, C. Booker, R. Y. Li, X. T. Zhou, T. K. Sham, X. L. Sun and Z. F. Ding, *J. Am. Chem. Soc.* **2007**, *129*, 744.
- 179. X. Xu, R. Ray, Y. Gu, H. J. Ploehn, L. Gearheart, K. Raker and W. A. Scrivens, *J. Am. Chem. Soc.* **2004**, *126*, 12736.
- 180. H. Li, Z. Kang, Y. Liu and S. T. Lee, J. Mater. Chem. 2012, 22, 24230.
- 181. Y. Cui, Z. Hu, C. Zhang and X. Liu, *J. Mater. Chem. B* **2014**, *2*, 6947.
- 182. A. Pramanik, Z. Fan, S. R. Chavva, S. S. Sinha and P. C. Ray, Sci. Rep. 2014, 4, 6090.
- 183. W.-J. Niu, Y. Li, R.-H. Zhu, D. Shan, Y.-R. Fan and X.-J. Zhang, *Sens. Actuators, B.* **2015**, *218*, 229.
- 184. P. Shen and Y. Xia, Anal. Chem. 2014, 86, 5323.
- 185. Y. Dong, H. Pang, H. B. Yang, C. Guo, J. Shao, Y. Chi, M. Li and T. Yu, *Angew. Chem. Int. Ed.* **2013**, *52*, 7800.

- 186. X. Wang, L. Cao, F. Lu, M. J. Meziani, H. Li, G. Qi, B. Zhou, B. A. Harruff, F. Kermarrec and Y.-P. Sun, *Chem. Commun.* **2009**, *25*, 3774.
- 187. X. Li, S. Zhang, S. A. Kulinich, Y. Liu and H. Zeng, Sci. Rep. 2014, 4, 4976.
- 188. Y. Dong, J. Shao, C. Chen, H. Li, R. Wang, Y. Chi, X. Lin and G. Chen, *Carbon* **2012**, *50*, 4738.
- 189. Z.-H. Wen and X.-B. Yin, RSC Adv. 2016, 6, 27829.
- 190. S. Ghosh, A. M. Chizhik, N. Karedla, M. O. Dekaliuk, I. Gregor, H. Schuhmann, M. Seibt, K. Bodensiek, I. A. T. Schaap, O. Schulz, A. P. Demchenko, J. Enderlein and A. I. Chizhik, *Nano Lett.* 2014, 14, 5656.
- 191. V. Strauss, J. T. Margraf, C. Dolle, B. Butz, T. J. Nacken, J. Walter, W. Bauer, W. Peukert, E. Spiecker, T. Clark and D. M. Guldi, *J. Am. Chem. Soc.* **2014**, *136*, 17308.
- 192. S. K. Das, Y. Liu, S. Yeom, D. Y. Kim and C. I. Richards, *Nano Lett.* **2014**, *14*, 620.
- 193. Y. Fang, S. Guo, D. Li, C. Zhu, W. Ren, S. Dong and E. Wang, ACS Nano. 2012, 6, 400.
- 194. H. Li, X. He, Z. Kang, H. Huang, Y. Liu, J. Liu, J. Liu, S. Lian, C. H. A. Tsang, X. Yang and S. T. Lee, *Angew. Chem.* **2010**, *122*, 4532.
- 195. B. Kong, A. Zhu, C. Ding, X. Zhao, B. Li and Y. Tian, Adv. Mater. 2012, 24, 5844.
- 196. S. Zhu, S. Tang, J. Zhang and B. Yang, Chem. Commun. 2012, 48, 4527.
- 197. S. Zhuo, M. Shao and S. T. Lee, ACS Nano. 2012, 6, 1059.
- 198. V. Gupta, N. Chaudhary, R. Srivastava, G. D. Sharma, R. Bhardwaj and S. Chand, *J. Am. Chem. Soc.* **2011**, *133*, 9960.
- 199. X. Feng, V. Marcon, W. Pisula, M. R. Hansen, J. Kirkpatrick, F. Grozema, D. Andrienko, K. Kremer and K. Müllen, *Nat. Mater.* **2009**, *8*, 421.
- 200. X. Yan, X. Cui and L. Li, J. Am. Chem. Soc. 2010, 132, 5944.
- 201. D. Venkatakrishnarao, M. A. Mohiddon, N. Chandrasekhar and R. Chandrasekar *Adv. Opt.Mater.* **2015**, *3*, 1035.
- 202. N. Chandrasekhar, M. A. Mohiddon and R. Chandrasekar, *Adv. Opt. Mater.* **2013**, *1*, 305.
- 203. U. Venkataramudu, D. Venkatakrishnarao, N. Chandrasekhar, M. A. Mohiddon and R. Chandrasekar, *Phys. Chem. Chem. Phys.* **2016**, *18*, 15528.
- 204. P. Hui and R. Chandrasekar, Adv. Mater. 2013, 25, 2963.
- 205. N. Chandrasekhar and R. Chandrasekar, Angew. Chem. 2012, 124, 3616.
- 206. D. Venkatakrishnarao and R. Chandrasekar, Adv. Opt. Mater. 2016, 4, 112.
- 207. K. Takazawa, J. Inoue, K. Mitsuishi and T. Kuroda, *Adv. Funct. Mater.* **2013**, 23, 839.

- 208. Y. S. Zhao, H. Fu, A. Peng, Y. Ma, D. Xiao and J. Yao, Adv. Mater. 2008, 20, 2859.
- 209. C. Zhang, Y. S. Zhao and J. Yao, Phys. Chem. Chem. Phys. 2011, 13, 9060.
- 210. R. Chandrasekar, Phys. Chem. Chem. Phys. 2014, 16, 7173.
- 211. a) V. K. Praveen, C. Ranjith, E. Bandini, A. Ajayaghosh and N. Armaroli, *Chem. Soc. Rev.* 2014, 43, 4222; b) M. Urdampilleta, S. Klyatskaya, J.-P. Cleuziou, M. Ruben and W. Wernsdorfer, *Nat. Mater.* 2011, 10, 502; c) H. J. Kim, T. Kim and M. Lee, *Acc. Chem. Res.* 2011, 44, 72; d) E. N. Savariar, K. Krishnamoorthy and S. Thayumanavan, *Nat. Nanotechnol.* 2008, 3, 112.
- 212. J. Gierschner, S. Varghese and S. Y. Park, Adv. Opt. Mater. 2016, 3, 348.
- 213. A. D. Aléo, D. Gachet, V. Heresanu, M. Giorgi and F. Fages, *Chem. Eur. J.* **2012**, *18*, 12764.
- 214. S. Noel, C. Luo, C. Pinel and L. Djakovitch, Adv. Synth. Catal. 2007, 349, 1128.
- 215. A. D. Aléo, A. Felouat, V. Heresanu, A. Ranguis, D. Chaudanson, A. Karapetyan, M. Giorgi and F. Fages, *J. mat. Chem. C* **2014**, *2*, 5208.
- 216. D. V. Sevenard, O. G. Khomutov, N. S. Boltachova, V. I. Filyakova, V. Vogel, E. Lork, V. Ya. Sosnovskikh, V. O. laroshenkoe and G-V. Röschenthalerc, Z. Naturforsch. 2009, 64b, 541.
- 217. H. F. Shurvell and j. A. Faniran, Can. J. Chem. 1968, 46, 2089.
- 218. S. W. Yang, A. Elangovan, K. C. Hwang and T.-I. Ho, J. Phys. Chem. B 2005, 109, 16628.
- 219. S. Mukherjee and P. Thilagar, Chem. Commun. 2016, 52, 1070.
- 220. G. Rajendra Kumar, B. Santosh Kumar and P. Thilagar, *Dalton Trans.* **2019**, *48*, 6817.
- 221. S. Kim, S. W. Hwang, M. Kim, D. Y. Shin, D. H. Shin, C. O. Kim, S. B. Yang, J. H. Park, E. Hwang, S. H. Choi, G. Ko, S. Sim, C. Sone, H. J. Choi, S. Bae and B. H. Hong, *ACS Nano* **2012**, *6*, 8203.
- 222. S. J. Zhu, J. H. Zhang, C. Y. Qiao, S. J. Tang, Y. F. Li, W. J. Yuan, B. Li, L. Tian, F. Liu, R. Hu, H. N. Gao, H. T. Wei, H. C. Sun and B. Yang, *Chem. Commun.* **2011**, *47*, 6858.
- 223. S. Hu, A. Trinchi, P. Atkin and I. Cole, Angew. Chem., Int. Ed. 2015, 54, 2970.
- 224. M. Fu, F. Ehrat, Y. Wang, K. Z. Milowska, C. Reckmeier, A. L. Rogach, J. K. Stolarczyk, A. S. Urban and J. Feldmann, *Nano Lett.* **2015**, *15*, 6030.
- 225. S. Zhu, Q. Meng, L. Wang, J. Zhang, Y. Song, H. Jin, K. Zhang, H. Sun, H. Wang and B. Yang, *Angew. Chem. Int. Ed.* **2013**, *52*, 3953.
- 226. H. Ding, S.-B. Yu, J.-S. Wei and H.-M. Xiong, ACS Nano, 2016, 10, 484.

- 227. B. Kumar, M. Asadi, D. Pisasale, S. S. Ray, B. A. Rosen, R. Haasch, J. Abiade, A. L. Yarin and A. S. Khojin, *Nat. Commun.* **2013**, *4*, 2819.
- 228. A. C. Tamboli, E. D. Haberer, S. Rajat, K. H. Lee, S. Nakamura and E. L. Hu, *Nat. Photonics* **2007**, *1*, 61.
- 229. H. Taniguchi, J. Kido, M. Nishya and S. Sasaki, *Appl. Phys. Lett.* **1995**, *67*, 1060.
- 230. X. Guo, M. Baumgarten and K. Müllen, Prog. Polym. Sci. 2013, 38, 1832.
- 231. V. G. Kozlov, V. Bulovic, P. E. Burrows, and S. R. Forrest, Nature 1997, 389, 362.
- 232. X. Duan, Y. Huang, R. Agarwal and C. M. Lieber, *Nature* **2003**, *421*, 241.
- 233. Y. Lv, Y. J. Li, J. Li, Y. Yan, J. Yao and Y. S. Zhao, *J. Am. Chem. Soc.* **2017**, *139*, 11329.
- 234. R. Yan, D. Gargas and P. Yang, Nat. Photonics 2009, 3, 569.
- 235. H. Dong, Y. Wei, W. Zhang, C. Wei, C. Zhang, J. Yao and Y. S. Zhao, *J. Am. Chem. Soc.* **2016**, *138*, 1118.
- 236. H. Glowatzki, P. Sonar, S.P. Singh, A. M. Mak, M. B. Sullivan, W. Chen, A.T.S. Wee and A. Dodabalapur, *J. Phys. Chem. C* 2013, *117*, 11530.
- 237. Y. S. Zhao, P. Zhan, J. Kim, C. Sun and J. Huang, ACS Nano 2010, 4, 1630.
- 238. H. Meier, Angew. Chem. Int. Ed. 2005, 44, 2482.
- 239. Y. S. L. V. Narayana, M. Baumgarten, K. Müllen and R. Chandrasekar, *Macromolecules* **2015**, *48*, 4801.
- 240. H. Siegrist, C. Kloc, R. A. Laudise, H. E. Katz and R. C. Haddon, *Adv. Mater.* **1998**, *10*, 379.
- 241. P. Srujana and T. P. Radhakrishnan, Angew. Chem. Int. Ed. 2015, 54, 7270.
- 242. H.-B. Fu and Y. Yao, J. Am. Chem. Soc. 2001, 123, 1434.
- 243. H. Dong, C. Zhang and Y. S. Zhao, *J. Mater. Chem. C* **2017**, *5*, 5600.
- 244. A. Ajayaghosh, V. Praveen, C. Vijayakumar and S. J. George, *Angew. Chem.* **2007**, *119*, 6260.
- 245. A. Pan, W. Zhou, E. S. P. Leong, R. Liu, A. H. Chin, B. Zou and C. Z. Ning, *Nano Lett.* **2009**, *9*, 784.
- 246. A. Pan, H. Yang, R. Liu, R. Yu, B. Zou and Z. Wang, *J. Am. Chem. Soc.* **2005**, *127*, 15692.
- 247. X. Liu, Q. Zhang, J. N. Yip, Q. Xiong and T. C. Sum, Nano Lett. 2013, 13, 5336.
- 248. M. A. Dobrowolski, G. Garbarino, M. Mezouar, A. Ciesielskiac and M. A. Cyrańskia, *Cryst. Eng. Comm.* **2014**, *16*, 415.
- 249. S. E. Shim, S. Yang and S. Choe, J. Polym. Sci. A. Poly. Chem. 2004, 42, 3967.

- 250. M. Kivala, C. Boudon, J.-P. Gisselbrecht, B. Enko, P. Seiler, I. B. Müller, N. Langer, P. D. Jarowski, G. Gescheidt and F. Diederich, *Chem. Eur. J.* **2009**, *15*, 4111.
- 251. T. Edvinsson, C. Li, N. Pschirer, J. Schöneboom, F. Eickemeyer, R. Sens, G. Boschloo, A. Herrmann, K. Müllen and A. Hagfeldt, J. Phys. Chem. C. 2007, 111, 15137.
- 252. G. Zhou, M. Baumgarten and K. Müllen, J. Am. Chem. Soc. 2008, 130, 12477.
- 253. F. J. Chung, H. Y. Liu, B. Y. Jiang, G. Y. He, S. H. Wang, W. C. Wu and C.L. Liu, *J. Poly. Sci. Part A: Poly. Chem.* **2016**, *54*, 910.
- 254. D. S. Acker and W. R. Hertler, J.Am. Chem. Soc. 1962, 84, 3370.
- 255. J. S. Downey, G. McIsaac, R. S. Frank and H. D. H. Stover *Macromolecules*. **2001**, 34, 4534.
- 256. S. E. Shim, S. Yang, H. H. Chol and S. Choe, *J. Poly. Sci. Part A: Poly. Chem.* **2004**, *42*, 835.
- A. L. Sutton, B. F. Abrahams, D. M. DAlessansdro, T. A. Hudson, R. Robson and P. M. Usov, Cryst. Eng. Comm. 2016, 18, 8906.
- 258. S. Berger, H. Hartmann, M. Wanner, J. Fiedler and W. Kaim, *Inorg. Chimi. Acta* 314, 314, 22.
- 259. R. J. Dillon and C. J. Bardeen, J. Phys. Chem. A 2012, 116, 5145.
- 260. Y. S. L. V. Narayana, S. Basak, M. Baumgarten, M. Müllen and R. Chandrasekar, *Adv. Funct. Mater.* **2013**, 23, 5875.
- 261. E. M. Purcell, Phys. Rev. 1946, 69, 37.
- 262. S. R. Marder and J. W. Perry, Science **1994**, 263, 1706.
- 263. M. J. Cho, D. H. Choi, P. A. Sullivan, A. J. P.Akelaitis and L. R. Dalton, *Prog. Polym. Sci.* **2008**, *33*, 1013.
- 264. F. Peer and F. Hache, Chirality, 2005, 17, 421.
- 265. G. D. Fasman, *Circular Dichroism and Conformational Analysis of Biomolecules*, Plenum Press, **1996**.
- 266. N. Berova and K. Nakanishi, *Circular Dichroism: Principles and Applications*, Wiley-VCH, Weinheim, **2000**, 337.
- 267. A. Bobrovsky, V. Shibaev, A. Bubnov, V. Hamplova, M. Kaspar and M. Glogarová, *Macromolecules* **2013**, *46*, 4276.
- 268. P. Rizzo, C. Daniel and G. Guerra, *Macromolecules* 2010, 43, 1882.
- 269. E. A. Mamonov, I. A. Kolmychek, S. Vandendriessche, M.Hojeij, Y. Ekinci, V. K.

- Valev, T. Verbiest and T. V. Murzina, Phys. Rev. B 2014, 89, 121113.
- 270. E. Ozbay, *Science* **2006**, *311*, 189.
- 271. M. Aeschlimann, M. Bauer, D. Bayer, T. Brixner, F. J. García de Abajo, W. Pfeiffer, M. Rohmer, C. Spindler and F. Steeb, *Nature* **2007**, *446*, 301.
- 272. I. Lieberman, G. Shemer, T. Fried, E. M. Kosower and G. Markovich, *Angew. Chem. Int. Ed.* **2008**, *47*, 4855.
- 273. M. Schaferling, X. Yin and H. Giessen, Opt. Express 2012, 20, 26326.
- 274. S. Yoo and Q.-H. Park, Phys. Rev. Lett. 2015, 114, 203003.
- 275. N. Mitetelo, D. Venkatakrishnarao, J. Ravi, M. Popov, E. Mamonov, T. V. Murzina and R. Chandrasekar, *Adv. Opt. Mater.* **2019**, *7*, 1801775.
- 276. D. Venkatakrishnarao, E. A. Mamonov, T. V. Murzina and R. Chandrasekar, *Adv. Opt. Mater.* **2018**, *6*, 1800343.
- 277. F. Panzer, M. Sommer, H. Bässler, M. Thelakkat and A. Köhler, *Macromolecules* **2015**, *48*, 1543.
- 278. F. Panzer, H. Bässler and A. Köhler, J. Phys. Chem. Lett. 2017, 8, 114.
- 279. F. C. Spano and C. Silva, Annu. Rev. Phys. Chem. 2014, 65, 477.
- 280. D. Kim and J.-L. Brédas, J. Am. Chem. Soc. 2009, 131, 11371.
- 281. D. Alonso Doval and S. Matile, Org. Biomol. Chem. 2013, 11, 7467.
- 282. F. C. Spano, Acc. Chem. Res. 2010, 43, 429.
- 283. K. Hirose, S. Miura, Y. Senda and Y. Tobe, *Chem. Commun.* **2012**, *48*, 6052.
- 284. R. Gatri, I. Ouerfelli, M. L. Efrit, F. S. Spirau, J.-P. Porte, P. Valvin, T. Roisnel, S. Bivaud, H. A. Kilig and J.-L. Fillaut, *Organometallics* **2014**, 33, 665.
- 285. H.-J. Deussen, E. Hendrickx, C. Boutton, D. Krog, K. Clays, K. Bechgaard, A. Persoons and T. Bjørnholm, *J. Am. Chem. Soc.* **1996**, *118*, 6841.
- 286. H. Zhang, X. Zheng, R. T. K. Kwok, J. Wang, N. L. C. Leung, L. Shi, J. Z. Sun, Z. Tang, J. W. Y. Lam, A. Qin and B. Z. Tang, *Nat. Commun.* **2018**, *9:4961*, DOI: 10.1038/s41467-018-07299-3.
- 287. A. Banerjee, A. A. Ogale, C. Das, K. Mitra and C. Subramanian, *Heat Transfer Eng*, **2005**, *26*, 41.
- 288. K. Sugioka, M. Meunier and A. Piqué, *Laser Precision Microfabrication*, Springer Series in Materials Science, **2010**, vol. *135*, Springer-Verlag Berlin Heidelberg.
- T. P. Martin, A. J. Wise, E. Busby, J. Gao, J. D. Roehling, M. J.Ford, D. S.Larsen,
 A. J. Moulé and J. K. Grey, *J. Phys. Chem. B* 2013, 117, 4478.
- 290. N. Zhou and Y. Zhao, J. Org. Chem. 2010, 75, 1498.

References

291. M. E. Ziffer, S. B. Jo, Y. Liu, H. Zhong, J. C. Mohammed, J. S. Harrison, A. K.-Y Jen and D. S. Ginger, *J. Phys. Chem. C* **2018**, *122*, 18860.

Ph. No: +91-9550251262

E-mail: radhikavatikunta@uohyd.ac.in

Curriculum Vitae

Personal Details:

Name Radhika Vattikunta Father's name V. Bhaskar Naidu

Nationality Indian

Marital Status Not Married



Education Details:

2014-2019	Ph.D. in Materials Chemistry under the supervision of Prof. R. Chandrasekar, School of Chemistry, University of Hyderabad, India. Thesis Title : "Organic and Polymer Nonlinear Optical Micro-Resonators – A Single-Particle Micro-Spectroscopy Investigation"
2010-2012	M.Sc in Organic Chemistry with 82.2% at Sri Venkateswara University, Tirupati, Andhra Pradesh, India.
2007-2010	B.Sc in Chemistry , Biotechnology and Computer applications with 85.5% at Vignana Sudha Degree. College, Chittoor, Andhra Pradesh, India.
2004-2006	Intermediate in Chemistry, Physics and Biology with 97.1% at Sri Chaitanya Junior College, Tirupati, Andhra Pradesh, India.
1999-2004	S.S.C. with 93.2% at A.P. Residential school, Andhra Pradesh, India.

Awards and Recognitions:

- 2016-2019 Awarded as a Senior Research Fellow by CSIR-India.
- 2014-2016 Awarded as a Junior Research Fellow by CSIR-India.
- **February-2013** Qualified **GATE** in All India Level by New Delhi, India.
- June-2013 Qualified All India Level UGC-JRF by New Delhi, India.
- April-2012 Prof. M. C. Chenna Reddy memorial Gold medal in M.Sc Organic Chemistry by S V University, India.
- April-2012 Prof. S. Jayarami Reddy memorial Gold medal in M.Sc Organic Chemistry by S V University, India.
- April-2012 Prof. D. Bhaskar Reddy memorial Gold medal in M.Sc Organic Chemistry by S V University, India.
- April-2010, College topper in Bachelor's degree under S V University, India.

Organic and Polymer Nonlinear Optical Micro-Resonators - A Single-Particle MicroSpectroscopy Investigation

by Radhika Vattikunta

Submission date: 06-Dec-2019 03:46PM (UTC+0530)

Submission ID: 1228491675

File name: Radhika thesis 6-12-2019.pdf (8.39M)

Word count: 27366

Character count: 143131

Organic and Polymer Nonlinear Optical Micro-Resonators - A Single-Particle Micro-Spectroscopy Investigation

ORIGINALITY REPORT

23%

4%

21%

7%

SIMILARITY INDEX

INTERNET SOURCES

PUBLICATIONS

STUDENT PAPERS

PRIMARY SOURCES

Radhika Vattikunta, Dasari Venkatakrishnarao, Mahamad Ahamad Mohiddon, Rajadurai Chandrasekar. "Self-Assembly of "Chalcone" Type Push-Pull Dye Molecules into Organic Single Crystalline Microribbons and Rigid Microrods for Vis/NIR Range Photonic Cavity Applications", ChemPhysChem, 2016

5%

Publication

Dasari Venkatakrishnarao, Chakradhar Sahoo, Radhika Vattikunta, Mari Annadhasan et al. "2D Arrangement of Polymer Microsphere Photonic Cavities Doped with Novel N-Rich Carbon Quantum Dots Display Enhanced One- and Two-Photon Luminescence Driven by Optical Resonances", Advanced Optical Materials, 2017

4%

Radhika Vattikunta, Dasari Venkatakrishnarao, Chakradhar Sahoo, Sri Ram Gopal Naraharisetty et al. "Photonic Microresonators from Charge Transfer in Polymer Particles:

4%

Toward Enhanced and Tunable Two-Photon Emission", ACS Applied Materials & Interfaces, 2018

Publication

Radhika Vattikunta, Dasari Venkatakrishnarao, 4 Chakradhar Sahoo, Sri Ram Gopal Naraharisetty et al. "Photonic Microresonators from Charge-Transfer in Polymer Particles toward Enhanced and Tunable Two-Photon Emission", ACS Applied Materials & Interfaces, 2018

Publication

www.freepatentsonline.com 5 Internet Source

1%

1%

Theresa Eder, Thomas Stangl, Max Gmelch, 6 Klaas Remmerssen, Dirk Laux, Sigurd Höger, John M. Lupton, Jan Vogelsang. "Switching between H- and J-type electronic coupling in single conjugated polymer aggregates", Nature Communications, 2017

Publication

Dasari Venkatakrishnarao, Evgeniy A. Mamonov, Tatiana V. Murzina, Rajadurai Chandrasekar. "Advanced Organic and Polymer Whispering-Gallery-Mode Microresonators for Enhanced Nonlinear Optical Light", Advanced Optical Materials, 2018

<1%

Publication

Dasari Venkatakrishnarao, Chakradhar Sahoo, <1% 8 Evgeniy A. Mamonov, Vladimir B. Novikov et al. "Chiral organic photonics: self-assembled microresonators for an enhanced circular dichroism effect in the non-linear optical signal", Journal of Materials Chemistry C, 2017 Publication Tsuboi, Taiju, Zhong-fu An, Yosuke Nakai, Jun <1% 9 Yin, Run-feng Chen, Hui-fang Shi, and Wei Huang. "Photophysical properties of chirality: Experimental and theoretical studies of (R)- and (S)-binaphthol derivatives as a prototype case", Chemical Physics, 2012. Publication <1% Dasari Venkatakrishnarao, Mohamad Ahmed 10 Mohiddon, Rajadurai Chandrasekar. "The Photonic Side of Curcumin: Microsphere Resonators Self-Assembled from Curcumin Derivatives Emitting Visible/Near-Infrared Light", Advanced Optical Materials, 2017 Publication tsukuba.repo.nii.ac.jp <1% Internet Source Yemineni S. L. V. Narayana, Dasari 12

Venkatakrishnarao, Arani Biswas, Mahamad

Range Whispering Gallery Resonance from

Ahamad Mohiddon et al. "Visible-Near-Infrared

Photonic µ-Sphere Cavities Self-Assembled from a Blend of Polystyrene and Poly[4,7-bis(3-octylthiophene-2-yl)benzothiadiazole- -2,6-bis(pyrazolyl)pyridine] Coordinated to Tb(acac) ", ACS Applied Materials & Interfaces, 2015 Publication

13	Submitted to Savitribai Phule Pune University Student Paper	<1%
14	onlinelibrary.wiley.com Internet Source	<1%
15	Wei Zhang, Jiannian Yao, Yong Sheng Zhao. "Organic Micro/Nanoscale Lasers", Accounts of Chemical Research, 2016 Publication	<1%
16	Dasari Venkatakrishnarao, Yemineni S. L. V. Narayana, Mahamad A. Mohaiddon, Evgeniy A. Mamonov et al. "Two-Photon Luminescence and Second-Harmonic Generation in Organic Nonlinear Surface Comprised of Self- Assembled Frustum Shaped Organic Microlasers", Advanced Materials, 2017 Publication	<1%

Zhi-Hui Wen, Xue-Bo Yin. "Excitation-independent carbon dots, from photoluminescence mechanism to single-color application", RSC Advances, 2016

<1%

Publication

18	Kowtoniuk, W.E "Synthesis and competency of a novel dicationic phase-transfer catalyst", Tetrahedron: Asymmetry, 20040112 Publication	<1%
19	Wen-Jun Niu, Ye Li, Rong-Hui Zhu, Dan Shan, Yan-Rong Fan, Xue-Ji Zhang. "Ethylenediamine-assisted hydrothermal synthesis of nitrogen-doped carbon quantum dots as fluorescent probes for sensitive biosensing and bioimaging", Sensors and Actuators B: Chemical, 2015 Publication	<1%
20	Submitted to University of Hyderabad, Hyderabad Student Paper	<1%
21	thesis.library.caltech.edu Internet Source	<1%
22	www.beilstein-journals.org Internet Source	<1%
23	www.google.com Internet Source	<1%
24	Submitted to SASTRA University Student Paper	<1%
25	Submitted to Cardiff University Student Paper	<1%